iarigai
print and media research
www.iarigai.org

Advances in Printing and Media Technology

Vol. XLVI(VI)

Edited by Cathy Ridgway

Darmstadt
MMXIX

stuttiarigairt 2019

Advances in Printing and Media Technology

Proceedings of the 46th International Research Conference of iarigai
Stuttgart, Germany, 15–18 September 2019

Published by the International Association of
Research Organizations for the Information,
Media and Graphic Arts Industries
Darmstadt, Germany, 2019

Edited by Cathy Ridgway, Oftringen, Switzerland

Online edition
ISBN 978-3-948039-01-1
ISSN 2409-4021
DOI 10.14622/Advances_46_2019

Contents

Letter from the Organizer

Introduction to the proceedings of the iarigai conference 2019

The iarigai International Research Conference is the major scientific and technical annual event in the field of research in print and media. This year's conference, the 46th on "Advances in Printing and Media Technology" took place in Stuttgart, Germany from 15th to 18th September 2019, hosted by the Stuttgart Media University of Applied Sciences (Hochschule der Medien – HdM).

After the welcome reception on Sunday evening the first main conference day started with keynote speeches from industrial partners or industrial associations followed by one and a half day of parallel scientific tracks with top quality presentations. On the last conference day an industrial visit to Elanders printing group rounded up the program.

The topics covered during the two conference days dedicated for presentations showed the broad spectrum of the research going on in our industry. The majority of the submitted papers were in the field of process technology, however, colour science, print inspection, quality control and media perception were also included and especially hot topics like wearable electronics.

For those interested in rheological aspects of the printing process technology the talks on in-situ observations with high speed cameras of the screen printing and the roto-gravure process were for sure the highlights. However, there were very many other top level presentations, just to mention the paper on "Smart Materials Detection Using Computer Vision" who won the prize for the best presentation by voting of the participants.

I hope you will enjoy reading and we can stimulate you to submit a paper for the next conference at Clemson University Greenville, SC USA.

With my best regards,

Prof. Dr.-Ing. Gunter Hübner,
Conference Chair

Links:
Conference website: https://www.iarigai-stuttgart-2019.de/
Website of the IARIGAI: http://www.iarigai.org
Website of the HdM: www.hdm-stuttgart.de

Video Capturing of the Paste Transmission Process during Screen Printing – the impact of paste rheology on the screen printing process

Karim Abdel Aal, Ceren Yüce, Chenhui Xu and Norbert Willenbacher

Karlsruhe Institute of Technology (KIT)
E-mails: karim.abdelaal@kit.edu; norbert.willenbacher@kit.edu

Short abstract

In this study we present an experimental setup, which allows the real time imaging of printed fine line patterns in flatbed screen printing during the printing process. The width of printed lines is of great importance for the application of the screen printing technology in the field of solar cell front side metallization, where a high aspect ratio is mandatory. The setup consists of a high-speed camera, a camera adapter suitable for mounting a microscope objective, as well as a transparent printing substrate. The designed setup is applied to test new and innovative paste formulations for the application in front side metallization of solar cells. The used metallization paste formulations are based on the capillary suspension concept and therefore do not use any polymeric thickeners or thixotropic agents. This leads to a higher purity of the sintered metallization finger line. The paste rheology is characterized in terms of the paste yield stress as well as the fracture strain in uniaxial elongational deformation. The achievable insights into the paste transfer process during screen printing is demonstrated using three different model pastes. With the use of high-speed video recording during the printing experiments formation and spreading of the printed metallization finger is monitored and changes due to sample composition are discussed.

Keywords: high-speed imaging, solar cell metallization, capillary suspension concept, screen printing

1. Introduction and background

The production of energy from renewable resources is gaining increasing relevance and photovoltaics technology plays an important role in the given field. With having a global peak capacity of 402.15 GWp installed in 2017 it can be expected, that the global installed photovoltaic capacity will grow up to about 630 GWp by the end of 2019 (Werner, et al., 2017). Due to its cost efficiency, the ease of the process and its speed the screen printing process is the state of the art in industrial solar cell front side metallization (Schubert, Huster and Fath, 2006; Erath, et al., 2010; Lorenz, et al., 2017). In order to reduce shading losses, it is necessary to minimize the line width of the printed front side contacts while maintaining a high aspect ratio. To accomplish this goal, it is important to look at the printing process itself, as well as to tailor the printing paste rheology to meet the complex requirements. Conventional pastes applied in the front side metallization of solar cells consist of the silver particles, glass frit and a vehicle which is composed of organic solvents and rheology additives like thickeners or thixotropic agents (Faddoul, Reverdy-Bruas and Blayo, 2012). In order to achieve a high conductivity in the sintered contact line it is important that non-conductive impurities burn off during the sintering process. It has already been shown, that an alternative formulation avoiding non-volatile ingredients for conductive inks based on the capillary suspension principle is possible (Schneider, Koos and Willenbacher, 2016) such as front side metallization of solar cells, without non-volatile, organic additives that often deteriorate electrical properties. Adding a small amount of a second, immiscible fluid to a suspension creates a network of liquid bridges between the particles. This capillary force-controlled microstructure allows for tuning the flow behavior in a wide range. Yield stress and low-shear viscosity can be adjusted such that long-term stability is provided by inhibiting sedimentation, and, even more importantly, narrow line widths and high aspect ratios are accessible.

These ternary mixtures, called capillary suspensions, exhibit a strong degree of shear thinning that allows for conventional coating or printing equipment to be used. Finally, the secondary fluid, beneficial for stability and processing of the wet paste, completely evaporates during drying and sintering. Thus, we obtained high purity silver and nickel layers with a conductivity two times greater than could be obtained with state-of-the-art, commercial materials. This revolutionary concept can be easily applied to other systems using inorganic or even organic conductive particles and represents a fundamental paradigm change to the formulation of pastes for printed electronics. Highly conductive, printable pastes from capillary suspensions (Schneider, Koos and Willenbacher, 2016. The capillary suspension concept is based on particle – liquid – liquid interactions, which appear if both liquids are not miscible (Koos, 2014). The capillary suspension phenomenon leads to the formation of a network stabilizing the sample at rest which on the other hand disappears under the influence of shear forces. This allows the paste to pass even very narrow gaps in the mesh of the screen and regain its structure shortly after cessation of the strain.

Numerical simulations have been employed to predict the release of the ink from the screen and its dependency on the surface energy of the printing paste, the emulsion layer on the screen and the substrate (Schwanke, 2010). Despite that, it is of high scientific value to capture the printing process with a high-speed imaging device during real printing experiments. Printing on a glass substrate enables footage of the paste spreading during the printing from below the substrate, while the surface properties of the glass can be changed from its intrinsic hydrophilicity to a hydrophobic behaviour using a silylation reaction (Bossler, et al., 2018). This kind of reaction to alter the surface properties of glass substrates has already been used to modify silica particles (Bossler, et al., 2018). It has been shown with zinc oxide model pastes, that this high-speed video capturing opens up the possibility to compare and evaluate different paste formulations with respect to their printability, the relevant time scales of the physical effects and the paste behaviour during the process of printing (Xu and Willenbacher, 2018).

These studies revealed, that for the zinc oxide model pastes based on conventional formulation approaches with rheological additives the time scale of the relevant process is on the order of about 50–100 ms. Thus structure recovery tests like the frequently used three interval thixotropic test cannot cover the relevant time scale (Xu and Willenbacher, 2018).

One of the difficulties of high-speed video captures is to bring enough light into the system to generate clear images at frame rates of 500 fps to 1 000 fps with the corresponding short shutter times of up to 0.002 seconds to 0.001 seconds.

In this work we present a setup, which opens up the possibility to capture the release of the paste during the fine line screen printing process. Furthermore, we show the application of such a system by comparing three capillary suspension formulations for solar cell front side metallization with respect to the change of their lateral dimension while printing a solar cell pattern.

2. Materials and methods

The high speed image capturing setup requires a high-speed camera with the option to adjust the shutter time (e. g. Photron FastCam – X1024 PCI) as well as an adapter to ensure that enough light will be transmitted into the system to allow the capturing of clear pictures at low shutter times. Therefore, the light will be focused just on the spot where the actual image is taken by the camera adapter without the use of an independent exposure unit. The setup has been used to monitor and compare the paste spreading of three capillary suspension model pastes for solar cell front side metallization. These pastes do not use any rheological additives but a secondary fluid immiscible with the bulk fluid used to suspend the particles to induce self-assembly of the particles into a percolating network stabilizing the sample.

2.1 Camera adapter for high-speed video imaging

The design of the camera adapter for the high-speed video imaging is shown in Figure 1. The device consists of a LED light source, which is attached at the side of the camera adapter (1). On the bottom of the adapter a C-mount thread (2) is attached to allow for a connection to the standardized camera mounting system. A beam splitter (3), which is framed by an appropriate mounting (4) can be fixed by two polymer screws on the sides of the system. An additional mounting (5) is used to attach the objective (6) providing the necessary magnification of the picture. The objective is fastened with the help of the polymer screws attached at the side of this mounting. The setup is adaptable to different microscope objectives like the Olympus "LMPLFLN 10x" or a Nikon "LU Plan ELWD 20x/0.4A". Due to light reflections caused by the beam splitter and the mounting itself, it is important that the camera software allows a precise shutter control to achieve a clear image (e.g. Photron Fastcam Viewer).

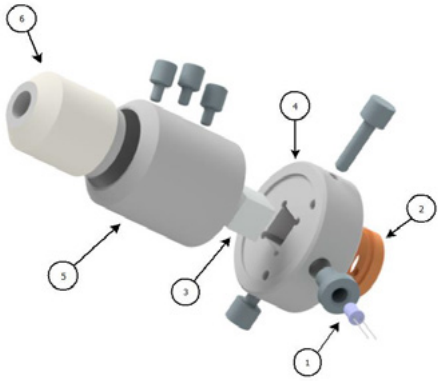

Figure 1: Camera adapter for high-speed video imaging with light source (1), C-mount thread (2), beam splitter (3), housing parts (4, 5) and microscope objective (6)

2.2 Formulation of capillary suspension printing pastes

With the use of the capillary suspension concept three pastes with different secondary liquids were designed, paste 1, paste 2 and paste 3, respectively. The different secondary liquids lead to different yield stress values in the corresponding pastes. The three model pastes were formulated, based on hydrophobically modified silver particles (Metalor Technologies (UK) Ltd., Product code K-7418P). The particles are of a spherical shape with an average diameter X_{50} = 2.05 µm and 99 % of all particles are smaller than 4.78 µm. The particles were suspended at a mass fraction of 82.0 % in glycerol as a bulk phase together with 5 vol. % of the secondary liquid in a non-contact planetary mixer (SpeedMixer™, Hausschild GmbH) for 30 seconds at 2 000 rpm. The deagglomeration step was performed in a three-roll mill (EXAKT 80E, EXAKT Advanced Technologies GmbH) at 90 rpm with stepwise decreasing gaps from 40 µm to 7 µm. To remove incorporated air bubbles a final speed mixing step with the settings mentioned above was conducted.

The pastes were characterized by measuring the yield stress on a stress controlled rheometer (Haake RS150, Thermo Fisher Scientific) with a vane-and-cup geometry in a stepwise controlled creep test. The Measuring program consist of 41 measurement points distributed logarithmically in a range from 1 Pa to 5 000 Pa at 23 °C. The fracture strain in uniaxial elongational deformation was determined using a capillary breakup elongation rheometer (HAAKE CaBER1, Thermo Fisher Scientific, Karlsruhe, Germany) with a video recording modification according to the protocol described by Yüce and Willenbacher (2017).

Printing was performed using a lab scale screen printer (EKRA E2, ASYS Group GmbH). The protocol includes a printing speed of 100 mm/s, a flooding speed of 400 mm/s, a snap off distance of 1.6 mm, and a squeegee pressure of 75 N/cm. The observed pattern is a 35 µm screen opening in a screen with an emulsion layer thickness of 17 µm (Mesh 360; Thread 16 µm; Tension 25 N/cm).

Pictures of the paste spreading process were taken with the objective “Olympus LMPLFLN 10x” at a rate of 1 000 fps, resulting in a size of 0.724 µm per pixel at a resolution of 1 708 x 832 pixels.

3. Results and discussion

The three prepared model pastes strongly differ with respect to their yield stress and fracture strain as is shown in Figure 2. Obviously, the rheological parameters are linearly related for the pastes investigated here. The higher the yield stress, the more rigid is the paste, which leads to a breakage at lower strains.

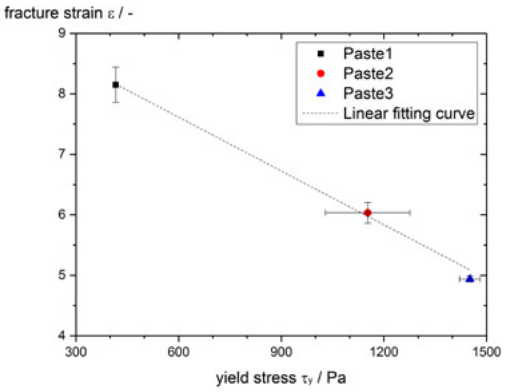

Figure 2: Fracture strain versus the yield stress of the three model capillary suspension pastes

This behaviour of the capillary suspension model pastes fits well with earlier results found investigating the paste rheology of model silver pastes using thixotropic agents and ethyl cellulose binder to adjust the paste rheology (Yüce, König and Willenbacher, 2018).

The fracture strain of a paste also has an impact on the screen printing process. The high-speed video captures in earlier investigations with zinc oxide model pastes have shown, that the length of the cling zone, i. e. the zone where the screen sticks to the substrate in between the squeegee and the screen snap off, is dependent on the height of the fracture strain (Xu and Willenbacher, 2018). The printing tests performed here with the capillary suspension silver pastes support this finding.

In Figure 3 the length of the observed cling zone and the measured fracture strain are correlated. There is a clear trend to a lower cling zone length with decreasing fracture strain visible, which supports the hypothesis that these quantities are directly correlated irrespective of the paste formulation concept and hence of additive used to control rheology.

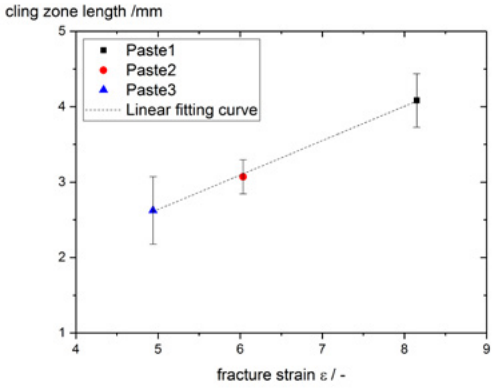

Figure 3: Length of the observed cling zone versus the measured fracture strain

Figure 4 demonstrates the evolution of the printed metallization finger width during the printing process. The process can be divided into three regimes. In the beginning, 5 ms after the passage of the squeegee the width significantly exceeds the screen opening which indicates that the paste is getting pushed in between the screen and the substrate due to the high pressure of the squeegee coupled with incomplete sealing of the gap between screen and substrate by the emulsion layer. The observed minimum in the finger width occurs at about 26 ms to 40 ms after the squeegee passage which roughly corresponds to the snap off time. All pastes show the same pattern of spreading, retraction and spreading again and considering the scatter in data for several printing runs with the same paste there is no significant difference in the absolute values of transient finger width. This behaviour seems to be characteristic for capillary suspensions and the time evolution of finger width seems not to depend on the paste's yield stress. Earlier studies with ZnO pastes including conventional polymeric rheology control agents, however, exhibited a monotonic increase in finger width (Xu and Willenbacher, 2018). Due to cohesive forces in the paste and the snap off of the screen the paste gets pulled back. The subsequent broadening of the fingers is a result of the sagging due to gravitation and an equilibrium value is reached after about 150 ms, which is in the same range as observed for conventional ZnO pastes in the aforementioned study (Xu and Willenbacher, 2018).

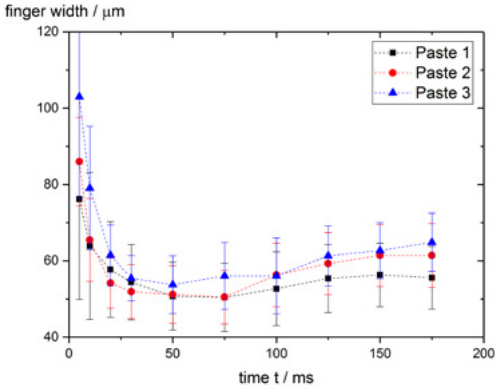

Figure 4: Evolution of the finger width over time during the printing process

The here presented setups offers new opportunities to evaluate pastes, printing screens as well as the different printing parameters in terms of the paste transfer to the substrate and printed fine line structure width.

4. Conclusions

The implemented high-speed video recording system for the screen printing process opens up new opportunities to gain insights in the interplay of the printing parameters, the screen properties and the paste properties. A possible adjustment of the used glass plates surface hydrophobicity offers the opportunity to change the pairing of surface energies of screen emulsion, substrate and paste. The setup allows a real time recording of paste injection, line formation and spreading with high spatial and temporal resolution. For the capillary suspension pastes investigated here the evolution of finger width can be divided into three regimes, a regime of spreading of the paste due to the pressure of the squeegee, a regime of retraction and minimum finger width, shortly after the screen snap off and a regime of subsequent sagging and broadening of the structure due to gravity. This is different from the monotonic spreading observed earlier for ZnO pastes including conventional polymeric rheology control agents and the total duration of fine line formation is about 150 ms for the capillary suspension pastes, which is slightly higher compared to the ZnO pastes (Xu and Willenbacher, 2018). The length of the cling zone increases linearly with increasing fracture strain, similar as that of the conventional ZnO pastes. The here prepared capillary suspension model pastes show a reciprocal relation of fracture strain and paste yield stress. A similar correlation was observed in an

earlier study based on silver model pastes formulated with the aforementioned conventional stabilization concept (Yüce, König and Willenbacher, 2018)rheology and screen-printed line morphology is essential. Three model pastes with similar silver content and corresponding vehicles differing in their thixotropic agent content were investigated. Rheological properties (yield stress, viscosity, wall slip velocity, structural recovery, and fracture strain. Further investigations with the presented setup will allow for an evaluation of the influence of different printing parameters, as well as different screen and paste properties on paste injection and line formation.

Acknowledgements

Financial support by the foundation '100 prozent erneuerbar' is greatly acknowledged.

References

Bossler, F., Maurath, J., Dyhr, K., Willenbacher, N. and Koos, E., 2018. Fractal approaches to characterize the structure of capillary suspensions using rheology and confocal microscopy. *Journal of Rheology*, 62(1), pp. 183–196. https://doi.org/10.1122/1.4997889.

Erath, D., Filipović, A., Retzlaff, M., Goetz, A.K., Clement, F., Biro, D. and Preu, R., 2010. Advanced screen printing technique for high definition front side metallization of crystalline silicon solar cells. *Solar Energy Materials and Solar Cells*, 94(1), pp. 57–61. https://doi.org/10.1016/j.solmat.2009.05.018.

Faddoul, R., Reverdy-Bruas, N. and Blayo, A., 2012. Formulation and screen printing of water based conductive flake silver pastes onto green ceramic tapes for electronic applications. *Materials Science and Engineering: B*, 177(13), pp. 1053–1066. https://doi.org/10.1016/j.mseb.2012.05.015.

Koos, E., 2014. Capillary suspensions: particle networks formed through the capillary force. *Current Opinion in Colloid & Interface Science*, 19(6), pp. 575–584. https://doi.org/10.1016/j.cocis.2014.10.004.

Lorenz, A., Linse, M., Frintrup, H., Jeitler, M., Mette, A., Lehner, M., Greutmann, R., Brocker, H., König, M., Erath, D. and Clement, F., 2017. Screen printed thick film metallization of silicon solar cells – recent developments and future perspectives. In: P. Verlinden, R. Kenny and P. Helm, eds. *Proceeding of the 35th European Photovoltaic Solar Energy Conference and Exhibition*. Brussels, Belgium, 24–28 September 2017. Munchen, Germany: WIP, pp. 819–824. https://doi.org/10.4229/35thEUPVSEC20182018-2DV.3.65.

Schneider, M., Koos, E. and Willenbacher, N., 2016. Highly conductive, printable pastes from capillary suspensions. *Scientific Reports*, 6(August): 31367. https://doi.org/doi: 10.1038/srep31367.

Schubert, G., Huster, F. and Fath, P., 2006. Physical understanding of printed thick-film front contacts of crystalline Si solar cells - review of existing models and recent developments. *Solar Energy Materials and Solar Cells*, 90(18–19), pp. 3399–3406. https://doi.org/10.1016/j.solmat.2006.03.040.

Schwanke, D. ed., 2010. *Entwicklung nanotechnologischer Siebbeschichtungen und daran angepasster Pastensysteme für den Fine-Line-Druck von keramischen Schaltungsträgern: Ergebnisbericht des BMBF-Verbundprojekts 'nanoSieb'*. Templin, Germany: Detert.

Werner, C., Gerlach, A., Breyer, C. and Masson, G., 2017. Established and emerging solar markets in 2017: overview on global solar market development. In: P. Verlinden, R. Kenny and P. Helm, eds. *Proceeding of the 35th European Photovoltaic Solar Energy Conference and Exhibition*. Brussels, Belgium, 24–28 September 2017. Munchen, Germany: WIP, pp. 2109–2121. https://doi.org/10.4229/35thEUPVSEC20182018-7DO.3.2.

Xu, C. and Willenbacher, N., 2018. How rheological properties affect fine-line screen printing of pastes: a combined rheological and high-speed video imaging study. *Journal of Coatings Technology and Research*, 15(6), pp. 1401–1412. https://doi.org/10.1007/s11998-018-0091-2.

Yüce, C., König, M. and Willenbacher, N., 2018. Rheology and screen-printing performance of model silver pastes for metallization of Si-solar cells. *Coatings*, 8(11): 406. https://doi.org/10.3390/coatings8110406.

Yüce, C. and Willenbacher, N., 2017. Challenges in rheological characterization of highly concentrated suspensions – a case study for screen-printing silver pastes. *Journal of Visualized Experiments*, 122: e5537. https://doi.org/10.3791/55377.

High Speed Imaging of Ink Separation in Screen-Printing

Sarah-Jane Potts, Chris Phillips and Tim Claypole

Welsh Centre for Printing and Coatings, College of Engineering, Swansea University, Bay Campus, Crymlyn Burrows, Swansea SA1 8EN, UK
E-mail: Sarah-Jane.Potts@Swansea.ac.uk

Short abstract

Screen-printing is a versatile process used to print a wide range of printed electronics. However, there is a limited understanding of how the ink is deposited from the mesh to the substrate. Mathematical models have been suggested in the past, but there is not sufficient experimental evidence to validate them. In order to identify key transfer mechanisms and their impact on the process, an investigation was instigated which focussed on the separation mechanism occurring when the mesh is contacted and released from the substrate. high-speed video imaging was used to assess the deposition and separation of a commercial carbon ink when printed at a range of line widths from 50 µm to 400 µm as an essential step in the development and validation of predictive models. The length of ink bridging the mesh and substrate increased with line width. The ink separation process could be split up into separate stages of adhesion, extension, flow and separation suggested in the theory by Messerschmitt. The adhesion and extension stages were longer than the flow and separation stages for all line widths assessed.

Keywords: carbon, inks, printed electronics

1. Introduction

Due to its versatility and ability to print a relatively wide viscosity range of inks, screen printing is widely used in the manufacture of a range of printed electronics applications including printed antennas (Janeczek, et al., 2012), resistive heaters (Philip, et al., 2016), sensors (Tehrani, et al., 2014), printed batteries (Tehrani, et al., 2015), and Perovskite PV (Zhang, et al., 2015; Baker, et al., 2017).

However, due to limitations in modelling the rheological properties of screen-printing inks (Riemer, 1988b: 1988c; 1989), it has been a challenge to develop predictive models of the screen-printing process. This leaves a lack of understanding in the physics mechanisms which enable screen printing to occur. Computational fluid dynamics (CFD) models have been developed to assess the both Newtonian and Non-Newtonian inks (Riemer, 1989; Fox, Claypole and Gethin, 2003; Kapur, et al., 2013; Xu and Willenbacher, 2018) based on mathematical models derived by Riemer (1971; 1988a, 1988b; 1988c) and Messerschmitt (1982) to predict how the ink flows during the deposition of the ink and following separation from the mesh. Riemer (1988b) suggested that there are two key forces occurring during separation, where the wires are pulled up by the forces acting in the mesh and countered by a downward force acting between the paste and mesh.

Alternatively, Messerschmitt suggested that these separation forces would be insufficient to break the adhesion between the ink and the mesh, but could induce a flow which would create a shearing action within the ink, that could cause a cohesive failure (Fox, Claypole and Gethin, 2003). Messerschmitt summarised this process as four key stages of ink transfer, consisting of adhesion, extension, flow and separation. The final stage consisted of ink splitting, where ink remains on both the surface of the mesh and the surface of the substrate in the form of the print. (Messerschmitt, 1982)

A high-speed video imaging study on fine line screen printed ZnO pastes was conducted by Xu and Willenbacher (2018), where the deposition process was imaged from below the substrate, looking up at the print. Their work identified three main regions, including the pre-injection zone (the ink deposited ahead of the squeegee), the cling zone, from the nip contact point to snap off position as defined by Riemer (1989), as well as the paste spreading, where the ink slumps after it has been deposited. Although these findings provide an insight into the size of the cling zone and quantity of paste spreading after print deposition, they do not confirm whether or not the separation models suggested by Riemer and Messerschmitt were in fact correct.

In order to identify key transfer mechanisms and their impact on the process, an investigation was instigated which focussed on the separation mechanism which occurring when the mesh is contacted and released from the substrate. This has implications for the development of scalable processes, material optimization and ultimately productivity.

2. Materials and methods

2.1 Screen-printing visualisation method

Printing was conducted on a custom-made screen-printing simulation rig, as illustrated in Figure 1, using a 110 mm × 80 mm polyester mesh at 22.5º with 61 threads per cm, 64 µm thread diameter and 12-micron emulsion (produced by MCI Precision Screens), a 2mm snap-distance, 70-75 Shore A hardness diamond squeegee and print speeds of 300cm/s. The substrate was PET (polyethylene terephthalate—Melinex® 339, DuPont Teijin Films (175 µm thickness) opaque white). The print image consists of a continuous 32 mm long line made up of five 6 mm long sections as shown in Figure 2. High speed imaging was conducted with a Photron FastCam Mini High-Speed Camera (Figure 1), with backlighting.

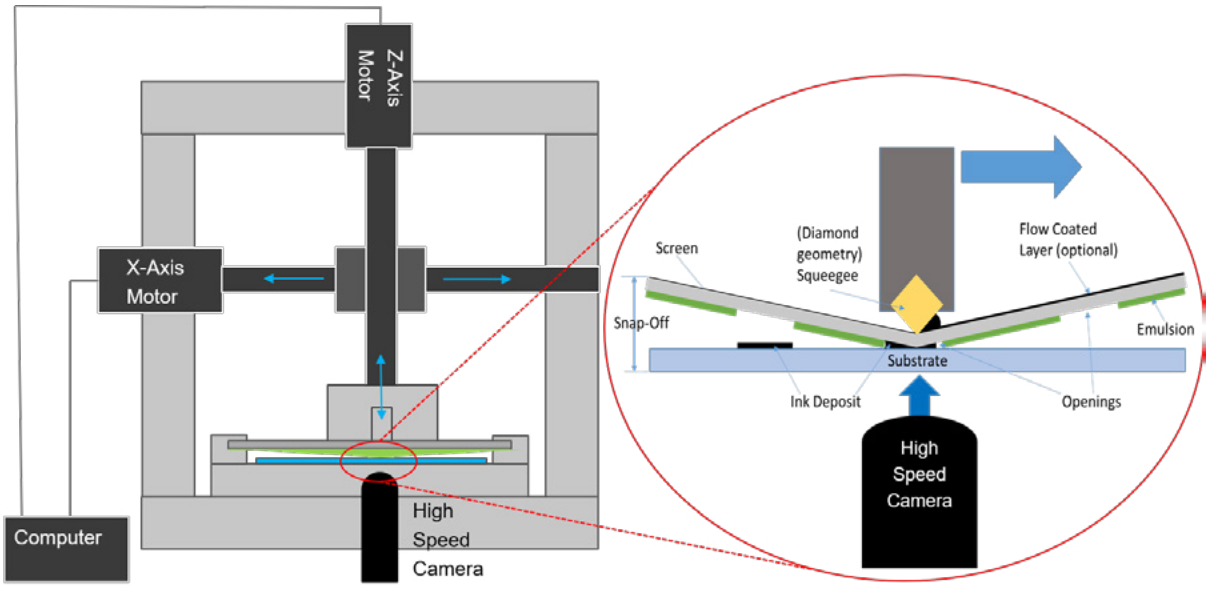

Figure 1: Diagram of the custom-made screen-printing simulation rig with a cross sectional schematic diagram of the screen-printing process, showing the positioning of the high-speed camera

Figure 2: Print image design consisting of 6mm long sections reducing from 400 µm to 25 µm (400 µm, 200 µm, 100 µm, 50 µm and 25 µm) in line width

2.2 Ink

A carbon ink by Gwent Electronics Materials (GEM) (GEM C2150317D3 carbon paste (38-42 % solid content)) was used. The shear viscosity of the ink was measured using a rheometer (Gemini Bohlin Nano, Malvern Instruments) with a 2° 20 mm stainless steel cone and a parallel plate held at 25 °C over a shear rate range of 1 s^{-1} to 100 s^{-1}. Ink viscosity was measured as the shear rate was increased to 100 s^{-1} and then reduced back to 1 s^{-1}. As shown in Figure 3 (a), the ink is highly pseudoplastic, with a reduction in viscosity as the shear stress is increased, particularly from 1 s^{-1} to 50 s^{-1}. The viscoelasticity of the ink was also assessed using an oscillatory test conducted at 1 Hz over a strain range from 0.1 to 10. At the linear viscoelastic region, at a strain of around 0.3, the ink displays a phase angle (loss angle) of around 30º which increases with strain, as shown in Figure 3b.

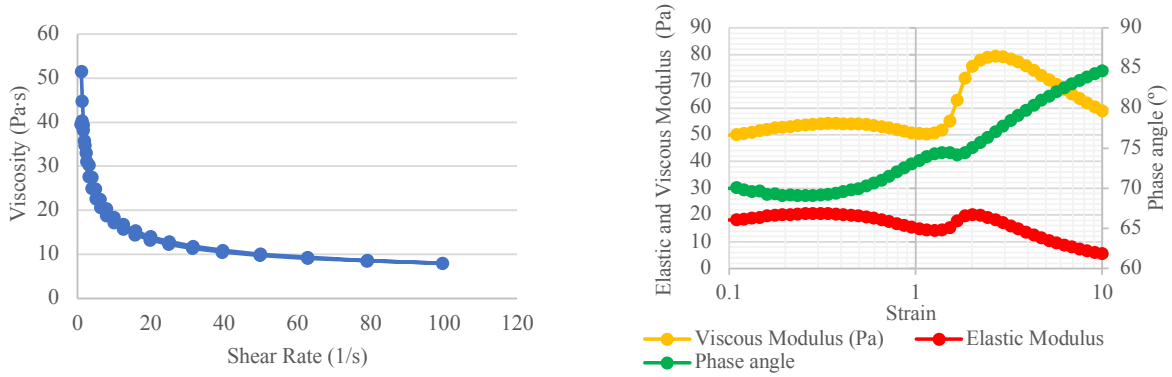

a) *b)*

Figure 3: Viscosity profile (a) and viscoelastic profile (b) of the carbon ink assessed

2.3 Printed ink geometry and surface topography measurement

Print topography analyses were conducted to assess the printed lines. White light interferometry (NT9300, Veeco Instruments, Inc., Plainview, NY, USA) was used to measure a full three-dimensional surface profile of the printed line geometries at five times magnification over 4 evenly spaced intervals. Geometric features were assessed by taking discrete measurements over the 1.2 mm-length sections measured by the interferometer (736 measurements at 1.67 µm intervals for each measured section). From this the standard deviation in line width and thickness was calculated.

2.4 Assessment of high-speed camera images

The high speed camera images were assessed using ImageJ (Rueden, et al., 2017)) to quantify the lengths of different regions of the print cycles. Measurements of these lengths were conducted over 15 evenly spaced intervals throughout the section of the print runs where the full contact region could be clearly identified and measured. From these 15 measurements, the average region lengths and their standard deviations were calculated.

3. Results

3.1 Printed ink geometry and surface topography measurement

Topographies for the different printed line widths are displayed in Figure 4. with the corresponding average printed line widths and film thicknesses for the continuously printed lines shown in Figure 5.

The average film thicknesses increased with line widths. Leading to an overall large increase in the volume of ink being deposited. However, as the ink used is optimised for large area prints rather than fine lines, there is a lot of ink slump and spreading around the line edges. This means that far greater line widths are produced than the size of the lines on the mesh. Although the trends for the increase in line width and film thickness are consistent with one another, as shown in Figure 5.

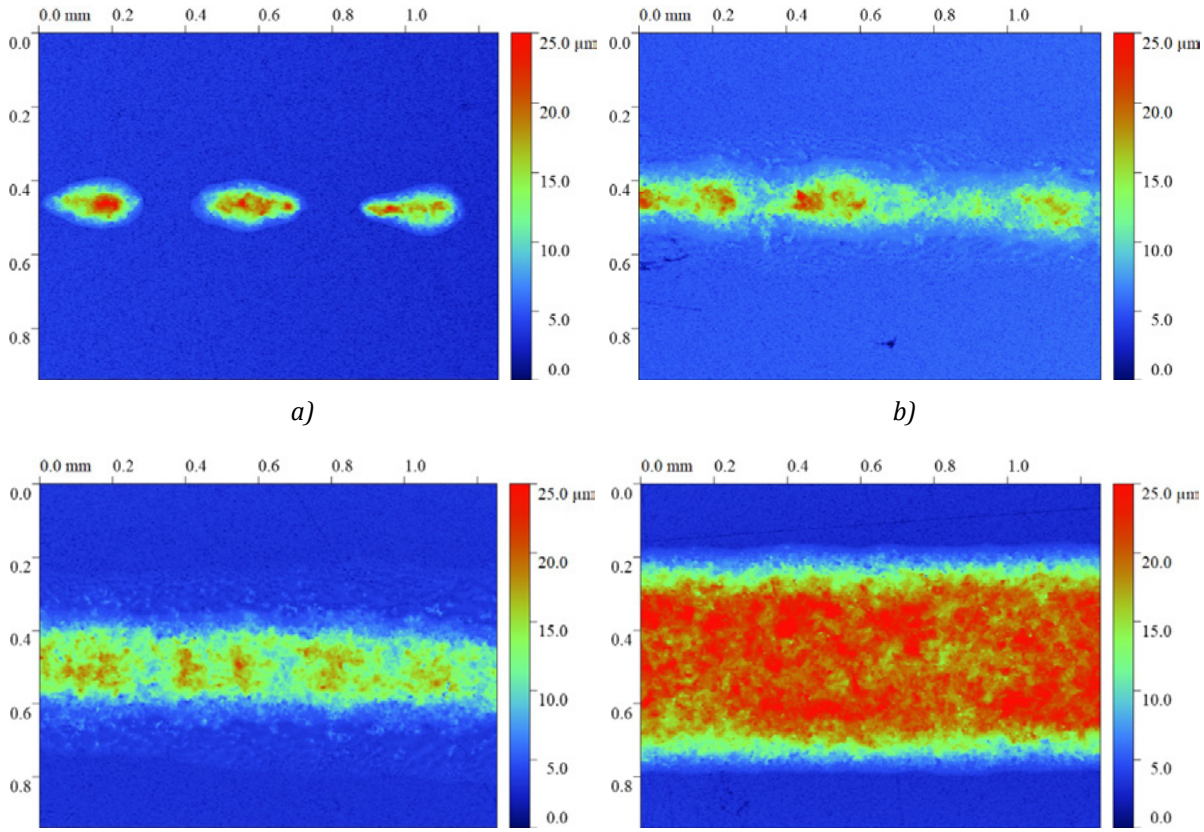

Figure 4: White light interferometry images of the prints conducted through the (a) the 50 µm line, (b) 100 µm line, (c) 200 µm line and (d) the 400 µm line

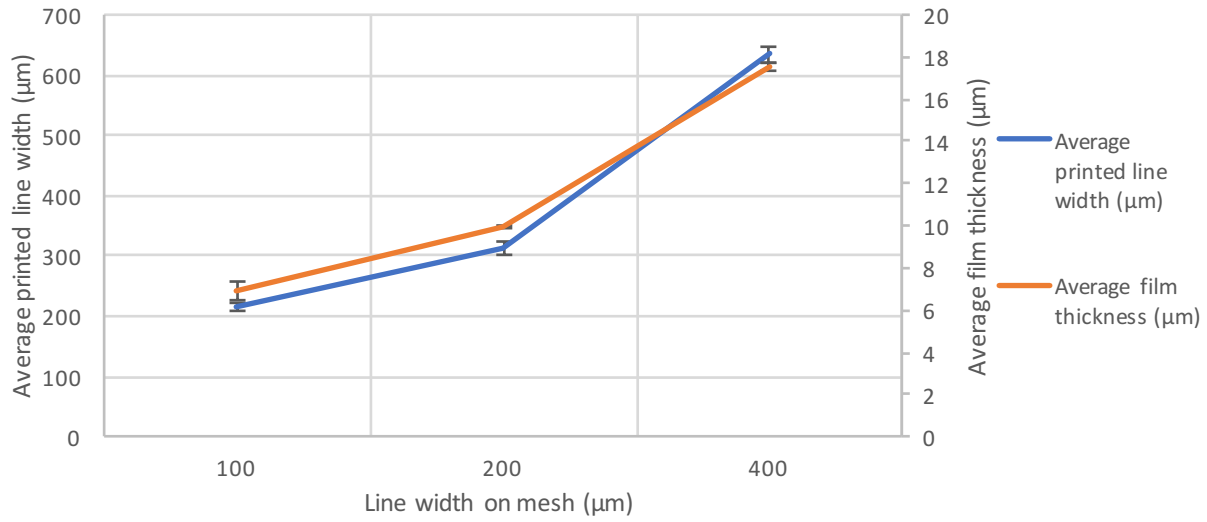

Figure 5: Change in average printed film thickness and line width with increases in line width on mesh

3.2 Assessment of high-speed camera images

The ink deposition process could be split up into quantifiable regions. The flow mechanisms observed in Figure 6 are best supported by Messerschmitt's theory (Messerschmitt, 1982) with four stages of ink deposition; adhesion, extension, flow and separation, Where the separation forces appear to induce a flow that causes a shearing action, leading to the ink splitting. (Messerschmitt, 1982) There was no clear correlation with Riemer's theory of the mesh forcing the ink onto the substrate as columns which remain on the substrate due to adhesion and slump once the mesh is removed. (Riemer, 1989) However, Messerschmitt's theory did not outline the length or duration of the four stages, which can be quantified with these results. Together, these make up the ink separation stages. The overall length of the full contact region, including the paste flow region ahead of the squeegee, was also measured.

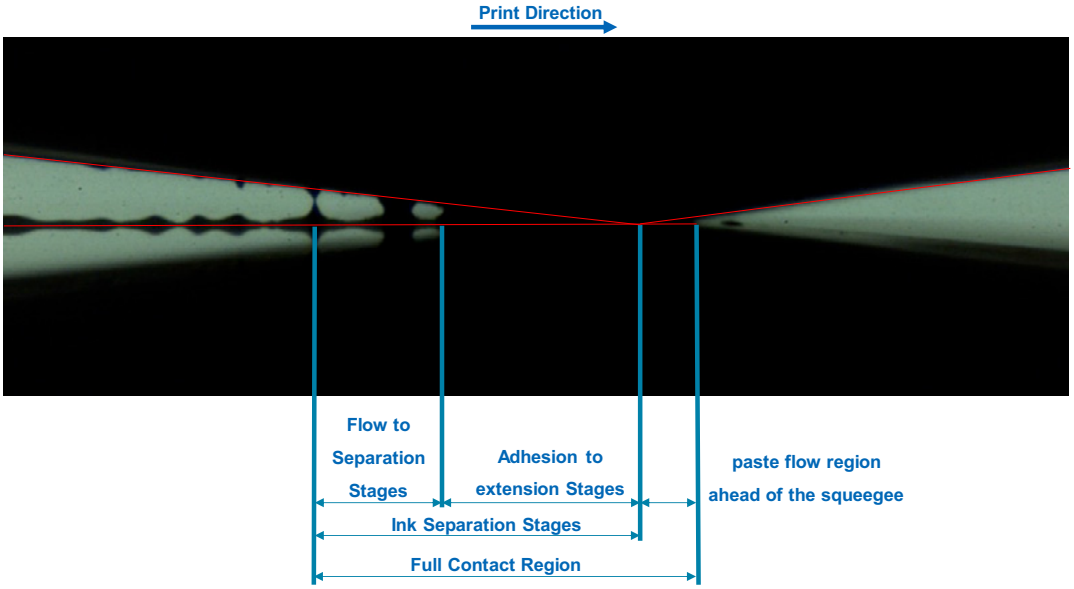

Figure 6: Different stages occurring during ink deposition and separation

The images of each line width, (Figure 7), were measured to identify the change in the length of different flow regions with increasing line width, (Figure 8).

The length of the contact regions tended to increase with line width. The 50 µm line produced a non-continuous line, due to the mesh hole thread sizes and ink particle sizes being too large to print a continuous line. This line width was assessed only in relation to the points of separation, as shown in the in Figure 8a. The other printed line widths were also assessed over regular time intervals with measurements taken every 3 frames (0.024 s) to provide a representative study of the print duration, (Figure 8b).

The 50 µm line produced the shortest contact region out of the line widths. It was also found to have a flow to separation region which was greater than the adhesion to extension region. The 100 µm line had a larger overall contact region (when measured in relation to separation points) (Figure 8), but with a reduction in the average length of the flow to separation stages and an increase in the average length of the adhesion to extension regions, along with an increase in the paste flow region ahead of the squeegee. The same trends are seen with the measurements conducted over regular time intervals (Figure 8b). The alteration in the ratio of the ink separation stages lengths is most likely as the 100 µm line produced a continuous print. When increasing the line width to 200 µm, there is an increase in all of the contact regions when measured both in relation to the snap positions and over regular time intervals. This is also observed when increasing the line width further to 400 µm.

There is a near linear increase in the average full contact regions, with an overall increase in the adhesion to extension stages and the flow to separation stages, where the adhesion to extension stages remained longer than the flow to separation stages for the 100 µm, 200 µm and 400 µm lines. This could be due to increases in line width leading to increases in adhesive forces, causing the ink to remain bridging the mesh and substrate until a separation distance capable of producing sufficient shear force is reached. As the film thickness increases with increasing line widths, the increase in contact region lengths may lead to more ink remaining on the substrate during separation.

The distances between the separation positions were also measured over the print cycle for the different line widths. However, these could not be quantified for the 400 µm line as there were multiple openings in parallel across the line width, making it unclear as to which point was separating using 2-dimensional assessments. The average distances between separation points for the line widths assessed are shown in Figure 9. The 50 µm line had an average distance of 477 µm between each of the separation points, located on each of the discrete deposits. For the continuous lines, the average distance between separation points was 294 µm for the 100 µm line and 323 µm for the 100 µm line. This variation in frequency of separation positions, as well as variations in separation region lengths, could be due to fluctuations in ink flow over the print duration due to the complex rheological profile of the ink, the range of particle sizes in the ink and changes in the angle between the mesh and substrate (snap-off angle) as well as print pressure during separation. By comparing these lengths with microscopy images of the mesh used, separation was found to occur around every two to three threads for these 100 µm and 200 µm lines (Figure 10).

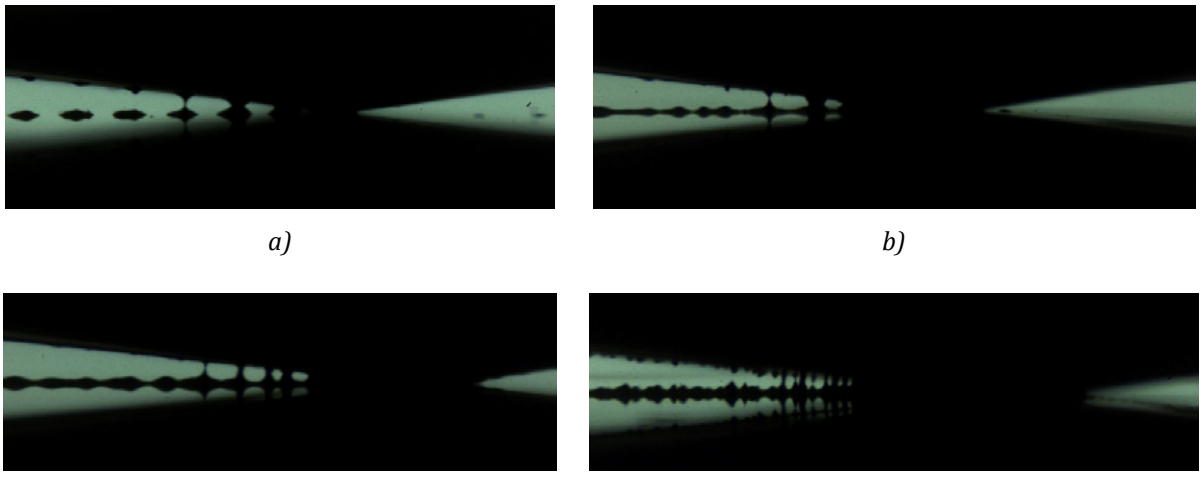

a) *b)*

c) *d)*

Figure 7: High-speed camera images of the deposition of (a) the 50 µm line, (b)100 µm line, (c) 200 µm line and (d) the 400 µm line

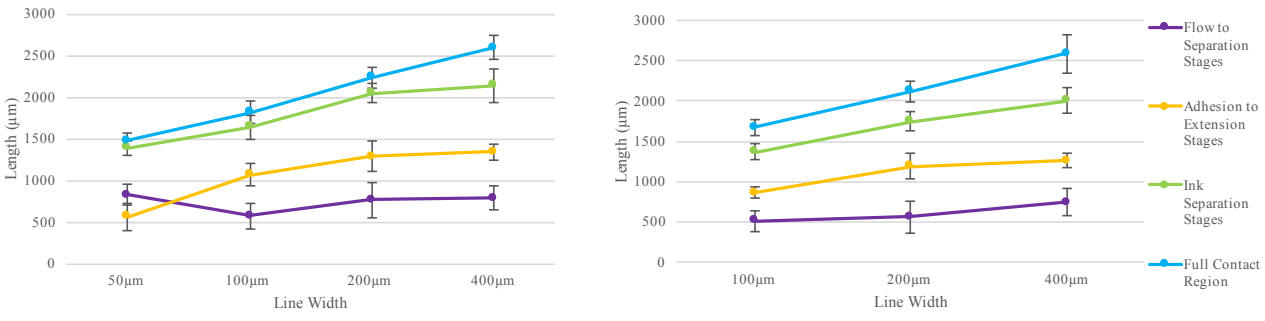

a) *b)*

Figure 8: Change in contact regions with line width (a) in relation to snap positions and (b) when conducted over regular time intervals (Image J)

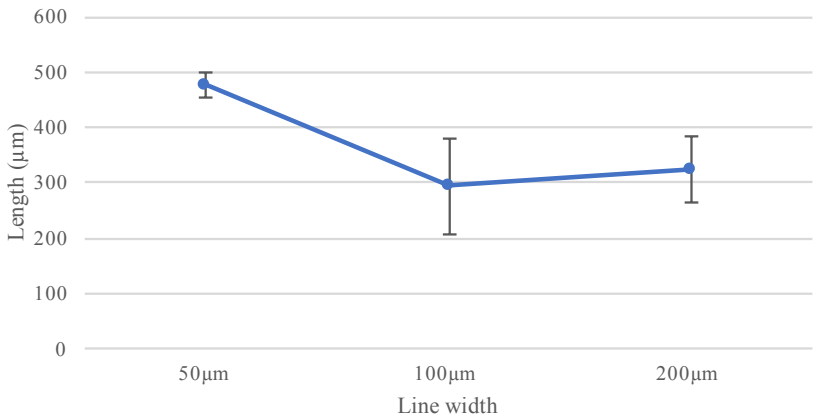

Figure 9: Average distance between separation points for different line widths

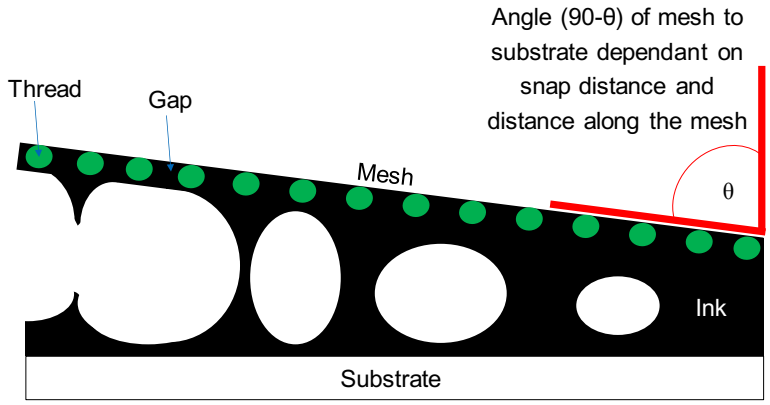

Figure 10: Schematic diagram of the separation mechanisms occurring based on the results for the GEM carbon-based ink

5. Conclusions

This study has identified a way of imaging and quantifying the deposition and separation of ink during mesh contact and release from the substrate. The results support the theory suggested by Messerschmitt, with the four stages of ink deposition consisting of adhesion, extension, flow and separation were identified. The length of the region in simultaneous contact with both the substrate and mesh increased with line width. The increase in line width also lead to an increase in the film thickness of the printed lines, where the adhesion to extension stages were longer for lines produced as a continuous print than the flow to separation stages, with both lengths increasing with line width. Further work could be conducted to identify the effect of altering the rheological properties of screen printable inks and printing parameter settings on the ink deposition and separation processes, to assess whether these parameters could affect the size and occurrence of these ink separation stages.

Acknowledgements

The authors would like to acknowledge the funding from the European Social Fund via the Welsh Government, the Engineering and Physical Sciences Research Council (grant reference: EP/L015099/1) and icmPrint that has made this research possible. The authors would also like to that other members of WCPC who helped make this work possible, especially Yin Cheung Lau and Ben Clifford, as well as other members of Swansea University, especially Eifion Jewell.

References

Baker, J., Hooper, K., Meroni, S., Pockett, A., McGettrick, J., Wei, Z., Escalante, R., Oskam, G., Carnie, M. and Watson, T., 2017. High throughput fabrication of mesoporous carbon perovskite solar cells. *Journal of Materials Chemistry A*, 5(35), pp. 18643–18650. https://doi.org/10.1039/c7ta05674e.

Fox, I.J., Claypole, T.C. and Gethin, D.T., 2003. An experimental investigation into ink transfer using a roller squeegee in high-speed screen printing. *Proceedings of the Institution of Mechanical Engineers, Part E, Journal of Process Mechanical Engineering*, 217(4), pp. 307–321. https://doi.org/10.1243/095440803322611679.

Janeczek, K., Jakubowska, M., Młożniak, A. and Kozioł, G., 2012. Thermal characterization of screen printed conductive pastes for RFID antennas. *Materials Science and Engineering: B,* 177(15), pp. 1336–1342. https://doi.org/10.1016/j.mseb.2012.01.014.

Kapur, N., Abbott, S.J., Dolden, E.D. and Gaskell, P.H., 2013. Predicting the behavior of screen printing. *EEE Transactions on Components, Packaging and Manufacturing Technology,* 3(3). pp. 508–515. https://doi.org/10.1109/TCPMT.2012.2228743.

Messerschmitt, E., 1982. Rheological considerations for screen printing inks. *Screen Printing*, 72(10), pp. 62–65.

Philip, B., Jewell, E., Greenwood, P. and Weirman, C., 2016. Material and process optimization screen printing carbon graphite pastes for mass production of heating elements. *Journal of Manufacturing Processes*, 22(1), pp. 185–191. https://doi.org/10.1016/j.jmapro.2016.03.001.

Riemer, D.E., 1971. The direct emulsion screen as a tool for high resolution thick film printing. In: *21st Electronic Component Conference Proceedings*. Washington, DC, USA, 10–12 May 1971. New York, USA: IEEE, pp. 463–467.

Riemer, D.E., 1988a. Analytical engineering model of the screen printing process: Part I. *Solid State Technology*, August 1988, pp. 107–111.

Riemer, D.E., 1988b. Analytical engineering model of the screen printing process: Part II. *Solid State Technology*, September 1988, pp. 85–90.

Riemer, D.E., 1988c. *Ein Beitrag zur Untersuchung der physikalisch-technischen Grundlagen des Siebdruckverfahrens*. Doctoral dissertation.Technische Universität Berlin.

Riemer, D.E., 1989. The theoretical fundamentals of the screen printing process. *Microelectronics International*, 6(1), pp. 8–17. https://doi.org/10.1108/eb044350.

Rueden, C.T., Schindelin, J., Hiner, M.C., DeZonia, B.E., Walter, A.E., Arena, E.T. and Eliceriri, K.W., 2017. ImageJ2 : ImageJ for the next generation of scientific image data. *BMC Bioinformatics*, 18: 529. https://doi.org/10.1186/s12859-017-1934-z.

Tehrani, Z., Burwell, G., Mohd Azmi, M.A., Castaing, A., Rickman, R., Almarashi, J., Dunstan, P., Miran Beigi, A., Doak, S.H. and Guy, O.J., 2014. Generic epitaxial graphene biosensors for ultrasensitive detection of cancer risk biomarker. *2D Materials*, 1(2): 025004. https://doi.org/10.1088/2053-1583/1/2/025004.

Tehrani, Z., Korochkina, T., Govindarajan, S., Thomas, D.J., O'Mahony, J., Kettle, J., Claypole, T.C. and Gethin, D.T., 2015. Ultra-thin flexible screen printed rechargeable polymer battery for wearable electronic applications. *Organic Electronics*, 26, pp. 386–394. https://doi.org/10.1016/j.orgel.2015.08.007.

Xu, C. and Willenbacher, N., 2018. How rheological properties affect fine-line screen printing of pastes: a combined rheological and high-speed video imaging study. *Journal of Coatings Technology and Research*, 15(6), pp. 1401–1412. https://doi.org/10.1007/s11998-018-0091-2.

Zhang, L., Liu, T., Liu, L., Hu, M., Yang, Y., Mei, A. and Han, H., 2015. The effect of carbon counter electrodes on fully printable mesoscopic perovskite solar cells. *Journal of Material Chemistry A*, 3(17), pp. 9165–9170. https://doi.org/10.1039/C4TA04647A.

Screen Printed Supercaps using Hydrogels as Electrolyte

Christoph Heckel[1], *Andreas Willfahrt*[1,2], *Thomas Fischer*[1], *Florian Nufer*[1], *Jonas Hötzel*[1], *Erich Steiner*[3] *and Gunter Hübner*[1]

[1] Innovative Applications of the Printing Technologies (IAD), Stuttgart Media University, Nobelstr. 10, 70569 Stuttgart, Germany
[2] Laboratory of Organic Electronics, Department of Science and Technology, Linköping University, SE-60174, Norrköping, Sweden
[3] Stuttgart Media University, Nobelstr. 10, 70569, Stuttgart, Germany
E-mails: willfahrt@googlemail.com; fischert@hdm-stuttgart.de; steiner@hdm-stuttgart.de; huebner@hdm-stuttgart.de

Short abstract

The performance of screen-printed coplanar micro supercapacitors was evaluated using various parameters. The electrode widths and distances of 250 and 500 µm, respectively, were selected in a range that is well reproducible in screen-printing. The printed electrodes contain activated carbon of three different types. The activated carbon is dispersed in a corn starch hydrogel produced by ultrasonic treatment of water, glycerol and starch. The addition of the retarding agent glycerol improved the processability in screen-printing significantly. When comparing the specific capacitances of coplanar micro supercapacitors with stack design supercapacitors, both types show similar results of about 27 $F \cdot g^{-1}$. In order to achieve similar performance, however, the coplanar design requires a multiple of the footprint of the stacked design. In addition, coplanar micro supercapacitors require high-precision processing. A major advantage, however, is the small layer thickness of the coplanar electrodes, which are ideal for flexible applications.

Keywords: screen-printing, micro supercapacitors, gel polymer electrolyte, printed energy storage, printed batteries, printed supercapacitors, hydrogels, activated carbon

1. Introduction

The terms smart objects, smart wearables – here both in combination with printed electronics – and more and more the term Internet of Things (IoT) describe fashionable and fancy devices that are intended to raise interest and the desire "must have" of the end user. After a long period of just demonstrating a lot of ideas and techniques some first products that have the potential for commercial success appear, mainly they are hybrid comprising of conventional electronics and printed functionality. However, almost all of them need an energy supply to function well. At this point, this work tries to contribute with printable energy supplies making it possible to run autarkic without a connection to the power grid.

Two main systems of printed energy storage can be distinguished, chemical and capacitive energy storage. The first system is dominated by printed batteries, which are distinguished in both non-rechargeable primary systems and rechargeable secondary systems. In this work, however, the focus is on the second system, the capacitive storage. Quite easy to manufacture with printing techniques are supercapacitors, which cannot deliver large amounts of energy, but high transient currents. For example, they can serve as a buffer between the energy sink and the energy source. Supercapacitor is the generic term for the three categories Electric Double-Layer Capacitor (EDLC), Pseudo Capacitor and Hybrid Capacitor (Kim, et al., 2016). Furthermore, a distinction must be made between symmetric and asymmetric capacitors. With EDLC, energy storage takes place by charge accumulation at the interface between the electrolyte/separator and the surface of the electrodes. At the metallic electrode, these charge carriers are electrons or holes, in the separator the positive or negative ions of the electrolyte accumulate at the interface to the electrode. In pseudo capacitors, the energy is mainly stored by faradaic processes, i.e. chemical reactions

of the ions with the electrodes, which also occur in batteries. In the hybrid system, both principles are used for energy storage. The symmetrical structure is based on electrodes of the same material, usually electrical conductors with a high specific surface, such as activated carbon, carbon nanotubes (CNTs) or graphene. Possible materials for electrodes of pseudo capacitors are transition metals like RuO_2 or MnO_2 or organic conductors like PEDOT:PSS or polyaniline. In the asymmetric design, one electrode consists of a material with double layer properties and the second electrode consists of a pseudo-capacitive material that undergoes faradaic reactions.

The capacitors can be manufactured in different layouts. In printing technology, two basic designs are possible: the stacked and the coplanar one, see Figure 1. The designs differ in the processing of the printed structures. For instance, in the coplanar design, functional layers are located side by side in one plane (Sun, et al., 2018). In the stack construction, the electrodes are sandwiching the separator soaked with electrolyte. The layers must be stacked or flapped on top of each other in a step following the printing process (Huebner and Krebs, 2015; Lehtimäki, et al., 2014).

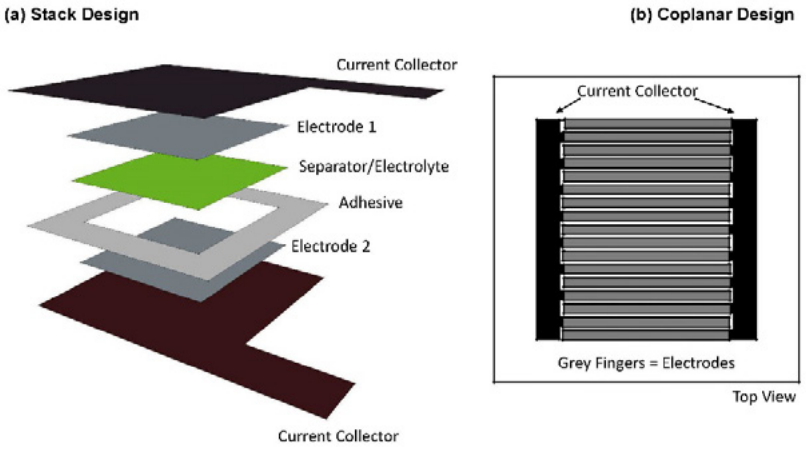

Figure 1: Printed supercapacitor structures (a) stacked and (b) co-planar design (Willfahrt, et al. 2018)

What both designs have in common is that the current collectors required for electron extraction often consist of a silver layer for maximum conductivity and a carbon-black layer printed over it for chemical passivation. However, the encapsulation conditions are different. The stacked capacitors are bonded after being laid on top of each other. Due to the barrier properties of the substrate, which may consist of a compound material such as PET-Al-PET, a particular stability of the electrochemical system against the environment can be expected. This is important, since it is necessary to prevent drying of the electrolyte or unwanted chemical reactions of the functional layers taking place. In coplanar structures, the functional layers can be encapsulated with an insulating polymer foil by lamination. If compound materials with high barrier properties are used, the expected stability against environmental influences is comparable with both systems.

In order to achieve the longest possible gap between the electrodes (short ways for ion transport), the coplanar structure can be designed to use interdigitating finger structures. However, then these finger structures must provide high edge accuracy and small gaps making it a challenge for the printing process. Although there is literature on the subject of coplanar supercapacitors, little is known about the restrictions in terms of electrode dimensions of printed devices.

An EDLC usually consists of electrodes with a very large surface area. An often-used electrode material is activated carbon, which is porous and provides the high surface area. The electrolyte between the electrodes should have a high ionic conductivity. In order to prevent an electrical short circuit between the

electrodes, separators are used. Typically, the separator is a non-woven fleece soaked with electrolyte so that the transport of the ions is ensured during charging and discharging of the capacitor.

A supercapacitor is charged with a slightly higher voltage than its nominal voltage, since a rather high internal resistance of several tens to hundreds of ohms can occur. However, if the voltage is too high, the supercapacitor may be damaged, as the electrolyte decomposes. With an aqueous electrolyte, the maximum voltage is approx. 1.23 V. Above this voltage electrolysis of water begins. With organic solvents or ionic liquids, the maximum charging voltage is higher.

The scope of this work is the comparison between the coplanar and the stack design of screen-printed supercapacitors. Both approaches possess advantages and disadvantages on their own: the coplanar design facilitates thin and flexible devices. However, the needed total area is larger than with the stack design. The latter implies a higher overall thickness of the device, but simpler processing due to simple structures. Since printing intrinsically is a high volume process, the idea of printed electronics also is associated with high-volume production but the devices may show a low performance. For easy and high volume production processes, further it is advisable to design the devices with environmentally friendly substances to assure easy disposal. Thus, in this investigation printing inks were prepared and examined that are based on mixtures of corn starch and carboxylic acid, i.e. maleic acid and/or lactic acid. These materials can be called hydrogels.

2. Materials and methods

2.1 Definition of supercapacitor structures

Pei, et al. (2017) report on micro supercapacitors produced by inkjet printing where the fingers are 9 mm long and 500 µm wide. Hu, et al. (2014) uses a conventional office laser printer for structuring the functional layers and achieve finger widths of at least 300 µm. Using a photolithographic process, the authors Beidaghi and Wang (2012) were able to produce even smaller structures. The finger widths are 100 µm with a length of 2.5 mm and a distance between the fingers of 50 µm. Likewise, the micro supercapacitors have been produced lithographically by Wu, et al. (2014), reaching finger widths from 1 175 µm to 219 µm. The authors show that by reducing the finger widths and the distances between the fingers, the electrochemical performance of the micro supercapacitors produced in this way can be significantly increased. Although the authors Hu, Pei and Ye (2015) prefer other processes than screen-printing in the production of micro supercapacitors, they also point out that the printing process has advantages, e.g. low costs, low complexity of the process and scalability. As a result of the literature study and taking into account previous considerations, the finger widths and distances of the coplanar supercapacitors were determined for this work as shown in Table 1.

Table 1: Electrode length and number of fingers

Finger width/finger distance [µm]	250/250	250/500	500/250	500/500	stack
Number of fingers	38	25	19	26	2
Actual Electrode Area [cm^2]	0.26	0.17	0.13	0.18	1
Total Area of Capacitor [cm^2]	13.3	13.2	13.8	13.3	1

Finger length of electrodes: 34 mm, mean thickness of electrode fingers: 20 µm

2.2 Choice of screen mesh

The activated carbon and carbon-black layers were printed with 77-48 PET screen mesh in first trials. It was selected after the smallest structure width of 200 µm had been specified for the carbon-black current collectors, which were covered with a 250 µm wide activated carbon layer.

$$s_{\min} = 2d + w \quad [1]$$

Equation [1] is the rule of thumb for determining the minimum feature size s_{min} that can be printed with a given mesh, where d is the thread diameter and w the mesh opening. Thus, the 77-48 mesh allows a minimum finger width of 173 µm, so that the target of 200 µm should easily be achieved. During printing trials, however, it was observed that the activated carbon (AC) layer printed with a 77-48 mesh having a mesh opening w of 77 µm did not produce a homogeneous printout. Agglomerates of the AC particles, which do not pass smoothly through the screen mesh, could cause this. Therefore, a 48-55 mesh was found to be appropriate for the electrode inks. It offers a high open mesh area percentage of 52.8 % and a high mesh opening with 151 µm.

2.3 Ink preparation

After manual mixing of water and activated carbon particles, starch and glycerol were added and mixed by manual stirring. In order to bring the low-viscosity starch-water suspension into a condition suitable for screen-printing, the usage of an ultrasonic homogeniser is helpful. The sonotrode tip is immersed in the liquid so that the cavitation forces lead to high shearing and heating of the mixture. Due to high pressure and temperature peaks as well as released shear forces, starch is broken down and wetted by water molecules and begins to gel. The hydrogel used for the AC electrodes was physically modified, i.e. the gel was obtained by ultrasound treatment only without the addition of a chemical modifier. The gel polymer electrolyte additionally contained a particular amount of carboxylic acid, i.e. maleic acid and lactic acid. The acid was intended to chemically modify i.e. crosslink corn starch. Furthermore, the excess of acid acts as electrolyte.

The energy input and the duration of homogenisation are determined by the volume and composition of the hydrogel. In the immediate vicinity of the horn tip, the shear force attains its maximum. The temperature also reaches its highest values here, so that gelation progresses faster locally around the sonotrode horn tip than in the surrounding areas in the mixing container. The homogeneity of the gel therefore depends on the volume and the mixing ratio of the starting materials. More homogenous gels were obtained by moving the sonotrode horn tip during the ultrasonic treatment and subsequently stirring the gel with a spatula after sonication. The resulting hydrogel ink showed good printability and a similar consistency to conventional screen-printing ink, which can be seen, e.g. in the characteristic “rolling” of the ink, i.e. the formation of a bulge in front of the moving squeegee.

2.4 Activated carbon electrodes

Activated carbon (AC) can be purchased in powder or granular form in various particle or grain sizes. All activated carbons used for the experiments are fine-grained powders that can be incorporated into printing inks without further processing. Depending on the manufacturer, most of the particles are smaller than 100 µm in diameter, see Table 2.

*Table 2: Four different activated carbon powders were examined (*Data extracted from datasheets)*

Sample	Particle size* [µm]	Specific surface area (BET) [m^2/g]	pH value*
AC1	D90: < 100	1 808	7
AC2	D95: < 80	1 340 (1 350*)	4
AC3	D95: < 75	900 (900*)	8–9
AC4	D95: < 90	1 033	9–11

AC1 = Norit A Supra EUR, AC2 = CW20, AC3 = TH90G, AC4 = Adsorba-A-P 6

Activated carbon serves as electrode material. The specific surface area of the activated carbon particles ought to be as large as possible, as the capacitance of the supercapacitor depends on it. Moreover, the compatibility of the size of the electrolyte ions with the pore size is crucial. This is the only way to ensure optimum deposition of the ions on the carbon surface, which leads to a high capacitance (Hu, Pei and Ye, 2015). Four different activated carbon powders were provided by their manufacturers: ADSORBA-A-P 6 from ETC engineering & technology consulting GmbH (Burgau, Germany), Silcarbon CW20 and Silcarbon TH90-G from Silcarbon Aktivkohle GmbH (Kirchhundem, Germany) and Norit A Supra EUR from Cabot (Rheinfelden, Germany). The Brunauer, Emmett and Teller (BET) measurement of specific surface area was used to verify the data provided by the manufacturers.

Table 3: Master formulation of electrode ink with activated carbon particles.

Content	Mass [g]	Concentration [wt.%]
H_2O	20	53.3
Activated carbon (AC)	10	26.6
Cornstarch	2.5	6.6
Glycerol	5	13.3

The master formulation of the electrode ink according to table 3 was developed after preliminary tests and the successful examination of printed supercapacitors in stacked design. The recipe was adapted to the requirements of the finger electrodes of the coplanar design. The addition of glycerol improved stability of the ink and delayed the drying of the electrode ink in the screen. Without glycerol, it was literally impossible to process the inks properly at least with the 250 µm finger electrodes. The formulation for all electrode inks, as shown in Table 3, differed only in the type of activated carbon powder.

2.5 Printing of coplanar finger structures

The coplanar and the stacked micro supercapacitors comprise of four successively printed layers. The current-collectors are made of silver ink LOCTITE EDAG PM 406 E&C (Düsseldorf, Germany) covered by a carbon-black (LOCTITE EDAG PF 407C E&C) layer for chemical passivation. As substrate, PET film Bleher Optimont 501 (Ditzingen, Germany) was used.

2.6 Rheological characterisation

Rheological measurements were performed with an Anton Paar MCR300 Rheometer (Ostfildern, Germany), deploying a plate-plate system PP25 with a diameter of 25 mm at 500 µm measurement gap. The temperature control unit TEK 150P was held at 23 °C. Rheoplus Software was used for data analysis.

2.7 Electrochemical characterisation

The screen- and stencil-printed supercapacitors were characterised by cyclic voltammetry (CV) and galvanostatic charge/discharge with potential limitation (GCPL). The CV measurement allows for a quick impression of the performance of the component under investigation. The instruments used for the investigation are BCS-805 battery cycling system and SP300 potentiostat, both from the manufacturer Bio-Logic Science Instruments (Seyssinet-Pariset, France). The capacitance of the capacitor was determined by constant current GCPL measurement using the EC-Lab software from Bio-Logic. According to the Bio-Logic (2014) application note #51, the capacitance C is calculated using the equation where is the total charge stored or released by the supercapacitor. ΔE_{WE} is the difference between the initial and final potential on either charging or discharging process. The accuracy of this method was verified by comparing different measurement methods on components with known characteristic values.

The capacitance is often related to the mass m or the area A of the supercapacitor, depending on whether material or process properties are of interest. It is then referred to as the specific capacitance C_{sp}, which enables better comparability of test results. The specific capacitance C_{sp} in $F \cdot g^{-1}$ is obtained by division of the capacitance C by the mass of one electrode m when symmetric electrodes are used.

3. Results

Before the supercapacitors are fully assembled, the printing process of the electrode inks was investigated. During this procedure, it soon turned out that the formulations with AC2 did not fulfil basic requirements, i.e. achieving a weight content of more than 40 %. Therefore, the subsequent plots do not contain values from AC2.

3.1 Viscosity and flow behaviour of the electrode inks

The progression of the viscosity variation of the electrode inks indicates how stable the ink is over a certain period of time. A significant change in viscosity indicates that the paste may cause problems during the printing process so that the open screen areas become clogged and an uneven or incomplete release of the printing ink from the screen mesh is the result. Corresponding rheological measurements are presented in Figure 2.

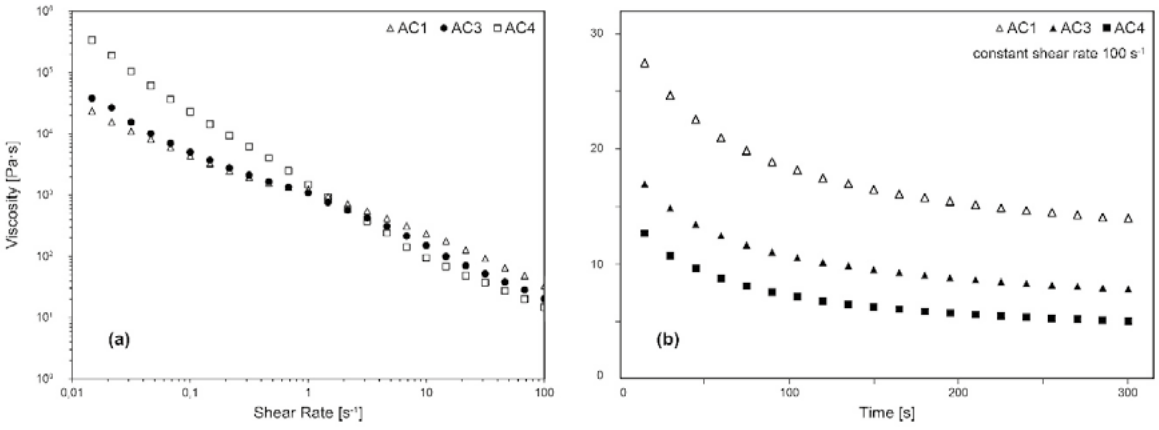

Figure 2: Rheological measurements: (a) shear thinning indicated by decreasing viscosity with increasing shear rate and (b) thixotropic behaviour of all electrode inks indicated by decreasing viscosity at constant shear rate

The ink AC4 shows the lowest viscosity change and the lowest measured viscosity value. Electrode ink AC1 achieves the highest viscosity value and the most significant viscosity change.

Further, it could be observed that all three inks show a slight change in their shear thinning behaviour and the time dependent decrease of viscosity already after a storage of 24 h, although it was always tried with sufficient stirring to homogenise as best as possible.

Due to the test results of the rheological measurements and the subjective perception of the ink behaviour during the print tests according to Table 4, only small amounts of ink were produced immediately before each print tests.

Table 4: Subjective impression when printing the electrodes

Inks	AC1	AC3	AC4
Ultrasonic processing	6 min	3 min	4 min
Perception of processability	Good flooding and print behaviour on all structures, but no optimum ink transfer when released, some residues in meshes.	Good flooding and print behaviour on all structures, good ink transfer to the substrate – ink "rolls" very well in the screen.	Good flood and print behaviour at line widths of 500 µm. Problematic with the 250 µm line widths, especially 250/500, as no uniform printout is possible.
Perceived homogeneity	+++	++	+
Stability while printing	+	++	+++

3.2 Printing of coplanar design with different electrode inks and dimensions

The print tests included four interdigitating structures according to Table 1 and Figure 1b, 250/250, 250/500, 500/250 and 500/500. The first number indicates the line width of the electrodes, the second the distance between the electrode fingers. Each variation was printed with the inks AC1, AC3 and AC4, which are printed on already applied and dried current collectors consisting of silver and carbon black. The test was always carried out in the same sequence in which the AC paste is first produced freshly and immediately afterwards the finger structures were printed with ascending line width and/or spacing distance (1: 250/250, 2: 250/500, 3: 500/250, 4: 500/500). Due to the high water content and the tendency of the inks to dry in the screen, the finer structures were printed first, as the viscosity of the pastes increased considerably over time and the printing behaviour deteriorates noticeably.

3.3 Printing of stack design as reference

As a reference a supercapacitor was printed and assembled in stack design according to Figure 1a.

From preliminary tests, it was known that the amount of electrolyte could influence the measured capacitance. Therefore, three different volumes of the electrolyte HCl (2.86 mol/l) were applied in stacked supercapacitors with an electrode area of 1 cm^2 in order to investigate the influence of the electrolyte volume on the specific gravimetric capacitance C_{sp} (Figure 3). The smallest electrolyte volume of 25 µl achieved the highest specific capacitance. The results of 50 µl and 100 µl differ not too much. Accordingly, the following experiments were performed with 25 µl electrolyte per cm^2.

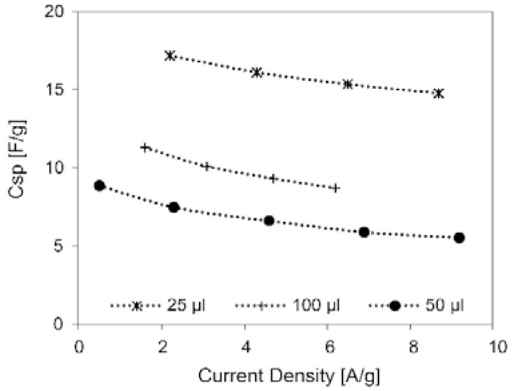

Figure 3: Effect of electrolyte volume on the gravimetric specific capacitance C_{sp}; the lowest volume achieved the highest C_{sp}

There is also a dependency of the specific capacitance from the chosen charge/discharge current what can be seen in Figure 4.

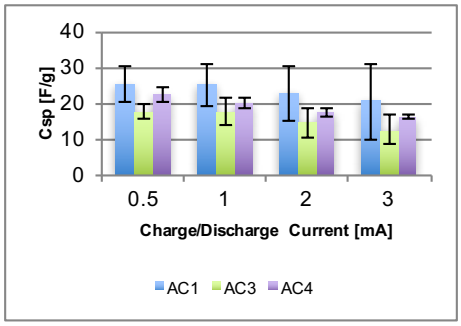

Figure 4: Specific capacitance of stacked design supercapacitors with an active area of 1 cm², nonwoven separator and 20 µl 2.86 m/l HCl

3.4 Results coplanar vs. stack design

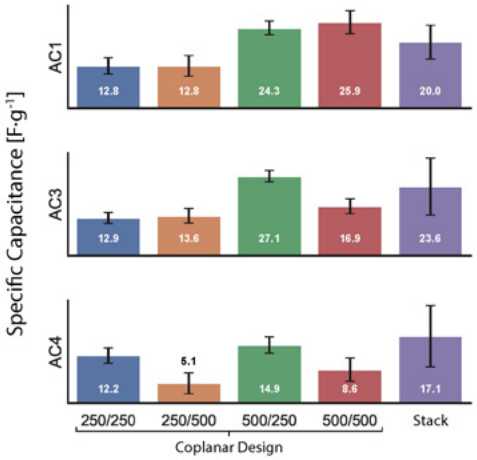

Figure 5: Comparison of the specific capacitance of different activated carbon inks and electrode widths as well as distances between the electrode fingers

Figure 5 shows the specific capacitances provided by the combinations of three AC inks and four structure settings of the coplanar printed supercapacitor. These were determined using the GCPL method with a charging and discharging current of 0.5 mA and a potential range between 0 and 600 mV. Each value shown represents the average of three individual values. The nonwoven separator was soaked with 340 µl

of 2.86 molar HCl. The results of the screen-printed coplanar supercapacitors are compared to the results obtained with a stacked design.

The difference in C_{sp} depends on the structure width and the distance. The smaller line thickness results in a smaller C_{sp}, however, the influence of the distance between the lines is smaller. In general, AC4 does not appear to be suitable for printed coplanar supercapacitors since this ink always achieves the lowest specific capacitance.

The specific capacitances of the broader electrode fingers are higher. At the smaller distance (500/250) AC3 reaches the highest specific capacitance of 27 $F \cdot g^{-1}$. At 500/500 AC1 reaches its maximum value of 26 $F \cdot g^{-1}$.

With the stack design, again AC1 attains the highest C_{sp} with 28 $F \cdot g^{-1}$. The results of AC1 and AC3 are comparable with the coplanar 500/500 combination. Further, AC4 is performing better with the solid electrode area as a part of the stack design. Here, the ink provides a competing C_{sp} of 22 $F \cdot g^{-1}$.

The conclusion to be drawn here is that both designs provide comparable results. With the coplanar design, the combination of broader electrode fingers with smaller spacing leads to the highest C_{sp} using AC3. In literature (Wu, et al., 2014) it is claimed that reducing finger width goes with increasing C_{sp}. The reason is supposed to be better device performance due to increased ion diffusion. Additionally, the slope of decreasing C_{sp} with increasing scan rate is smaller with a shorter distance between the electrodes. As a consequence, the coplanar design offers higher rate capability (Diederichsen and Hao, 2013).

In Figure 5 we clearly see the trend of a better performance with the larger line width. This certainly is related to the formulation of the ink, especially the size and possible agglomerations of AC particles. As listed in Table 2, the range of particle sizes is broad and the sizes are rather high. We cannot exclude a sieving effect, i.e. larger particles and/or agglomerated of smaller particles may remain in the screen mesh.

The repeatability, indicated by the standard deviation represented by the error bars, is similar for all samples except AC3 and AC4 with the stacked design, which is slightly higher. The processability of the electrode inks depends on their homogeneity, i.e. how well the particles are dispersed and whether agglomerates of the activated carbon can form. In addition, the water-based ink system is susceptible to water evaporation. The AC inks used in preliminary tests did not contain any vehicle (plasticiser) other than water. In the first experiments, the electrode paste formulation from earlier studies showed a rapid clogging of the small line widths, so that the initially used ink formulations were modified by the addition of 13.3 % mass fraction of glycerol. It acts as a humectant and, due to its hygroscopic properties, helps to maintain the processability of AC inks over a longer period of time.

In Figure 6 the specific capacitances of all variations are shown. The constant current charging and discharging was performed at discrete currents of 0.5, 1, 2, 3, 4, and 5 mA.

Experience with stack design has shown that the specific capacitance decreases almost linearly with increasing charge/discharge current. This is due to the shorter period for the ionic charge carriers to penetrate into deeper pores of the activated carbon and to induce charge at the interface between electrolyte and electrode. However, the curves of the printed coplanar supercapacitors exhibit significantly different shapes than expected. Partially, the expected progression may be observed, e.g. for the specimens at 250/250, AC1 and AC4 at 250/500 and AC4 at 500/500. However, the other data curves show more or less pronounced discontinuities, which may be due to a disturbed function of the supercapacitor. One conceivable reason for this might be that the coplanar electrodes are more susceptible to interference from the aqueous electrolyte than the stacked electrodes. Due to a higher aspect ratio (height:width) in coplanar de-

sign, it may be assumed that the cohesion of the electrode layer is lower than in stack design. It is assumed that the electrolyte will partially detach the electrode material.

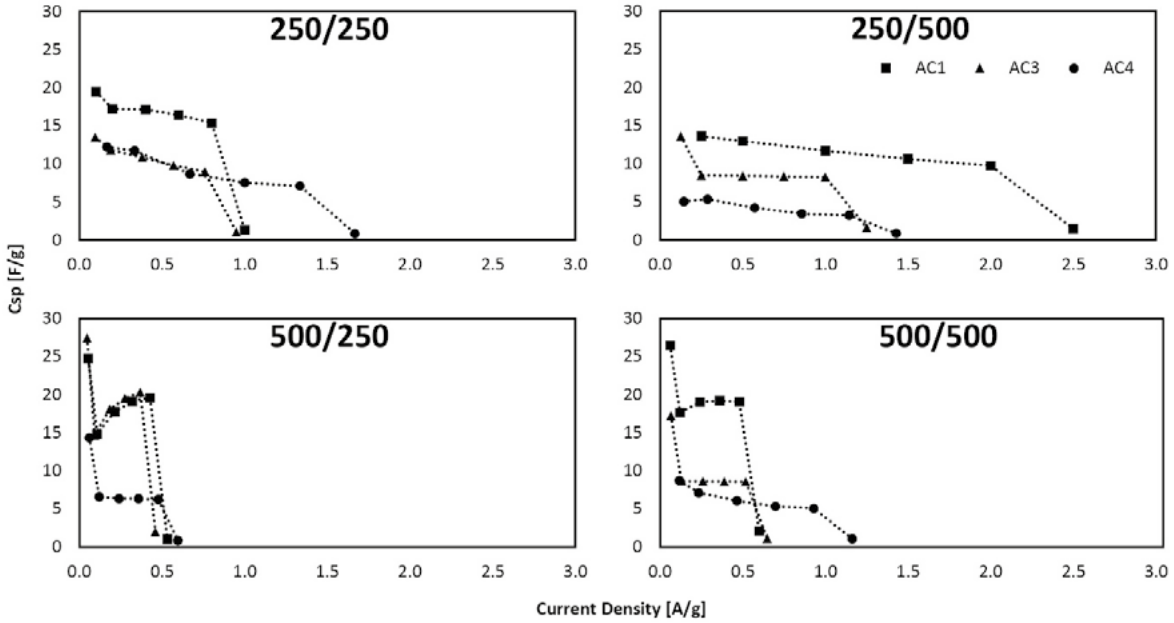

Figure 6: Current density of three activated carbon inks and four different structural combinations of line width and distance

In general, at the highest charge/discharge current the capacitance drops to a very low value in all measurements. The final potential seems to have been reached too quickly without real penetration of the pores by the ions.

3.5 Areal specific capacitance

The areal specific capacitance C_{spA} relates the performance of the printed supercapacitor to its actual geometric size. Printed energy devices are mostly constraint by the overall thickness and/or the available area that is determined by the application. If flexibility is required, the thickness is the bottleneck. If the size of the devices is limited, the area is limiting the performance. In the worst case, a flexible and small sized device is required. The coplanar design is more reasonable up to a certain maximum thickness. If higher layer thicknesses are acceptable and flexibility of the device is less important, the stack design makes more sense.

The comparison of the different designs can of course also be made with regard to the surface and edge quality. The coplanar design offers the advantage over the stack design that the distances between the electrodes are theoretically clearly defined. This is not the case with stack design because the electrode surface has a certain roughness and the separator, whether nonwoven or gel polymer electrolyte, also has a certain inhomogeneity. As a result, a more homogeneous electric field is expected with the coplanar structuring of the electrodes.

The closer one gets to the resolution limits of screen-printing, the lower the edge quality of the printed structures and thus also the performance of the supercapacitor.

In screen-printing, a saw tooth effect can be seen, so that the edges of the electrode fingers appear irregular. Figure 7 shows the influence of the finger width on the edge quality. The lines with a nominal width of 250 µm have visible constrictions that keep the effective line width significantly smaller. This manifests

itself in an increased resistance but also in variations of the distance and thus of the local capacitance. The advantage of the clearly defined electrode gap, an already mentioned advantage over the stack design, is then eliminated. There are thinkable methods for improvement of the print quality. Ink formulations containing thixotropic agents for levelling after print and using meshes with higher open area percentage (stainless steel instead of PET) could be helpful.

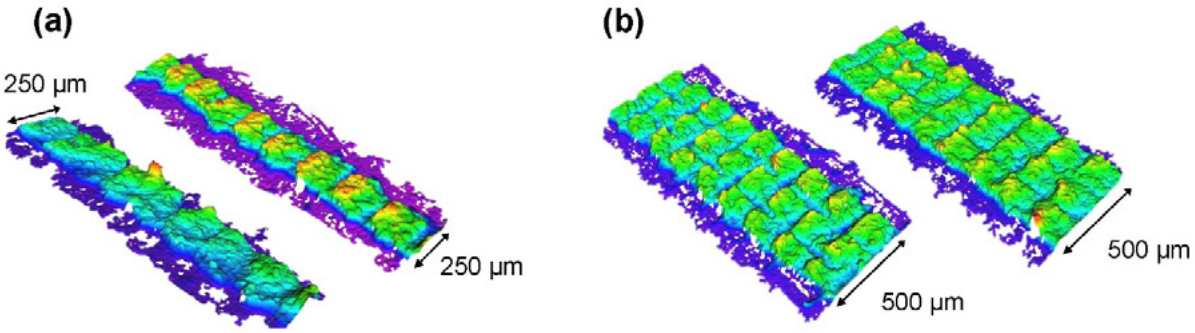

Figure 7: 3D-Microscope images of coplanar electrode fingers; (a) 250 µm and (b) 500 µm line width; Mesh marking is pronounced in both cases, the edges of the thinner finger structures are of significantly inferior quality

The actual electrode area of the coplanar micro supercapacitor is calculated using the values shown in Table 1. The mean ink film thickness of about 20 µm is estimated by optical and mechanical measurements, the number of electrode pairs varies with the finger dimensions. With the smallest finger widths and distances, 38 pairs of electrodes can be created on the given area. The normalised areal specific capacitances are plotted in Figure 8a. The plots indicate better performance of coplanar supercapacitors in terms of the actual areal capacitance, which we have defined as the area covered by the finger electrodes. The structure combination 500/250 provides the highest actual areal specific capacitance. However, if we consider the entire surface area covered by the supercapacitor including the distances between the finger electrodes, the area required for coplanar design is significantly larger than for stack design, as shown in Table 1. In Figure 8b the difference becomes very clear. Note that the y-axis is broken in order to increase clarity of the diagram. Also with this representation, the results of the smaller finger widths are negligibly small.

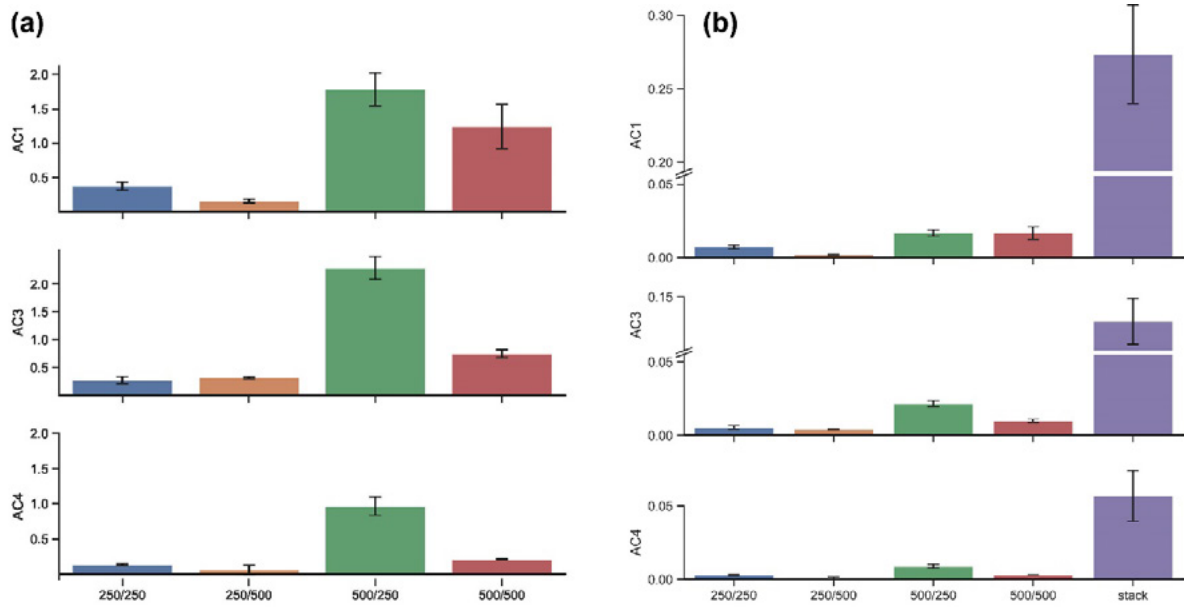

Figure 8: (a) actual, normalised areal specific capacitances and (b) the capacitance related to the total area of printed coplanar in mA; AC1 in stacked design achieved much higher areal capacitance of 273 mA·cm^{-2}.

3.6 Mass deposition depending on structure size

As shown in Figure 9, the linewidth/gap combination 500/250 performs best, followed by the 500/500 combination in terms of the transferred mass of electrode ink. The significantly lower mass transfer with the smaller line widths reflects the problems of printing with clogging of the openings and drying of the ink in the screen. The result of the 500/500 combination with AC4 is surprising, because here a higher electrode mass is expected. Further, it is surprising that the 1 cm × 1 cm electrode of the stack design also achieves a smaller mass transfer than almost every coplanar design. The larger error bar, on the other hand, indicates a higher deviation of the individual measurements.

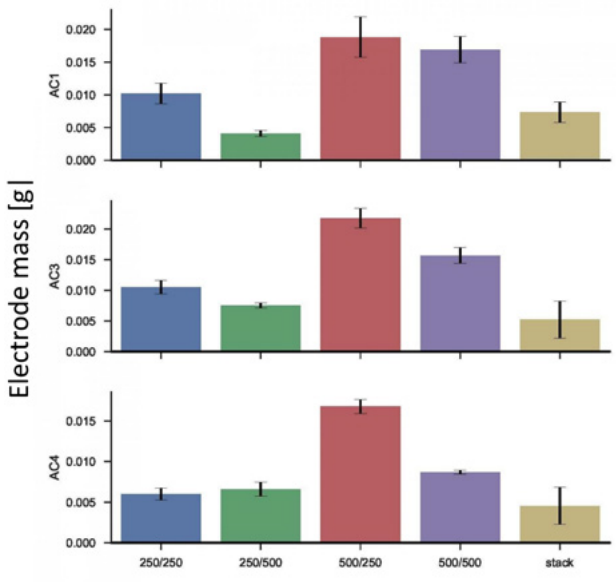

Figure 9: Influence of the design parameters on the electrode mass transfer

4. Conclusion

The examination of coplanar micro supercapacitors showed that it is an alternative way of producing printed energy storage devices. The selection of the structure width and distance is crucial. Increasing line width increased also capacitance, but this depends on several issues, foremost the electrode material, i.e. the size of the used particles and the tendency for agglomeration. The combination of different activated carbon powders with different geometric dimensions has shown that not all combinations work equally well. AC4 has only delivered usable results with the stack design electrodes. For all coplanar combinations, this ink drops off in comparison with the other formulations. AC3 provided the highest gravimetric specific capacity for the 500/250 design combination, which matches the highest C_{sp} of the stack design with AC1 of approximately 28 F·g^{-1}. This ink also provided the highest specific capacitance of roughly 27 F·g^{-1} with coplanar supercapacitors. C_{sp} is only slightly lower for AC1 with the coplanar design combination 500/500 and 500/250. In general, AC1 is the most stable in all variations, only the 250/500 variant is slightly less stable. However, this combination seems to be difficult in general, since all three electrode inks deliver only low C_{sp}. Although the coplanar design requires a significantly larger area than the stack design for the same performance, it can be advantageous if, for example, a low device thickness is required.

Acknowledgement

The authors declare they have no potential conflict of interest.

A semi-automatic screen/stencil printing machine Asys Ekra X1 (Bönnigheim, Germany) was used for all print tests. Screen meshes PET 1500 77-48 and 48-55 by SEFAR (Thal, Switzerland) were used and photoemulsion KIWOCOL POLY-PLUS SRX by. Kissel + Wolf (Wiesloch, Germany). We thank the vendors for their support.

Additional Information

We are deeply distressed that our student and co-author Christoph Heckel died so young on October 29, 2018. We dedicate this work to him.

References

Beidaghi, M. and Wang, C., 2012. Micro-supercapacitors based on interdigital electrodes of reduced graphene oxide and carbon nanotube composites with ultrahigh power handling performance. *Advanced Functional Materials,* 22(21), pp. 4501–4510. https://doi.org/10.1002/adfm.201201292.

Bio-Logic, 2014. *Supercapacitor characterization by galvanostatic polarization method*. [pdf] Bio-Logic Science Instruments. Available at: <https://www.bio-logic.net/wp-content/uploads/20140430-Application-note-51.pdf> [Accessed March 2019].

Diederichsen, S.E. and Hao, C.Y., 2013. *Fabrication of interdigitated micro-supercapacitors for portable electronic devices*. [pdf] Nanyang Technical University. Available at: <https://pdfs.semanticscholar.org/cd0a/64fe53b07cecd0b169869e06a04ed957e4ac.pdf> [Accessed March 2019].

Hu, H., Zhang, K., Li, S., Ji, S. and Ye, C.. 2014. Flexible, in-plane, and all-solid-state micro-supercapacitors based on printed interdigital Au/polyaniline network hybrid electrodes on a chip. *Journal of Materials Chemistry A*, 2(48), pp. 20916–20922. https://doi.org/10.1039/C4TA05345A.

Hu, H., Pei, Z. and Ye, C., 2015. Recent advances in designing and fabrication of planar micro-supercapacitors for on-chip energy storage. *Energy Storage Materials*, 1, pp. 82–102. https://doi.org/10.1016/j.ensm.2015.08.005.

Huebner, G. and Krebs, M., 2015. Printed, flexible thin film batteries and other storage devices. In: S. Logothetidis, ed. *Handbook of flexible organic electronics: materials, manufacturing and applications.* Cambridge, UK: Woodhead Publishing, pp. 429–447.

Kim, J.H., Choi, H.J., Kim, H.-K., Lee, S.-H. and Lee, Y.-H., 2016. A hybrid supercapacitor fabricated with an activated carbon as cathode and an urchin-like TiO_2 as anode. *International Journal of Hydrogen Energy*, 41(31), pp. 13549–13556. https://doi.org/10.1016/j.ijhydene.2016.06.018.

Lehtimäki, S., Li, M., Salomaa, J., Pörhönen, J., Kalanti, A., Tuukkanen, S., Heljo, P., Halonen, K. and Lupo, D., 2014. Performance of printable supercapacitors in an RF energy harvesting circuit. *International Journal of Electrical Power and Energy Systems*, 58, pp. 42–46. https://doi.org/10.1016/j.ijepes.2014.01.004.

Pei, Z., Hu, H., Liang, G. and Ye, C., 2017. Carbon-based flexible and all-solid-state micro-supercapacitors fabricated by inkjet printing with enhanced performance. *Nano-Micro Lett*ers, 9(2): 19. https://doi.org/10.1007/s40820-016-0119-z.

Sun, J., Cui, B., Chu, F., Yun, C., He, M., Li, L. and Song, Y., 2018. Printable nanomaterials for the fabrication of high-performance supercapacitors. *Nanomaterials*, 8(7): 528. https://doi.org/10.3390/nano8070528.

Willfahrt, A., Fischer, T., Sahakalkan, S., Martinez, R., Krebes, M. and Steiner, E., 2018. Parameter evaluation of printed primary Zn/MnO_2 batteries with nonwoven and hydrogel separators. *Flexible and Printed Electron*ics, 3(4): 045004. https://doi.org/10.1088/2058-8585/aae6b3.

Wu, Z.-S., Parvez, K., Feng, X. and Müllen, K., 2014. Photolithographic fabrication of high-performance all-solid-state graphene-based planar micro-supercapacitors with different interdigital fingers. *Journal of Material Chemistry A,* 2(22), pp. 8288–8293. https://doi.org/10.1039/C4TA00958D.

Reinventing the Wheel: an attempt to create an objective technical color wheel for Pantone colors by using hue angles (h_{ab}) as the deciding factor

Michael Abildgaard Pedersen

The Danish School of Media and Journalism, Department of Media Production and Management, Copenhagen
E-mail: map@dmjx.dk

Short abstract

This study attempts to find an objective method to determine whether a given color is yellow, orange, or red, simply by evaluating its technical values and without looking at the color. After a review of the early Pantone Matching System and the current Pantone Formula Guide Coated, the first attempt to create a color wheel was to some extent possible. This was done firstly by selecting already named Pantone colors and colors that unambiguously belong to a particular color group, and secondly by using their hue angles (h^*/h_{ab}) to determine the boundaries surrounding the orange color group in the CIE a^*b^* projection circle. By this method, the orange color group is determined to be located between 41.5° and 85° (h_{ab}). However, more in-depth studies are required to verify or falsify this methodology.

Keywords: color wheels, Pantone, hue angles, color groups

1. Introduction and background

For years we have been able to determine whether a color difference is acceptable or not, simply by calculating the Delta-E values (ΔE_{ab} and ΔE_{00}). In principle, it's possible to evaluate color differences without looking at the colors. Likewise, it would be useful if it were possible to determine a color's affiliation to a particular color group simply by looking at its objective values. For instance, is Pantone 116 C yellow or orange?

In 2017, a study showed that it was possible to calculate the exact complementary color to a specific Brand Color (Pedersen, 2017). This study will use the same form of practical trigonometry and calculation to determine the point at which a yellow color ceases to be yellow because it has changed into orange, and the point at which orange has changed into red. The assumption is that there must be a specific technical limit between these color groups.

It is not a new issue. Many others have tried to categorize colors and define boundaries between color groups.

As we all know, the wheel was invented approximately 300 years ago. In 1704 Newton published his seven-color wheel, in 1810 Goethe published his six-color wheel, and in 1905 Munsell published his 10-color wheel. What Newton's, Goethe's and Munsell's color wheels had in common was that they all set clear boundaries between their hues or color groups.

During this 300-year period, many other color pioneers have contributed to color science with their versions of the color wheel. In the 1930s the CIELAB color system that we still use today was introduced, and in 1976 the CIE a^*b^* projection circle arrived (Berns, 2000). In the CIE a^*b^* projection circle, hue angles define four main color groups (red = 0°, yellow = 90°, green = 180° and blue = 270°).

In 2012, ISO TC-130 introduced hue angles as aim values for the ink solids CMY. As the only one of the eight process standards in the ISO 12647 series, ISO 12647-6:2012 (International Organization for Standardization, 2012) defined aim values as CIELAB metric hue angles (h_{ab}). Thus, ISO TC130 defined cyan, magenta, and yellow color areas in the CIE a^*b^* projection circle, specified by hue angles. However, this process standard has now been withdrawn and a new version is under development.

In 2016 John Seymour defined those Pantone colors that unambiguously belong to a particular color group and plotted these areas into the CIE a^*b^* projection circle, e.g., orange color group: h^*57–67 C^*67–96 L^*62–72 (Seymour, 2016). However, this included only a limited number of Pantone colors.

Many industries use their own color system and their own color wheel. The paint industry, architects and designers use the NCS color circle which is divided into 40 hues. The coatings and decorative industry uses the RAL Design color circle, which is divided into 36 hues and constructed to follow the CIE a^*b^* projection circle.

In the graphic arts industry, we primarily use the Pantone Color System, and the current Pantone Formula Guide is built upon 17 hues or basic colors (Pantone, 2019). We also use the CIELAB color system for quality control.

However, the Pantone Color system doesn't have an official color wheel to navigate from, and there seems to be no direct relationship between the CIELAB system and the Pantone system.

While existing color wheels (Newton, Goethe, Munsell, RAL, NCS) were created from the visual spectrum (on a scientific basis), around which a model was built, with colors determined and placed inside their models, a future Pantone color wheel will have to be built in the opposite manner. It is necessary to begin with existing physical color samples, after which a model can be built.

The reason for this is that Pantone is a practical color mixing system where physical printing inks are used to mix all of Pantone's different colors. The Pantone colors already exist, but can they be placed systematically into a color circle?

This study will seek to create a Pantone color wheel that follows the CIE a^*b^* projection circle and sets clear boundaries between color groups. At the same time, it attempts to set clear rules for when a given color belongs to a specific color group, determined solely by its technical values.

2. Materials and methods

In this study, the orange color group on coated paper is used as an example, after which the same systematics might be used to determine other boundaries between other color groups.

Two physical color sample catalogs have been used. Firstly, the *Pantone Matching System, Printers Edition* from 1973 (containing the same original colors and structure as the first edition, in 1963), and secondly the *Pantone Formula Guide Coated, The Plus Series* 2019.

These have been used to visually find specific colors, color order, and color group ranges. All colors were evaluated in a *Largo Ortospectra* viewing booth at 5000 K.

The Pantone CIELAB data from all 1867 Pantone colors in the 2019 edition of *Pantone Formula Guide Coated* was downloaded from Pantone Color Manager software v.2.3.1.260 for Windows and stored in

Excel. Hue angles (h^*/h_{ab}) and chroma values (C^*) were applied using the formulas from ISO 13655:2009, section 5.3.2 (International Organization for Standardization, 2009).

Although there most certainty are differences between Pantone colors from 1963, 1973, and 2019, it will not make any sense to measure a 46-year-old Pantone fan (PMS 1973). Therefore, all values for the 1973 edition were taken from Pantone's digital 2019 version. For example, the CIELAB values for the old PMS 116 C (from 1973) are indicated with CIELAB values from 2019. The purpose of this study is not to investigate color differences from year to year.

No measurements have been made in this study.

3. Results and discussion

Pantone has no official color wheel, such as Munsell, RAL or NCS. However, its website has a link to an unofficial color wheel from *Before&AfterMagazine* called *"Our Color Wheel"* (McWade, 2006). Thus, Pantone must vouch for this color wheel. Nevertheless, it is unofficial and it is built in a illogical and non-technical way, showing the lightest tints (hue+white) in the center and the darkest shades (hue+black) at the outer edge (Figure 1). It seems that the Pantone lightness axis is placed where CIELAB shows chroma, and the Pantone chroma axis is placed where CIELAB shows lightness. Therefore, this wheel cannot be transferred to CIELAB.

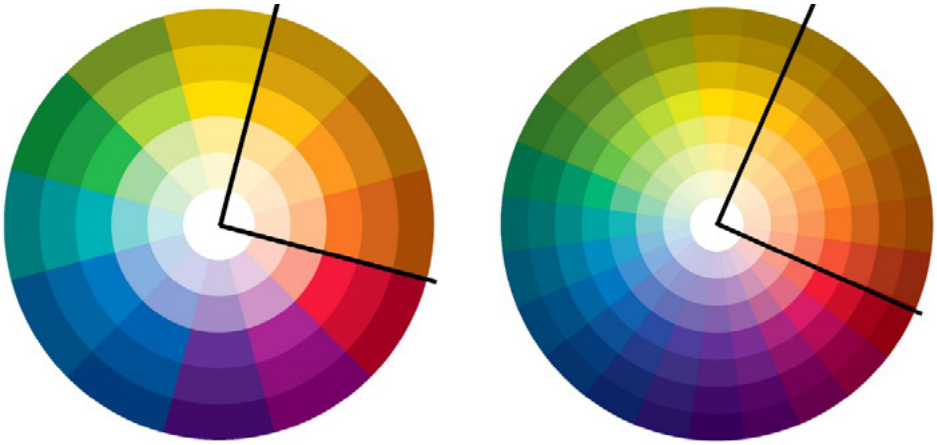

Figure 1: Two versions of "Our Color Wheel" from Before&AfterMagazine; left: divided into 12 hues/5 steps; right: divided into 24 hues/7 steps; added lines show orange areas of 90° placed differently

Thus, it is necessary to return to the original Pantone catalog to analyze the underlying ideas behind the Pantone System. When Pantone published its color catalogue, *Pantone Matching System, Printers Edition* (PMS) in 1963, it contained 497 colors marked with three-digit reference numbers beginning with PANTONE 100 (yellow). The 497 colors were made by mixing some of the eight primary colors (basic colors), black, and transparent white.

According to Pantone, the colors were *"arranged in chromatic format"*, meaning that each page has seven colors where the middle color is the pure hue. Colors above are the pure hue mixed with transparent white (lighter), while colors below are the pure hue mixed with black (darker). This is probably the reason for the structure of *Our Color Wheel*.

The 1963 (1973) fan deck had 72 pages. Page 1 displayed the eight primary colors (basic colors). The following pages included seven colors each: one pure hue as the center color, three shades (hue+black) and

three tints (hue+transparent white). Pantone called this *"the center line concept"*. The content was distributed as follows:

- 36 pages with 36 secondary colors (pure hues mixed by two primary colors) used as the centerline color;
- eight pages with eight primary colors used as the centerline color;
- seven pages with 49 different grays;
- 20 pages of 20 tertiary colors (mixed by three primary colors) used as centerline colors.

Thus, the original Pantone system had 44 pure hues (eight primary colors and 36 secondary colors).
In the traditional PMS fan deck, the three-digit Pantone numbers were numbered consecutively and arranged clockwise, largely following the CIE *a*b** projection circle, starting with yellow colors on the first pages, then orange colors, red colors, and so on, ending with the green colors (Figure 2).

Figure 2: The 1963 (1973 edition) of the PMS color catalogue; left: PMS page 1 showing the eight primary colors; right: PMS page 9 showing a secondary color (151) as the centerline color

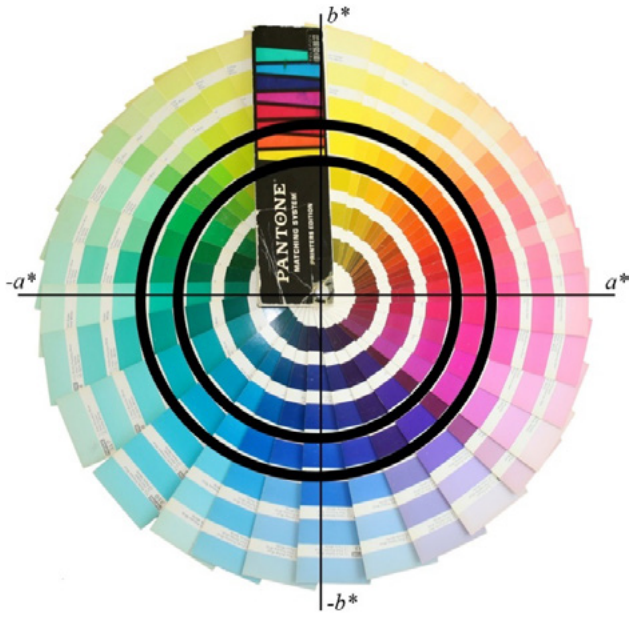

*Figure 3: PMS 1963 (1973) fan deck pages forming a CIE a*b* projection circle; centerline colors (secondary colors) are marked in between the bold circles. Axis for CIE a* and b* added*

By selecting the original 44 pure hues from the PMS centerline concept, a picture of a color wheel begins to be drawn (Figure 3). In Figure 4 the eight primary colors and the 36 secondary colors forming the original PMS are plotted into the CIE *a*b** circle.

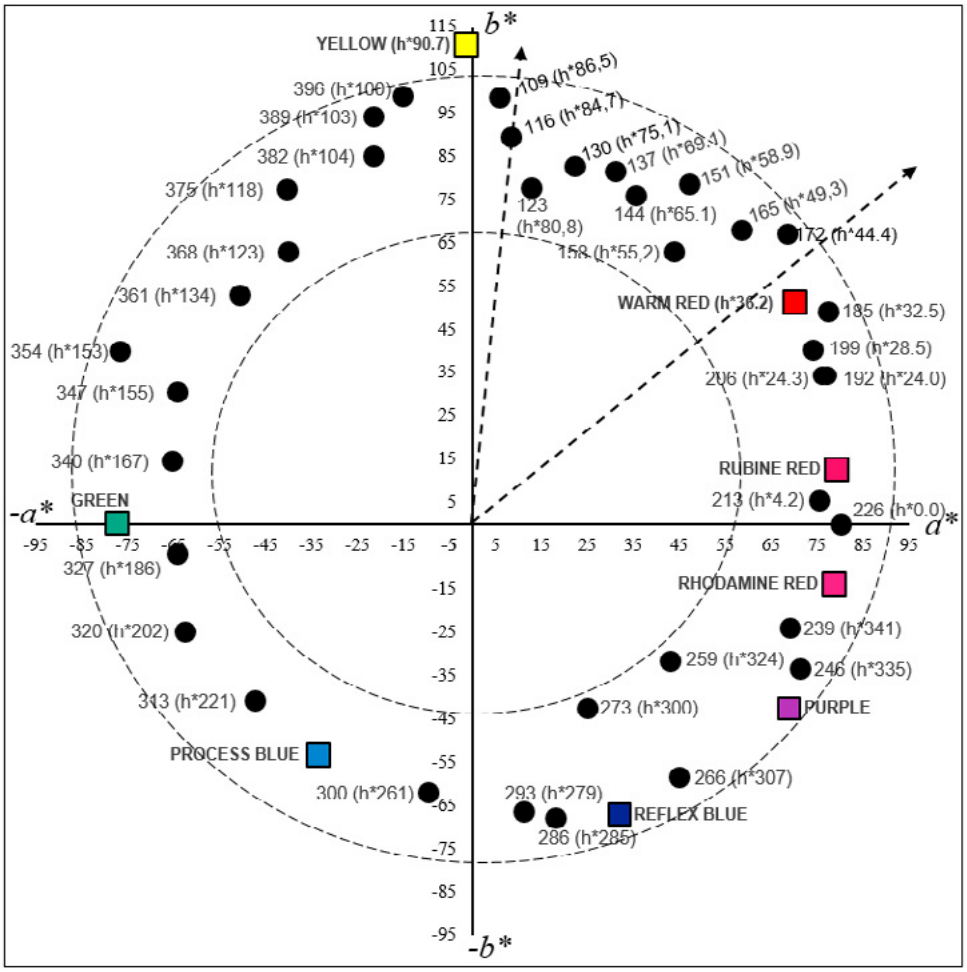

*Figure 4: PMS 1963 (1973) CIE a*b* coordinates for eight primary colors and 36 secondary colors plotted into the CIE a*b* circle; the orange color group seems to be between h*36.2 to h*44.4 and between h*80.8 to h*84.7*

However, from 1987 Pantone added many new colors provided with four-digit numbers and inserted them chromatically in between the original colors. In addition, five new primary colors were added (Yellow 012, Orange 021, Red 032, Blue 072 and Violet) (Herbert, 2019).

Since then, Pantone has added more and more colors each year, and has changed the paper from a yellowish paper to wood-free paper containing OBA. The 2019 edition of Pantone Formula Guide Coated now contains 1 867 colors mixed from the 17 basic colors, black, and transparent white. In Figure 5 all 1 867 current colors are plotted into the CIE *a*b** projection diagram.

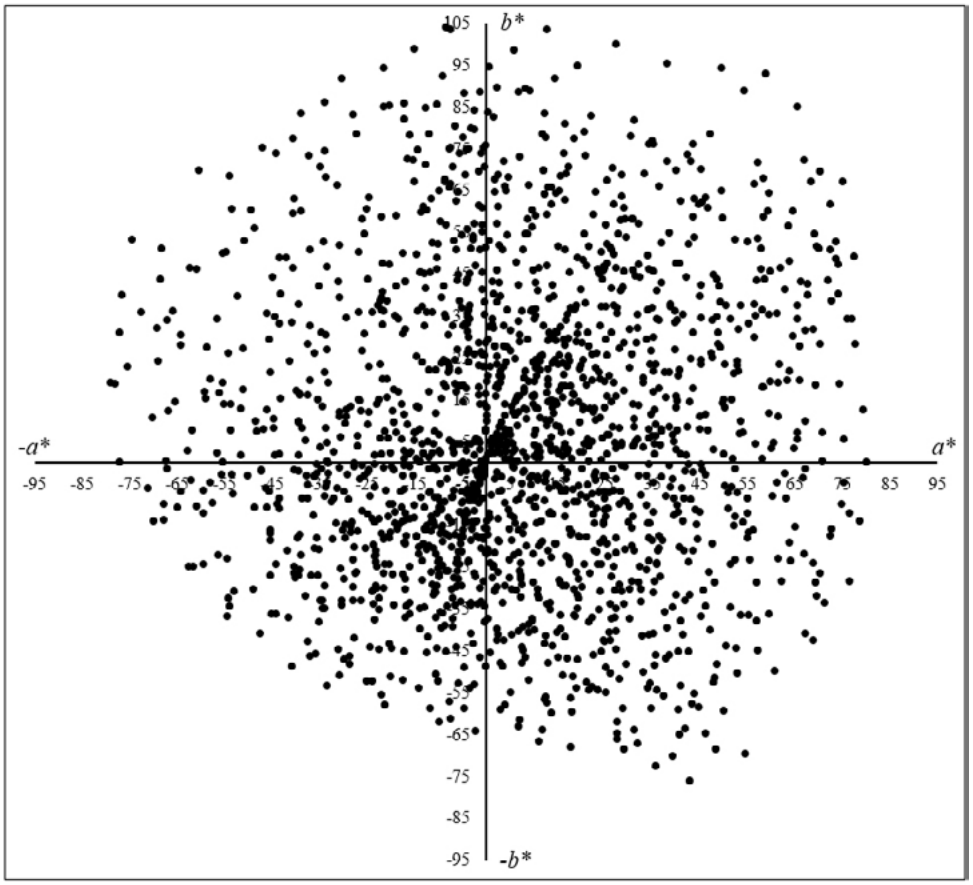

Figure 5: All 1 867 Primary, Secondary, Tertiary, and Quaternary Colors from Pantone Formula Guide Coated 2019

This color space spans from L^* 7.9 to 92.1 and from C^* 0.2 to 110.9. All 360 hue angles (h^*) are represented when only whole rounded numbers are used. However, more than 1 800 different hue angles (h^*) are represented when defined by two-digit decimals.

Therefore, it might be difficult to find one particular hue angle that separates two color groups. The first step could be to plot all 17 primary colors and 90 secondary colors from the 2019 version of the Formula Guide (Figure 6).

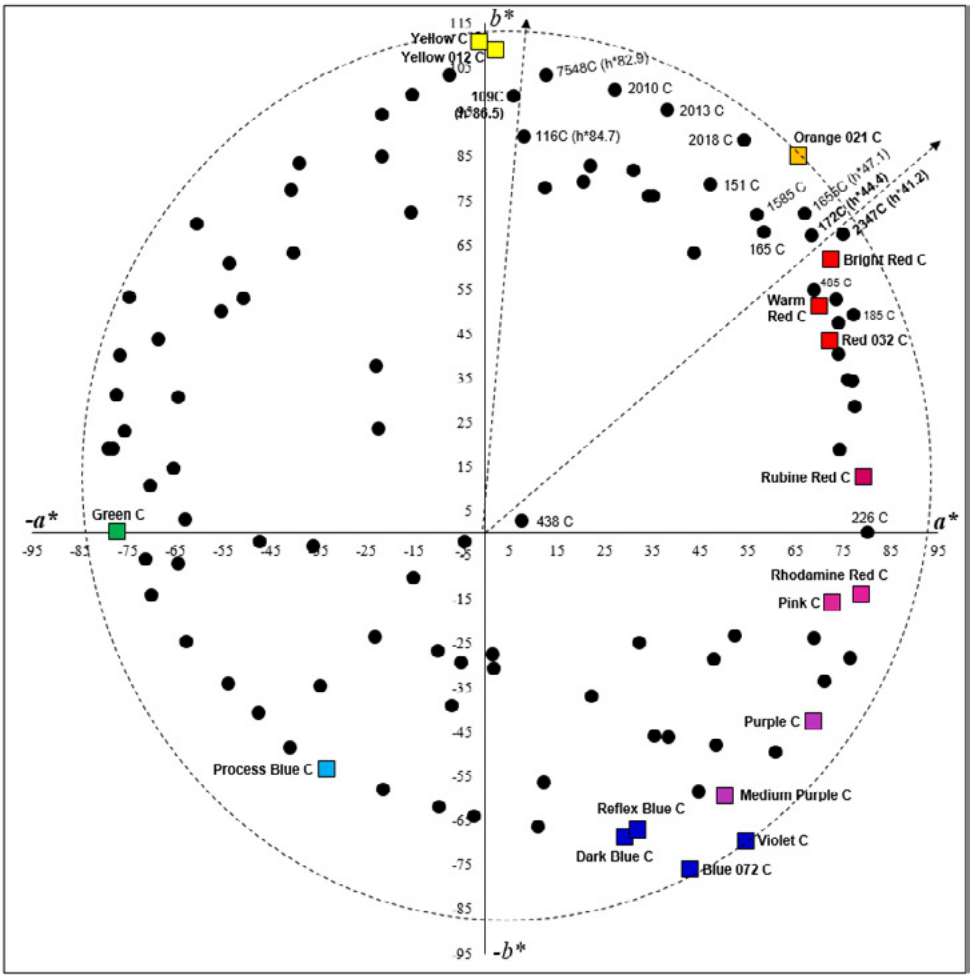

*Figure 6: Formula Guide Coated 2019 CIE a*b* coordinates for all 17 primary colors (squares) and 90 secondary colors (bullets); the orange area apparently lies between 42° and 85°*

An attempt to use a single page from the Pantone fan deck as a decisive factor gave a somewhat unexpected result. Due to the structure of each page in the Formula Guide, one might expect all seven colors from the same page to have approximately the same hue angle. But they do not, and there is a huge difference between the same color on coated and uncoated paper.

The color mixing from the same pure hue/ink (151 C&U) shows a span from h*52.2° to h*71.1° (Δh_{ab}18.9 and ΔH^*_{ab}18.7). In general, the colors are much more reddish on uncoated paper (Figure 7).

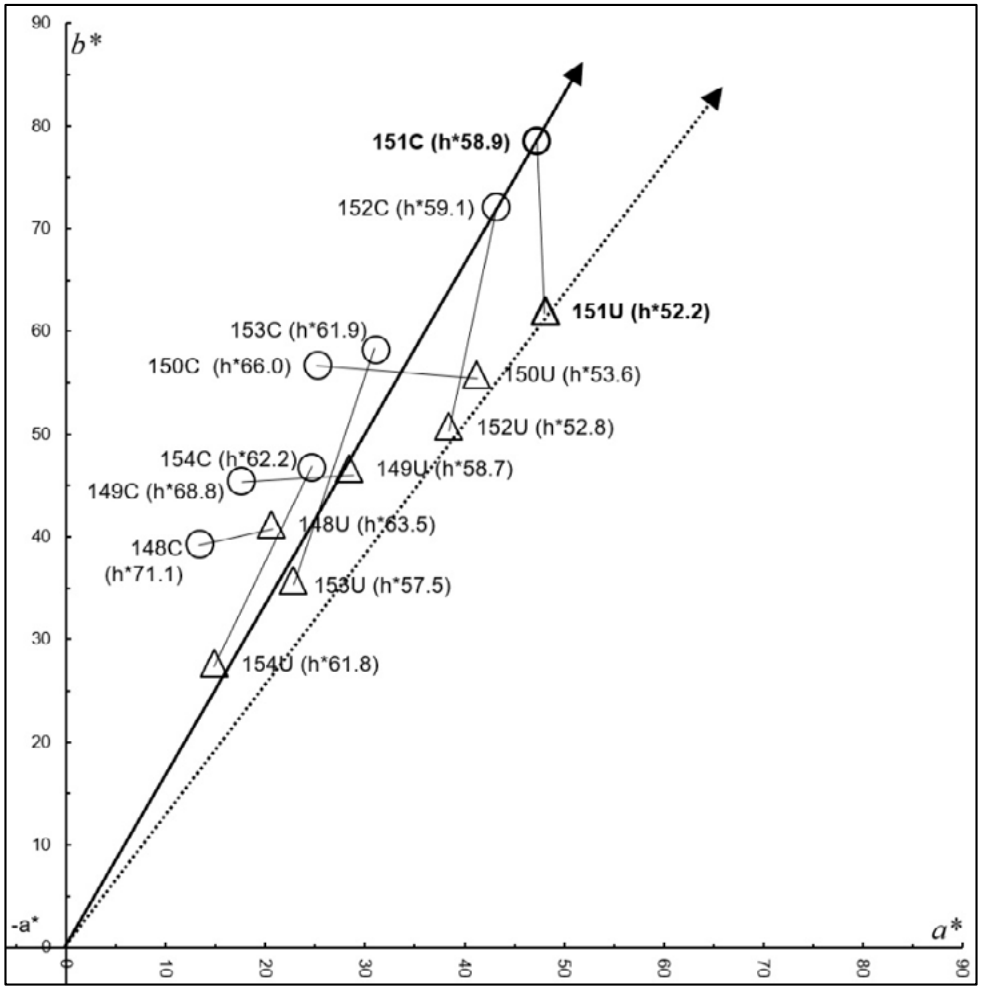

*Figure 7: Seven Pantone colors from page 21 C (circles), h_{ab} from 58.9° to 71.1°(Δh*12.2), and the corresponding seven colors from page 21 U (triangles), h_{ab} from 52.2° to 63.5°(Δh*11.3)*

Therefore, it is not possible to use one page in the Pantone fan deck as the defining factor. It is necessary to look at some of the secondary and tertiary colors that appear to be placed on the borders between color groups.

In the Pantone Formula Guide some of the colors are already named *Red, Orange, Yellow*, etc. Pantone Orange 021 C has a hue angle (h_{ab}) of 52.3°. In the same Pantone Formula Guide other colors can clearly be identified as being orange, light orange, or dark orange. For instance: 123 C (*h**80.8), 130 C (*h**75), 137 C (*h**69), 7548 (*h**82.9), 141 C (*h**81.5), 144 C (*h**65), 151 C (*h**59), 158 C (*h**55), 165 C (*h**49), 171 C (*h**41.7), and 172 C (*h**44.4). This is a span from 41.7° to 82.9°.

Moving onward in the numbered pages of the Formula Guide, the first colors named red (and so not orange) are Warm Red C (*h**36), Red 032 C (*h**31) and Bright Red C (*h**40.4). Other clearly red colors close to orange are 485 C (*h**38), 486 C (*h**37.5), 185 C (*h**32.5), 186 C (*h**30.6), and 2347 C (h*41.2).
Therefore, the border between red and orange seems to be placed between 41.2° (red 2347 C) and 41.7° (reddish orange 171 C). It will be simple to assume that the limit is h_{ab} 41.5°.

At the other end of the orange area, moving upwards to yellow, Pantone Yellow C has a hue angle of 90.7° and Pantone Yellow 012C has a hue angle of 88.9°.

Other colors close to orange can clearly be identified as being yellow. For instance: 113 C (*h**91.1), 104 C (*h**90.2), 106 C (*h**93.2), 114 C (*h**90.1), 108 C (*h**89.6), and 115 C (h*88.9). The lowest hue angle in this part of the yellow group is 88.9° (Yellow 012 C).

On the next pages, Pantone 109 C (*h**86.5) and 116 C (*h**84.7) seem to be a more reddish yellow and thus appear to be on the border between yellow and orange. The clearly orange 130 C (*h**75) is placed on page 7, and on page 9, Pantone 122 C (*h**84.5) and 123 C (*h**80.8) appear to be more orange than 109 C (*h**86.5) and 116 C (*h**84.7).

It might seem that the limit between yellow and orange is found between the reddish yellow 109 C (*h**86.5) and the light yellowish orange 122 C (*h**84.5), presumably at h_{ab} 85°.

As one of the consequences, Pantone 116 C (*h**84.7) is included in the orange color group. Figure 8 shows all the mentioned colors.

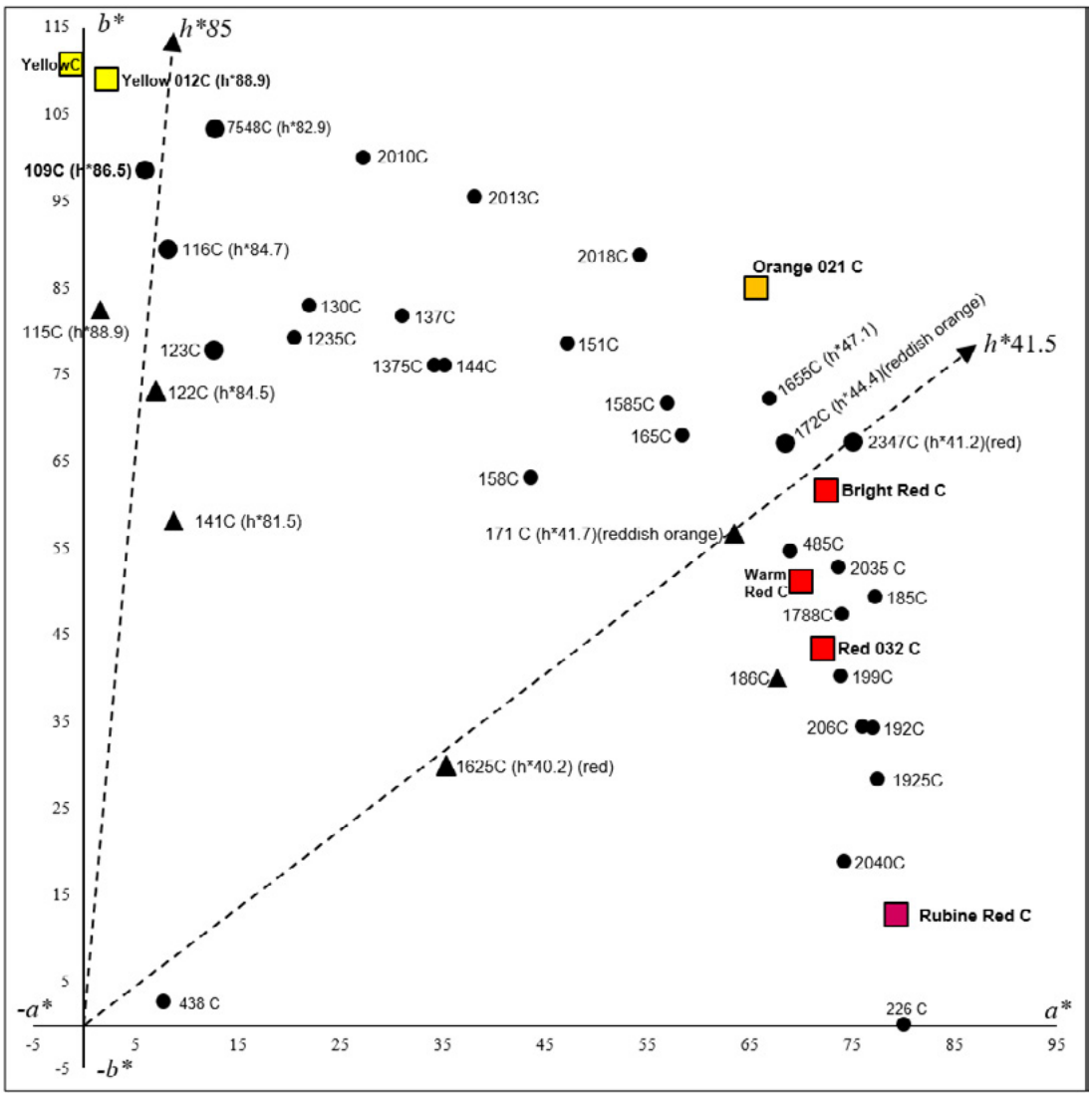

*Figure 8: A zoom-in on the upper right quadrant in the CIE a*b* projection diagram; primary colors (squares); secondary colors (bullets); and selected tertiary colors (triangles)*

Although this approach contains some uncertainties, the orange color group for Pantone C can be defined as lying between 41.5° and 85° in the CIE *a***b** projection circle.

By sorting all 1 867 Pantone colors by hue angle in Excel, it was possible to find the orange color group consisting of 342 Pantone C colors (Figure 9).

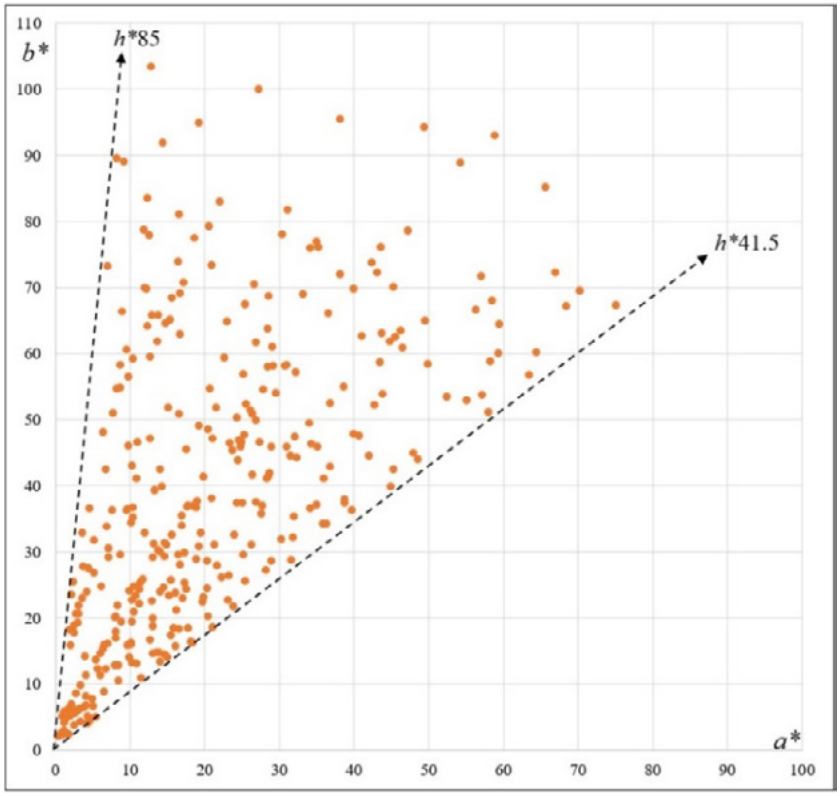

Figure 9: 342 colors from Pantone Formula Guide C, located in the orange color group (41.5°–85°)

However, these 342 colors also include three black colors (Black C, Black 4C, and Black 7C), 11 gray colors (Warm Gray 1 to 11C), and other colors in the dark brownish area.

Since it would not make sense to describe many of them as being orange, it is necessary to set up additional limits to exclude these colors without excluding the bright pastel colors and dark orange colors.

3.1 Preliminary Results

Setting a limit of C_{ab} > 15 and another limit of L^* > 30 excludes 57 colors, including black, gray, and some of the colors in the darkest area, leaving 285 colors for the orange area (Figures 10 and 11).

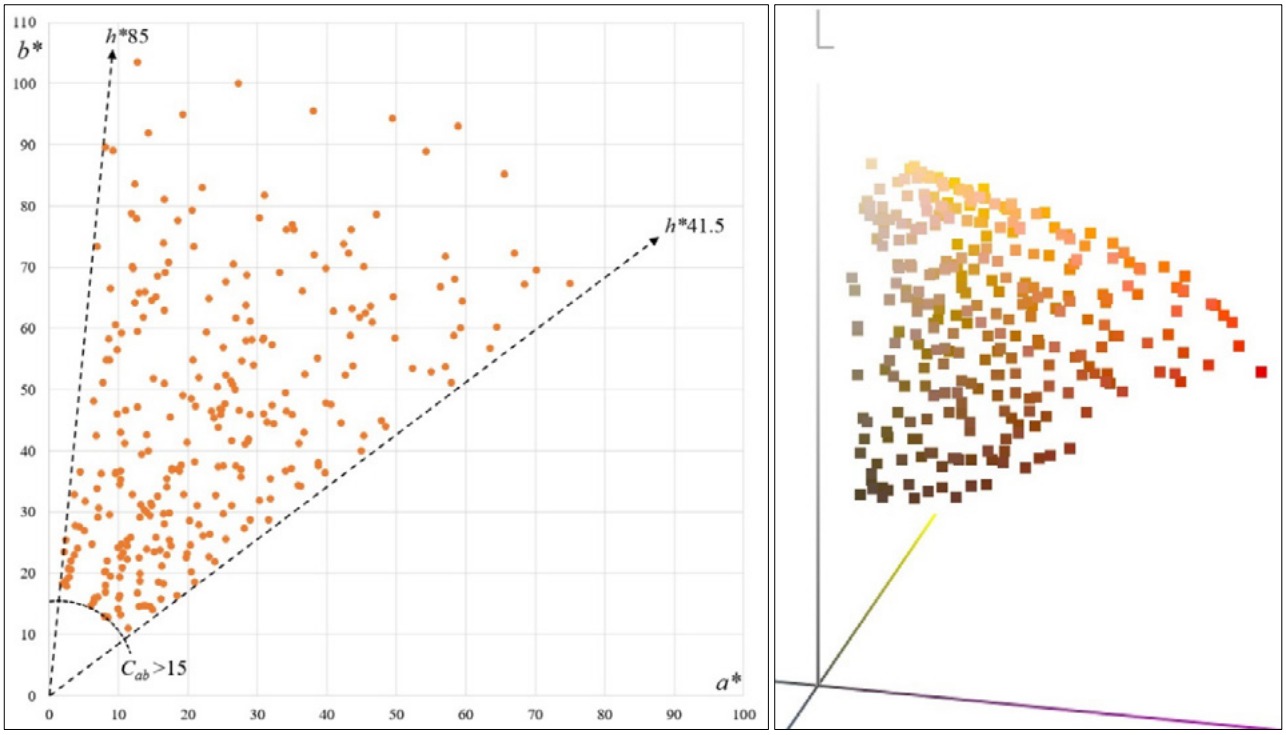

Figure 10: 285 colors in the orange color group, defined by h 41.5–85, C* > 15 and L* > 30; left: illustrated in a CIELAB a* b* diagram, right: illustrated in "3D" showing Lightness*

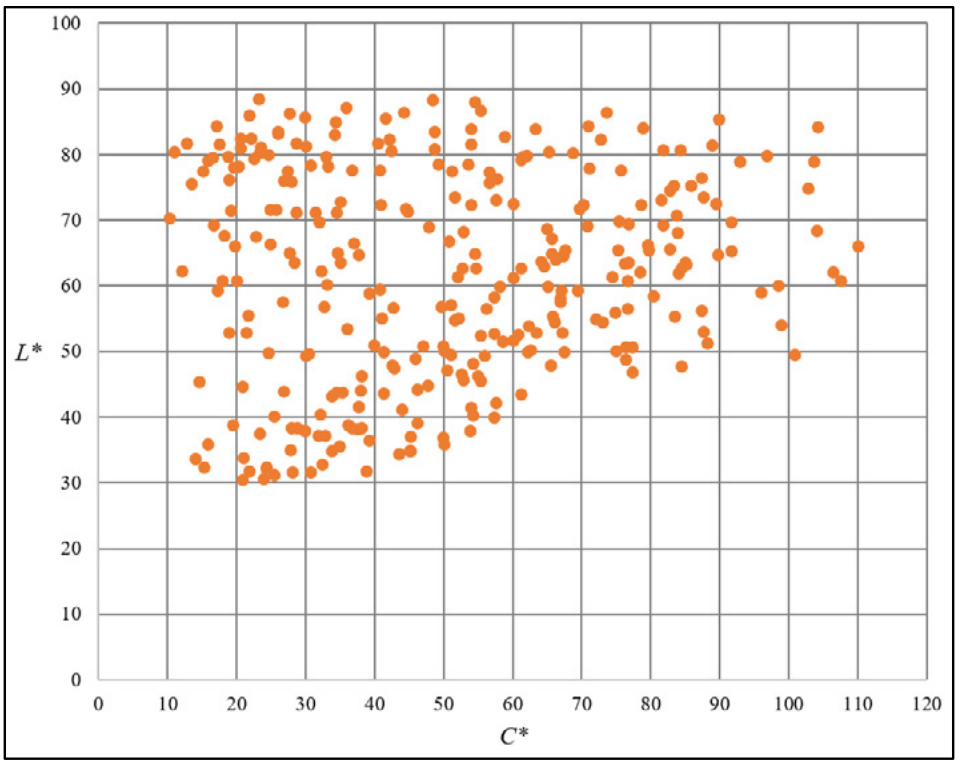

Figure 11: Orange color group in a CIELAB Chroma versus Lightness diagram

The first preliminary sketches for a Pantone color wheel are shown in Figures 12 and 13.

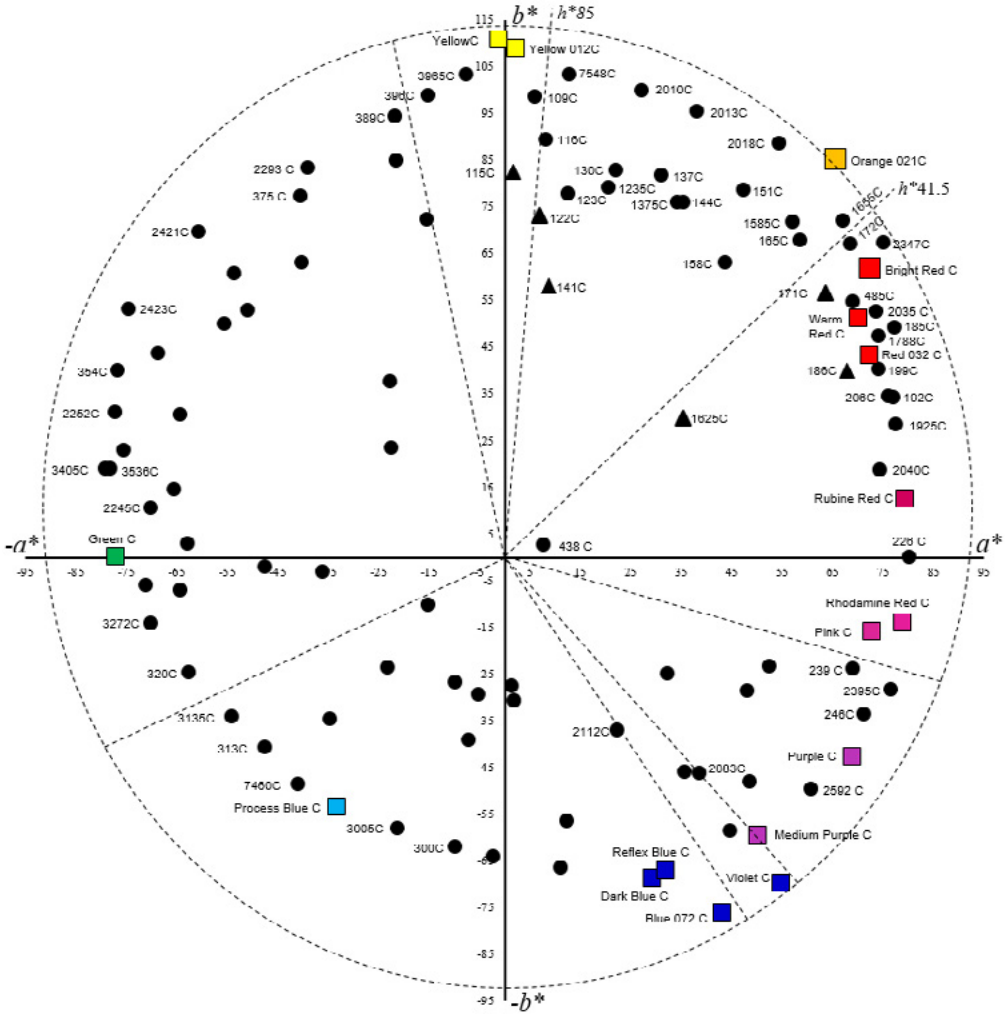

Figure 12: Preliminary rough sketch for a future Pantone Coated color wheel

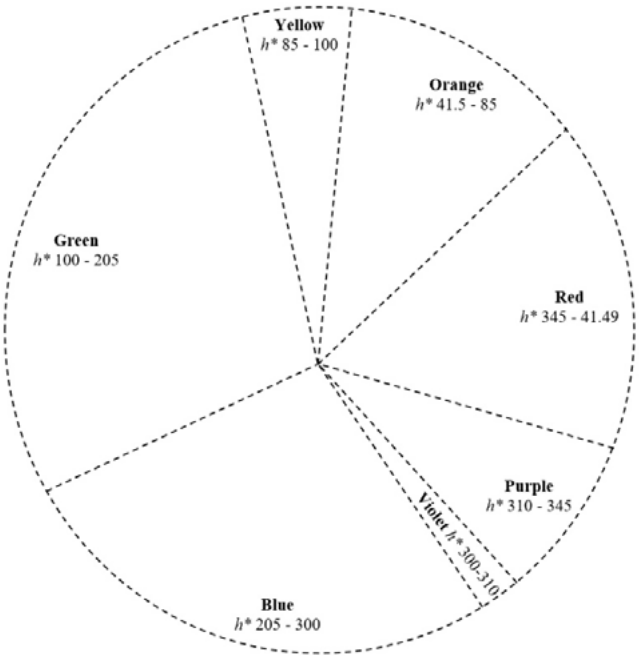

Figure 13: Estimated preliminary sketch for a future Pantone Coated color wheel

4. Conclusions

The first step in creating a color wheel for Pantone colors has to some extent been possible by setting up three technical criteria:

Pantone Coated; orange color group = h_{ab} 41.50°–85.00°, C^*_{ab} > 15.00 and L^* > 30.00 [1]

Thus, if a Pantone Coated color meets these criteria, it is orange. However, this results in very narrow and sharp borders between color groups. Decimals determine whether a color belongs to the orange or red color group. This does not seem to be ideal and might be too uncertain.

Thus, it might be necessary to set up other criteria and to analyze many more Pantone colors to determine all the main Pantone color groups in the CIE a^*b^* projection circle (yellow, green, blue, violet, purple, and red). It is also obvious that each substrate type must have its own color wheel and criteria.

References

Berns, R.S., 2000. *Billmeyer and Saltzman's principles of color technology.* 3rd ed. New York: John Wiley & Sons.

Herbert, L., 2019. *The Pantone Matching System® and Pantone formula guides*. [online] Available at: <pantone.com/pms-spot-color-information-formula-guides> [Accessed April 2019].

International Organization for Standardization, 2012. *ISO 12647-6:2012 Graphic technology — Process control for the production of halftone colour separations, proofs and production prints — Part 6: Flexographic printing*. Geneva: ISO.

International Organization for Standardization, 2009. *ISO 13655:2009 Graphic technology — Spectral measurement and colorimetric computation for graphic arts images.* Geneva: ISO.

McWade, J. ed., 2006. Our color wheel. *Before & After*. [online] Available at: <https://www.pantone.com/downloads/articles/pdfs/BA0646OurColorWheel.pdf> [Accessed April 2019].

Pantone, 2019. *Formula guide | coated & uncoated*. [online] Available at: <www.pantone.com/products/graphics/formula-guide> [Accessed April 2019].

Pedersen, M.A., 2017. The Yin and Yang of colors – how to calculate the exact complementary color to a specific chromatic Brand Color. In: P. Gane, ed. *Advances in Printing and Media Technology: Proceedings of the 44th International Research Conference of iarigai*. Fribourg, Switzerland, September 2017, pp. 119–128.

Seymour, J., 2016. *Unambiguous regions in color space for the basic chromatic colors.* [online] Available at: <http://johnthemathguy.blogspot.com/2016/> [Accessed April 2019].

Conditions for Colorimetric RGB-Luminescent-Printing

Marc Hunsänger[1] *and Armin Weichmann*[2]

[1] Bergische Universität Wuppertal
[2] Hochschule der Medien, Stuttgart
E-mails: marc@hunsaenger.info; weichmann@hdm-stuttgart.de

Short abstract

Luminescence is used in many different areas, for example in order to verify the success for bio-chemical reactions, but also in security printing. On nearly every identification or passport document, as well as bank notes such elements can be found. This paper is the proof of concept for a silkscreen printing process using three luminescent inks for red, green and blue, which are not invisible under illumination without UV and which give a reasonable colour gamut under UV exposure of 365 nm.

Keywords: luminescence, colour management, security printing

1. Introduction

Luminescentinks convert UV radiation to visible light (Noto, et al., 2016) and are common in security printing. Morić Kolarić, Žiljak Stanimirović and Bak (2015) for example describe an application with a combination of two luminescent colours. However, few security features use combinations of inks to generate RGB halftone pictures. The commercial available process INFACIO® by Gieseke + Devrient uses inks, which reveal the coloured image under UV lighting (Gausemeier, Glatz and Lindemann, 2012, p. 247), but they use pigments, which are recognizable under pure visible lighting (wavelength ~ 400–700 nm) too. TrueVision from GEMALTO (Gemalto, 2018), on the other hand, s not able to produce a reasonable colour gamut under UV exposure of 365 nm. However, this is the UV lighting condition the International Civil Aviation Organization (ICAO) suggests in its "Best practice guidelines for optical machine authentication" as a part of recommendations for the standardisation of travel documents (International Civil Aviation Organization, 2018).

Schiffmann, (2017) in a patent reveals a possible separation method for more than one colour. However, there are currently no colourimetric standards defined in order to determine the colour accuracy of images printed with luminescent inks. Christensen and Wolf (2106) describe "multidimensional fluorescent security features", like pattern codes and You, et al. (2016) a method to produce multi-layered QR-codes. Both do not aim at a colourimetric correct reproduction of RGB halftone images.

This paper is proof of concept of a silkscreen printing process which is able to reproduce RGB halftone images under pure 365 nm illumination and provides notes and suggestions for a colour management system (CMS) which is able to deal with luminescent colours.

2. Materials and methods

In security applications the most used and best available light sources for UV light radiate at a wavelength of 365 nm. UV light at shorter wavelengths is used too, as a single light source or in combination with the 365 nm, but is far less commonly available and significantly more expensive. Longer UV wavelengths are

also common. However, their emission maximum is not far from the lower end of the visible spectrum and the UV light sources usually have a wavelength distribution where their wing to the longer wavelengths contributes significantly to the blue response purple and therefore disturb the colours, which result from the luminescence. Furthermore, the absorption properties of the appropriate pigments are much worse than those usable with 365 nm. As already said, the ICAO suggests this wavelength (International Civil Aviation Organization, 2018). For this reason, the authors investigated the application of an ink set for printing true colours with this illumination only.

To get enough pigment for a bright image, luminescent inks need a layer thickness of a couple of micrometers. A high layer thickness is as well recommended to compensate the rather poor lightfastness of the pigments. Within the conventional printing processes silkscreen printing is the only one to provide such high layer thickness.

The principle of screen printing is comparable to stencils. A polymer mesh is stretched over an aluminium frame with a tension of several 15–20 N/cm. To produce the printing form, a photopolymer layer is applied on both sides of the mesh. This photopolymer layer is then hardened by UV radiation through a transparent film with the image as black, radiation blocking elements. Where the UV radiation was blocked the polymer remains soft and after the exposure these areas are washed out with water and only the screen remains. In these areas the ink can pass through the open mesh while the polymer blocks ink transfer.

The thickness of the polymer layer together with the mesh thickness mainly defines the volume and thickness of the transferred ink layer according to Equation [1].

$$V_{\text{wet ink}} = \frac{d_{\text{screen}} \cdot A_{\text{open}}}{100} \quad \left[\frac{cm^3}{m^2}\right] \qquad [1]$$

where d_{screen} is the thickness of the screen [µm], A_{open} the open area of the screen [%] and $V_{\text{wet ink}}$ the resulting wet ink volume.

The dry ink film consists of the solids, which are the components of the ink without the solvent. Therefore, has to be multiplied with the percentage of the solids in the ink, mainly the pigment and binder.

Since there were no processing instructions or processing recommendations for the screen inks supplied, practical processing parameters had to be found experimentally. The for silkscreen printing unusually low viscosity of the ink of about 80 mPa·s led to the use of fine screens.

As it was intended to print with conventional screening the colour sequence played an important role. The alternative would have been to print every colour in small dots non overlapping. However, this needs a very tight register and small printed elements, which both is not the strength of silk screen printing. Additionally, more pigment can be deposited when printing multi layered. Therefore, we decided for the conventional printing approach.

2.1 Screen

In this work, the main focus was on a round-to-round screen from ESKO. However, a line screen and a special wave moiré screen were also tested. It seems that for the colour impression the screen has only a subordinate influence. However, the trials show that due to the big part of highly volatile solvents, the silkscreen is at risk for clogging. To reduce the cleaning effort and get a longer open time, a hybrid screen consisting of a frequency modulated screen (dot size constant, density of dots according to tonal value) for the light tones and an amplitude modulated screen (number of dots per area constant, size of dots according to tonal value) for the remaining tonal values was used. The threshold for switching between FM screen

and AM screen was at about 20 % coverage. The 50 µm to 80 µm proofed to be a practicable range for the size of the smallest printing dot.

2.2 Silkscreen preparation

For the production of the silkscreens digitally imaged films were used. The film production was carried out with two filmsetters, ESKO CDI and Kodak Flexel. Both devices have a resolution of at least 1000 l/cm and the reproduction of the different tonal values is sufficient differentiated for this evaluation. Further experiments could make use of a linearization by evaluating a process calibration sheet.

The silkscreens for the green and blue inks were produced with the same parameters. The screens were coated via an automatic coating machine to ensure high reproducibility and consistency. A coating ratio of 1:1 (blade side/pressure side) was used. This resulted in a total form thickness (including mesh) of 42 µm, which led consecutively to the same (wet) ink thickness on the substrate. As the red ink has the lowest conversion ratio of the incident UV radiation, for the red colour a silkscreen polymer coating with a coating ratio of 2:1 (blade side/pressure side) was used, and thus the total layer thickness was 48 µm, resulting in an about 15 % higher ink thickness and therefore higher remission intensity. For all silkscreens, a mesh fabric with a thread thickness of 31 µm and a thread count of 150 l/cm was used.

2.3 Printing

The printing experiments described in this paper were performed at "Hochschule der Medien" in Stuttgart with industrial standard silkscreen printing equipment. The luminescent ink used is provided by a leading provider of security inks. To avoid additional nonlinear effects besides the luminescence of the inks, *EPSON SPP 205 proof paper* was used as the printing substrate. This paper is free of optical brightener agents (OBA), which was proven by Bohn (2018, p. 65). Thus we assume that the paper influence to the light emitting properties of the ink can be neglected. A second substrate *LAHNPAPER neobond* was used additionally, as this substrate is applied for documents like a 'Fahrzeugschein' or other official documents with an estimated lifetime of several years and is therefore of high interest in the frame of an application of this paper. However, this substrate is not examined in detail yet and the OBA content is not known.

Due to the limited amount of ink and substrate the printing process was performed manually by trained personnel.

2.4 Measurements

The printed samples and test charts where spectrally measured at "Bergische Universität Wuppertal" via a tec5 MultiSpecPro UV-VIS spectral photometer. This device utilises on the receiving side a spectral resolution of 1 nm with a photodiode array. The monochromatic illumination of the sample is realized via a high-pressure mercury lamp and a monochromator with a 3 600 l/cm optical grating. The monochromator was designed in the frame of the dissertation of Bohn (2018). The measurement geometry utilises an illumination angle of 45° and a measurement angle of 0°. The monochromator was set to 365 nm. The device delivers spectral intensity distributions, with a full-width-half maximum of approx. 5 nm. To calculate absolute values in normal colourimetry with subtractive colours the measured value would have to be related to the amount of incident white light. Every 5 nm or 10 nm section of the spectrum would be compared against the incident radiation, usually a "white" light, normally in graphic arts industry the D50 standard lighting. As in this setup no "white light" exists, only UV radiation, there is no incident light in the respective section of the spectrum, which could be compared against the measured spectrum. The luminescent ink acts like a light source by itself. On the other hand, as multiple layers of inks are applied on top of each other, where the layers above the lower ones absorb light according to their pigment properties, we are bound

to the subtractive colour model. Therefore, calibration to absolute values cannot be performed within the standard toolset of colourimetry. Hence the calculations were made with relative numbers, indicated by counts, and only these are displayed in the figures.

3. Results and discussion

In Figure 1 the emissions of the three inks illuminated with the same level of UV radiation are shown together with the emission of this UV illumination reflected by the paper.

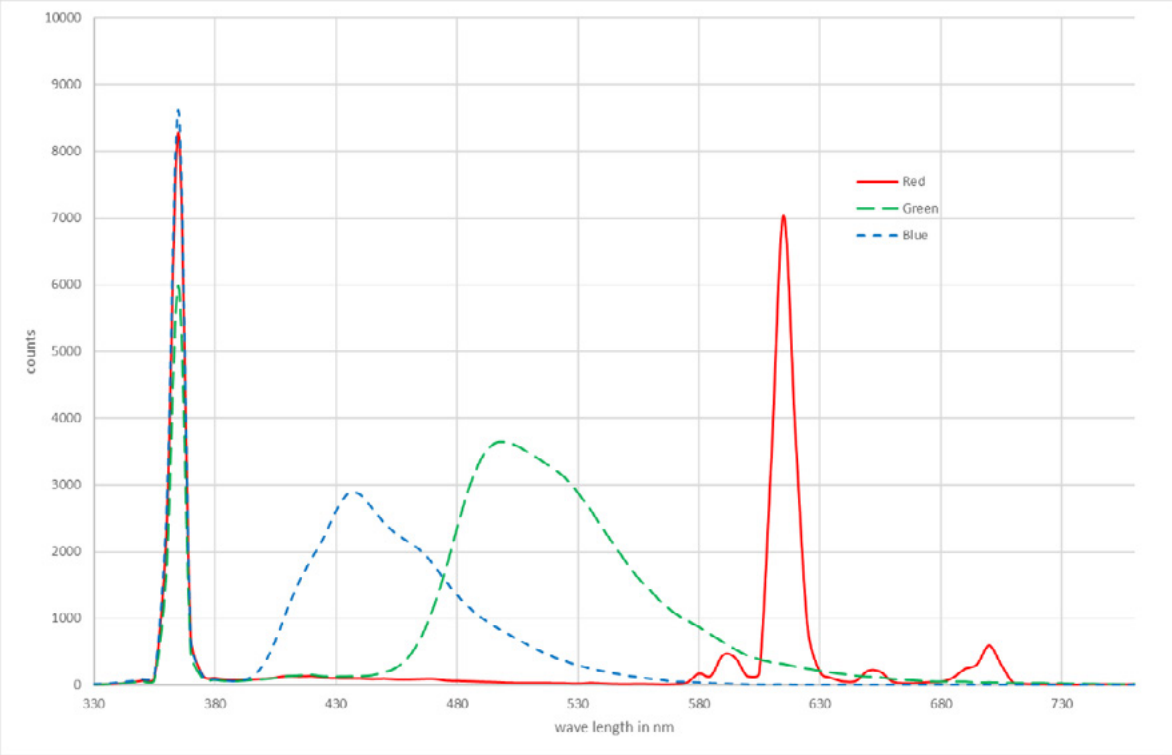

Figure 1: Emission curves for the three inks with monochromatic illumination at 365 nm

The incident UV illumination intensity divides in the not processed part, which is reflected by the paper and results in the peak at 365 nm. The bigger part of the radiation is transformed by the three luminescent inks into red, green and blue respectively. The peak of the red ink is the highest, but also the smallest. As the integral over the spectrum relates to the converted energy, red has the lowest total energy in this respect. The ratio of the three inks' spectral energies is R : G : B = 34.8 % : 100 % : 64.2 % with green as the most effectively light transforming ink. Blue is only 2/3rd as effective, red only about 1/3rd, even with the 15 % thicker ink layer compared to the blue and green ones.

Green is set to 100 %, as it has the highest conversion energy. This has to be seen as a relative number and does not mean 100 % reflectance, but as stated above (see 2.4), a calibration against the incident radiation is impossible here.

Figure 2 shows the absorption curves of the used inks in the wavelength range of 335 nm to 435 nm. It can clearly be seen that the absorption of the green pigment is highest in the relevant area of 365 nm. Additionally, the red curve shows that for the red pigment 365 nm is in the absorption shoulder of the pigment and therefore even small variations of the incident wavelength are magnified and would lead to significant changes in absorption rate. One future issue is to model this influence and determine the necessary tolerances of the light source.

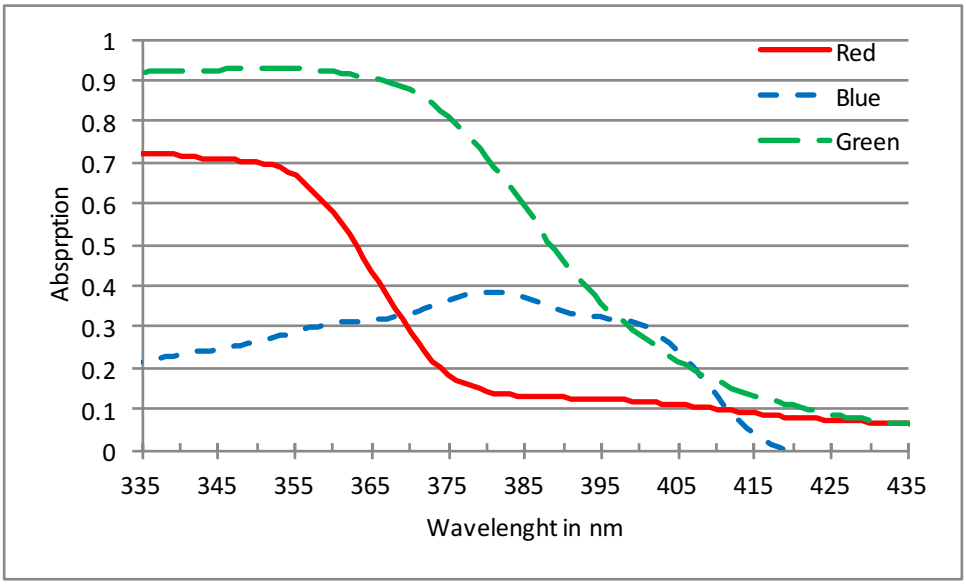

Figure 2: Absorption curves for red and blue ink

3.1 Colour sequence

It should be noted that the visual assessment of the sample surfaces was quite problematic. The light intensity of the printed surface differs greatly from the light intensity of the environment and light sources of 365 nm, which illuminate a reasonably large area homogenously were not at hand. Further efforts might develop a suitable Colour Appearance Model (CAM), which could simulate the physiological effects when using strongly different illumination levels. (Fairchild, 2013, p. 349ff).

In the XYZ resp. xyY colour space neutral grey is represented by the value (x,y) = (0.33, 0.33) (see Figure 4). Under the simplified assumption that the spectral curves add linearly one can take the spectra of Figure 1 and rate a ratio of these three spectra with the standard spectral value curves, so that the resulting x,y value yields a neutral grey (0.33, 0.33). This condition is fulfilled with a mixture of spectrum R 74 %, spectrum G 100 % and spectrum B 50 %. Printing the three inks with this tonal values while maintaining the layer thickness of the respective inks should then display a neutral grey.

However, the real prints show that this could be only a zeroth order approximation. It would only hold, when the three inks were printed adjacent to each other only. Disadvantageous to this setup is, that the total amount of pigment (the sum of all three inks) is only one third of a 100 % / 100 % / 100 % overprint of the three inks and therefore the luminance, which is proportional to the amount of pigment, is much lower than with overprint. The reduction of red and blue to 74 % and 50 % would reduce the luminance even further. Furthermore, if more than one ink is printed on the same spot, the white point is not independent of the colour sequence. This is not too surprising, as the inks modify the spectrum of the incident light while the radiation penetrates them to reach the underlying ink and modify afterwards the emitted light of the underlying ink too. As luminance is of high importance for a bright image, we aimed for the higher brightness instead of the easier reproduction of a neutral grey.

Figure 3 shows the appearance of different ink compositions when printed with three different ink sequences, red – green – blue, blue – green – red, green – blue – red (inks printed from left to right). As can be seen in figure 3 the ink sequence red – green – blue could realize significantly less contrast than the others. To minimize the waste of ink this sequence was neglected during further tests.

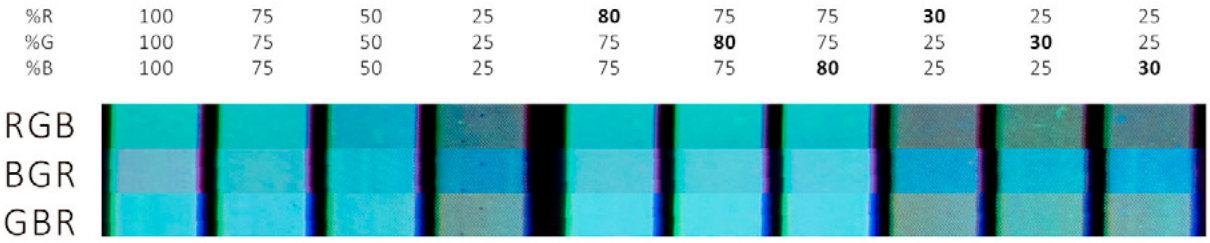

Figure 3: Photograph of samples of three different colour sequences; for better visibility the differences are enhanced

As expected, the other two ink sequences did not print to neutral grey either.

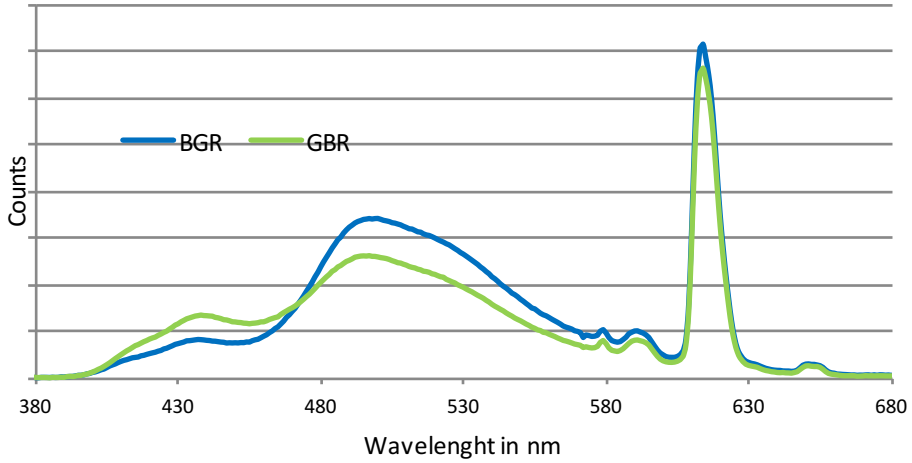

Figure 4: Spectral distribution of the 100% overprints of the ink sequences BGR and GBR

The observation of the spectra of R = G = B = 100 % on different substrates also confirms this. Figure 4 shows that the "GBR" ink order has a more even spectral distribution than "BGR". The resulting chromaticity coordinates (x, y) of the CIE XYZ colour space are BGR (0.31, 0.51) and GBR (0.30, 0.35). These coordinates are noted in Table 1 together with the coordinates of the single inks at 100 %. In Figure 5 they are positioned in the CIE 1931 colour space chromaticity diagram. With a distance of 0.036 GBR is significantly nearer to the white point than BGR, with a distance of 0.181, however, remains a bit too greenish.

Table 1: Chromaticity coordinates of the primary inks and the 100 % overprints for the ink sequences BGR and GBR

Inks	x	y
R	0.630	0.311
G	0.219	0.532
B	0.150	0.087
GBR	0.300	0.350
BGR	0.310	0.410

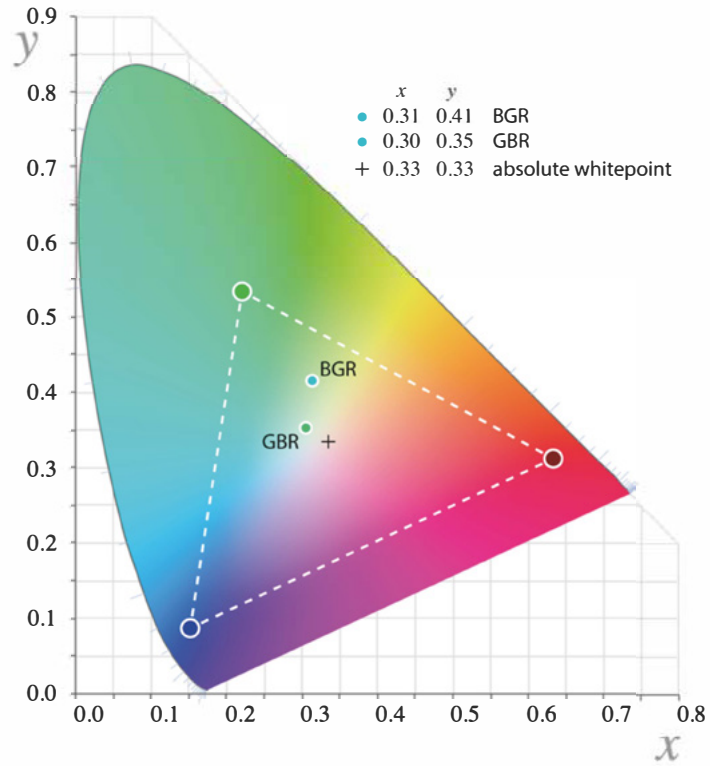

Figure 5: Chromaticity coordinates of the 100 % overprints for the ink sequences BGR and GBR and the three primary colours of the three inks within the CIE 1931 colour space chromaticity diagram

On the other hand, the eye retunes itself to different lighting conditions by chromatic adaptation and our brain sets even strongly colours with a big deviation from neutral to white. The best known example for this adaptation is that paper seems to be white to our brain under illumination A, which represents the light of an incandescent lamp and is objectively strongly yellowish. Therefore, the 100 % overprint of GBR can be used as the white point of our colour prints.

Based on the first print trial, gradation curves for the silkscreen films production had to be defined. The observation of the different colour patches showed a saturation effect within the overprints above tonal values of GBR (75 %, 75 %, 75 %). So these regions were clipped out. Additionally, the green ink appeared to have an over proportional effect when present in a patch. A comparable effect was found by Bohn (2018, p. 99ff), which he named *greening*. It is assumed that this effect appears due to the high conversion rate and the broad spectral distribution of this ink, which can be observed in the spectral curves in Figure 1 and Figure 2. Therefore, the maximal amount of the green ink was reduced further to 50 % leading to a maximal ink application with tonal values of GBR (50 %, 75 %, 75 %).

Due to the observation of greening in the test prints in the lighter tones too, the gradation curve of green was lowered in this area even more. The gradation curves were applied using Adobe Photoshop. The actual curves were found by an iterative process with the aim to get the maximum modulation out of the picture

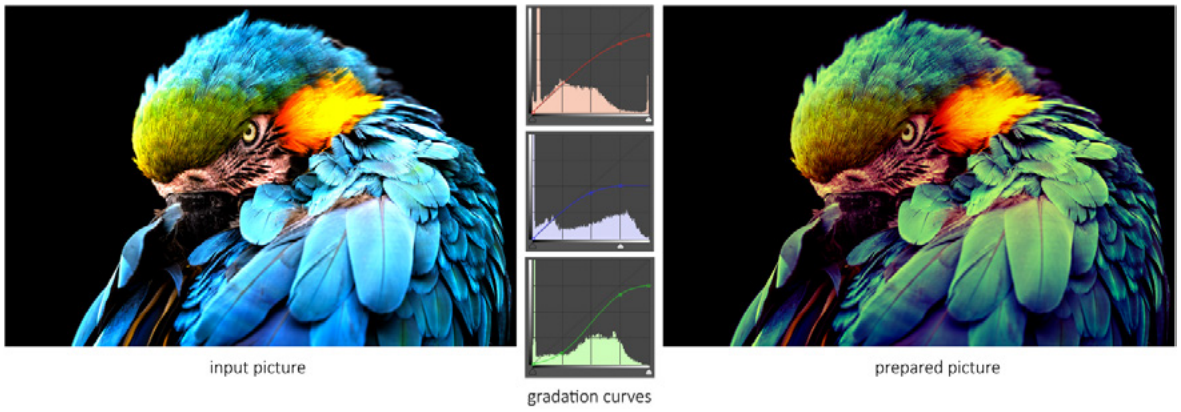

Figure 6: Image preparation with gradation curves

By using the (x,y) values of the reference colour stimuli of red, green and blue a 3D matrix profile was generated within Photoshop. Analogously to self-luminous displays, as white point Standard CIE Illuminant E was chosen. Figure 7 visualizes the mapping of the "custom profile".

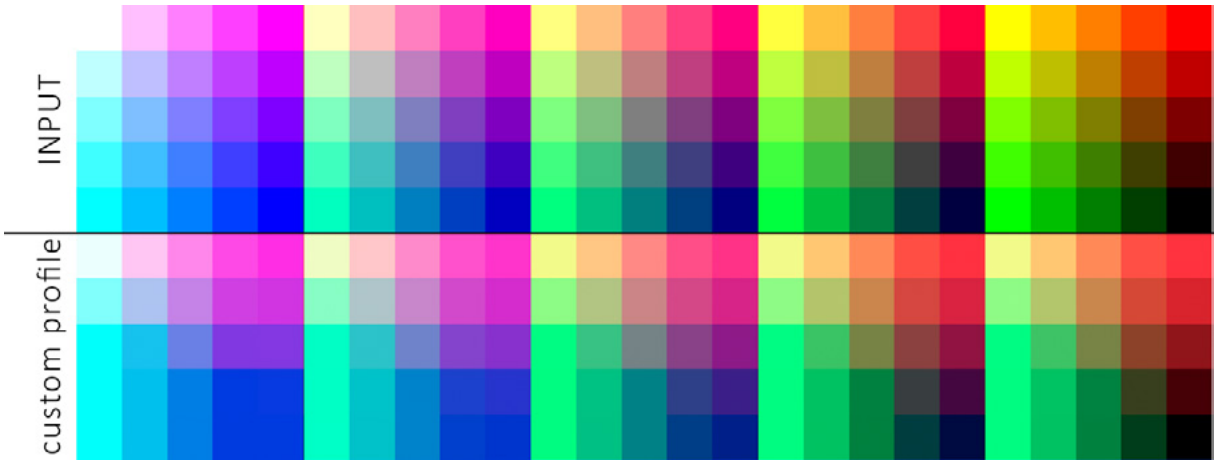

Figure 7: Image preparation

With this approach bright and pleasing colours could be accomplished. As an example, the image of a parrot is displayed in Figure 8. The image preparation is shown in figure 6 together with the gradation curves applied. However, approximate colourimetric correctness cannot be reached by this method. Therefore, a colour profile based on a colour chart with a sufficient number of colour patches will be the consequent next step.

Figure 8: Parrot reproduced with manual gradation curves

4. Conclusions

This work shows that true colour printing with UV luminescent inks is possible and can be implemented by simple means. In contrast to various patented methods, it was shown that even with common UV radiation sources with a wavelength of 365 nm only, true colour images can be reproduced. However, the spectral properties of the inks are not optimal and overprint leads to a reduction in gamut. An optimal mixture for white must be defined (also from visual evaluation). A visual intensity determination with a couple of test persons seems useful additionally in order to be able to perform a “standardization” of individual colours.

In a first step, a 3D matrix colour profile (CIEXYZ as PCS) was created by assessing the printed patches and defining gradation curves manually. By creating this colour profile and describing the approach to colour value calculation, the production of print templates was greatly simplified. An ICC LUT-profile generated with a colour chart should improve colour accuracy. However, due to the characteristics of luminescent inks they can be brighter in some areas of their spectrum than the substrate brightness and one has to deal with “negative” dot gain. Annex A of Specification ICC.2:2018 (International Color Consortium, 2018) describes methods to deal with fluorescence phenomena and might be appropriate to tackle this problem.

The spectral properties of the pigments contained in the inks limit the gamut and the overprint of more than one ink leads to additional absorption and non-linear effects. However, the results obtained are satisfactory for continuing the work. In a next step we aim at a working model of true colour print with luminescent inks. If in security applications elements are printed in true colour and the colours together with its tolerances can be defined, automated tests for colour values can be performed. Today mainly pattern matching is the state of the art. Measuring colour in a combination of three inks could extend these evaluations. Reproduction of such colour elements by printing of three inks in correct colour sequence which leads to a defined colour is clearly a complex task and therefore could increase the difficulty in counterfeiting.

Acknowledgements

Prof. Dr. U. Jung and Dr. D. Bohn from BUW supported the project in an early state with their experience at the UV/VIS spectral photometer. M.Sc. S. Riegel and Dipl.-Ing. (FH) B. Michl from HdM supported the author during the printing tests.

References

Bohn, D., 2018. *Entwicklung einer lichtartunabhängigen Weißpunktanpassung für Proof-Prozesse auf Basis des Verdruckens von optischen Aufhellern unter spezieller Berücksichtigung von chemischen und farbmetrischen Effekten.* Dr.-Ing. Dissertation*.* Bergische Universität Wuppertal.

Christensen, P.R. and Wolf, M.O., 2016. Photopatterned multidimensional fluorescent images. *Advanced Functional Materials*, *26*(46), pp. 8471–8477. https://doi.org/10.1002/adfm.201603294.

Fairchild, M.D., 2013. *Color Appearance Models*. 3rd ed. Chichester, UK: Wiley.

Gausemeier, J., Glatz, R. and Lindemann, U., 2012. *Präventiver Produktschutz: Leitfaden und Anwendungsbeispiele*. München, Germany: Carl Hanser.

Gemalto, 2018. *True Vision: brilliant true-color image under UV*. [online] Available at: <https://www.gemalto.com/govt/security-features/sealys-true-vision> [Accessed 12 April 2019].

International Civil Aviation Organization, 2018. Best practice guidelines for optical machine authentication. [pdf] Available at: <https://www.icao.int/Security/FAL/TRIP/Documents/Best%20Practice%20Guidelines%20for%20Optical%20Machine%20Authentication%20V1.2.pdf> [Accessed 12 June 2019].

International Color Consortium, 2018. *Specification ICC.2:2018: Image technology colour management - Extensions to architecture, profile format, and data structure*. [pdf] Available at: <http://www.color.org/specification/ICC.2-2018.pdf> [Accessed 13 April 2019].

Morić Kolarić, B., Žiljak Stanimirović, I. and Bak, I., 2015. Security offset printing with twin colours by means of CMYF separation. *Journal of Print and Media Technology Research*, 4(2), pp. 111–118. https://doi.org/10.14622/JPMTR-1432.

Noto, L.L., Swaart, H.C.,Mothudi, B.M., Mbule, P.S. and Dhlamini, M.S., 2016. The dynamics of Luminescence. In: J. Thirumalai, ed. *Luminescence: an outlook on the phenomena and their applications*..Rijeka, Croatia: IntechOpen. pp. 13–32. https://doi.org/10.5772/65050.

You, M., Lin, M., Wang, S., Wang, X., Zhang, G., Hong, Y., Dong, Y., Jin, G. and Xu, F., 2016. Three-dimensional quick response code based on inkjet printing of upconversion fluorescent nanoparticles for drug anti-counterfeiting. *Nanoscale*, 8(19), pp. 10096–10104. https://doi.org/10.1039/c6nr01353h.

Influence of Colour and Gloss on the Visual Perception of Embossed Prints

Jennes Hünniger, Simon Hamblyn and Engisch Lutz

HTWK Leipzig, Gustav-Freytag-Straße 42, 04277 Leipzig
E-mail: jennes.huenniger@htwk-leipzig.de

Short abstract

Embossing of paperboard packaging and other paper products is used to provide both a haptic and a visual effect. This is often used on printed and varnished finishes, however, little research currently exists of how the visual aspect of the embossing is affected by the colour and finish used. Two studies, each with 40 test subjects were undertaken, to investigate the how gloss and ink colour affected the perception of the height of an embossed pattern. Paperboard samples were produced using different combinations of colour and varnish finishes, which were then embossed to provide the same embossing height on each. The samples were then visually assessed during controlled experiments. The results showed that the combination of ink and varnish on embossed board samples have a significant influence on the visual impact of an embossing. Within a colour set, the perception of height was linked to the gloss level. The embossing was perceived as being higher on glossier finishes, than those with a matt finish. However, there was also in interaction between the ink colour and the gloss, where for a similar gloss value, an embossing on a darker colours was perceived as being higher than those on a lighter colour. Therefore, a combination of a darker ink colour and higher gloss level would result in a larger visual impact. However, while this combination produced the greatest perception of height, only a part of the embossing was visible to the test subjects under the test conditions used due to how the light was reflected from the glossy surface. However, the combination of black ink with a matt finish resulted in the entire embossing being observed albeit with a lower visual impact. These studies therefore highlight the difficulty in designing packaging to provide the optimal visual impact under all conditions.

Keywords: embossing, surface properties, visual assessment, height

1. Introduction and background

The wide range of products at point-of-sale has meant that the graphical design of packaging has become an important part of the unique selling point of a product. Elaborate designs, colours and refinement techniques such as surface finishes, metallic effects and embossing are used to attract the attention of the buyer. The interaction between colour and surface properties of the material and its influence on the optical effect of embossing is crucial, but is often ignored.

Embossing is a forming process used to create a relief or raised pattern in the surface of a material. The substrate is pressed between one or more dies containing a relief pattern using high pressure and sometimes heat (Bleisch, et al., 2006) to leave a replication of the pattern in the surface of the material. This pattern is not only tactile, but can also be used to visually enhance the visual impact and impart a luxury feel to packaging (Kirwan, 2013). Embossing is often used to highlight elements of the design such as lettering and logos. Often the relief height of the embossing is given as the most important measure of its quality.

How an object and its surroundings, such as a product on a shelf, are perceived visually by an observer depends on the structure and function of the human eye, the experience of the observer, the colour temperature of the light, the angle of light and the viewing angle as well as the interplay of light and shadows (Zwimpfer, 2012; Nänni, 2008). The visual perception of our environment is essentially based a two-di-

mensional projection of the world on the retina of the eye. Nevertheless, we see our environment not in two-dimensions, but as a three-dimensional space. The interplay of different depth stimuli and subjective empirical values creates a three-dimensional image of what is interpreted by the brain. Oculomotor stimuli describe the tactile change in the shape of the lens in the eye as well as the movement of the eyes when looking at objects that are near or far. They play a role especially when looking at objects from a short distance. Monocular deep stimuli require only one eye and use two-dimensional information and movement. Experience-based information about relative and familiar sizes, sharpness, colour gradients, texture gradients, shadows, and occlusion of objects is used to perceive the existing depth. In addition, information from the observer's position to the object and the movement of the observer is also used. Stereoscopic depth stimuli use information from the two different viewing angles of both eyes. A pivotal part of the information is the so called traverse disparity (Wallach and Bacon, 1976), which compares how the alignment of homologous elements differs between the two eyes (Heller, 2006; Goldstein, 2008; Metzger, 2008).

Another influencing factor is the perception and effect of colour. Although colour can be described by means of colour models, it is a subjective sensation of the sensory organ of the eye. When describing the colour of an object, one speaks of the body colour, which is determined by the absorption capacity of the material. When light strikes an object, some of the wavelengths are absorbed and some are reflected (Hunt, 2004). The part that is reflected is perceived by the eye. The spectral composition of the illumination is dependent on the light source and influences the composition of the perceived hue (Küppers, 2004; Ottersbach, 2004).

While the type of light source influences the perceived colour, the position of the light source affects the shadows cast by the object. In addition to sharp lines or points, the eye primarily needs light and shade in order to distinguish a three-dimensional form on a surface. The shadow of an object is essential for the perception of three-dimensional bodies and structures. The influence of lighting is evident when viewing surfaces under different lighting conditions and positions. For example, in diffused light, small structures on the surface of paper are not observed. However, if there is a directional light source that illuminates the surface at a shallow angle, even the smallest undulations in the surface will be visible due to the contrast from shadows that are formed. It therefore depends to a large degree on the position of the light source whether depressions and elevations or structures are perceived on a monochromatic surface or not. (Metzger, 2008; Liu and Todd, 2004; Mamassian and Landy, 2001)

This research forms part of a larger study into the factors affecting the impact of embossing of paperboard. In this research, visual assessments were performed to investigate how the ink colour and gloss level affect the visual perception of the height of an embossed surface.

2. Materials and methods

Two separate studies, each with 40 test subjects, were performed. The test subjects for both studies ranged in age between 20 and 60; all were classified as having normal vision either with or without glasses. In the first study, only cyan, yellow and white samples were used in combination with different surface finishes. The second study, repeated some of the tests from the first study, but black was also included to extend the date set.

2.1 Sample preparation

Samples were prepared using a white multilayer coated paperboard (Stora Enso Ensocoat 230 g/m^2). These were cut to a size of 230 mm × 80 mm. Some of the samples were then printed using either a black, cyan or yellow process offset printing ink (Sun Chemical Sunlit SKF) with 100 % coverage using a printability tester, while other samples remained unprinted. To ensure the colour was consistent between samples;

the colour and optical density were measured with an X-Rite SpectroEye spectrophotometer. Some of these samples were also coated using either a gloss (Hartmann F1000) or matt (Hartmann F3000) offset varnish to provide different gloss levels. The gloss was measured according to DIN EN 14086 (Deutsche Institut für Normung, 2003) at an angle of 60° with a Minolta Multigloss 268 glossmeter. The sample types are listed in Table 1. At total of 8 samples were produced and characterised for each sample group.

Table 1: Ink and varnish combinations for the sample types

Sample group	Ink colour	Varnish
1	Black	Gloss
2	Black	Matt
3	Black	Unvarnished
4	Cyan	Gloss
5	Cyan	Matt
6	Cyan	Unvarnished
7	Yellow	Gloss
8	Yellow	Matt
9	Yellow	Unvarnished
10	Unprinted (White)	Gloss
11	Unprinted (White)	Matt
12	Unprinted (White)	Unvarnished

The gloss levels differed depending on the combinations of ink and varnish (Figure 1).

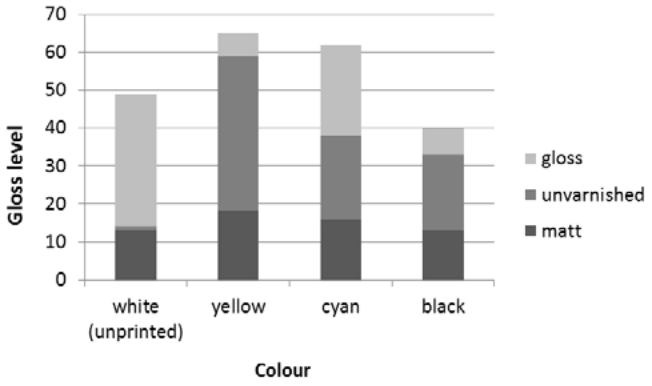

Figure 1: Average gloss measurements for the different colour and varnish combinations

Generally the samples with the gloss varnish had highest gloss levels and the samples with the matt varnish the lowest, but the actual gloss level was also highly dependent on the colour. Overall the yellow samples had the highest gloss levels; however, there was little difference in gloss level between the gloss varnish and the non-varnished ink film. For the unprinted samples, the there was little/no difference in gloss between the non-varnished and matt varnished finishes. The cyan samples displayed the largest differences in gloss levels between the different finishes. While the black samples had the lowest overall gloss levels, which was probably due to its absorption characteristics.

The samples were then embossed using a pair of dies to leave a relief pattern in the surface of the paperboard. A schematic of the embossing process is shown in Figure 2. The embossed pattern consisted of a Sunburst pattern (80 m × 45 mm), with lines with a nominal width of 1.5 mm at an angle of 11.25°. The

lines on the embossing dies had a triangular shape in cross-section. The same force of 6 000 N was used for each sample.

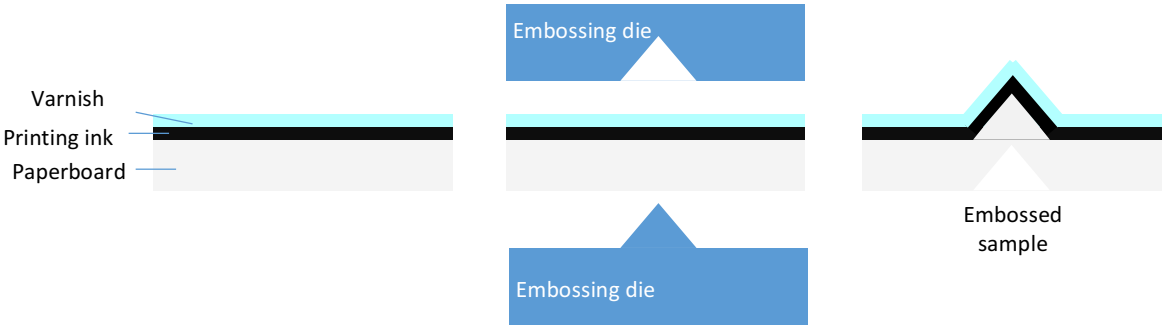

Figure 2: Embossing of samples

The topography of the embossed lines, were measured using a Keyence 3D Microscope using the fringe projection technique. A typical profile of an embossed line is shown in Figure 3. The height, width and slope angle of the embossed lines were measured. The average embossing height of the prepared samples was 111 ± 2 µm.

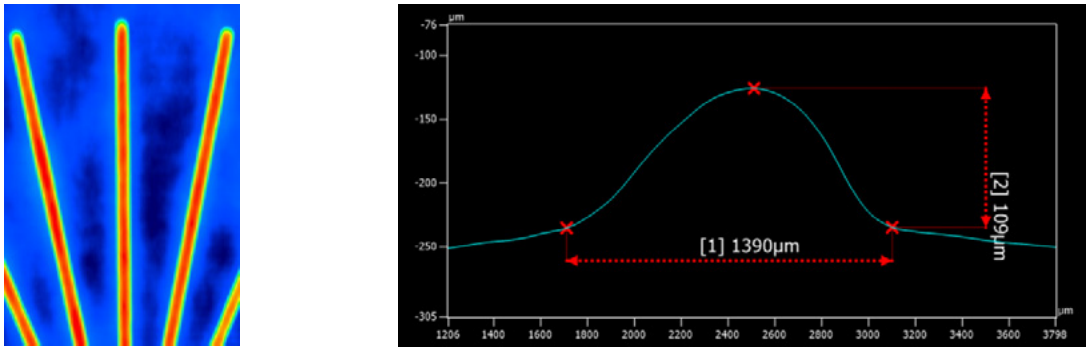

Figure 3: Topography measurements of the embossed lines

2.2 Subject testing

The test environment was designed to ensure that all test subjects viewed the samples under the same conditions. The test subjects were positioned in front of a light box on an adjustable chair to achieve a viewing angle of 60°. The samples were positioned in the light box under a D50 illuminant on a sample table at an angle of 35° to the plane and at a distance of 15 cm from the outer edge. The samples were located within a neutral grey frame in order to focus the view of the observer on the embossing (Figure 4).

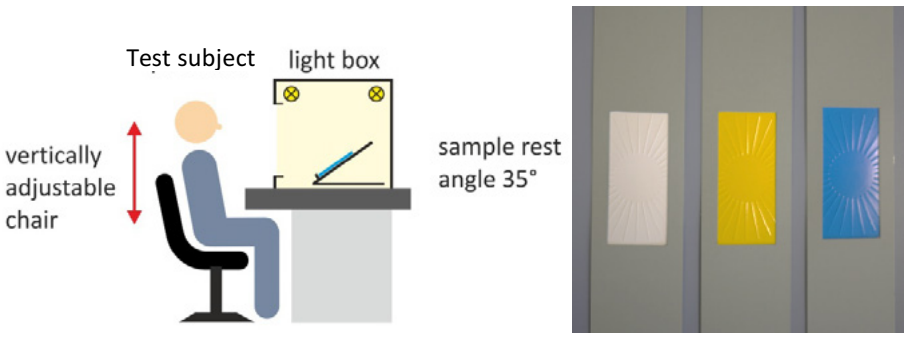

Figure 4: Test setup (Hünniger, 2013) and embossed samples (Maaß, 2014a)

In order to investigate the influence of colour and gloss on the perceived height of an embossing, two types of visual assessment test were carried out. The test subjects were first asked to rank a series of the same colour samples in order of the most prominent embossing to the least. These were then scored from 1 to 4, with the sample deemed to have the most prominent embossing awarded 4 points and the least prominent 1 point. These tests also included two identical unvarnished samples as a control. The subjects were not informed that the embossing height was in fact the same for each sample regardless of colour or gloss.

To further distinguish between the effect of colour and the effect of gloss on the perception of the embossing, the test subjects were asked visually evaluate pairs of samples of the different colour and varnish combinations from Table 1 and select the sample with the most prominent embossing. This sample was then scored with a value of 2 points, while the other sample given a score of zero. If no difference was perceived, both samples received 1 point. The points were then tallied for each sample. Included were also control samples of non-embossed and non-varnished cyan and yellow samples which subjects compared with their embossed counterparts. Examples of the two test types are shown in Figure 5.

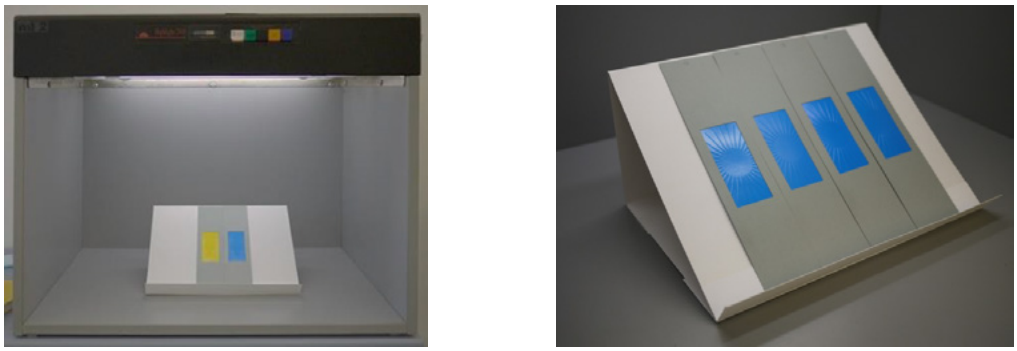

Figure 5: Pair test (left) and ranking test (right) (Maaß, 2014b)

3. Results and discussion

The results from the second study confirmed the trends observed in the first study; therefore the results presented are mostly from the second study. For the ranking tests, where several samples, of the same colour, were sorted according to their perception of the embossing height, in almost all cases the samples were ranked in order of their gloss level, where the samples with the highest gloss deemed to have the highest embossing. This is shown in Figure 6.

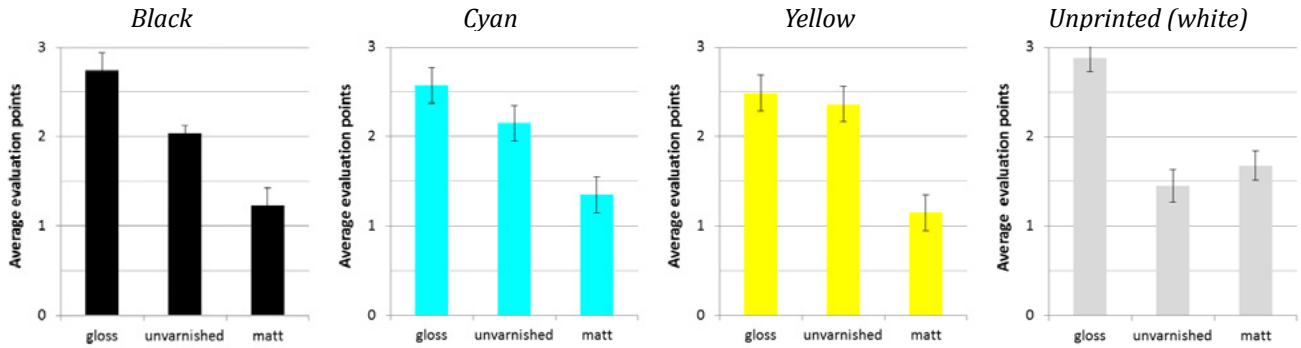

Figure 6: Average ranking for each colour

For the yellow samples, the test subjects could not easily distinguish a height difference between the gloss and non-varnished finishes. This corresponded to the small differences in gloss levels measured between these two finishes (shown in Figure 1). This was also the case for the unprinted samples, where there was

virtually no difference in gloss level between the non-varnished and the matt varnished samples and which resulted in the test subjects rating these two samples similarly, albeit with the matt finish being rated as having a slightly higher embossing. For the black and cyan samples there were distinct differences between the test subject's perceptions of the embossing height for the different finishes, which roughly corresponded with the differences in gloss levels measured. However, the test subjects perceived a larger difference in the embossing height between the gloss and non-varnished samples for the black samples than for the cyan samples. This was despite the difference in gloss values between non-varnished and gloss varnished finishes for the black samples being smaller than for the cyan. This suggested that although the gloss was important, the colour also played in a large role in the height perception.

Unknown to the test subjects, the ranking test included two identical non-varnished samples. These were included as a reference to determine if the subjects ranked these equally or not. The results of these are shown in Figure 7. For the black samples, in 92 % of cases these samples were considered as being identical. However, this was not so clear with the other colours. For white and yellow, these samples were only rated as identical by 77 % and 67 % of the test subjects respectively. For the cyan samples 82 % of the test subjects correctly identified that the samples were identical.

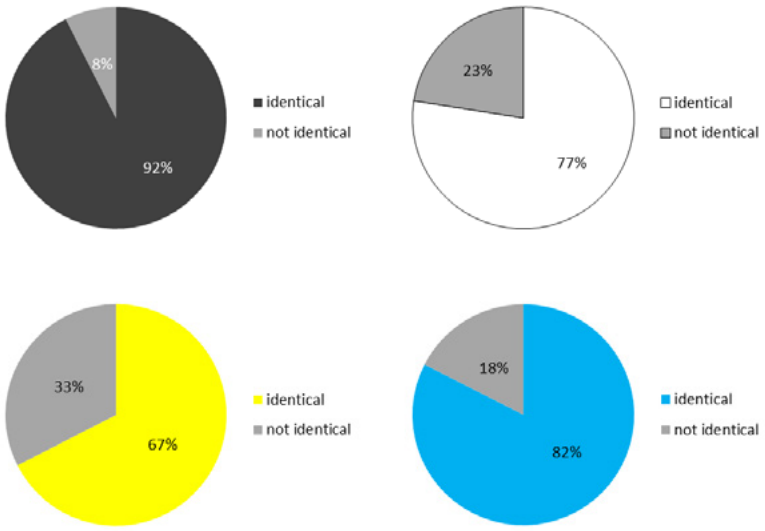

Figure 7: Results of the control test with identical samples

The results of the ranking tests showed that within a colour set, the gloss had a significant effect on the perception of the embossing. The pair tests showed that colour was also significant factor in how the embossing height was perceived, with the embossing on the black ink being more often perceived as the highest, followed by cyan. However, while most test subjects rated the embossing height on the black samples as being higher than those on white samples, for the other combinations of colours, this was not so clear. The results also showed that the interaction between the colour and the gloss was also significant. During the pair test it was possible to compare different colour and finish combinations with that had similar gloss values. The test subjects were asked to award two points to the sample with the highest embossing (with zero points to the other), or when both samples were perceived to having the same embossing height, one point was awarded to each. The results are shown in Figure 8.

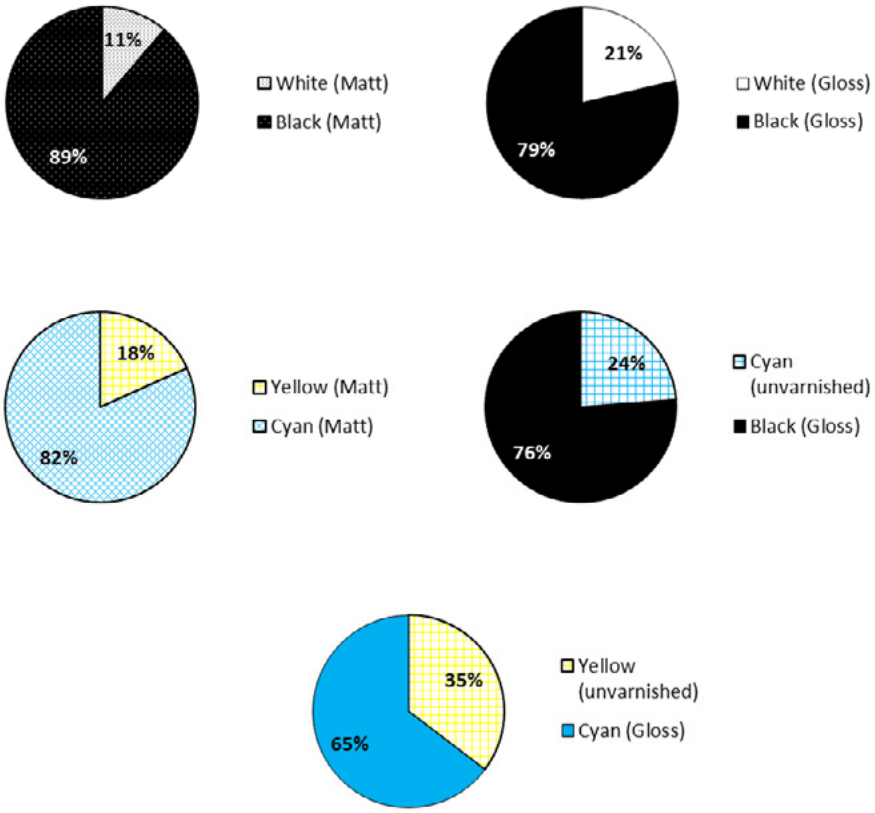

Figure 8: Height perception based on a comparison of two samples with similar gloss levels

For some combinations there was a clear difference in the height perception between samples. For example, when the test subjects were asked to compare the Matt Black sample with the Matt White sample, both had the same gloss value of 13, however, the test subjects awarded 89 % of the points to the black; therefore the majority of the test subjects clearly perceived the embossing as being higher on the black sample than on the white sample. Whenever, two samples with similar gloss levels were compared, the majority of test subjects selected the samples with the darker colour as having the higher embossing height, such as when comparing black and white samples and black and cyan samples. In the case where the gloss levels were very high, such as when comparing the Gloss Cyan sample with the Unvarnished Yellow sample (gloss values of 62 and 59, respectively), a higher embossing height was generally perceived on the cyan, but the results were not as conclusive as the samples with lower gloss levels.

4. Conclusions

The laboratory studies have been conducted to assess how colour and gloss of printed and varnished paperboard affect the visual impact of an embossing. Generally, glossier surfaces resulted in a higher embossing height being perceived, but the colour also had a significant effect. In the paired tests, the test subjects rated the embossing on darker colours (black and cyan) as having a higher embossing height as those on lighter colours (yellow and white). However, the embossing on black ink was perceived as being more pronounced than the other colours. Overall, the embossing on the black samples with a gloss varnish were perceived to have the highest relief, however, the test subjects also observed that under the test conditions, only a portion of the embossing was visible. This was largely due to the scattering of light caused by the interaction between the angle of illumination, the viewing angle and the gloss of the sample. This was not the case with the black samples with a matt varnish; the entire embossed pattern could be seen due to different light scattering characteristics. Therefore study highlights the complex interactions that

exist between the light absorption and reflection influenced by the colour and the gloss of the surface, the viewing and illumination conditions and also differences between the perceptions of different observers. Designers must therefore be aware that depending on the colours and finish used, the visual impact that they are seeking by embossing, may not be achieved.

References

Bleisch, G., Goldhahn, H., Schricker, G. and Vogt, H. eds., 2006. *Lexikon Verpackungstechnik*. Heidelberg: Hüthig.

Deutsche Institut für Normung, 2003. *DIN EN 14086 Papier und Pappe - Bestimmung des Glanzes - Messung mit einem parallelen Strahl bei* 45°, DIN-*Verfahren; Deutsche Fassung EN 14086:2003*. Berlin: DIN.

Goldstein, E.B., 2008. *Wahrnehmungspsychologie: der Grundkurs*. Heidelberg: Spektrum Akademischer Verlag.

Heller, E., 2006. *Wie Farben wirken: Farbpsychologie, Farbsymbolik, kreative Farbgestaltung*. Reinbeck bei Hamburg: Rowohlt Taschenbuch.

Hünniger, J., 2013. *Untersuchung von Einflussparametern zur qualitätsgerechten Ausformung von neuartigen 3D-Prägestrukturen*. Masterarbeit. HTWK Leipzig.

Hunt, R.W.G., 2004. *The reproduction of colour*. 6th ed. Chichester: John Wiley & Sons.

Kirwan, M.J. ed., 2013. *Handbook of paper and paperboard packaging technology*. 2nd ed. Chichester, West Sussex: Wiley-Blackwell.

Küppers, H., 2004. *Das Grundgesetz der Farbenlehre*. 11th ed. Köln: DuMont.

Liu, B. and Todd, J.T., 2004. Perceptual biases in the interpretation of 3D shape from shading. *Vision Research*, 44(18), pp. 2135-2145. https://doi.org/10.1016/j.visres.2004.03.024.

Maaß, O., 2014a. *Untersuchung der Einflussparameter unbedruckter und bedruckter Oberflächen auf die optische Wirkung einer Prägung*. Bachelorarbeit. HTWK Leipzig.

Maaß, O., 2014b. *Glanz, Farbe und Struktur – Weiterführende Untersuchungen der Einflussparameter unbedruckter und bedruckter Oberflächen auf die optische Wirkung einer Prägung*. HTWK Leipzig.

Mamassian, P. and Landy, M.S., 2001. Interaction of visual prior constraints. *Vision Research*, 41(20), pp. 2653–2668. https://doi.org/10.1016/S0042-6989(01)00147-X.

Metzger, W., 2008. *Gesetze des Sehens*. 4th ed. Magdeburg: Klotz .

Nänni, J., 2008. *Visuelle Wahrnehmung / Visual perception: eine interaktive Entdeckungsreise durch unser Sehsystem / an interactive journey of discovery through our visual system*. Sulgen: Niggli.

Ottersbach, J., 2004. *Bedruckstoff und Farbe: eine Werkstoffkunde für Drucker und andere Fachleute der Druckindustrie*. Itzehoe: Beruf und Schule.

Wallach, H. and Bacon, J., 1976. Two forms of retinal disparity. *Perception & Psychophyisics*, 19(5), pp. 375–382. https://doi.org/10.3758/BF03199396.

Zwimpfer, M., 2012. *Licht und Farbe: Physik, Erscheinung, Wahrnehmung*. Sulgen: Niggli.

Innovative experimental Setup enables in-situ Investigation of Doctor Blading Process

Thorsten Bitsch, Julian Schäfer, Sebastian Melsa and Edgar Dörsam

Institute of Printing Science and Technology, Darmstadt Technical University, Magdalenenstr. 2, 64289 Darmstadt
E-mails: bitsch@idd.tu-darmstadt.de; schaefer@idd.tu-darmstadt.de; s.melsa@web.de; doersam@idd.tu-darmstadt.de

Short abstract

The doctor blading process is one of the most important processes in gravure printing, and in several other metering techniques. The understanding of the underlying flow conditions and their importance for the printing process is of great physical and technical interest. Gravure printing is one of the most precise printing techniques with a high reproducibility and massive production outputs. Especially since the appearance of printed electronics a deeper understanding of the doctor blading process is indispensable. Previous experimental investigations in this field were performed with tools and methods which are hardly comparable with the doctor blading as it is performed in high-precision gravure printing presses. Therefore, we aim to present an experimental setup we designed to perform in-situ high-speed experiments in the field of doctor blading. This setup is a high-precision lab device that realises the discrepancy of imitation of a printing press and experimental observability. We go on to present some ideas of new measuring concepts which offer a deeper insight into the physics behind doctor blading.

Keywords: gravure printing, doctor blading, in-situ, fluid mechanics, engineering physics

1. Introduction and background

1.1 Doctor blading process and recent studies

The doctor blading process finds application in printing and coating as well as in non-printing processes, e.g. windshield wiper, and is of superordinate importance. Especially in printing, doctor blading fulfils two key tasks, which are shown in Figure 1. First, the doctor blade wipes off excessive fluid from the printing form after the fluid acquisition. Second, doctor blading ensures the exact dosage of the fluid on the printing form and is thus, alongside other factors, responsible for the exact conformance with the requirements of printed products. Particularly this fact is of great relevance in the production of printed electronics where precise layer thicknesses and homogeneity are essential (Nisato, Lupo and Ganz, 2016; Bornemann, Sauer and Dörsam, 2011).

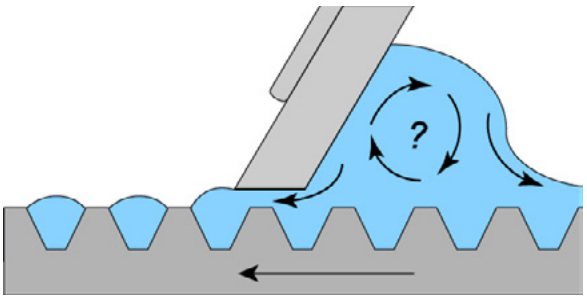

Figure 1: Sketch of the doctor blading process; the doctor blade glides over a moving surface and performs the accurate volumetric delivery wetting whilst forming complex flow fields in the fluid

Doctor blading has remained in focus of theoretical and experimental research since the growing request for increasing printing precision and production output. Deeper understanding and optimization of doctor blading has been investigated for more than 50 years (Scheuter and Bognar, 1968; Strauß, 1975). Especially since the manufacturing of printed electronics products, many research groups are focused on the optimization of the doctor blading process in gravure printing to increase its precision. Yet the understanding of the doctor blading process remains a black box and novel experimental work is either rare or over-simplified, as the process itself is a complex system and for its description one needs fundamental knowledge of lubrication theory, fluid dynamics, material science, contact mechanics etc. Trying to assume the real fluid behaviour in the complex doctor blading process by, e.g., upscaled experiments leads to a blurry prediction of the ongoing physics, since it is debatable which simplifications and assumptions are justified. Most popular are planar printing forms, which are used for instance by Hariprasad, et al. (2016) or Kitsomboonloha, et al. (2012), as the implementation of measurement equipment is easy in comparison to fast rotating cylinders. Frequently, special manufacturing techniques or materials are used, to imitate printing forms that are not common in industrial printing systems (Kitsomboonloha and Subramanian, 2014).

Extreme flows with high shear rates underneath the doctor blade are induced by high speeds (~10 ms^{-1}) and small length scales (< 100 µm). The physical quantities extending over many orders of magnitude are the greatest challenge in observing the doctor blading process. In addition, industrial printing systems have complex machine geometry and are designed to be enclosed, not least to fulfil safety conditions and to keep production processes pristine from contaminating disturbances, such as dust. This is shown in Figure 2.

Figure 2: Insight into a gravure printing press doctor blading unit; only the doctor blade's backside is accessable and only a small part of the printing form cylinder are not enclosed

This impedes the usage of measurement equipment to analyse fluid properties such as film thicknesses, applied forces or fluid pressures. The lack of experimental access to the processes that actually take place underneath a doctor blade under printing conditions forces experimentalists to rely on even more physical assumptions and approximations. This situation has prompted us to construct an innovative experimental setup with which the unadulterated doctoring process can be investigated without losing the real physical conditions.

1.2 Gravure printing background

The gravure printing process can be divided into five sub-processes as presented by Bornemann and Dörsam (2013). Usually, these sub-processes are based on the path of the fluid from the ink acquisition to the drying on the substrate. In the first sub-process, the acquisition, a fast rotating printing form cylinder is wetted by a fluid or ink. Here the printing and non-printing parts on the printing form cylinder surface are wetted equally. In the second sub-process, the doctor blade glides over the fast moving surface with a defined line pressure onto the cylinder to wipe off excessive fluid from the non-printing parts and to dose the fluid in the cells constituting the printing area. In the third sub-process, the fluid transfer from the

printing form to the substrate takes place and in the fourth sub-process a fluid film formation and drying (fifth sub-process) occurs. The whole gravure printing process is shown schematically in Figure 3.

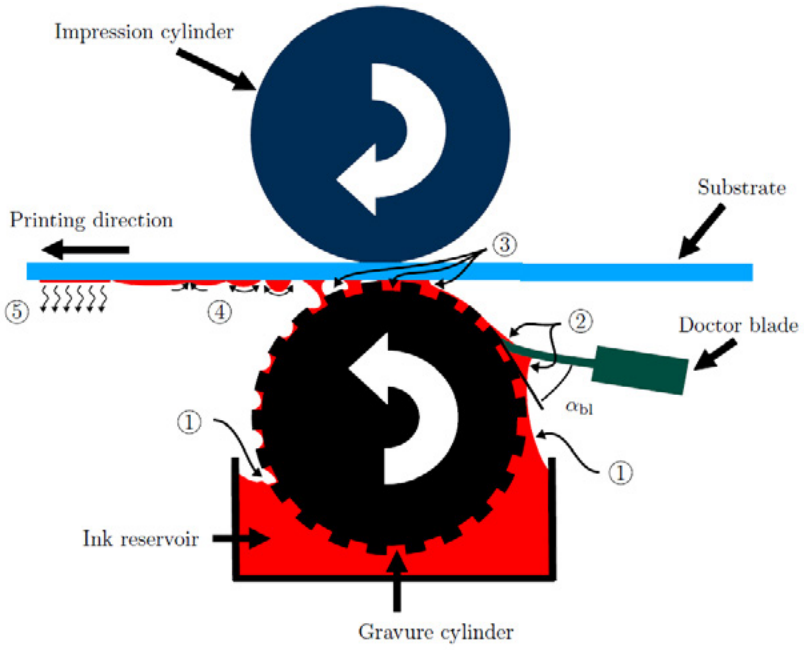

Figure 3: Schematic sketch of the gravure printing process and its division into five sub-processes: (1) wetting of printing form cylinder with the printing liquid; (2) the doctor blade process; (3) the printing liquid gets transferred to the substrate; (4) the fluid film formation process on the substrate; (5) drying and post-processing (Bornemann and Dörsam, 2013)

Wiping off excessive fluid and dosing happens in terms of a high shear rate in the small edge between doctor blade and printing form cylinder. Due to the fast surface motion of the printing form in relation to the doctor blade, the forces and pressures at the blade tip are enormous. For non-Newtonian fluids, this can lead to shear thinning effects, resulting in a decreased dynamic fluid viscosity and thus a decreasing capillary number, which is important for adequate cell filling in the dosing process (Kipphan, 2001; Gray, 2003).

1.3 Aim of research

The aim of our study is to provide experimental access to an accurate as well as a realistic doctoring process and to investigate flow phenomena in the high shear rate range directly at the doctor blade. With the help of high-speed camera measurement technology, these phenomena are to be observed detailed both spatially and temporally resolved. In this way, we want to understand how the fluid behaves in the narrow wedge between the printing form cylinder and doctor blade and how the doctor blade doses the fluid pressing it into the cells. This is necessary because the fluid's wetting or de-wetting behaviour is on other time scales than gravure printing. That's why the doctor blading processes often called a forced wetting process. In the first place, we introduce our innovative experimental setup for the in-situ investigation of the doctoring process in Section 2. Here we concentrate on the two key features of the setup that are the printing form cylinder in sleeve technology, on which a wide variety of printing forms or surfaces can be used (Section 2.1), and the adaptive and adjustable doctor blade holder (Section 2.2), which provides exact alignment of the blade. After discussing possibilities that result from the experimental setup in Section 3, we conclude and provide an outlook in Section 4.

2. Experimental setup

The challenge of the design was the creation of an experimental setup that imitates the doctoring process of a commercial gravure printing system while allowing assembly space and free visibility on the doctor blading process for its observation. The system, therefore, has to provide sufficient stability over time. Thus, the machine frame is made out of 30 mm thick aluminium plates. This frame holds the bearing for the printing form cylinder (see Section 2.1), a vertical adjustable mounting system for the fluid reservoir and the doctor blade unit (see Section 2.2) is attached. Figure 4 shows a CAD-model of the complete experimental setup. Technical specifications of the setup are listed in Table 1.

Table 1: Technical specifications for the designed experimental setup for blade doctor blading investigations

Description	**Value**
Printing speed	Max. 10 ms^{-1}
Max. loading force of doctor blade	200 N
Accuracy loading force of doctor blade adjustment	5 N
Expanded uncertainty of measurement system for loading force of doctor blade	1.03 N
Accuracy of pressure sensor	6 kPa
Range of blade angle	30°–90°
Form cylinder diameter	220 mm
Form cylinder width	100 mm
Range of doctor blade width	15 mm–80 mm
Accuracy of torque measurement	0.1 %

2.1 Printing form cylinder

The printing form cylinder is designed in sleeve technology and consists of three important components. The core is formed by the master cylinder with a diameter of 165.637 mm driven by a servomotor from Yaskawa (type SGMGV-13D3A6H), whereby the servo motor delivers a torque of 8.34 Nm.

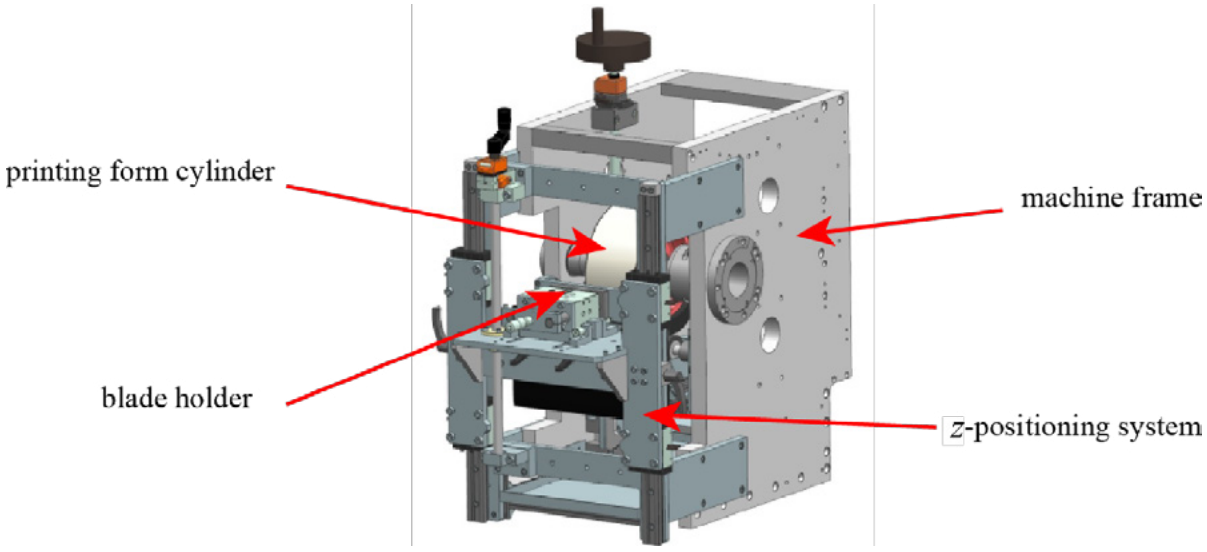

Figure 4: Computer aided design model of the experimental setup (Melsa, 2018)

In combination with the servo controller (type SGDV-5R4DE1A), the rotational speed can be continuously adjusted and the applied torque can be determined with an accuracy of 0.1 % of the rated torque moment; with precision of an increment corresponding to 8.34 mNm. By determining the torque, it is possible to estimate the energy converted in the doctoring process. Friction losses in the bearing of the printing form cylinder must be taken into account in an exact estimation. A carbon fibre adapter from Polywest GmbH + Co. KG is used to adjust the outer diameter of the master cylinder to a standard size for printing sleeves in industrial gravure systems. The adapter is mounted on the master cylinder by frictional engagement. The third component is the printing sleeve, being 220 mm in diameter and 100 mm in width, which contains the engraved print pattern. This is a chrome-plated copper cylinder with a wall thickness of approx. 0.5 mm, which is applied to the carbon fibre adapter by thermal joining.

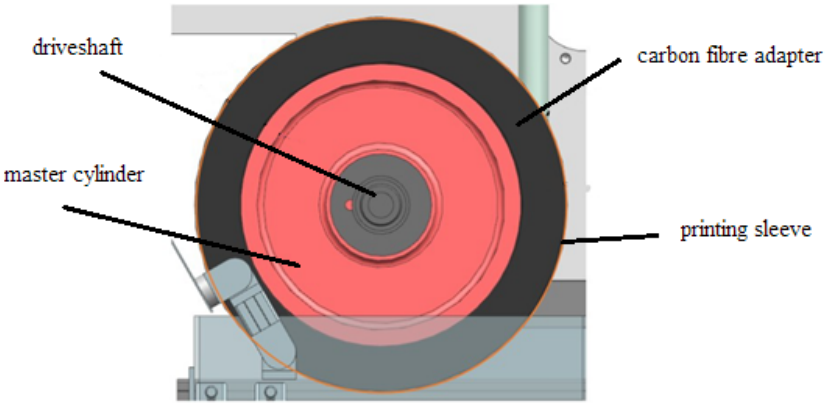

Figure 5: Cross section of the printing form cylinder: grey, driveshaft; red, master cylinder; black, carbon fibre adapter; orange, printing sleeve (Melsa, 2018)

Figure 5 shows the structure of the printing form cylinder. The great advantage of sleeve technology lies above all in the simpler handling of the printing forms compared to solid cylinders. At the same time, manufacturing costs are reduced due to the decreased use of materials. The torque of the motor and the mass moment of inertia of the printing plate cylinder limit the maximum rotational speed of the cylinder to 870 min^{-1} (rpm). With the outer diameter of the printing form cylinder of 220 mm, a possible printing speed of approx. 10 ms^{-1} results, corresponding to the speed of commercial gravure printing systems.

2.2 Doctor blade unit

The doctor blade unit is used to clamp a doctor blade, press it against the printing form cylinder at a defined angle and force in a defined position. The doctor blade unit consists of two main components, the doctor blade holder and the doctor blade positioning.

2.2.1 Doctor blade holder

The doctor blade holder consists of a top and bottom part between which the doctor blade is clamped. In the bottom part, two micrometer screws can be inserted as end stop to align the doctor blade with a precision of 10 µm. This allows the use of blades with widths from 15 mm up to 80 mm in consideration that two thirds of the blade width clamped in the blade holder. The holder also facilitates the use of back up blades. This expanded design with a variable end stop enables the use of a broad variety of different doctor blade products (see Figure 6). Due to the rotatable bearing of the clamping jaws, doctor blade angles between 30° and 90° are possible. An electronic angle scale provides an accuracy of 0.5°.

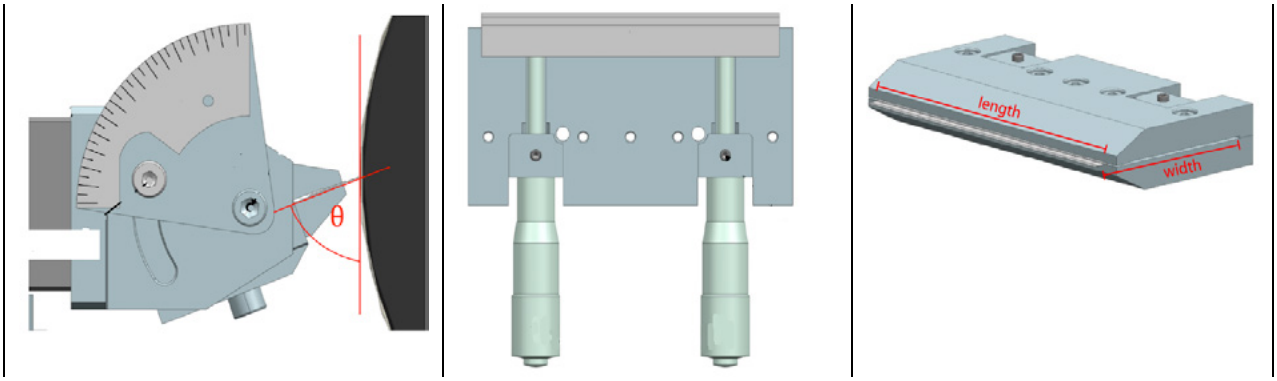

a) *b)* *c)*

Figure 6: Three different perspectives of the doctor blade holder: a) the view from the side with a scale for the doctoring angle θ, b) top view with the two green micrometre screws for precise control of blade edge parallelism, and c) blade holder unit without micrometre screws. (Melsa, 2018)

For fine adjustment regarding maintaining parallel contact between the doctor blade and the printing form cylinder the complete doctor blade holder can be rotated ± 1.25° in the horizontal plane. The doctor blade contact pressure is controlled via a guided pneumatic drive in conjunction with a pressure regulator and permits contact forces of up to 200 N with an accuracy of 5 N. Contact force is obtained by an integrated strain gauge load cell in the pneumatic drive. This type of load cell was chosen because of its good low level of creep performance at static loads. The expanded uncertainty of the contact force measurement system determined to a level of confidence of 95 % is 1.03 N. The uncertainty of the calibrating measurement of the guided pneumatic drive including the built-in loading cell and the uncertainty of the regression line, were determined according to the standard JCGM 100:2008 (Bureau International des Poids et Mesures, 2008).

2.2.2 Doctor blade positioning

To ensure that the doctor blading process is precise, despite any small deflections of the doctor blade unit, the positioning unit is constructed in an axisymmetric way. To minimise the angular displacement between the doctor blade and the printing form cylinder due to bearing clearances and imprecisions, the vertical sliding guide is designed to be well distanced from the centre where the doctor blade holder is positioned. Thereby, external vibrations and perturbations are avoided. This positioning additionally results in a good visibility and a spacious accessible assembly to investigate the doctor blading process.

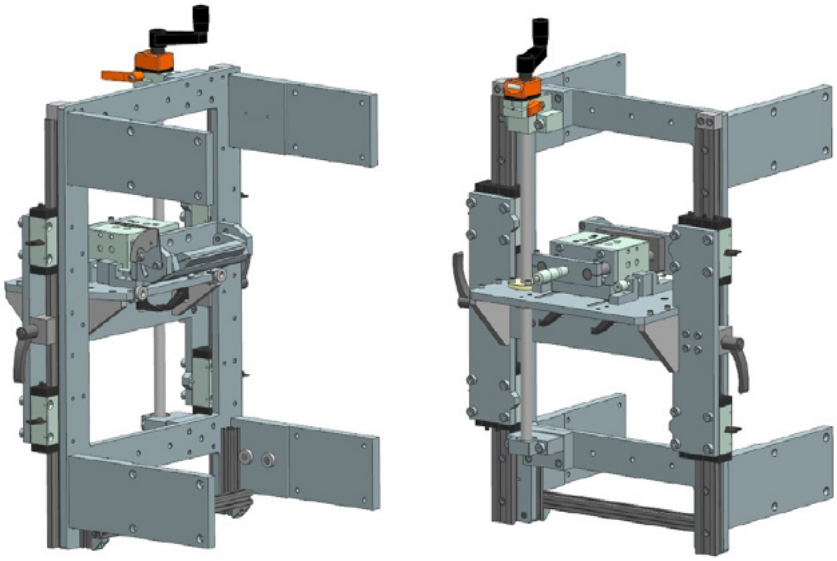

Figure 7: Construction of the blade holder with stiff z-positioning system (Melsa, 2018)

3. Results and discussion

New and innovative measurements shall be implemented on the experimental setup presented. As an outlook we want to present an idea about how to achieve optical access to what happens near the blade edge during the doctoring process. We used a custom-built PMMA-tube as cylinder jacket with an acceptable diameter and circularity. The interface between PMMA jacket and driveshaft is a 3D printed PLA core. A self-made prism holder places an optical prism under the PMMA jacket. The experimentalist can observe the flow field under the blade. Even if our first prototypes are 3D-printed the stiffness and circularity is sufficiently high to perform adequately.

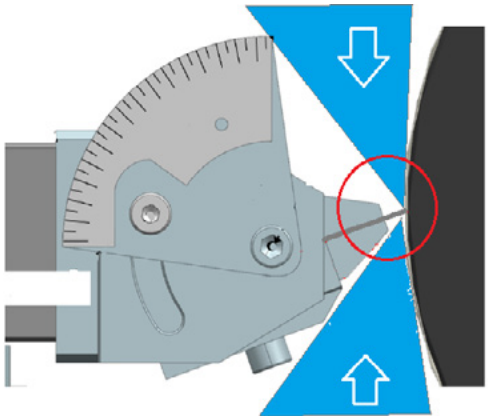

Figure 8: Construction sketch of the blade holder's side view; the red circle marks the position of the doctor blade; the blue areas show the observation spaces from top and bottom

In further steps we want to perform high-resolution high-speed flow field observations under a doctor blade. For that we want to try different dyes and possibly coloured particles to implement a particle tracking velocimetry analysis (Park and Kihm, 2006).

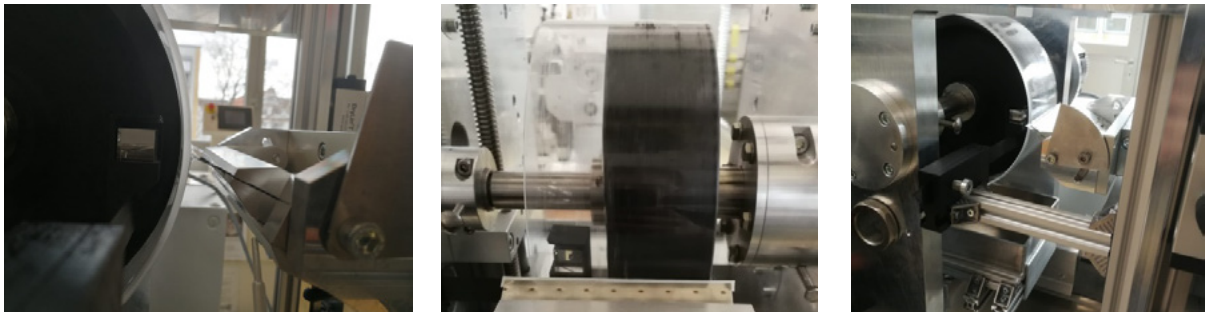

Figure 9: Three different perspectives of the first mounted prototype of the transparent hollow cylinder; its adapter core was made out of 3D- printed PLA, the cylinder's jacket is a high-precision custom-built PMMA tube

4. Conclusions and outlook

The doctoring process and how it is performed in gravure printing is hard to investigate and thus it is hard to understand and to predict. We planned, designed and built an experimental setup, which imitates the doctor blading process used in a real gravure printing system and enables new experimental measuring concepts. We presented two key components of the setup, which are the doctor blade holder unit and the z-positioning unit and presented a transparent printing form cylinder for a new measurement concept. The setup enables observation of the doctor blading process using a high-speed camera from almost every solid angle. Here, methods of particle tracking velocimetry will be applied to observe the fluid's flow field

underneath the doctor blade tip optically. This can be interesting for research groups that are specifically concerned with flows in narrow gaps or wedges, since the most diverse surfaces can be applied to the printing form cylinder, and gaps with varying geometries can be generated.

Acknowledgements

We kindly acknowledge the financial support by the German Research Foundation (DFG) within the Collaborative Research Centre 1194 "Interaction between Transport and Wetting Processes", Project C01.

References

Bornemann, N., Sauer, H.M. and Dörsam, E., 2011. Gravure printed ultrathin layers of small-molecule semiconductors on glass. *Journal of Imaging Science and Technology,* 55(4), pp. 040201–1–0400201–8. https://doi.org/10.2352/J.ImagingSci.Technol.2011.55.4.040201.

Borneman, N. and Dörsam, E., 2013. A flatbed scanner for large-area thickness determination of ultra-thin layers in printed electronics. *Optics Express*, 21(19), pp. 21897–21911. https://doi.org/10.1364/OE.21.021897.

Gray, T. ed., 2003. *Gravure: process and technology*. 2nd ed. Rochester, NY: Gravure Education Foundation and Gravure Association of America.

Hariprasad, D.S., Grau, G., Schunk, R. and Tjiptowidjojo, K., 2016. A computational model for doctoring fluid films in gravure printing. *Journal of Applied Physics,* 119(13): 135303. https://doi.org/10.1063/1.4945030.

Bureau International des Poids et Mesures, 2008. *JCGM 100:2008 Evaluation of measurement data – guide to the expression of uncertainty in measurement.* Paris: JCGM/WG 1.

Kipphan, H. ed., 2001. *Handbook of print media: technologies and production methods*. Berlin: Springer.

Kitsomboonloha, R., Morris, S.J.S., Rong, X. and Subramanian, V., 2012. Femtoliter-scale patterning by high-speed, highly scaled inverse gravure printing. *Langmuir,* 28(48), pp. 16711–16723. https://doi.org/10.1021/la3037132.

Kitsomboonloha, R. and Subramanian, V., 2014. Lubrication-related residue as a fundamental process scaling limit to gravure printed electronics. *Langmuir,* 30(12), pp. 3612–3624. https://doi.org/10.1021/la404938z.

Melsa, S., 2018. *Development of a test rig to observe the doctor blading process in gravure printing,* Master's thesis. Technical University of Darmstadt.

Nisato, G., Lupo, D. and Ganz, S., 2016. *Organic and printed electronics: fundamentals and applications.* Singapore: Pan Stanford.

Park, J.S. and Kihm, K.D., 2006. Three-dimensional micro-PTV using deconvolution microscopy. *Experiments in Fluids,* 40(3): 491. https://doi.org/10.1007/s00348-005-0090-9.

Scheuter, K.R. and Bognar, D., 1968. Beitrag zum Rakelproblem. *Druck Print,* 105(4), pp. 293–299.

Strauß, K, 1975. Modell der Strömung, die sich am Rakelmesser einer Beschichtungsanlage einstellt. *Rheologica Acta,* 14(12), pp. 1058–1065. https://doi.org/10.1007/BF01515901.

An experimental and numerical cooperative Research Concept for Doctor Blading

Thorsten Bitsch[1], *Julian Schäfer*[1], *Elisabeth Diehl*[2], *Hans Martin Sauer*[1], *Edgar Dörsam*[1] *and Stefan Ulbrich*[2]

[1] Institute of Printing Science and Technology, Darmstadt Technical University, Magdalenenstr. 2, 64289 Darmstadt
[2] Research Group Nonlinear Optimization, Darmstadt Technical University, Dolivostr. 15, 64293 Darmstadt
E-mails: bitsch@idd.tu-darmstadt.de; schaefer@idd.tu-darmstadt.de; diehl@mathematik.tu-darmstadt.de; sauer@idd.tu-darmstadt.de; doersam@idd.tu-darmstadt.de; ulbrich@mathematik.tu-darmstadt.de

Short abstract

We present a novel concept of a combined numerical and experimental study of the doctor blading process in gravure printing. This combination serves the reconstruction of viscous flows in the blading process which is difficult to achieve by measurement, or by simulation alone. Examples are the role of the shape of the blade tip, the filling of the gravure cells on the printing cylinder, the effect of the ink chamber geometry on transport, pressure, and shear of the ink, as well as of the air bubble released from the cells when filling. For numerical simulation of such flow problems the particular challenge arises from the enormously varying scales which extend from the microscopic sub-µm-range (under the blade tip and inside the cells) to the cm-range in the ink chamber, where complex eddy flows may arise. Comparison with high-speed video records of flow velocities taken at the blade tip can supplement detailed information on the liquid boundary conditions at the blade tip, while simulation can calculate the flow and shear patterns in complex geometries which are impossible to detect by direct observation. We want to present our concept for the better understanding of the fluid behavior during the shearing by a blade and the fluid film formation.

Keywords: FV simulation, VOF method, gravure printing, blade coating, fluid formation, forced wetting, fluid flow

1. Introduction and background

The control of the ink flows in the ink acquisition system of a printing unit is a key feature of efficient process and machine design. The central aspect is the constant and reliable dosing of ink in the gravure patterns of the printing cylinder over a broad range of printing velocities. In the presently upcoming discontinuous sheet-fed gravure technology as is used in high-quality package applications and in functional and electronics printing, a fast equilibration of the fluid-dynamical parameters is required. Other issues are the reduction of air entrainments and ink foaming, and, most important, of blade wearing effects during the gliding over the gravure cylinder. Due to the growing interest in printed electronics the control and measurability of ink transport and wetting/dewetting effects under the blade, there exists still a strong demand for optimization of the liquid-solid and liquid-air interface dynamics under the blade. (Jeon, Kim and Kim, 2017)

In a gravure unit the doctor blade accomplishes ink dosing on the µm-scaled gravure patterns on the printing cylinder. The gliding blade induces pressure gradients and transport flows. Considerable fluid shear stress is built up across gravure cells, forcing the ink to supplant the air from the cells. The ink shear has to be sufficient to push the liquid-air contact line through the cell interior. For this purpose it has to exceed the capillary that entrap the air in the cells. This capillary pressure is of order of $p \sim \sigma / a$, where $\sigma \sim 30...40$ mN/m is the surface tension of the ink, and a is the length scale of the finest gravure texture which is typically in the sub-µm range, and can easily reach values comparable to atmospheric pressure. On the other hand, the ink shear under the doctor blade roughly equals $\tau \sim \eta v/d$, where $\eta \sim 1...50$ mPa·s is

ink viscosity, $v \sim 0{,}1\ldots10$ m/s blading velocity, and d is the liquid film thickness between the doctor blade tip and the cylinder surface. Air bubbles will only detach from the gravure if $\tau > p$. This has an important implication on the capillary number $Ca = \eta v/\sigma$ of the ink flow under the doctor blade. Filling of the gravure cells is possible only if

$$Ca > d/a \qquad [1]$$

The liquid film thickness d can thus not be larger than the finest gravure scale a if cell filling should be complete. This implies that the control of the thickness of the flow channel under the doctor blade, and thus the liquid film thickness left on the gravure cylinder behind the blade is of utmost importance. We have thus designed a unique experimental platform for fluid flow studies in the doctor blading process. This platform, and the blading geometries which can be studied, are furnished with a Finite Volume (FV) fluid simulation. In this way those dynamical parameters can be determined which are not directly accessible by measurement. Simulation is employed to study the detailed pressure and shear distribution, the formation of the liquid film under the doctor blade, the motion of particles and air bubbles conducted with the ink. The effect of specific ink chamber and doctor blade geometries can easily be checked in this manner.

2. Materials and methods

In this chapter we want to present the two different methods we use.

2.1 Experimental approach

As mentioned in chapter 1 we elaborated a new concept of an experimental doctor blading setup which allows for a direct observation of such blades from all principal perspectives. The setup consisted of a digital servo drive, ensuring precise cylinder rotation and printing speed of up to ~10 m/s. The machine frame was constructed in a way that allows the observation from top, from the side, and, if transparent materials were used, from the outer radial and the center perspective. The doctor blade could be placed at different lateral positions relative to the cylinder axis such that the cylinder tangent at the blading position could be rotated relative to gravity direction. The blading angle between doctor blade and cylinder tangent could be controlled independently. Commercial printing machines usually implement only one such position. This prohibits studying the effect of gravity on the retention of ink behind the doctor blade, at given orientation of the blade versus the cylinder.

The blade was pneumatically pressed against the cylinder. This enabled the adjustment of different blading forces. The blade holder had the option to change the blade angle in positive and negative blading positions and allowed the formation of a fixed slit between cylinder and blade tip with micrometer screws. The blade holder was adequate for conventional as well as for self-made blades. With a doctor blade made of a transparent material it was possible to observe the fluid flow under and behind the blade. We designed a transparent printing form cylinder which allows, by an optical deflection prism, to observe the blade from the bottom side. Figure 1 shows a sketch of the doctor blading process investigated in this work. The doctor blade was suspended on the machine frame by a rotational bearing for adjusting the blading angle θ. The suspension distance between bearing and tip is denoted with h. The width $b << h$ of the contact zone at the blade tip is microscopic. For setting up a numerical model of this blading arrangement one could assume that the gliding face under the blade tip and cylinder surface were parallel, forming a gap of height D. The rear face of the doctor blade and the moving cylinder surface defined boundary conditions for the liquid flow in the ink reservoir behind the blade. The set of boundary conditions was completed by assumptions on the liquid-air-interface, i.e. the height r_{fill} of the filling level, and, optionally, on additional features of the ink meniscus.

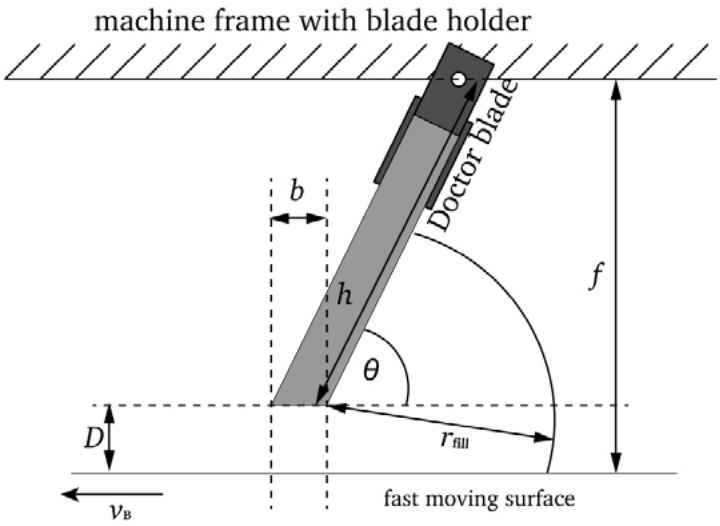

Figure 1: Sketch of the doctor blading principle investigated

Figure 2 shows the surface of a wetted gravure cylinder just after leaving the gliding zone under the blade tip. As a liquid we used glycerol. By its relatively high viscosity the capillary number of the liquid flow is large even at moderate velocities. Thus, viscous forces become relevant compared to the effect of static ink capillarity in the gravure. Effects such as liquid bridge formation on the walls beneath each gravure cell and the edge of the gliding doctor blade could be observed, transporting ink that is in excess of the static cell volume. In order to show that this is truly an effect of viscous shear the surface of a non-rotating printing form is shown as well.

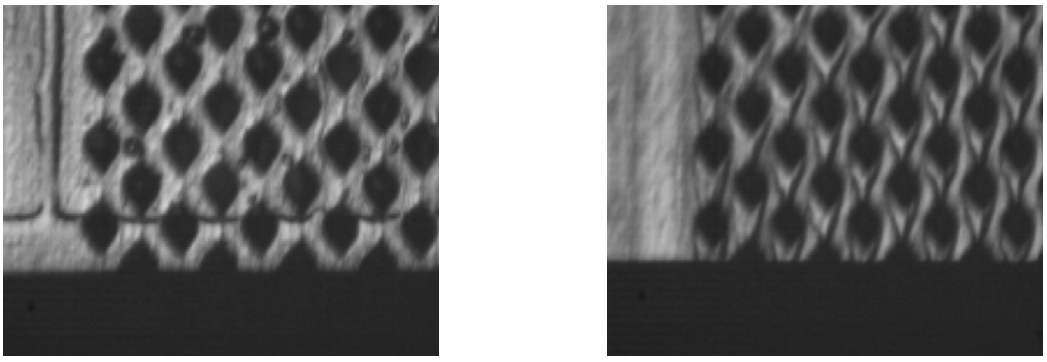

Figure 2: Left: high-resolution picture of a printing form; right: same printing form in motion with velocity of 1,25 ms^{-1}; the black bar on the bottom shows the backside of the blade (used liquid: glycerol; cell distance ~100 µm)

Other observations (Kitsomboonloha and Subramanian, 2014) concern wetting or de-wetting effects that depend on the shape of the blade tip. For elastic blades even the doctor blade angle becomes variable, which has, in turn, an influence on the shape of the gliding zone under the tip of the blade. This effect is shown by Jeon, Kim and Kim (2017). The contact zone shaping by solid-to-solid contact is not part of the simulation. We focus on the blade shape and its influence on the fluid film formation, and the developing flow patterns close to the doctor blade. We used pristine one step doctor blades and started a doctor blading process on a gravure cylinder under defined conditions shown in Table 1. The forces applied on the doctor blade were varied, whereas the other parameters were kept constant. The tip shapes of different blades were analysed subsequently using an optical profilometer.

Table 1: The used doctor blading parameters for the experimental approach

Parameter	**Value**
Printing speed	4 m·s^{-1}
Blade type	IX stainless 25.0 mm × 0.2 mm / 0.1 mm × 1.3 mm
Blade manufacturer	Daetwyler SwissTec
Used Liquid	Glycerol
Duration of doctor blading	45 min
Force variation	0.25 N·mm^{-1}–1.5 N·mm^{-1}
Initial doctor blade angle	60°

2.2 Numerical approach

From a numerical point of view, the doctor blading process can be described as a free surface fluid flow. The macroscopic fluid flow can be modelled with the aid of conservation equations including, for example, conservation of mass and momentum. In our approach, we get a solution of our problem by solving the Navier-Stokes equations, a set of non-linear partial differential equations (PDEs), and a transport equation together with appropriate initial and boundary conditions. The incompressible Navier-Stokes equations consist of a momentum and continuity equation:

$$\rho\left(\frac{\partial \vec{u}}{\partial t} + \vec{u} \cdot \nabla\vec{u}\right) = -\nabla p + \mu\nabla^2\vec{u} \qquad \text{(Momentum equation)} \qquad [2]$$

$$\nabla\vec{u} = 0 \qquad \text{(Continuity equation)} \qquad [3]$$

In general, the Navier-Stokes equations do not have an analytic solution. With the help of simulations, these problems can be solved approximately. A direct numerical solution based approach is being pursued, because an instable flow is suspected in the gap between the wall and the tip of the doctor blade. If the grid size is fine enough, the almost turbulent behaviour can be resolved with this approach. For the numerical simulations we use the open source software OpenFOAM, a C++ library for the solution of continuum mechanics transport processes. It contains the application interFoam, a solver for two incompressible and immiscible phases using finite volume discretisation on collocated grids. InterFoam has proven to be an appropriate choice for the simulations due to its flexibility, accuracy and robustness as well as its inherent mass conservation property (Deising, Marschall and Bothe, 2016). The regular interFoam solver algorithm is based upon the Volume of Fluid method (VOF). The VOF method is conducive to the capturing and handling of a moving contact line on a fixed mesh. The idea is to define a function that indicates where the domain is filled with fluid and where it is filled with another fluid or phase.

$$\alpha(t,\vec{x}) := \begin{cases} 1 & \text{if } \vec{x} \in \Omega_l \\ 0 & \text{otherwise} \end{cases} \qquad \text{(Indicator function)} \qquad [4]$$

where Ω_l is the liquid phase region. In a discrete sense this function provides a volume fraction field, that indicates if a control volume is filled with the respective fluid or not. The advection of the flow inside the domain, more precisely of the interface, is described with the VOF transport equation.

$$\frac{\partial \alpha}{\partial t} + \vec{u} \cdot \nabla\alpha = 0 \qquad \text{(VOF transport equation)} \qquad [5]$$

The solution of the PDEs is accomplished by converting them into systems of difference equations by linearising them and applying discretisation procedures (Weller, et al.,1998). Beyond flow profile and shape of the liquid volume, also pressure and shear distribution and liquid-solid contract line dynamics of the liquid volume can be derived once a numerical solution of the above equation is known.

3. Results and discussion

At this point we want to mention that the actual doctor blade angle which is formed near the blade tip is strongly dependent on the applied force, as predicted by Jeon, Kim and Kim (2017). We define this angle as the effective doctor blade angle. The reason for this is caused by the deflection of the elastic blades. Our results are shown in Figure 3.

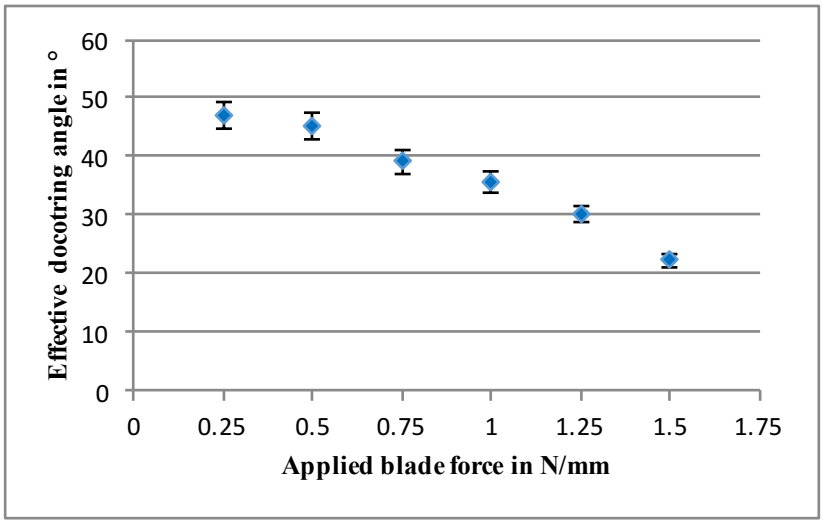

Figure 3: Influence of the applied blade force on effective doctor blade angle's formation

We also observed that the blade deformation is not only related to purely plastic deformation. We found that blade wearing and blade tip deformation leads to metallic particles along the blade edge (Figure 4).

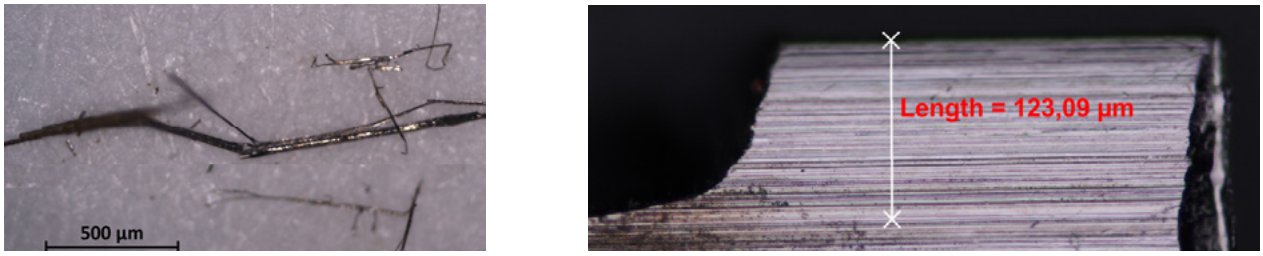

Figure 4: Left: metallic particles observed near the blade edge after 45 minutes of doctor blading; right: doctor blade after extreme wearing and material erosion

3.1 Comparison to numerical research

In comparison to the experimental investigations, some simplifications and assumptions have to be made in the numerical analysis. We assume that only Newtonian fluids are considered, and that particles and surfactants are absent. At first we used water, which could be replaced by other fluids with simple parameter adjustments. Another simplification was that the printing form was plain, and did not exhibit engraved cells. The focus was on the flow behavior in the gap and behind the doctor blade as well as on the description and investigation of the lubricating film.

In a first step, the close vicinity of the doctor blade tip was simulated. The dimensions of the domain were 1 mm × 0.5 mm (Figure 5), and a collocated uniform mesh was used, created with the standard OpenFOAM meshing routine blockMesh. Ink was dragged from behind the blade left) through the gap. It left the simulation domain on the right border. The lower domain wall was assumed to move with uWall = 1 $m \cdot s^{-1}$.

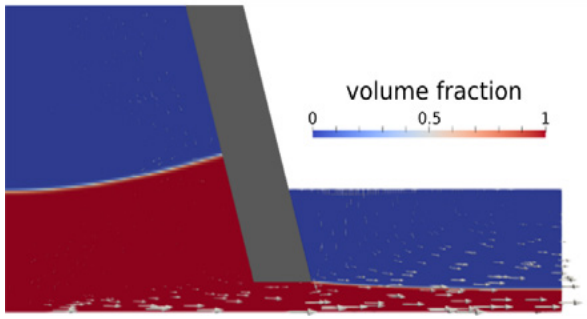

Figure 5: Setup and initial state (left) and simulation (right) of the doctor blade test case

In this scenario, a stationary flow resumed after a short period of time, and a uniform lubrication film was formed (Figure 5). Here, the velocity of the fluid is represented by arrows. The highest velocities were observed at the lower wall. In analogy to figure 1 we assumed two sharp edges at the tip of the doctor blade. These represented the effect of wear of the doctor blade, and is a particular challenge for the numerical considerations, as actual doctor blade angle is dynamic, and stabilizes only when tip shape and lubrication film approach the equilibrium. The simulations indicate that the fluid does not pass across this corner, and that the fluid meniscus is pinned there. Taking a finite radius for the doctor blade tip instead pinning is temporarily suspended (Figure 6).

Figure 6: Simulations with different shapes of the doctor blade

However, we expect fluid accumulation at the tip of the doctor blade. This indicates that the contact angle model requires adjustments. Furthermore, the question of the final equilibrium of wall velocity and fluid level in the reservoir needs to be clarified in further investigations. It may turn out that there is no stable equilibrium possible.

4. Conclusions and outlook

As already mentioned a large variety of different profiles have been elaborated for doctor blades which were optimized for specific printing tasks. However, as there apparently is no generally decided prescription, the blade is commonly selected from customary reasons. In order to save resources, and to make process design more transparent, a digital tool for doctor blade optimization is aspired. Depending on the geometry and angle of the doctor blade, on the gravure pattern, ink properties, and, specifically, on the microscopic ink flow field at the tip of the doctor blade deliberate predictions should be possible. Our goal is to understand the formation of an ink film as uniform as possible, independent of the filling level in the ink reservoir and the cylinder speed. A further question we want to pose is whether we can qualitatively describe the wearing effects of the doctor blade, and to obtain estimates on the feasibility of alternative printing plate materials. We observed not only significant deformation of the doctor blade by elastic deformation. We also observed material erosion, indicating an unstable lubrication. Such creation of metallic particles at the blade tip has severe impact on functional printing as mentioned before.

In further investigations optical high-speed camera observations of the fluid behavior under the blade edge could be performed. For this we want to use tracking particles and dyes to visualize the flow field near the blade edge under different doctor blading conditions and compare our observations with the FEM-simulated data.

Acknowledgements

We kindly acknowledge the financial support by the German Research Foundation (DFG) within the Collaborative Research Centre 1194 "Interaction between Transport and Wetting Processes", Project B04 and C01.

References

Deising, D., Marschall, H. and Bothe, D., 2016. A unified single-field model framework for volume-of-fluid simulations of interfacial species transfer applied to bubbly flows. *Chemical Engineering Science*, 139(January), pp. 173–195. https://doi.org/10.1016/j.ces.2015.06.021.

Jeon, S.W., Kim, C. and Kim C.H., 2017. Control and measurement of doctoring angle at deformed state in doctoring apparatus for printed electronics. *International Journal of Precision Engineering and Manufacturing,* 18(5), pp. 633–639. https://doi.org/10.1007/s12541-017-0076-6.

Kitsomboonloha, R. and Subramanian, V., 2014. Lubrication-related residue as a fundamental process scaling limit to gravure printed electronics. *Langmuir,* 30(12), pp. 3612–3624. https://doi.org/10.1021/la404938z.

Weller, H.G., Tabor, G., Jasak, H. and Fureby, C., 1998. A tensorial approach to computational continuum mechanics using object-oriented techniques. *Computers in Physics*, 12(6), pp. 620–631. https://doi.org/10.1063/1.168744.

Smart Materials Detection using Computer Vision

Mustafa Bilgin and Johannes Backhaus

University of Wuppertal, Rainer-Gruenter-Straße 21, 42119 Wuppertal, Germany
E-mails: bilgin@uni-wuppertal.de; jbackhaus@uni-wuppertal.de

Short abstract

Smart materials detect autonomously changings of environmental conditions such as temperature (thermochromism), water / humidity (hydrochromism), UV/Vis light (photochromism), mechanical stress (piezochromism), acids (pH-chromic) and more. The irreversible colour changing of smart materials can be used to "translate" the particular colour information into the degree of contamination, such as a printable sensor. Integrated into a smart code, besides static data (2D) also dynamic sensor data (3D) can be stored. The aim of this study is the computer vision based image detection and interpretation of a smart material surface. The particular colour information will be transformed into the degree of contamination. The limits of feasibility will be examined on a laboratory scale and comparison with reference colour values.

Keywords: smart materials, neural networks, computer vision, smart code, piezoelectric inkjet

1. Introduction and background

Smart Materials can show a hydrochromic (water/humidity), photochromic (UV/Vis light), thermochromic (temperature), piezochromic (pressure) and other behaviours. They gradually can shift between two states by changing their colour. Photochromic compounds show a light detecting behaviour. If the surface of a photochromic compound is exposed due to UV-light, it changes its colour gradually from one colour state to another colour state. The pH-chromic compound is used to determine the acid or base capacity of a substance. This e.g. can be used to monitor the freshness of foodstuffs. These materials are autonomous and independent of electrical circuits and electrical sources. A camera system can optically read the individual smart materials surfaces. Thus, by the recorded colour values can be concluded with a change in colour in terms of the degree of contamination. This colour changing behaviour can be used to develop printable sensors (Bilgin and Backhaus, 2017). That way, it is possible to store dynamic information (Smart Materials) about possible deviations and static consumer or product information inside a smart code. By means of computer vision, it is possible to automate tasks by processing, analysing, interpreting, and manipulating digital image information. This paper shows functions for recording a smart code and its subareas. The concept behind our intended application can be found under Bilgin and Backhaus (2017).

For evaluating a smart code, the following steps are necessary: Most of the code readers operate with a binarisation initiated by a prior grayscale transformation. This reduces the data volume with regard to short processing time. It is also helpful to crop the image to a smaller size without the data getting lost. However, a grayscale transformation is not adequate for coloured sensor data as meaningful data can be lost. In this way, image files created in RGB can be processed in different colour conversions such as CIE $L^*a^*b^*$, which can be used as a reference colour system. It is important to use these colour systems to evaluate or calibrate the colours. Being JPG files, camera images often do not contain the device's profile (ICC), but either one of the standard profiles sRGB or Adobe RGB. These determinants must be controlled. The CIE $L^*a^*b^*$ colour space contains all colours independent of any device. It therefore allows lossless conversion of colour information from one colour system to another, from one device type to another. This provides a subsequent interpretation of the colour information in statements about the degree of contamination. However, in

order to correct the image information, the use of morphological operators can be useful. A further aspect is erosion, which causes false classifications to disappear due to erosion. These can be connected image areas. On the other hand, dilatation can be used to compress or strengthen partial areas in a pixel group, to fill holes, to close cracks. The combination of smart materials, smart devices and smart codes will allow the construction of an Internet of Things in which all components communicate in an autonomous network to perform predetermined tasks, provide consumer information, collect feedback on their products and provide information on critical environmental impacts throughout the transport process (Ashton, 2009).

1.1 Objective of code development

The Smart Code in this work is to be divided into three main areas: the static area for text content, the finder pattern area for identifying and aligning the code and the dynamic area for smart materials (printable sensors). The special feature of the static area is that the Braille font is to be used. With the help of the smartphone camera, visually impaired people or the unimpaired can read out the content of the code or touch it manually. In addition, the dynamic range in the smart code can be optically read out and results on the respective state of the smart materials can be output e.g. auditory.

2. Materials and methods

2.1 Instruments

The smart code samples (containing smart materials) were printed with a piezoelectric inkjet printer (Epson WorkForce WF-3620). Technical parameters: Print Head: PrecisionCore; Thin Film Piezo element: 1/1000 mm; Droplet Size: 2.8 pl (range of 1.5–32.5 pl); Nozzle Configuration: 800 Nozzles Black (K), 256 Nozzles per Colour (CMY); Printing Resolution: 4 800 × 2 400 DPI.

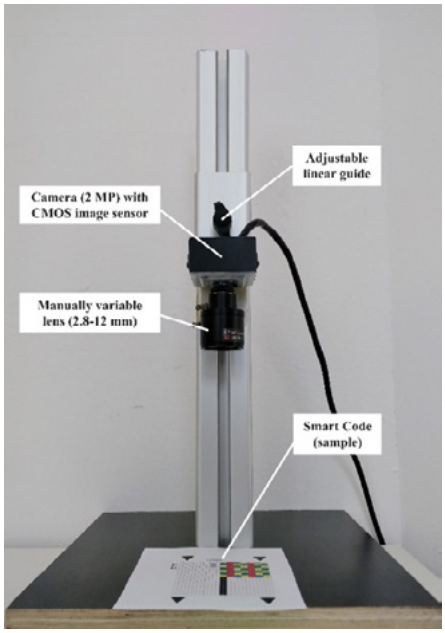

Figure 1: Adjustable camera setup

The smart codes were captured (Figure 1) with a 2.07 MP camera (ELP-USBFHD01M-BFV-D) with CMOS image sensor and a manually variable 2.8–12.0 mm lens – the focus of the camera is manually adjustable. The camera has an image resolution of 1080P (1920 × 1080 pixels). The experimental setup is based on an adjustable linear guide. Thus, the camera can be moved vertically. In this publication, however, the lighting

conditions are uncontrolled. However, the construction can be placed in a light chamber in order to realize the evaluation under a reference daylight illuminant (e.g. D50). The recording of the samples is done in real time and under real conditions.

For reference purposes, samples were measured with a spectral densitometer (TECHKON SpectroDens) to analyse their characteristic RGB and CIE *L*a*b** values and to compare them with values detected and analysed by the computer vision. Technical parameters: polarising filter: off; type of illuminant: D50, 2° standard observer; diameter of measuring orifice: 3 mm. This paper uses the Open Source Computer Vision Library (OpenCV, 2019), an open source computer vision and machine-learning library, for image processing. The algorithms can be used to recognize faces, identify objects, classify human actions in videos, track camera movements, track-moving objects, recognize scenes or, as in this case, detect smart codes and evaluate partial areas. The programs for analysing the smart codes were programmed in Python. For this purpose, other libraries like NumPy were used. NumPy extends Python with functions for scientific computing and numerical computation (OpenCV, 2019).

2.2 Standardization

All experiments were carried out under controlled laboratory conditions – reproducibility was ensured by an air conditioning system and deviations were recorded in protocols. Temperature: 20 °C +/– 1 °C; relative humidity: 55 % +/– 1 %) were controlled.

2.3 Materials

All materials, which were used for this research, are listed in Table 1. To ensure the reproducibility, all experiments are based on standardised substrates Inapa tecno. The smart material used for the experiments is photosensitive Prussian blue, described in Bilgin and Backhaus (2018).

Table 1: Materials

Substrates for printing	Inapa tecno, oxygen pure high-white recycled paper, Format: 210 mm × 297 mm (A4), Grammage: 80 g/m^2
Dye	Photosensitive Prussian blue, CAS Number: 14038-43-8, Chemical formula: $C_{18}Fe_7N_{18}$, Molar mass: 859.24 g·mol^{-1}
Water-based base ink	E24, Octopus Fluids GmbH & Co KG, Colour: colourless, pH: 7,86, Conductivity: (mS/cm): <5, Viscosity (mPa·s): 3,00

2.4 Test chart

The initial intention was to modify a standard QR code and design dynamic areas (for smart materials) within the code. However, this idea was dropped because the QR codes are designed only for static data. Dynamic (i.e. information changing) areas avoid decoding the QR code. Consequently, a simple smart code containing static and dynamic areas was designed and prototyped in laboratory scale (Figure 2) The code is divided into three sections. The first area (red framed) shows three finder patterns (squares) in three corners. They are required to identify the smart code and determine the inner coordinate system of the code. The second area (grey hatched) is the static data area in which 54 characters of text information can be placed. The third area (yellow framed) is the dynamic area that consists of several cyan, magenta and yellow caches which here serve as placeholders for three different smart materials.

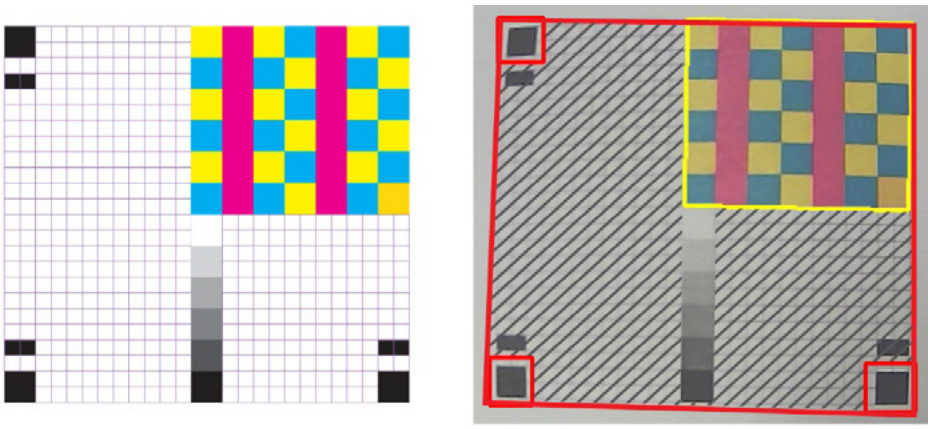

Figure 2: The test chart shows a smart code prototype

3. Results and discussion

3.1 Static data: encoding and decoding

There are many methods to encode information. Therefore, there are many coding schemes (Morse characters, nautical signal flags, semaphore, binary, numbers to letters conversion and more). However, this paper focuses on Braille (Figure 3). It usually consists of six embossed dots, but it was later adapted to computer language and consists of 8-point characters (International Organization for Standardization, 2001; ISO/IEC International Standard, 2011) used by visually impaired people. This scheme allows 256 different characters to be displayed. A special requirement in the coding of the static content is that visually impaired people can read the content manually by touching it. However, the static data should also be readable and converted into an alphanumeric text (Latin alphabet) for persons who do not master the Braille writing process. This can be done with the smartphone camera. The dynamic part of the code is also machine-readable and is evaluated by computer vision.

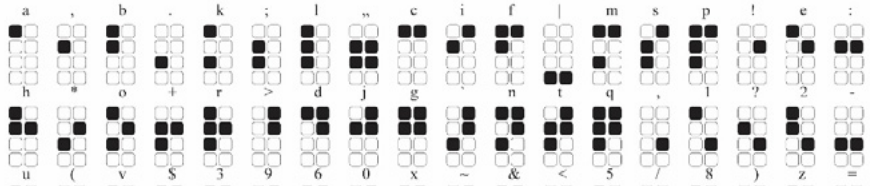

Figure 3: Unicode 8-dot Braille characters

A usual scanner recognizes an image pixel by pixel. Here, a function is used that helps to identify points, whose dimensions, distances and respective colour information are required. The Hough Transformation (Hough, 1962) is a method for detecting straight lines, circles (such as the Braille points) or any other parameterizable geometric shapes in a binary black-and-white image. In the following example (Figure 4) the Hough Circle method was applied. The captured image of the sample used for the recognition of a Braille line and the application of the Hugh method must be prepared: initially, an 8-bit image is converted to grayscale in order to reduce the entire image information to essential information. For the recognition of Braille points we refer to the OpenCV function cv2.HoughCircles in corresponds to Yuen, et al. (1990).

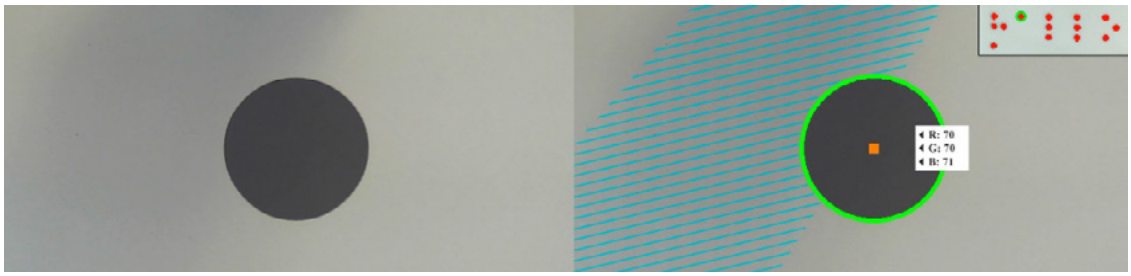

Figure 4: Circle Hough transform

The static area of the code is very important for a calibration of the camera in order to avoid external optical influences when analysing the colour of the sensitive dynamic code. By detecting the black points from the Braille scheme and the colour information of the white background, it is possible to use these information for a calibration of the camera. Each point of the Braille scheme and its adjacent background can be used to calibrate both the exposure rate and the white balance of the camera properties. The blue hatched area shows the influence of shadows, which can falsify the colour value. Influencing factors of ambient light and shade must be taken into account in a later real-time correction. The current actual value can be compared with the known target value of the individual points in order to identify deviations and use them for further statistical evaluations. The Braille point described in the example illustrates one of many possible colour information from varying Braille points used in the calibration area (chapter 3.4) to adjust the camera.

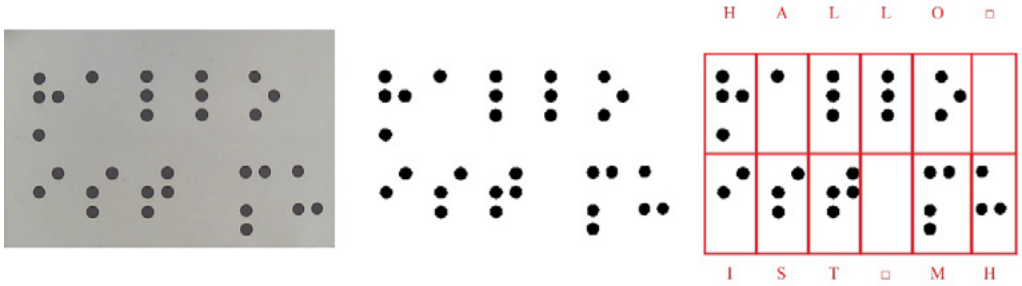

Figure 5: Steps of image analysis : left original colored image; middle: binarisation process after thresholding algorithm; right: pattern recognition (circle draw)

Figure 5 shows the original image (left), its binarized pattern by the Otsu's clustering-based image thresholding method (middle). The dots are grouped into the particular characters (right). This is achieved by measuring the distances between the dots and grouping them by vertical and horizontal segmentation. After identification of the individual groups and comparison with a Braille library, the characters are decoded.

3.2 Smart code: area recognition

Problem characterisation: In the following, we will demonstrate recognition algorithms that use a QR code as an example. The geometric form of the Finder pattern of the QR code is the same as in our smart code. By using a common static code such as the QR code, we want to provide an easier understanding of the following steps. Area recognition in a smart code involves the recognition of position markers (finder pattern) and the retrieval of data (static) and sensor (dynamic) areas.

Typically, the image of the camera captured the code is shaded, partial, or blurred. The code itself as well as the distance of single dots to each other or their patterns are distorted in both directions. All these erroneous parameters must be corrected before the code can be decrypted. High demands are placed on

these corrections, especially with regard to robustness and reliability. Various suitable methods and algorithms have to be applied for the individual steps of error correction: e.g. the Circle Hough Transformation (geometric correction) described above or the Canny Algorithm (background suppression, edge detection and edge correction). These and other methods are available in program libraries and must be integrated operatively during programming (Figure 6).

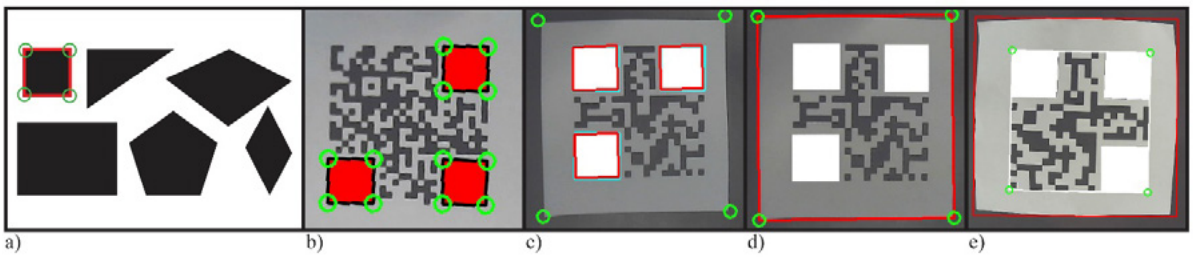

Figure 6: Position marker recognition by geometric shaping

By recognition of geometric patterns, the individual position markers can be identified and therefore the data area as well as the sensor areas of a dynamic smart code can be located. This is particularly demonstrated in the prototype of the smart code in Figure 7. Based on the relative distances of the position markers distortions of the code can be balanced out. If the code is rotated, this will also be corrected. The square bars below and above the position markers identify the smart code as a code differing from a similar random pattern. In addition, the dynamic range for sensitive colours is identified.

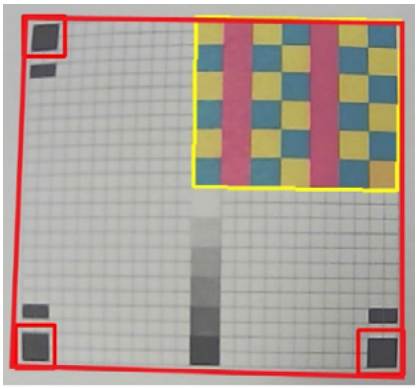

Figure 7: Smart code prototype

3.3 Dynamic data: colour recognition

The following section deals with the evaluation and identification of the dynamic area (printable sensors) of the smart code. The respective Smart Materials are filled into the printer's cartridges instead of cyan, magenta and yellow. These three cartridges will contain a photochrome ink (photosensitive), pH-chrome ink (acid sensitive) and hydrochrome ink (humidity/ water sensitive). The black ink cartridge contains regular ink to prints all the static information of the code, including the finder pattern. The colour-separated areas (by delimiting the colour ranges), such as the yellow squares, three magenta lines and the cyan squares represent the smart materials and their cartridges (Figure 8).

By detecting the dynamic area of the smart code, the colour values – of a specific position – inside of the dynamic code can be analysed. The status (degree of the contamination) of the individual smart material can be interpreted by means of the colour information. The aim is to identify the current colour values of each smart material and compare them with the measured colour reference before. This way, it is possible to refer the specific colour values with the dimension of the contamination. In this context, as well all RGB colour information of the background can also be used for colour correction of the dynamic code in order

to get finally the true colour information. However, the colours in Figure 8 show significant deviations, due to the camera detection. This indicates the necessity of a calibration of the colour values of the camera. This is planned to be realised in one of the next project steps by application of a neural network.

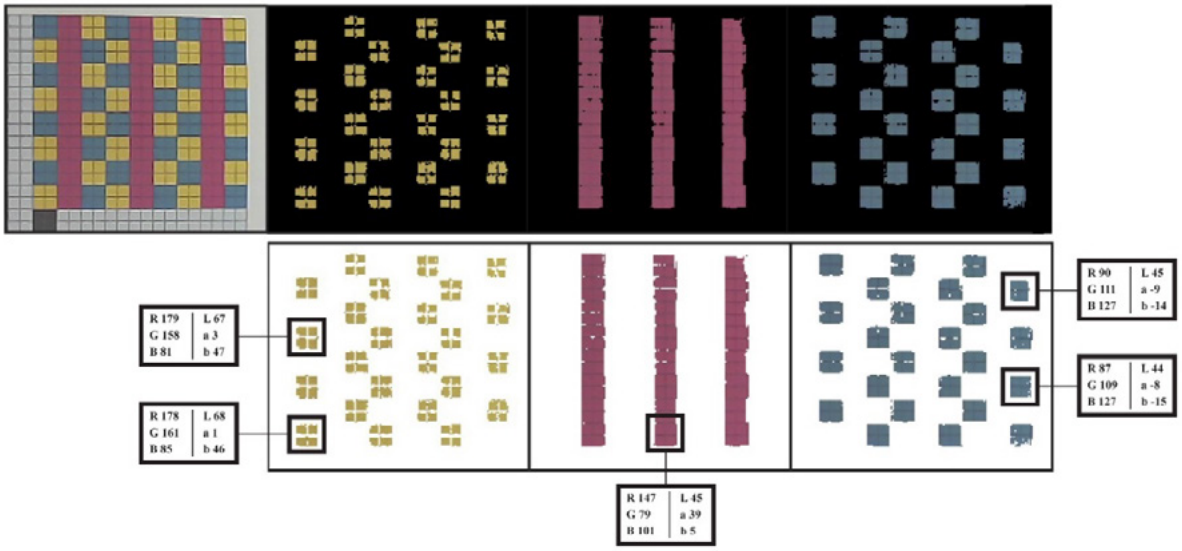

Figure 8: Color detection and separation

The photochromic surface in Figure 9 can be analysed by measurement of the RGB and CIE $L^*a^*b^*$ values or alternative by RGB greyscale and L^* values. Therefore it is possible to store information about critical deviations in a range from 0 (white) to 255 (black) in RGB or 0 (black) to 100 (white) in L^*. A smart device can identify the RGB or CIE $L^*a^*b^*$ values of the different colour shades (smart dots) and compare them with the initial RGB or CIE $L^*a^*b^*$ values and set the colour difference (ΔE^*_{ab}) into correlation with the irradiated quantity of light (photons) of the contamination.

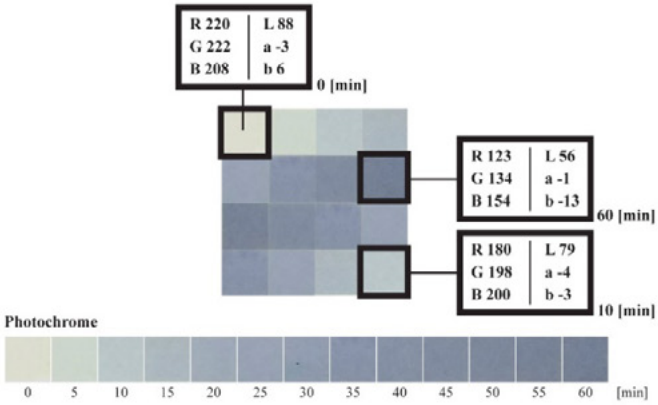

Figure 9: Smart material: photochromic ink

The photochromic ink is described in Bilgin and Backhaus (2018). Table 2 shows the measurement data of the photochromic surfaces. A non-contaminated surface can be defined with an (R, G, B) tuple of (220, 221, 208) and a maximum exposed surface (60 minutes or longer UV exposition) can be described as a tuple of (121, 129, 150); 10 minutes exposition RGB is (174, 182, 188). The data of Table 2 allow deducing on the UV contamination of a product. As well, areas can be grouped in order to classify the quality of a product, e.g. good, moderate, and poor. Another application may be the indication of the entire UV intensity during the crosslinking process of UV printing ink or UV varnish or at crosslinking of UV adhesives.

Table 2: Measurement data of photochromic surfaces when UV exposed

Min of UV exposure	0	5	10	15	20	25	30	35	40	45	50	55	60
R	220	207	174	189	163	156	149	140	137	131	128	126	121
G	221	214	182	197	172	163	157	148	145	139	136	133	129
B	208	205	188	199	183	181	176	168	166	157	155	150	150
*L**	88	85	79	74	70	68	65	61	60	58	57	54	54
*a**	−2	−5	−4	−3	−2	−1	−2	−1	−1	−1	−1	−1	−1
*b**	7	4	−2	−5	−8	−11	−12	−13	−11	−12	−12	−11	−13
Δ*E*	12.8	6.1	5.9	5.7	22.3	26.1	2.0	4.5	1.0	1.7	3.3	1.4	

3.4 Calibration

In the following, the calibration of the camera is discussed. The aim was to control the exposure and the white balance with a kind of colour checker function. The defined grey tones in Figure 10 were integrated into the smart code and can be used for the calibration process. By capturing the smart code by using a code reader, the small areas within the grey areas (5 × 5 pixels) are captured in real time. Thus, the grey values and also the black values (Braille dots) in the data area are used to realize a correct exposure and white balance.

This was realized as described below:

First, the grey fields and their respective RGB colour values were measured and an average value determined (actual state). Next, the respective RGB averages were compared with those of the reference table (target state) and the respective deviation ΔE^*_{ab} was calculated. The deviation ΔE^*_{ab} was used as a colour check function to control the OpenCV exposure and white balance functions. The process was repeated as long until an acceptable exposure and white balance was achieved.

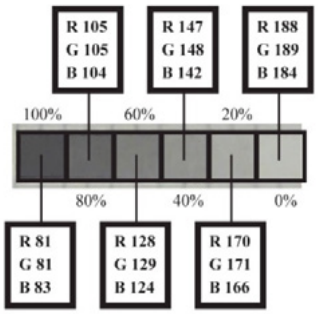

Figure 10: Correct exposure and white balance using the colour checker function

Distortion manifestations such as barrel or fish eye effects have also to be corrected. The distortion matrix can be determined and corrected by using the asymmetric circle pattern resulting from the data range (Braille dots). Different lighting conditions – under the influence of light and shadow – have a significant effect to build a robust colour recognition system while doing colour interpretation.

The implementation of controlled light conditions outside the industrial field of application would significantly improve the detection of Smart Materials, as varying light conditions and shadow influences have a significant effect on the detection of colour fields. However, controlled lighting conditions in the hand of the consumer would lead to considerable restrictions in handling and flexibility. For this reason, test equip-

ment for evaluating the quality of barcodes works with a construction geometry that encloses the barcode and works an defined light source for example infrared light (ISO/IEC International Standard, 2009). The focus of this research project is on consumer cameras. Calibration is to be achieved by identifying colour fields (as with a colour reference card, which can be used to set the colour calibration of the camera) and by profiling common smartphones.

4. Conclusions

It is possible to generate, print and read out a dot matrix code containing dynamic fields of sensitive inks with the camera of a smartphone. Furthermore, the colour information of the dynamic areas can be interpreted and correlated with corresponding contaminations. In laboratory scale, individual steps were shown to develop a smart code and to read it with a smartphone camera. To what extent the developed methods prove to be robust and to what extent the degree of several simultaneous contamination with the methods can be referenced and reproducibly determined must be demonstrated in comprehensive laboratory tests, whereby the developed process procedures must also be evaluated and readjusted. As soon as this will be verified, the data flow and the server operations can be designed and implemented in the Internet of Things applications.

Here, some key steps are shown to develop a multifunctional sensor that works without its own power supply. The reading of the sensor information is possible by means of consumer devices and the interpretation of the information does a server within Internet of Things. Today, low availability of suitable, irreversible, sensitive dyes, which are inkjet printable is problematically, yet. However, it should be supposed that this bottleneck quickly will be overcome as soon as these multifunctional, current less sensors have been developed beyond the laboratory scale and a market potential is identified.

References

Ashton, K., 2009. That 'Internet of Things' thing: in the real world, things matter more than ideas. *RFID Journal,* [online] 22 June. Available at: <www.rfidjournal.com/articles/view?4986> [Accessed 6 March 2019].

Bilgin, M. and Backhaus, J., 2017. Smart packages by means of intelligent codes. In: P. Gane, ed. *Advances in Printing and Media Technology: Proceedings of the 44th International Research Conference of iarigai*. Fribourg, Switzerland, September 2017. Darmstadt: iarigai, pp. 89–96.

Bilgin, M. and Backhaus, J., 2018. Development of a unidirectional switchable photochromic ink for smart packaging. In: P. Gane, ed. *Advances in Printing and Media Technology: Proceedings of the 45th International Research Conference of iarigai.* iarigai, Warsaw, Poland, 3–7 October 2018. Darmstadt: iarigai, pp. 55–63.

Hough, P.V.C., United States Atomic Energy Commission, 1962. *Method and means for recognizing complex patterns*. US. Pat. 3,069,654.

ISO/IEC International Standard, 2009. *ISO/IEC 15420:2009 Information technology — Automatic identification and data capture techniques — EAN/UPC bar code symbology specification*. Geneva: ISO/IEC.

ISO/IEC International Standard, 2011. *ISO/IEC 10646:2011 Information technology – Universal coded character set (UCS). Unicode*. Geneva: ISO/IEC.

International Organization for Standardization, 2001. *ISO/TR 11548-1:2001. Communication aids for blind persons – Identifiers, names and assignation to coded character sets for 8-dot Braille characters – Part 1: General guidelines for Braille identifiers and shift marks*. Geneva: ISO.

OpenCV, 2019. OpenCV: about. [online] Available at: < www.opencv.org/about.html> [Accessed 6 March 2019].

Yuen, H.K., Princen, J., Illingworth, J. and Kittler, J., 1990. Comparative study of Hough transform methods for circle finding. *Image and Vision Computing,* 8(1), pp. 71–77. https://doi.org/10.1016/0262-8856(90)90059-E.

Designing an Industrial Product following Criteria for Circular Economy: what product designers should consider – a case study based on a printing press

Michael Has

International school of paper, print media and biomaterials, 461 Rue de la Papeterie, 38402 Saint-Martin-d'Hères, France

Short abstract

This case study presents a Life Cycle Analysis (LCA) to an industrial product which, during its use, will manufacture consumer goods. Here the example of printing was assessed. The target was: a) to see whether the proposed structure would be suitable to interpret data, identify shortcomings and needs in order to b) identify alternative design options and solutions for improvement. The systems under view are large format printers used in professional environments. Different sets of data were accessed for different phases in a system's life. These were compared and related, in case only one set was accessible. The phases in life of such an industrial product are *manufacturing*, *transport* to customer, *use phase* (production of prints), *transports* for recycling/ refurbishment associated with *recycling/refurbishment or scrapping*. The criteria applied were material and energy flows, consumption of materials in terms of mass, impact of re-use and logistics. *In addition the effect of an extension of a system's lifetime to an average of 11 years has been looked at. From an ECO-Design perspective it is crucial that the relevant aspects (e.g. reduction of energy consumption during use etc.) are considered in the Product Design phase.* The main conclusion is that the ability of the system to consume recycled paper has a dominating effect on the systems' CO_2 footprint. The key obstacles to resolve are a consistent material strategy and the implementation of a worldwide logistics chain to ensure the return of the system under view.

Keywords: circular economy, life cycle analysis, carbon footprint, printing press

1. Introduction and background

The EU Framework Directive 2005/32/EC (European Parliament and Council Directive 2005/32/EC, 2005) is in place for more than a decade. It presents Eco Design criteria to follow when producing goods. Applying or not applying those criteria is subject to public discussion especially for consumer goods – lesser so for industrial goods.

The intent of this case study was to apply Life Cycle Analysis (LCA) criteria to an industrial product which, during its use, will manufacture consumer goods and to identify attention points for product design. These types of product are common. Printing tiles or producing light bulbs may serve as examples for this kind of product and the complexity of applying respective criteria (for paper see Has, et al, 2016). Here the example of printing was assessed, mainly to see whether the proposed structure would be suitable to interpret data, identify shortcomings and needs in order to identify alternative design options and solutions for improvement. The systems under view are large format printers used in professional environments. Different sets of data (Nimalasuriya, 2014; Zhao, 2013) were accessed for different phases in the system´s life and entwined life cycles (Has, et al, 2016, for example). These were compared and related, in case only one set was accessible.

2. Results and discussion

2.1 Manufacturing / refurbishment phase

For the analysis of material flows during the manufacturing phase, dedicated filters were applied to Enterprise Resource Planning (ERP) systems.

With the assumption that end of life is reached after the initial usage period, material consumption is separated into goods that can fully be reused (100 % reuse rate), recyclable materials (Al, Cu, Fe, certain plastics and other materials with an reuse rate of more than 50 %) and materials for which recycling for a reuse in a new system of the same kind is difficult (e.g. paper, wood, etc.). A high level balance is displayed in the Tables 1 and 2.

Table 1: Use of mostly reusable materials during manufacturing phase and, respectively recycling/refurbishment or scrapping (Zhao, 2013)

Material type	Weight in newly built system (kg)	Fraction of total weight (%)	Virgin material required for remanuf. for second life (kg)	Reuse rate (%)	Material consumption p.a. if lifetime is 7 years (kg)	Material consumption p.a. if lifetime is 11 years (kg)
Printed circuit boards and batteries	2.5	1.36	0	100	–	–
Wire harnesses	1.4	0.76	0	100	–	–
Motors*	2.5	1.35	0.01	99.6	–	–
Copper*	0.1	0.05	0.04	96	–	–
Plastics*	34	18.48	3	90	0.42	0.27
Ferro*	111	60.32	17	85	2.42	1.54
Aluminum	10	5.43	4	58	0.57	0.36

Material consumption for recyclable materials (Al, Cu, Fe, certain plastics) and materials, which can be re-used to a major extent (System 1).*

Table 2: Consumption of remaining materials during manufacturing and, respectively recycling/refurbishment or scrapping (Zhao, 2013)

Material type	Weight in newly built system (kg)	Fraction of total weight (%)	Virgin material required for remanuf. for second life (kg)	Reuse rate (%)	Material consumption p.a. if lifetime is 7 years (kg)	Material consumption p.a. if lifetime is 11 years (kg)
Paper	1	0.5	1 (new documents required)	0	1	1
Others	0.6	0.4	0.6	0	0.6	0.6

Material consumption during manufacturing (System 1).

The energy consumption during manufacturing has been disregarded as the energy consumed came from renewable sources (Nimalasuriya, 2014; Zhao, 2013). Often the value of scrapped materials for recycling is reduced if a variety of alloys and materials are used. Aside of a fitting return logistics avoiding variations of materials is a key aspect of a material strategy.

2.2 Use phase

Three mayor aspects need to be considered during the use phase. The net effect of:

1. electrical energy (using energy from renewable sources or not)
2. using recycled paper (or other recycled/recyclable materials) and
3. extending the lifetime of the product for a reduced carbon footprint.

The use of electrical energy is the dominant factor in the use phase. While the absolute energy consumption is a matter of system, the origin of the energy is not. Due to its larger size, the vendor of a system has a stronger buying power than most users. Consequently, while the fraction of green energy used in manufacturing can be assumed to be consistent at 100 %, the respective fraction at a customer's site cannot be determined. This impacts the assumed carbon footprint necessarily.

Energy use can be described with a user profile and the duration of use. The energy use is the sum of use during printing (~ 75 % of the time), ready (~ 15 %), energy safe (~ 10 %) and sleep times while switched on. The carbon intensity (kg CO_2/kWh) figure for electricity was provided by the IEA (Quadrelli, 2013) With a carbon intensity of 0.498 kg CO_2/kWh, the carbon emission is presented in Table 3.

Table 3: Energy consumption (Nimalasuriya, 2014)

Energy type	Carbon footprint p.a. (kg)
Electrical	763

Energy consumption (System 2).

The system characteristics are such that the use of electrical energy is independent of the printed substrate. During product design how an average (and extreme) user will utilize the system can only be assumed.

For the analysis of the material flow during the use phase, usage characteristics are key sources of information: they are indicators for anticipated energy usage, expendables and consumables. For the type of system under view, the duration of the use phase and the printing time determine the consumption of substrates. This direct translation of use time into volume would not be possible if the system offers different print modes involving different print speeds.

As indicated, the system's lifetime is planned for extension to 11 years. Naturally, the energy usage is constant over time. However, if the system can print on recycled paper, different carbon footprints provide a means for customers to reduce the total carbon footprint of the system during it's use phase (Holmenpaper, 2018). For the case under view (System 2), the saving potential is approximately 45 % of the absolute carbon footprint as seen in the Table 4.

Table 4: Carbon footprint use phase (Nimalasuriya, 2014)

Material type	Carbon footprint p.a. if lifetime is 7 years (kg)	Carbon footprint p.a. if lifetime is 11 years (kg)
Paper	3190	2980
Recycled paper	1970	1840

Carbon Footprint use phase (electrical Energy plus paper consumed) assuming
a) user profile as above and
b) 100 % usage of non-recycled or recycled paper. (System 2)

Assuming a second life for certain parts (while extending the first lifetime of the total system from 7 to 11 years and permitting a second lifetime of an equal length) naturally also leads to a more positive balance. The systems lifetime extension is possible by design, planning and testing plus an intensified use of preventive service and upgrades throughout the systems lifetime. Parts are replaced during preventive and maintenance service and collected or as far as possible made accessible for refurbishing. In case an extension of the local life is intended, in situ refurbishment can take place.

2.3 Transport phase

From a carbon footprint perspective the transport phase of a system involves packaging and the actual movement of the system. For packaging, wood is required to position and secure the system.

Table 5: Material consumption during transport (Zhao, 2013)

Material type	Weight in newly built system (kg)	Fraction of total weight (%)	Virgin material required for remanuf. for second life (kg)	Reuse rate (%)	Material consumption p.a. if lifetime is 7 years (kg)	Material consumption p.a. if lifetime is 11 years (kg)
Wood	20	10.87	20		20	20

Material consumption during transport, wood is required for transportation (pallets and, in this case, not returned to vendor). (System 1)

Depending on the distance different means of transportation can be assumed and calculated for. For this study an average distance between user and manufacturing site (1 000 km) and transportation by truck has been assumed and a web-based calculator has been used (EcoTransIT, 2018). This of course changes if transportation by air or ship and mixed means are considered.

2.4 Logistics

The circular economy concept of requires that the system involved is returned to the vendor or a second life is offered, for which logistics are crucial (Kuo, 2011). However, generally logistics provide a more complex obstacle and ideally the system is installed and operated close to the manufacturing site and hubs of central service and maintenance. In the field this ideal situation is often not met. For service and inbound logistics this is not a problem provided that the organization is fit for that. The return policy (outbound logistics) is more complex because

- upfront the customer has to agree to return the system
- the user/installation characteristics need to be considered
- and a collection and sorting process for differentiating parts to be restocked/reused without change, tested and repaired, refurbished, recycled to serve as primary resource, must be in place (Kuo, 2011).

The supply internal and external supply chain members such as the users, suppliers, and logistics centres need to be taken into account – but were not accessible for this study. The like for the infrastructure in place to collect also needs to accommodate a selection process between wanted and unwanted products.

To make the situation more complex, to plan for industrialized refurbishment of the system and appropriate re-use of parts, a reliable industrial process can only start enough parts are returned from the field and is of suitable quality for recycling and/or reuse. The number of machines in the field must be sufficient for a plannable and continuous materials flow. For local reflow and testing/repair, concepts can easily be established. However, given an international distribution of machines (which means scattered systems)

under view, return logistics involve complex efforts to also collect systems from areas remote for the vendor, and difficulties for planning.

Even if the energy used for transport is lower than the gained equivalent of material and energy for refurbishment, the question remains whether the effort required for setting up an organization and the respective logistics to implement returns, is worthwhile. There is no single answer to that question applicable for all kinds of systems and regions involved.

As indicated above, implementing a return strategy implies that, at the moment of signature of contract, a customer accepts to return the system after the use phase. Implicitly that questions the concept of ownership of what is bought as it is established in some markets. Although not in place yet for industrial goods, the circular economy concept demands legislation to require customers to commit to returning where possible products for refurbishment once the product reaches end of lifetime; for comparing regulations see European Parliament Directive 2012/19/EU (2012).

2.5 Comparison with data available

Comparing data achieved for large format printers as done here with printing presses is not self-explaining. However, one of the reasons to perform this study was that there is only very few literature data available on the topic. Data reported by FINAT (on production with conventional presses) yield to comparable results (Frost, et al., 2016). The study also states that self-adhesive paper and polymers are comparable. Within the window of insecurity the results reported here and by FINAT are comparable (Table 6).

Table 6: Comparison of carbon footprint assessed here with literature data

Material and other consumption in manufacturing process	FINAT Focus: print converter and substrates *	This study; 7y lifetime (11y)	This study; 7y lifetime (11y)
	(%)	(% CO_2 footprint, rounded), excluding manufacturing	(% CO_2 footprint, rounded), including manufacturing
Electricity and heat	31	45–75 (30–50)	38–60** (50–75**)
Label stock materials (note: 10–50 % of label material are waste according *)	63	25–55 (50–70)	13–71 (20–90)
Manufacturing of machinery	1*	–	11–28 (10–20)*
Packaging/transport	1	<1	<1
Printing inks	3	neglected	neglected
Waste	1	neglected	neglected
Water	0	neglected	neglected

Comparison of carbon footprint assessed here with data reported by FINAT (on production with conventional presses). Within the window of insecurity the results are comparable.

** (Frost, et al., 2016)*

*** Note that consumption of el. energy during manufacturing was set to 0 % due to CO_2-footprint-free electricity claimed by manufacturer.*

Heat consumption set to 0 – no data available.

3. Conclusions

Eco design requires access to a vast amount of data originating out of very different resources. The systems considered here have been analysed using LCA. The lifecycle has been split into manufacturing, transportation, use, transportation and repair/recycling. Furthermore the effect of an extension of lifetime has also been considered.

For the manufacturing/refurbishing phase, the access to relevant data for the analysis of industrial production turned out to be difficult. The type of system looked at here, data can often be found in ERP systems. In addition this study is based on data available from different sources. The combination of data provides insight into consumption structures during a system's life cycle. The system provides an example for a product type intended to serve for the production of other goods.

It was shown that the choice of material allows high return rates, limiting the amount of scrapped material.

For the use phase it turned out that the energy consumption for use and the ability of the system to print on recyclable material is most crucial.

Of course life cycle analysis is not a target in itself but a means to set priorities in subsequent design processes – usually named "Eco Design". Several sets of Eco Design-criteria are available in literature – but priorities to be set are likely to depend on the characteristics of the type of system targeted.

From an Eco Design perspective it becomes evident that, what should be influenced early on in the product design phase, are:

- reduction of energy consumption during use
- the ability of the system to print on recycled and recyclable material – e.g. paper (not to be taken for granted for certain marking technologies)
- the markets in which this is accepted: to print on bio-degradable substances
- the parts and material strategy to enable re-use and refurbishment as parts or as raw material a material strategy avoiding compound materials and variations of alloys in order to extend the value and recycling rate of the products parts
- the use of dedicated design measures plus service to extend lifetime (of the system itself and the parts) and enable a second life (or more) after refurbishment.

Limiting factors outside of a product design perspective turn out to be most significant, however. Especially the degree to which systems and parts are returned is a key for a successful reduction of the total environmental footprint. Legal boundary conditions (the question of return of the no-longer-used system) and the international logistics require to be solved for the vendor to gain full access to the existing resources and thereby optimize the implementation of circular economy.

Acknowledgements

Jeannette Berger, AnnChristin Englschalk, Johannes Steigerwald

References

EcoTransIT, 2018. *EcoTransIT: calculation parameters*. [online] Available at: <https://www.ecotransit.org/calculation.en.html> [Accessed March 2019].

European Parliament Directive 2012/19/EU of 4 July 2012 on waste electrical and electronic equipment (WEEE).

European Parliament and Council Directive 2005/32/EC of 6 July 2005 establishing a framework for the setting of ecodesign requirements for energy-using products and amending Council Directive 92/42/EEC and Directives 96/57/EC and 2000/55/EC of the European Parliament and of the Council.

Frost, C., Brase, I., Macaré, M., Gaasbeek, A., Coustillas, J. and Vleira, M., 2016. *Harmonized Life cycle assessment approach for the self-adhesive label industry*. [pdf] TLMi and FINAT. Available at: <https://higherlogicdownload.s3.amazonaws.com/TLMI/a44e81d8-31da-4e2e-952a-45727d1602bc/UploadedImages/LCA_-_Harmonized_Sector_Approach.pdf> [Accessed March 2019].

Has, M., Ringman-Beck, J., Robert, J.-F. and Williams, G., 2016. *Design and management for circularity – the case of paper*. [pdf] World Economic Forum. Available at: <http://www3.weforum.org/docs/WEF_Design_Management_for_Circularity.pdf> [Accessed March 2019].

Holmenpaper, 2018. *Data sheet for calculating the carbon footprint of printing/writing paper based on the 10 toes of CEPI framework*. [online] Available at: <https://www.holmenpaper.com/globalassets/holmenpaper/sustainability/carbon-footprint/cf-holmen-view-hallsta.pdf> (Accessed March 2019].

Kuo, T.C., 2011. The study of production and inventory policy of manufacturing/remanufacturing environment in a closed-loop supply chain. *International Journal of Sustainable Engineering*, 4(4), pp. 323-329. https://doi.org/10.1080/19397038.2011.593008.

Nimalasuriya, T., 2014. Environmental impact of large electronic products – don't judge a book by its cover. In: *CARE Innovation 2014: 10th International Symposium and Environmental Exhibition*. Vienna, Austria, 17–20 November 2014. Vienna, Austria: International CARE Electronics.

Quadrelli, R. ed., 2013. *CO_2 emissions from fuel combustion: highlights*. [pdf] International Energy Agency. Available at: <http://www.indiaenvironmentportal.org.in/files/file/CO2EmissionsFromFuelCombustionHighlights2013.pdf> [Accessed March 2019].

Zhao, Y., 2013, *Sustainable remanufacturing at Océ-Technologies: reducing CO_2 emissions with closed loop supply chains,* Master thesis. University of Tilburg.

Matching Lean Manufacturing and Industry 4.0 for the Graphic Communication – printing industry

Anastasios E. Politis[1,2,3,5], *Kenneth L. Macro*[2], *Georgios Gamprellis*[3,4,6], *Marios Tsigonias*[3,4,6] *and Christos Trochoutsos*[3,5,7]

[1] University of West Attica, Greece

[2] California Polytechnic State University, USA

[3] HELGRAMED- Hellenic Union of Graphic Arts and Media Technology Engineers, Greece

[4] National Printing Office, Greece

[5] Hellenic Open University, Greece

[6] GARDEN – Graphic Arts Research, Development and Engineering Institute, Greece

[7] Pressious Arvanitidis printing company, Greece

E-mails: politismedia@gmail.com; kmacro@calpoly.edu; gampgeo@gmail.com; tsigonias@yahoo.gr; chris.trochoutsos@gmail.com

Short abstract

Lean manufacturing is the most prominent philosophy for efficient business operation and management applied at the totality of an industrial setting. Industry 4.0 has been defined as a name for the current trend of automation and data exchange in manufacturing technologies. Previous research conducted, revealed that Industry 4.0 and Lean Manufacturing are strongly related by a quite diversified manner. The relation lies with the share of common strategic orientations for manufacturing and production operations and processes. This paper investigates the possibilities for matching Industry 4.0 with Lean manufacturing. In particular, the combination and convergence of both concepts are examined, towards the increase of efficiency of operational management in various settings. Further, the potential matching elements are related with the specific characteristics and needs of the Graphic Communication – Printing industry. Research conducted reveals that there are numerous ways to match Industry 4.0 elements in Lean manufacturing philosophy. Further, it has been concluded that specific elements of Industry 4.0 such as digitization, smart applications, the Internet of Things and advanced data handling, can be matched with Lean manufacturing philosophies to be applied in the Graphic Communication – Printing industry. Finally, intensive research is required in order to identify in detail the matching processes in this particular industrial setting.

Keywords: lean manufacturing, Industry 4.0, graphic communication, printing industry

1. Introduction and background

Lean manufacturing is the most prominent philosophy for efficient business operation and management, applied at the totality of an industrial setting. Industry 4.0 has been identified as an “umbrella” name for the current trend of automation and data exchange in manufacturing technologies.

This paper investigates the possibilities for matching Industry 4.0 with Lean manufacturing.

Research conducted, reveals that there are numerous ways to match various elements of Industry 4.0 in Lean manufacturing philosophy. Further, it has been concluded that specific elements of Industry 4.0 can be matched with Lean manufacturing philosophy to be applied in the Graphic Communication – Printing industry sector. Intensive research is required in order to identify in detail the matching processes in this particular industrial setting.

2. Lean manufacturing

Lean Manufacturing represents a philosophy for the establishment of efficient operational management of all functions of an organization or company (Netland, 2015). It has been developed by the Toyota executive Taiichi Ohno (1912–1990) as the Toyota Production System in Japan and popularized by James P. Womack and Daniel T. Jones in their 1996 book (Womack and Jones, 1996; Businessdictionary, 2019). The Lean principles have profoundly influenced manufacturing concepts throughout the world, as well as industries outside of manufacturing, including healthcare, software development and service industries. The benefits of Lean include reduced lead times, reduced operating costs and improved product quality (Rouse, 2018).

3. Industry 4.0

Industry 4.0 or the "Fourth industrial revolution" appears as an interesting global trend that defines the current trend of automation and data exchange (Ostdick, 2017; Politis, 2018), as well as the way to an Internet of Things, Data and Services in manufacturing technologies (Rüttimann, 2015). Ostdick proposes five key elements of Industry 4.0: Greater levels of product customization, Integration of Advanced Analytics, Pushing beyond postmodern ERP, Embracing the Internet of Things, Increased reliance (and positive outcomes) on Cloud technology (Ostdick, 2017). Rüttimann (2015) define that Industry 4.0 includes various elements ranging from the integration of cyber and physical systems, to the Internet of things, and from cloud and cognitive computing to various aspects of digitization.

4. Lean manufacturing in the Graphic communication – Printing industry

As Keif and Cooper (2007) point out, Lean is perceived as a way to recover income by improving operational efficiencies. Keif and Cooper state further that "Lean, is a realistic, logical, and proven response to fundamental business challenge". Macro (2017), suggests that "Lean implementation planning generally launches into three distinct phases of execution":

- Education about Lean
- Analysis of a job workflow
- Development of a TPM (Total Production Maintenance) plan

Macro (2017) proposes Lean tools and methods to be used for fixing typical problems in a printing company as illustrated in Table 1:

Table 1: Typical problems in a printing facility and lean tools and methods to fix them (Macro, 2017)

Printing facility typical problems	**Lean tools and methods**
Paper and Ink mislabeled and misplaced	5S, Work standards, Kanban
Printing press set-up and cycle time	Kaizen events, cycle time analysis, set-up reduction
Prepress, press and post-press equipment downtime and malfunction	Total productive maintenance problem, 5S
Mislabeling and improper disposal of chemicals	Work standards, visual workplace management, 5S
Underutilization of equipment	OEE – Overall Equipment Effectiveness, WIP-work in progress
Fluctuation of Product production and delivery time	Value Stream Mapping
Lack of experience on equipment operation	Knowledge management, training, work standards
Forklift and transportation accidents	Kaizen events, Visual workplace management, work standards, 5S

5. Industry 4.0 in the Graphic communication – Printing industry

Niemela (2016) argues that "Printing 4.0 megatrend applies for all graphic arts / graphic communication fields, namely Design, Prepress, Print and Finishing, at an integrated and connected workflow based on full digitalization". Further, according to Webb and Romano (2017), "we do need to be aware of what is happening with technology in general and how they affect print demand. Many print businesses dismissed the importance of the Internet in the 1990s, and of mobile in the 2000s. We shouldn't make that mistake again".

Eccles (2018), states that "there has been less obvious talk about Industry 4.0 in the sign and display market that are primarily addressed by FESPA".

6. Matching Lean manufacturing and Industry 4.0 concepts and elements

As it is stated in various studies (Rüttimann, 2015; Netland, 2015; Mrugalska and Wyrwicka, 2016), there is a strong relation of Industry 4.0 with Lean manufacturing. The relation lies with the share of common structures and elements for manufacturing and production operations and processes.

7. Results and discussion

Finally, a quite interesting matching structure of Lean manufacturing with Industry 4.0 is illustrated by Sanders, Elangeswaran and Wulfsberg (2016) in Table 2, where "Industry 4.0 is indeed capable of implementing Lean. It uncovers the fact that committing into Industry 4.0 makes a factory Lean besides being smart".

Table 2: Initial matching procedure of Lean manufacturing and Industry 4.0, specifically oriented for the Graphic communication – Printing industry/sector, based on Macro (2017), combined with Sanders, Elangeswaran and Wulfsberg (2016) and current research outcomes

Sector	**Lean manufacturing**	**Industry 4.0**
Graphic communication – Printing industry 3.0: Characteristics indicative of the requirements and needs that engaged current trends and levels of automation.	Philosophical and cultural foundation on holistic business/ company operations that include continuous improvement initiatives.	The introduction of elements and tools for smart automation and digitization and the creation of support systems for decentralized decision-making process.
Customers, Web-to-Print, Customer Relationship Management	Define, analyze, identify value for customer Define products and product families Customer involvement	Digital CRM Customer's real-time information Product monitoring and information IoT and remote systems, advanced web-to-print solutions
People Human capital development Continuous improvement of competences Training	People Involvement "Being" Lean instead of "Doing" Lean Team building, Teamwork Training procedures Knowledge management Visual management, Events organization and management	Smart feedback – visualization devices (for flow, value, products, processes) Improved Human – Machine/System interaction via advanced interfaces Supporting systems for company's human capital

Sector	Lean manufacturing	Industry 4.0
Workflow management and production JDF-JMF Customized MIS	Value Stream Mapping – VSM Continuous Flow Just in Time-JIT Work in Progress-WIP, Visual Management, Pull approach in production PDCA	Process tracking, integration & management, Advanced MIS Product tracking and monitoring with sensors Schedule tracking and Kanban updating
Standardization Quality management ISO 12647 G7 Production specification	Standardized work, Standard Operating Procedures – SOP VSM	Sensors – production tracking by smart systems Smart data collection Automatic evaluation on product specifications
Data flow, handling and processing (as a part of management and production workflow)	5S, JIT, TPM VSM, Standardization PDCA	Internet of Things – IoT Cloud Automation with advanced specific systems Automation application of systems for data identification, flow, monitoring, storage, accessing and quality Data tracking and monitoring
Production workflow – systems, machines, materials, movements, semi-products temporary storage of semi-products	Job Flow Analysis Gap Analysis via Lean Assessment tools Continuous flow 5S, VSM, PDCA	Self-maintenance assessment Improved Human – Machine/System interaction via advanced interfaces Supporting systems for company's human capital
Waste in physical and digital form	5S – Waste Management Waste identification initiatives and procedures	Digital tagging Digital visual information on waste
Smooth operation of systems, machines and equipment Inventories of orders, jobs and processes	Continuous flow VSM, Standardization, Total Productive Maintenance-TPM Visual management Takt time calculation	Digital tracking, Real-time inventory tracking
Setup time – Utilization rates	OEE-Overall Equipment Effectiveness Kaizen, Takt time, Cycle time, VSM	Automation (specified by type/structure of equipment) Self-optimization
Mistakes in production and production flow	Standardization, Visual management	Digital tracking systems Digital visual management and information Real-time visual information
Shop floor space	5S Visual management	Digital visualization systems Digital tags and space guidance and organization Movement tracking for materials and products

Research conducted, revealed that there are several paradigms and structures matching Lean manufacturing and Industry 4.0. However, it could not be quite clear how these can be matched, especially in a specific industrial / production domain. Both Lean manufacturing and Industry 4.0 concepts are significant for the Graphic communication – Printing industry. Lean manufacturing seems to be a necessary step towards efficient operational excellence in the sector and the companies. Hence, there seem to be a number of constraints.

As it regards Industry 4.0, a clear message from the investigation in the Graphic communication – Printing industry is that *not all* Industry 4.0 elements are applicable. Following this trend, the industry enters the debate with specific actions such as Print 4.0, Finishing 4.0, Packaging 4.0 and Paper 4.0.

Further, a research outcome is that there is no evidence found for actual and comprehensive relation of the concepts for the Graphic communication – Printing industry sector. Research conducted, revealed that there are reports and studies either in Lean manufacturing, or in Industry 4.0, not for both.

8. Conclusion – matching Lean manufacturing and Industry 4.0 for the Graphic communication – Printing industry, where to start?

Based on the discussion, for the time being, it is rather difficult to identify a starting point for concluding with the research. One idea is to define three starting points namely:

- The specific industrial setting, namely the Graphic communication – Printing industry.
- Lean manufacturing and
- Industry 4.0

Based on this consideration, it seems rather convenient to choose the starting point of the specific industrial domain, and therefore, to place the sectors' developments – the state-of -the-art, and then try to place the Lean manufacturing elements, with the specific Industry 4.0 elements that facilitate the better application of Lean manufacturing in the Graphic communication – Printing industry. It is important to mention that this mindset has the advantage to view the challenges from the sectors' viewpoint and angle – a look by insiders! This has happened a lot with other concepts such as customized Management Information Systems – MIS, specific – sector orientated ISO Standards, E-commerce platforms such as Web-to-Print, which are originating from the sector.

This approach has the advantage of the necessary deep knowledge of the Industry's specific characteristics and therefore it is possible to match Lean manufacturing and Industry 4.0 as integrated concepts in the Graphic communication - Printing industry environment.

As a result, it is suggested that the starting point can be the Graphic communication – Printing industry at its current – "state-of-the-art" level. This starting point can be named after "3.0 – Graphic communication – Printing industry 3.0" as the state-of-the-art setting, in terms of technological evolution and including current applications on digitalization and automatization.

As a result, the matching procedure can be based on Macro's concept for matching the specific industry needs with Lean manufacturing, proposed as "Lean printing" (Macro, 2017). This can be followed by matching and integrating elements of Lean manufacturing and Industry 4.0, setting the framework for the evolution of the Graphic communication – Printing industry in facilitating the sector's needs optimized for the future. This can be illustrated as follows:

The Graphic communication – Printing industry and its specific characteristics
(including requirements for operational excellence)

↓

The generic Lean manufacturing philosophy,
to be analyzed for application in the Graphic communication – Printing industry,
as the holistic concept and philosophy for total business operation.

↓

The specific Industry 4.0 elements for facilitating Lean manufacturing
as a holistic operational philosophy in the Graphic communication – Printing industry
by solving operation, workflow and production issues at the operational – production management level.

Matching elements presented in Table 2, should be considered as an initial effort for combining Lean manufacturing and Industry 4.0, for the Graphic communication – Printing industry and it is by far not complete. In column one, the sector's elements are not set into priority. In addition, the placement of Lean manufacturing and Industry 4.0 elements in columns two and three have not been based on priority criteria or degree of importance.

8.1 Further study

Indeed, research conducted so far should be considered as a first step. It is an initial approach in matching the various elements of Lean manufacturing and Industry 4.0 for the specific domain of the Graphic communication – Printing industry. Further research is required in more precise definition of the current level of automation and degree of digitization in the Graphic communication – Printing industry and a more comprehensive and concrete identification of Lean manufacturing elements, as well as a detailed implementation of Industry 4.0 elements is required.

Further, the matching process as well as the relation of elements in Table 4 need to be validated and updated with field research and in particular by getting feedback from the Graphic communication – Printing industry, based on interviews and/or surveys with the use of a questionnaire.

In addition, further study is required as it regards the nature – specialization of companies in various Graphic communication – Printing industry domains, that facilitate a different printing field. For example, it might be useful to define variations in commercial printing, packaging printing, large format and commercial screen and digital printing (just to name a few) and their specific needs of Industry 4.0 elements to be implemented in a Lean manufacturing philosophy.
It might be interesting to further implement the present study by identifying more precisely the Graphic communication – Printing industry evolution as "Graphic communication – Printing industry Lean 4.0" or simply "Printing Lean 4.0".

References

Businessdictionary, 2019. *Lean manufacturing*. [online] Available at: <http://www.businessdictionary.com/definition/lean-manufacturing.html accessed> [Accessed 27 March 2019].

Eccles, S., 2018. Industry 4.0 is starting to happen. *Fespa*, [online] Available at: <https://www.fespa.com/en/news-media/features/industry-4-0-is-starting-to-happen> [Accessed 4 April 2019].

Keif, M., and Cooper, K., 2007. Why Lean isn't working in the print industry, and what you should be doing about it! *GATFWorld*, 19(1), pp. 21–22.

Macro, K., 2017. Lean Printing. In: T.H. Netland and D.J. Powell, eds. *The Routledge companion to Lean management*. New York: Routledge, pp. 403–412.

Mrugalska, B. and Wyrwicka, M.K., 2016. Towards Lean production in Industry 4.0. In: *7th International Conference on Engineering, Project, and Production Management*. Bialystok, Poland, 21–23 September 2016.

Netland, T., 2015. Industry 4.0: what about Lean? *better operations*. [online] 16 March. Available at: <http://better-operations.com/> [Accessed 27 March 2019].

Niemela, B. ed., 2016. Print 4.0: wie die Druckindustrie die Vernetzung vorantreibt. *Deutscher Drucker*, 52/12.

Ostdick, N., 2017. 5 Key elements of Industry 4.0. *flexis* [online] 20 April. Available at: <https://blog.flexis.com/author/Nick-Ostdick> [Accessed 30 March 2019].

Politis, A., 2018. Industry 4.0: What does it mean for the graphic arts industry? In: P. Gane, ed. *Advances in Printing and Media Technology: Proceedings of the 45th International Research Conference of iarigai*. Warsaw, Poland, 4–7 October 2018. Darmstadt: iarigai.

Rouse, M., 2018. *Lean manufacturing (Lean production)*. [online] Available at: <https://searcherp.techtarget.com/definition/lean-production> [Accessed 27 March 2019].

Rüttimann, B., 2015. Von Lean zu Industrie 4.0: eine Evolution von einer visionären Idee zum realen Verstündnis. In: *Fertigungstechnisches Kolloquium*. Zürich, Switzerland, 26 November 2015.

Sanders, A., Elangeswaran, C. and Wulfsberg, J., 2016. Industry 4.0 implies Lean manufacturing: research activities in Industry 4.0 function as enablers for Lean anufacturing. *Journal of Industrial Engineering and Management*, 9(3), pp. 811–833. http://dx.doi.org/10.3926/jiem.1940.

Webb, J. and Romano, R. eds., 2018: Printing forecast 2018. *WhatTheyThink* [online] Available at: <https://store.whattheythink.com/downloads/printing-forecast-2018/> [Accessed 27 March 2019].

Womack, J.P. and Jones, D.T., 1996. Lean thinking: banish waste and create wealth in your corporation. Simon & Schuster. http://dx.doi.org/10.1038/sj.jors.2600967.

Cigarette Packaging: visual impact of shock pictures and embossment at the point of sale

Ulrich Nikolaus, Marie Olschowsky and Nadine Wittenberg

Leipzig University of Applied Sciences (HTWK Leipzig)
E-mail: ulrich.nikolaus@htwk-leipzig.de

Short abstract

Although visual perception still has the highest influence on purchase decisions at the Point of Sale (POS), these decisions are also influenced by tactile properties. For this reason, haptic effects become increasingly important in branches like the book industry, in cosmetics or in packaging design. In packaging, embossing is a technique often used to both highlight elements visually and to add haptic properties, but the perceptional impact of embossing has not yet been thoroughly investigated scientifically. Especially on cigarette packages, the embossing is often very prominent – but due to current changes in legislation, embossed elements on cigarette packets now have to compete with pictures of smoking related ailments that are added to the designs for shock value. While the initial goal of this study was to determine the visual impact embossed cigarette packs have at the Point of Sale, the above-mentioned changes in legislation raised the additional question if the potential beneficial effects attributed to embossment were able to compete with the visual impact that those shock pictures now have on the buyers' attention. In the eye tracking study described in this paper, the influence that embossing on cigarette packages has is compared to the one shock pictures have on human attention. The results show that shock pictures are so dominant at the visual level, that they not only surpass by far the attentional impact of the older textual warning messages, but of all logo and brand elements as well (whether they were embossed or not). At least on the visual level, the benefit of using embossment on cigarette packages is thereby been called into question.

Keywords: consumer packaging, embossment, shock pictures, visual perception, eye tracking

1. Introduction and background

Up into the 1980s, user-oriented product design was mainly restricted to visual effects (Grunwald, 2009, p. 12). However, buying decisions are also influenced by haptic properties. The human skin possesses a set of highly specialised receptors residing in different layers of skin to register tactile and haptic features – and the conscious perception about texture properties associated with these receptors can even override visual information (cf. Grunwald, 2008, p. 538). Thus, haptic properties of consumer packages may have a heavy impact on the perceived quality of products, influence the consumer's initial qualitative judgement (cf. Lefebvre, et al., 2010, p. 156), and may even influence taste sensations and evaluations (van Rompay and Groothedde, 2019). According to a study done by Tillmann (2016, p. 91), powers of recollection increase if surface structures are perceived both haptically and visually. This may be the reason why embossing is a refinement method that is becoming increasingly important in the packaging industry. This particularly applies to cigarette packages, where embossing is used often; sometimes to give the whole box a different texture, but in most cases (at least as far as the packages analysed in this study are concerned) to emphasize brand names or logo elements. By adding haptic features to product packaging, producers hope to influence the consumer's decision making process (Peck and Wiggins, 2006, p. 56). As a study commissioned by the European Association of Carton and Cartonboard manufacturers suggests, the producers try to find ways to address customers, influence buying decisions emotionally, increase brand awareness as well as customer loyalty and to convey an impression of superior quality (Pro Carton & Gruppe Nymphenburg Consult AG, 2008, pp. 28–29).

However, embossing does not only influence tactile perception, but also has a visual impact (cf. e.g. Hünniger, Hamblyn and Engisch, 2019). Embossed elements on packages are perceivable to the human eye (for instance due to shadow casting or changes in the texture of the surface), and thus can be used to highlight certain elements of design, such as brand names or logos (l.c.). Therefore, embossing might influence the consumer's reactions at the point of sale even before he takes a product out of the shelves and actually touches it. As immediate physical contact is mandatory for tactile perception, it seems reasonable that – while embossing is generally perceived both visually and haptically – the visual perception is of higher importance while the product is still on the shelves, whereas the tactile perception becomes more important as soon as the customer begins to actually handle the product. Within the framework of a larger project investigating the multimodal perception of embossment on consumer packaging, the aim of the study described in this paper was, in a first step, to focus on the visual impact embossed cigarette packages have on the consumer at the point of sale (POS). Only at a later stage, the haptic perception and possible mutual dependencies are planned to be taken into account, so that at first, both modalities will be analysed without interference.

By chance, the preparation of this study coincided with legislative changes concerning the placement of warning messages on cigarette boxes. In May 2016, new regulations entered into force in order to reduce the attractiveness of tobacco products on adolescents (German Federal Ministry of Food and Agriculture, 2018). Since then, tobacco products in Germany are required to carry health-related warnings (combinations of text and pictures) that have to cover at least 65% of both the front and the back side (l.c.) These warning messages thus changed the visual appearance of cigarette packages considerably, and those so-called shock pictures now compete with common visual elements such as brand names and logo elements (which may or may not be emphasized by embossing) for the users' attention.

In this paper, an eye tracking test will be described that compares the visual impact that embossed and unembossed visual elements on cigarette packaging have on the buyers' perception with the influence the shock pictures have both on smokers and non-smokers. These effects were tested in a competitive shelf environment, which means that the study focusses on the early stages of the purchasing process where the consumer has his first visual contact with the product.

2. Materials and methods

The study described in this paper consisted of several parts. In preparation for the eye tracking test, some necessary demographic data was collected from all participants by using a pre-screening questionnaire; in particular concerning the age, gender, smoking habits and (where applicable) the preferred cigarette brand(s). In this context, possible visual impairments were checked as well.

2.1 Stimulus design

Next, sample stimuli had to be prepared, representing both embossed and unembossed cigarette packages and comprising the mandatory shock pictures. As the test had to be performed using an eye tracking system where the stimuli had to be shown on a computer screen, the visual impression of real embossing had to be simulated. In order to do this, several photos of real-life cigarette packages were taken in a frontal view. Several popular cigarette brands were included, and for each of them, both a blue and a red design were chosen. Brands that used other main colours were excluded from the test in order to minimize the impact colour has on the test results that was detected in prior tests (Nikolaus and Geißler, 2013; Nikolaus and Bendlin, 2015).

The shock pictures used in the test were taken from the official selection prescribed by the European Union (2015) and were faithful reproductions of the actual design. Of the total of eight images included in the test, two featured rather disgusting views, whereas two others featured less controversial sights such as a man on a bed or the shape of an embryo shown in an ash tray. The four other pictures featured faces – two of them showing infants (one of them also contained a smoking mother). All these pictures were prepared in such a way that any of the shock pictures could be combined with any cigarette package (both embossed and unembossed).

2.2 Survey design

The post-test questionnaire that was to be completed immediately after the eye tracking test was intended to find out which packaging designs were actively remembered by choosing from a selection of designs that were both included and not included in the eye tracking test. Next, the designs actually used in the test had to be ranked according to their visual appeal. Last but not least, the test participants were asked if they had noticed embossing effects on the designs shown in the test. As for the shock pictures, all pictures shown in the test had to be ranked according to salience.

2.3 Eye tracking test setup

In order to recreate a rather realistic buying situation during the computer based eye tracking test, the simulated packaging designs had to be presented in simulated goods shelves (Figure 1). Trying to emulate a gradual approach to the point of sale, some additional photos were added.

Figure 1: Establishing shots shown for five seconds (first photo) or four seconds (all others) at the beginning of each test

The eye tracking began with a zoom in showing only three and then only two shelves, respectively. On the three shelf version, 24 packages (both embossed und unembossed, eight packages in each row) could be seen, whereas in the two shelf version, eight designs were included (four in each row). In a final step, several packaging designs (both embossed and unembossed) were shown as standalone products (Figure 2).

Figure 2: Three shelf and two shelf views as shown in the eye tracking test, followed by two individual packaging shots (here shown at reduced scale)

In total, 14 pictures were shown: four establishing shots, both shelf views and eight individual packages. The display time for each stimulus was determined in accordance with settings used in earlier tests (e.g. Nikolaus and Spieß, 2016) which were slightly adapted based on the results of some pilot tests.

2.4 Subjects

Fifty-one test participants were recruited for the experiments, 27 of them women, 24 males. Although an even distribution of smokers and non-smokers might have been desirable, only 19 (current and former) smokers could be found.

2.5 Apparatus and procedure

The stimuli were presented on a monocular, desktop based NYAN 2 XT/EDGE eye tracking system. User reactions were recorded and their visual scan paths were analysed. In order to assess the impact of embossing effects and the influence of the shock pictures, Areas of Interest (AOI) were defined beforehand to compare the fixation count, the time to first fixation, gaze durations, etc..

3. Results and discussion

The first step of the eye tracking data analysis consisted in an overall assessment of the dispersal of attention in the two- and three-shelf-views. As can be seen in the heat map on the left-hand side of Figure 3, the attention of the consumers is highest in the centre of the middle rack and on the upper shelf, where upmarket products are preferably positioned (Berghaus, 2005, p. 18). The heat map on the right-hand side, on the other hand, shows a clear focus of attention on the shock pictures – irrespective of whether the brand elements were embossed or not.

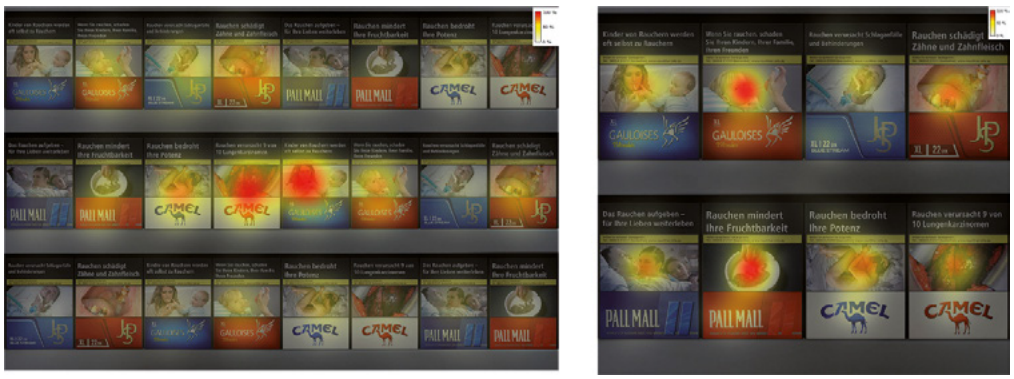

Figure 3: Heat maps illustrating the distribution of attention for three and two shelf stimuli, respectively; red areas indicate a high level of attention, yellow and green mark less salient areas; areas that got only minor (or no) attention are darkened

Regarding the distribution of attention between embossed and unembossed packages, no significant differences could be found. In both the two shelf and the three shelf view, unembossed elements even got slightly more fixations and were looked at *longer* than the embossed versions. The same applies for most of the standalone shots of embossed and unembossed packages; but in all cases, the differences were minimal and probably coincidental.

On the other hand, the test results showed a significant dominance of the shock pictures over the brand elements in every applied metric (time to first fixation, fixation count and fixation duration) (cf. Figure 4). In comparison with the textual warning messages that were already present on earlier cigarette pack designs,

however, the brand elements were able to prevail (irrespective of whether they were embossed or not). This result is further supported by answers in the post-test questionnaire: Here, the participants were asked (for each of eight stand-alone cigarette packs) to mark all design elements that they regarded as particularly noticeable. In sum, shocking pictures were marked 197 times on the various stimuli, branding elements 111 times and the textual warning messages only 28 times. From this it can be derived that – while the use on embossment for visual purposes may have been justified for older cigarette pack designs – it seems considerably less promising today.

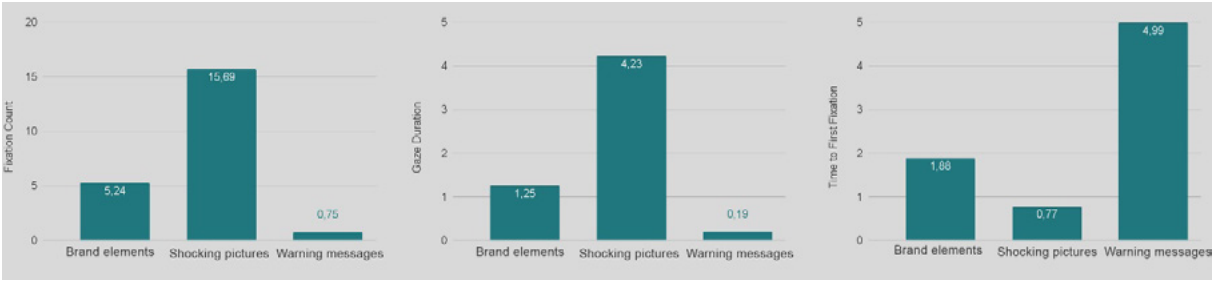

Figure 4: Sample eye tracking results showing the distribution of attention for selected design elements on cigarette packets in the three shelf version; the shock pictures got more fixations (fixation count) and were looked at longer (gaze duration) than other elements – and were noticed earlier (time to first fixation)

As for the three different types of shock pictures, only minor differences in fixation duration and fixation count could be detected: Pictures on which faces were visible were looked at significantly earlier than those with nauseating depictions, which in turn were more salient than rather neutral motifs. However, the motives shown had a significant impact on the optical attractiveness the participants attributed to the respective packaging designs: According to the post-test-questionnaire, 59 % of the participants assessed the overall appeal primarily on the basis of the shock pictures. 47 % of these participants classified designs that featured shock pictures with infants as visually pleasing – although the subtext explained that the children shown here were endangered by smoking. Nonetheless, these designs were described as "not that repulsive", "harmless", "least disgusting" or "not so bad".

Although the shock pictures had in all cases a much higher impact on the participant's visual perception than the embossed brand elements, some differences between smokers and non-smokers could be observed nonetheless. In the three shelf version, both the fixation count and fixation duration show significantly higher values for the brand elements if the corresponding viewers where smokers. Smokers, for instance, on average looked 0.73 seconds longer at brand elements than non-smokers. By contrast, non-smokers on average had a fixation duration that was 1.63 seconds longer for the area of interest containing the shock pictures (cf. Figure 5).

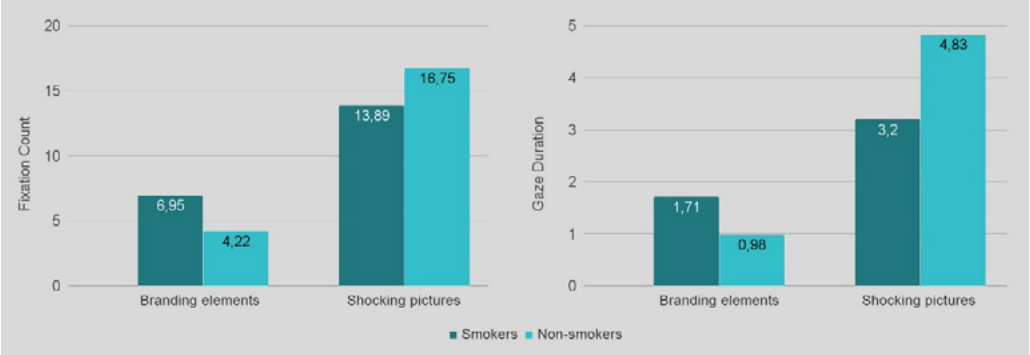

Figure 5: Eye tracking results showing the different gaze behaviour of smokers and non-smokers; smokers fixate brand elements significantly more often (fixation count) and longer (gaze duration) than non-smokers

The group comparison heat map shown in Figure 6 visualizes the observed difference between the gaze behaviour of smokers and non-smokers. Although all participants looked at the shock pictures rather intently, non-smokers looked at them even more, whereas the smokers devoted more attention to the brand elements.

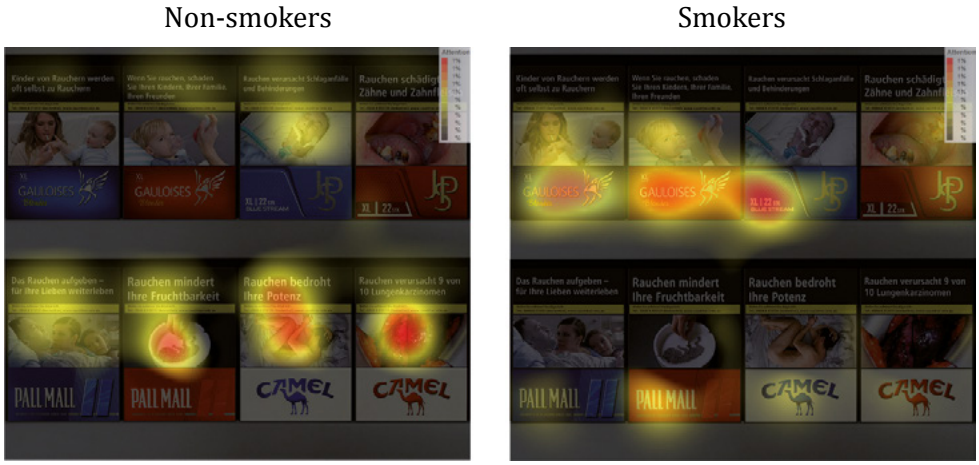

Figure 6: Sample group comparison visualizing differences in gaze behaviour between non-smokers (left) and smokers (right); while the non-smokers' attention is clearly more focussed on the shock pictures, the smokers show a comparably higher interest in the brand elements

4. Conclusions

If cigarette pack designers hope to achieve beneficial visual effects by embossing brand names or logos, these hopes (at least according to the results of the current study) mostly remain unfulfilled. Although it cannot be ruled out that a certain degree of highlighting and vision guidance could have been achieved by older packages that only featured textual warnings, these effects can no longer be observed in direct competition with the new pictorial representations.

On the other hand, the legislature requiring the inclusion of mandatory shock pictures on cigarette pack designs could feel vindicated by these results, as the shock pictures got a considerable higher attention than all other design elements. Especially shock pictures with faces on them were looked at significantly early. However, it should be noted that the effectiveness of the shock pictures decreased slightly in the further course of the test, which might point to a certain habituation effect. Furthermore, the shock pictures got less attention by smokers than by non-smokers, who were still able to direct more attention towards brand names and logos. This might indicate that while the shock pictures do have a certain dissuasive effect on non-smokers, their influence on habitual smokers is probably more limited, due to possible avoidance strategies.

With regard to the benefits of embossment used on cigarette packs, it can be said that although its visual impact at the Point of Sale may be lower than before, the benefits of haptic perception during handling have not yet been taken into account. Although the potential of embossment for visual highlighting seems to be rather limited (at least if the embossed elements have to compete with other, stronger visual stimuli), the haptic structure may still be able to convey a certain recognition value or luxury feel. It might be advisable to investigate this in a multimodal test scenario, where packages can be explored both visually and haptically – and by using stimuli with lower distractive properties than the cigarette packages with shock pictures on it proved to have.

Acknowledgments

The authors would like to thank Jennes Hünniger and Lutz Engisch for their invaluable help during the preparation of the test and Simon Hamblyn for fruitful discussions and proof reading.

References

Berghaus, N., 2005. *Eye-Tracking im stationären Einzelhandel.* Lohmar-Köln: Josef Eul.

European Union, 2015. *Kombinierte gesundheitsbezogene Warnhinweise für Rauchtabakerzeugnisse.* [pdf] Brussels: European Union. Available at: <https://ec.europa.eu/health/sites/health/files/tobacco/docs/healthwarnings_germany.pdf> [Accessed March 2019].

German Federal Ministry of Food and Agriculture, 2018. *Schutz vor den Gefahren des Tabakkonsums (Health protection from the harmful effects of tobacco consumption).* [Online] Bundesministerium für Ernährung und Landwitschaft. Available at: <https://www.bmel.de/DE/Ernaehrung/Gesundheit/NichtRauchen/_Texte/EUTabakproduktrichtlinieNeuordnung2014.html> [Accessed 29 March 2019].

Grunwald, M. ed., 2008. *Human Haptic Perception: Basics and Applications.* Basel: Birkhäuser.

Grunwald, M., 2009. Der Tastsinn im Griff der Technikwissenschaften? Herausforderungen und Grenzen aktueller Haptikforschung. *LIFIS-Online,* 9 January 2009. [pdf] Available at: <https://leibniz-institut.de/archiv/grunwald_martin_09_01_09.pdf> [Accessed March 2019].

Hünniger, J., Hamblyn, S. and Engisch, L., 2019. Influence of colour and gloss on the visual perception of embossed prints. In: C. Ridgway, ed. *Advances in Printing and Media Technology: Proceedings of the 46th International Research Conference of iarigai.* Stuttgart, September 2019. (Accepted for publication April 2019).

Lefebvre, A., Bassereau, J.F., Pensé-Lheritier, A.M., Rivére, C., Harris, N. and Duchamp, R., 2010. Recruitment and training of a sensory expert panel to measure the touch of beverage packages: issue and methods employed. *Food Quality and Preference*, 21(1), pp. 156–164. https://doi.org/10.1016/j.foodqual.2009.08.020.

Nikolaus, U. and Bendlin, S., 2015. Visual perception and recollection of pictures in packaging design. *Journal of Print and Media Technology Research*, 4(1), pp. 33–41. https://doi.org/10.14622/JPMTR-1420.

Nikolaus, U. and Geißler, A., 2013. Familiarity and color effects on consumer reactions to packaging design. In: N. Enlund and M. Lovreček, eds. *Advances in Printing and Media Technology: Proceedings of the 40th International Research Conference of iarigai*. Chemnitz, September 2013, Darmstadt: iarigai, pp. 383–390.

Nikolaus, U. and Spieß, J., 2016. The influence of location-related factors on the perception of billboard advertising. *Journal of Print and Media Technology Research*, 5(1), pp. 39–51. https://doi.org/10.14622/JPMTR-1601.

Peck, J. and Wiggins, J., 2006. It just feels good: customers' affective response to touch and its influence on persuasion. *Journal of Marketing*, 70(4), pp. 56–69. https://doi.org/10.1509/jmkg.70.4.056.

Pro Carton & Gruppe Nymphenburg Consult AG, 2008. *BrainPacs: Verpacken Sie limbisch!.* [pdf] Available at: <https://docplayer.org/docview/25/6840627/#file= /storage/25/6840627/6840627.pdf> [Accessed 22 March 2019].

van Rompay, T.J.L. and Groothedde, S., 2019. The taste of touch: enhancing saltiness impressions through surface texture design. *Food Quality and Preference*, 73(April 2019), pp. 248–254. https://doi.org/10.1016/j.foodqual.2018.11.003.

Tillmann, D., 2016. *Marktanalyse zum Einsatz haptischer Elemente auf Konsumgütern. (Market analysis concerning the usage of haptic elements on consumer goods).* Master's thesis. Leipzig University of Applied Sciences (HTWK Leipzig).

Bioprinting of thick, vascularized Tissues by Inkjet-Technology

Noreen Zönnchen[1], Raphaël Wenger[2], Muriel Mauron[2] and Fritz Bircher[2]

[1] Department of Engineering, Technische Universität Chemnitz, Germany

[2] iPrint Institute, University of Applied Sciences Western Switzerland, Fribourg, Switzerland

E-mails: noreen-zoennchen@tu-chemnitz.de; {raphaël.wenger; muriel.mauron; fritz.bircher}@hefr.ch

Short abstract

Single nozzle printing or extrusion technology is broadly used to deposit cell-laden hydrogels in tissue engineering. Inkjet printing was not, until recently, considered for the deposition of living cells, even though it would offer significant advantages. In this study, we are going to use industrial inkjet printing technology, which provides as well a high resolution and throughput to pattern a fibroblast laden tissue with vasculature-like channels, lined by HUVECs (human umbilical vein endothelial cells). We identified and tested different bio-inks, to fit the printing process and the biocompatibility. As an extracellular matrix for fibroblasts, we tested the properties of GelMa as a hydrogel. Pluronic F 127 will be used as volatile ink to apply the channel-construct that can be actively perfused afterwards and will supply the cells with growth factors and nutrients. In this project we describe the initial stage of the project, mainly focussing on the selection of the ink.

Keywords: tissue manufacturing**,** hydrogel, three-dimensional printing

1. Introduction

Bioprinting is a research field that kept growing for the last few years as three-dimensional printing moved in the focus of medical manufacturing. Most people are likely to envision the synthetic production of whole organs on the first hand when talking about bio-manufacturing. Still, it will remain a vision for some more decades to print whole functional systems, because of the complexity of different tissues, high strain and hormonal and enzymatic reactions. The current focus lies on the replication of long sustainable tissues. The medical industry is highly interested in the development of synthetic tissues being perfusable, biodegradable and adaptable in their properties. They can enable drug screenings, tissue replacements, wound dressing or disease modelling. Up to a few years ago, it was difficult to maintain living cells inside thicker layers of gel over long periods. Channels, just as fine as blood vessels, are needed to transfer nutrients and growth factors to the cells and to remove excess waste products. We are investigating a new approach for the fabrication of the vasculature. Using inkjet printing makes the choice of the hydrogel a complex subject in addition. Its properties do not only have to cover the biocompatibility, but also the printability.

1.1 State of the art

In bio fabrication, no matter which kind of cells are chosen, it is always necessary to embed them in an environment, similar to the extracellular matrix. So-called hydrogels – polymers that can soak water to several times their initial weight – are excellent candidates to fulfil this property. There are dozens of different types of natural or synthetic sources, having different advantages. (Murphy, Skardal, and Atala, 2013) Gelatine-methacrylate (GelMa) asserted itself as a low cost, simple to handle, biocompatible option, whose properties can be changed easily depending on the application (Billiet, et al., 2014; Pepelanova, et al., 2018; Yue, et al., 2015). This hydrogel derives from gelatine, based on denaturised collagen that mimics perfectly the connective-tissue-environment of the fibroblasts, we are going to use. Through the combination with methacrylate-groups, the gelatine can be modified to achieve gel-stability at temperatures up to

37 °C (incubation temperature). Also, for the cell-combination of fibroblasts and HUVEC, as in our application, GelMa shows promising results (Nichol, et al., 2010). It can be adapted in various ways to change not only its final stiffness and swelling behavior, but also its viscosity in the non-crosslinked state, to make it jettable (Hoch, et al., 2013).

Still, most research on 3D printing of vascularized tissues is based on other technologies than inkjet printing (Therriault, et al., 2005; Bertassoni, et al., 2014; Lee, et al., 2014; Jia, et al., 2016). In a recent study, a thick (>10 mm), vascularized tissue with a long-term proliferation of more than six weeks was achieved (Kolesky, et al., 2016). In this case, the use of a natural hydrogel, crosslinked by an enzymatic reaction that creates a final network of fibrin fibres, enabled a well-functioning 3D attachment of fibroblasts. They extruded Pluronic F 127 at room-temperature as volatile, three-dimensional, fine channel-system in a gel state and moulded the vasculature, together with the hydrogel both in a pre-extruded silicone cast. By cooling the volatile ink down to 4 °C it becomes liquid and can be flushed out of the channels. Then, the HUVEC cells can be injected for seeding and maintained by circulating growth-medium. Although the achievements are a huge step in tissue engineering, the procedure is slow. By using single nozzle or extrusion technology, only low throughputs and/or less accuracy is possible. Industrial inkjet-technology would enable the fast printing of several biosystems all in once. Figure 1 shows currently used additive manufacturing techniques comparing their resolution and throughput, clearly showing the unique capabilities of inkjet printing. It allows high resolution, high throughput and also, compared to e.g. DLP printing, the choice of different kind of inks.

The goal of the present study is to achieve the idea of a vascularized GelMa hydrogel, whose purpose can be adapted to several fields. The gel deposition by an industrial piezo inkjet setup can upscale the printing quantity and quality. The main goal is to install two printheads and one extrusion-syringe, to print the mould for the hydrogel by extrusion and the cell-laden GelMa and volatile ink (Pluronic F 127) by inkjet-technology all in one process. Therefore, a fast curing system is needed to build up stable layers. The UV irradiation was selected for that application. Different studies have shown no significant impact of UV light on cells, as long, as the irradiation-time and intensity are moderate (Bryant, Nuttelman and Anseth, 2000; Hoch, 2014; Nichol, et al., 2010). Also, the decision of the use of UV light forced us to find a mold material, being not only UV-cross-linkable but also biocompatible, extrudable in a range between 0 °C and 60 °C, stable at incubation- temperature and at best being soft and clear, in order to seal up the bioreactor.

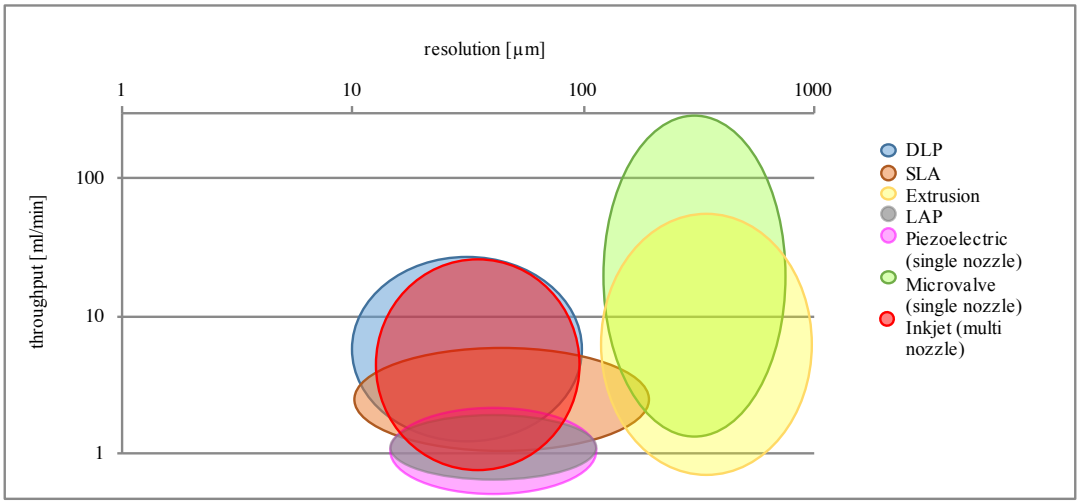

Figure 1: Additive manufacturing technologies compared by their throughput and resolution; Combining high resolution, comparable to Laser Assisted Printing (LAP), Laser-Based Stereolithography (SLA) and Digital Light Processing (DLP) and high throughputs as in Extrusion printing, Inkjet Technology has huge potential for bioprinting, by providing also a broad palette of possible inks

2. Materials and methods

2.1 GelMa synthesis

The synthesis of GelMa was performed by dissolving a mass fraction of 10 % gelatin (bovine skin type B 225g bloom, porcine skin type A 100g bloom; Sigma Aldrich, Buchs, Switzerland) in 100 ml of Dulbecco phosphate buffered saline (DPBS) at 60 °C for 2 hours under constant stirring. After lowering the temperature to 50 °C, 5.4 ml of methacrylic acid were added dropwise to reach a substitution degree of 60 %. By maintaining the temperature for 4 hours, the methacrylation could proceed. The reaction was stopped by the addition of 40 °C warm DPBS to reach 4.5 % of a mass fraction concentration of GelMa. Excess methacrylic acid and methacrylic anhydrides were removed by dialyzing the solution against daily changed, distilled water, through a 12-14 kDa molecular weight cut off dialysis tube at 40 °C for four days. Finally, the GelMa was frozen at −80 °C, and lyophilized for three days. The final degree of methacrylation was determined by ^{1}H-NMR – analysis.

2.2 Ink formulation

The hydrogel for the bio-ink was prepared under constant stirring at 40 °C with a dry mass fraction of 10 % and 12 % of GelMa, in either culture medium or demineralized water and 0.5 % photo initiator. The photo initiator composed of Irgacure 2959 (Sigma Aldrich, Buchs, Switzerland), dissolved at 1 % in deionized water. The photoinitiator has been previously tested to be biocompatible. GelMa dissolved in medium was used for cell-culture and in demineralized water for the determination of the mechanical properties. The volatile ink, destined for the print of the vascular channels, consisted of a mass fraction of 17 % Pluronic F 127 (Sigma Aldrich, Buchs, Switzerland), dissolved in deionized water. The cast material was a pre-prepared, clear, elastic resin, with 50 shore A (Formlabs Elastic Resin, Somerville, USA).

2.3 Rheological testing

The viscosity is an important property for inkjet-printing. Using a Xaar printhead, modified for bioprinting applications, inks between 2 mPa·s and 12 mPa·s can be used without clogging the nozzles. The viscosity of the non-crosslinked hydrogel was measured at room temperature and at 37 °C, which is the upper critical printing temperature, due to the denaturation of the cells. A piezo rheometer (Tri PAV, Cambridge, United Kingdom) was used to apply high frequencies up to 10 000 Hz on the ink, similar to the conditions in the printhead. The Pluronic ink needed to be measured with two different rheometers, to find the optimal printing temperature. The piezo-rheometer is based on a water-cooling system and can't reach temperatures below 16 °C. Though, since it is more representative, it was used as a control-measurement above the lowest water temperature. At temperatures between 3 ºC and 20 °C, the viscosity was measured by a rotation rheometer (Malvern Kinexus, Malvern, United Kingdom) which can only apply frequencies up to 1 000 Hz.

2.4 Mechanical testing

A volume of 1.5 ml of each formulation of GelMa (100/225 g bloom, 10/12 % dry mass) in a twelve well plate, were exposed to 40 mW/m^2 UV-light (320–500 nm; Excelitas Omnicure s2000, Ontario, Canada) for 180 s. After the addition of 1 ml of PBS to each sample, they were incubated for 24 h. Afterwards, the hydrogel was detached from the well and placed between two metal punching plates (Figure 2). The samples were pressed to half of their initial size at 36 °C environment temperature and the normal force against the plate was measured. To determine the compressive modulus, the linear region of the slope of strain against the stress was taken.

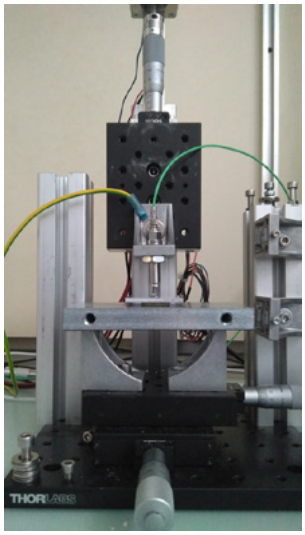

Figure 2: Pressure trial machine

2.5 Hydrogel swelling analysis

The crosslinking was performed in the same procedure as for the mechanical testing, followed by the initial weighing of the samples. For the swelling, 1 ml of PBS was added to each well. The hydrogel was then left in the incubator at 37 °C for 6 days. To check the change of the weight on a daily basis, the PBS was aspired and the residual liquid removed by paper wipes. The samples were detached from the wells and weighted again to calculate the swelling ratio which is the ratio between swollen and dry hydrogel.

2.6 Cell culture

After refreezing the umbilical vein endothelial cells (HUVEC), they were cultured in endothelial cell growth medium (ECGM; Sigma Aldrich, Buchs, Switzerland) at 37 °C and 5 % CO_2 atmosphere in the incubator. They could be used for several passages, done approximately two times a week. Passages need to be done, to transfer cells from the maximum level of proliferation to a new flask. The medium was changed every 2–3 days, depending on the confluence (ratio of cells covering the flask surface to the free surface). Same procedure was done with the fibroblasts (3T3 cells), by using DMEM medium with 10 % calf serum.

2.7 Cell seeding

For the cell's adhesion, a suspension of HUVECs in growth medium (40 000 cells per well) was added to a twelve well plate on a thin layer (500 µl) of sterile filtered (20 µm syringe filter), crosslinked hydrogel (100/225 g bloom, 12 % dry mass). One ml of growth medium was added afterwards. The well plate was left in the incubator for 48 h and the medium was changed daily. After the incubation time, the medium was aspired and the gel rinsed with PBS. Fluorescent staining of Calcein and Ethidium homodimer-1 (EthD-1) was prepared and added to the gel. After 30 min, a live/dead assay was performed, with a fluorescent microscope (Leica Paula, Wetzlar, Germany).

The 3T3 cells were encapsulated in the sterile filtered hydrogel (225 g bloom, 10/12 %) with ~ 670 000 cells per ml gel. In a twenty-four well plate, 3 samples of each formulation were crosslinked together with the cells in two steps (2 × 125 µl) for 10 s. After adding 500 µl of the medium, the samples were incubated for 24 h, 48 h and 72 h. A live/dead assay was performed with the Calcein-EthD-1 staining again. Using a confocal microscope (Zeiss LSM 710 meta, Oberkochen, Germany), cell proliferation in all layers of the hydrogel could be visualized.

2.8 Biocompatibility resin

The resin that will serve as co-printed mould-material, to keep the hydrogel long term stable, is crosslinked by a photo-initiator reaction. These photo-initiators are very toxic, when not cured evenly. That's why the compatibility needed to be tested. Therefore, small patches of the resin were crosslinked and either left in this condition, washed in isopropanol and cured for a second time or embedded in the GelMa in both already named versions. The patches were filled in twelve well plates, together with 50 000 3T3-cells and 1 ml medium or used to prepare supernatants (possible toxins of resin, diffused in medium). The supernatant was used in the same manner, as the patches. After incubating the samples together with a positive control group, without resin or supernatant and a negative control group, with latex, the confluency was measured after 24 h on a daily basis.

2.9 Removability volatile ink

The Pluronic F 127 at 17 % was heated up to 37 °C in the incubator to form a gel and filled in a syringe of the same temperature. With a 50 µm needle, a channel was inserted into a mould with warm (37 °C) hydrogel. Subsequently, the Pluronic was filled in this channel, using the same needle, by only exchanging the syringe. By cooling down the mould in the fridge to 4 °C, the Pluronic turns liquid. A syringe with cold water was then used, to flush out the Pluronic (Figure 3).

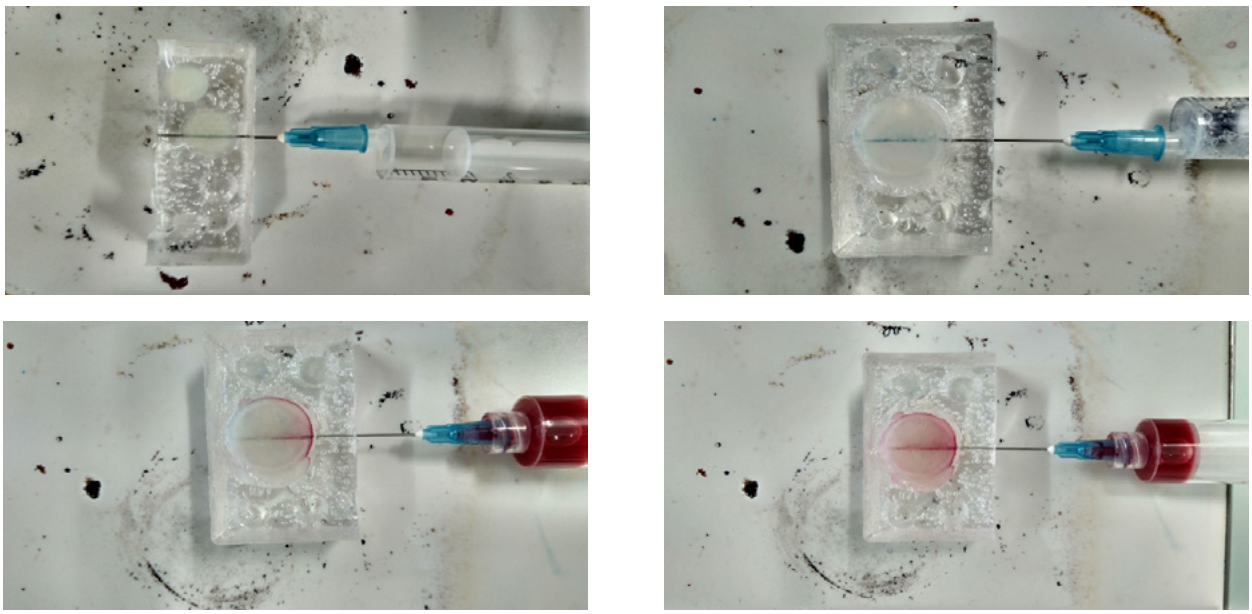

Figure 3: Row 1: applying a channel to the hydrogel and inserting the Pluronic coloured in blue (left to right), row 2: flushing out the cooled volatile ink by cold, red coloured water

2.10 Printing tests

Subsequently to the ink testing, trials on the printability of GelMa and Pluronic were performed. Therefore, a dropwatching camera at the printing platform guaranteed the capturing of the drop formation. GelMa at 8 % dry mass fraction and 225 g bloom was printed at 25 °C and Pluronic F 127 at 8 °C, at low jetting frequencies of 5 Hz. A Xaar 128 printhead was used for the application. Necessary modification of the inks could be revealed e.g. due to satellite drop formation. Following this, the printing of fine vascular-like patterns in several layers was proceeded with Pluronic hydrogel. The embedding in liquid GelMa with subsequent crosslinking enabled the determination of the volatile ink removal.

3. Results and discussion

3.1 Rheological testing

The rheological testing has shown that, at room temperature, a gelification of the GelMa is already noticeable. Therefore, the viscosity is not compatible with the printhead. At 37 °C, the gel is showing a huge shear thinning behaviour as a non-Newtonian liquid. This makes the hydrogel precursor jettable at high frequencies (Figure 4). The lowest viscosity of Pluronic F 127 at 17 % was measured at 17 °C (Figure 5). The lowest viscosity remains at the limit of what would be jettable. If it proves not to be printable, lower concentrations will be tested.

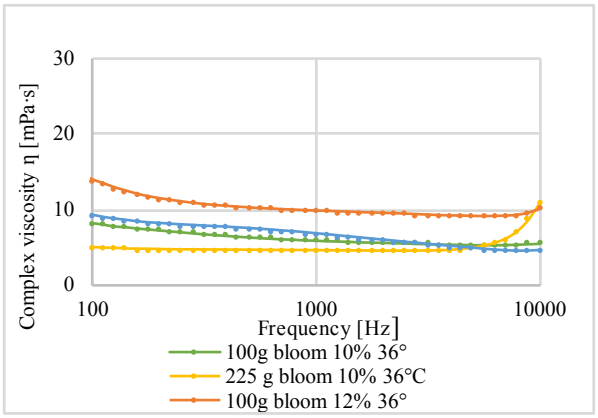

Figure 4: Viscosity of the preferred GelMa formulations at 37 °C

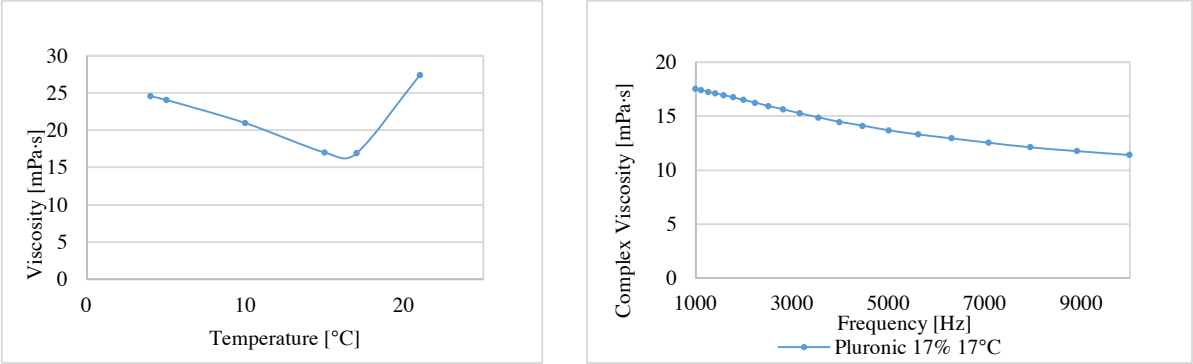

Figure 5: Viscosity of 17 % Pluronic F 127, showing the minimum at 17 °C, at 1 000 Hz shear rate (left), being still minimally out of the printable range at high frequencies (right)

3.2 Mechanical testing

The mechanical tests have shown high stiffnesses on all the gels, which can be explained by the high degree of methacrylation, dry mass and photo-initiator concentration. The higher these properties, the stiffer will the gel turn out. Next, the formulation of GelMa was optimized to figure out the small range of GelMa being as stiff as possible for easy micropatterning and still allowing the cells to proliferate and spread inside the gel. It turned out that the gel with 225 g bloom was more fragile, than the one with 100 g bloom. The 225 g bloom is an indicator for higher molecular strength of the gelatine. Therefore, this gel should be stiffer, than 100 g bloom. It can be supposed that the degree of methacrylation turned out lower in 225 g bloom, than in 100 g bloom. The ^{1}H-NMR- analysis will confirm the assumption. As expected, the use of 10 % dry mass formed softer gels, than 12 % in both cases (Figure 6).

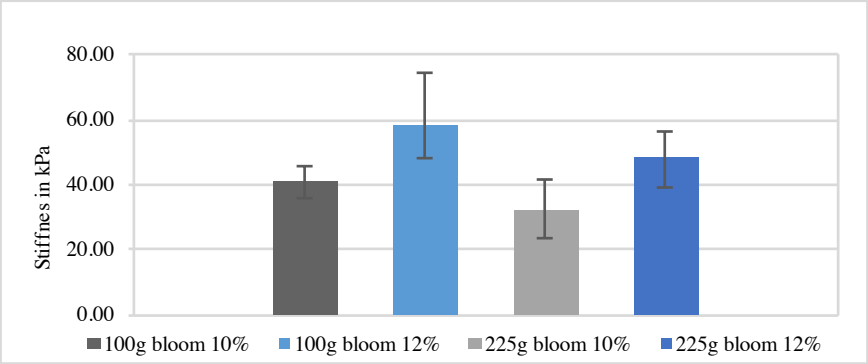

Figure 6: The Stiffness of the GelMA at swollen state at 37 °C, showing higher stiffness at 12 %, same as the overall stiffer gel based on 100 g bloom

3.3 Hydrogel swelling analysis

The evolution of the mass of the gels has shown no significant changes in the swelling ratio. During a six days trial, all the gels were stable. The higher density of the GelMa seems to increase the polymer network density and therefore reduce the pore sizes and the possibility of soaking up liquid.

3.4 Cell seeding

For the cell-attachment tests, we only moved on with the hydrogels of 12 % dry mass. This concentration leads to the stiffest gels, which have the best chances of enabling the printing of 3D vasculature-like channels. The confluence and viability of the HUVEC appeared much higher and vital, in the softer gel of 225 g bloom at 12 % than in 100 g bloom at 12 % (Figures 7 and 8). Cells prefer the bigger pore-size as an easier environment for their protein-attachment. This led to the decision, to test the cell encapsulation of the 3T3 cells only with GelMa based on 225 g bloom.

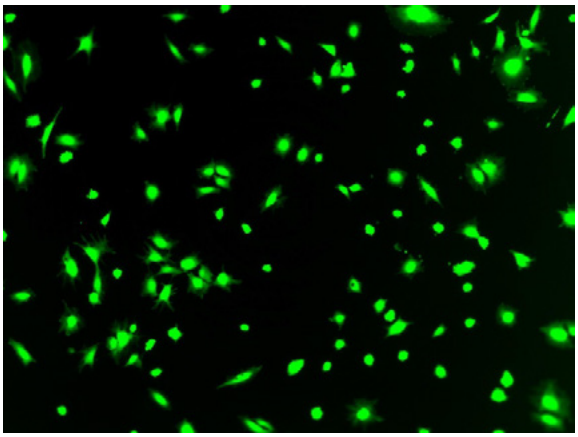

Figure 7: HUVECs on 12 % GelMa of 100 g bloom, cells are spreading less and staying spherical, they are more likely, to not proliferate on a long term

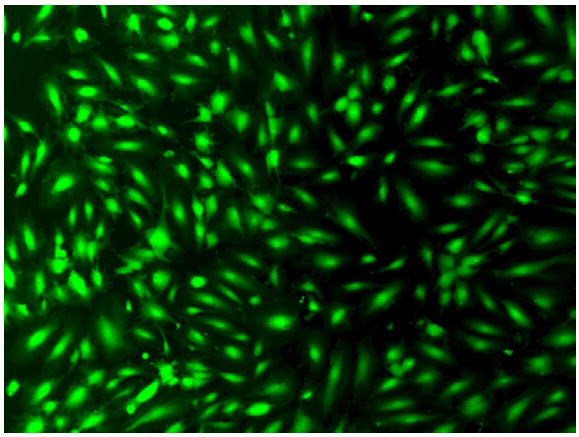

Figure 8: HUVECs seeded on 12 % GelMa of 225 g bloom, cells are evenly spread and form protein branches, the chance of a longer survival rate is higher on this gel, due to the lower stiffness

3.5 Cell embedding

Cell confluence and viability of 3T3 cells were tested in 225 g bloom hydrogel with 10 % and 12 % mass fraction, to be sure lowering the stiffness (at 10 %) even more, wouldn't lead to a huge increase of cell survival and spreading. The results have shown no significant difference in the cells proliferation between 10 % and 12 %. In both cases, cells were still alive after 72 h. Though, no cell spreading was visible (Figure 9). This is an advantage in our application, since we want the gel to be stable as long as possible. A rapid cell spreading would lead to a degradation of the hydrogel within days, preventing any long-term tissue maturation.

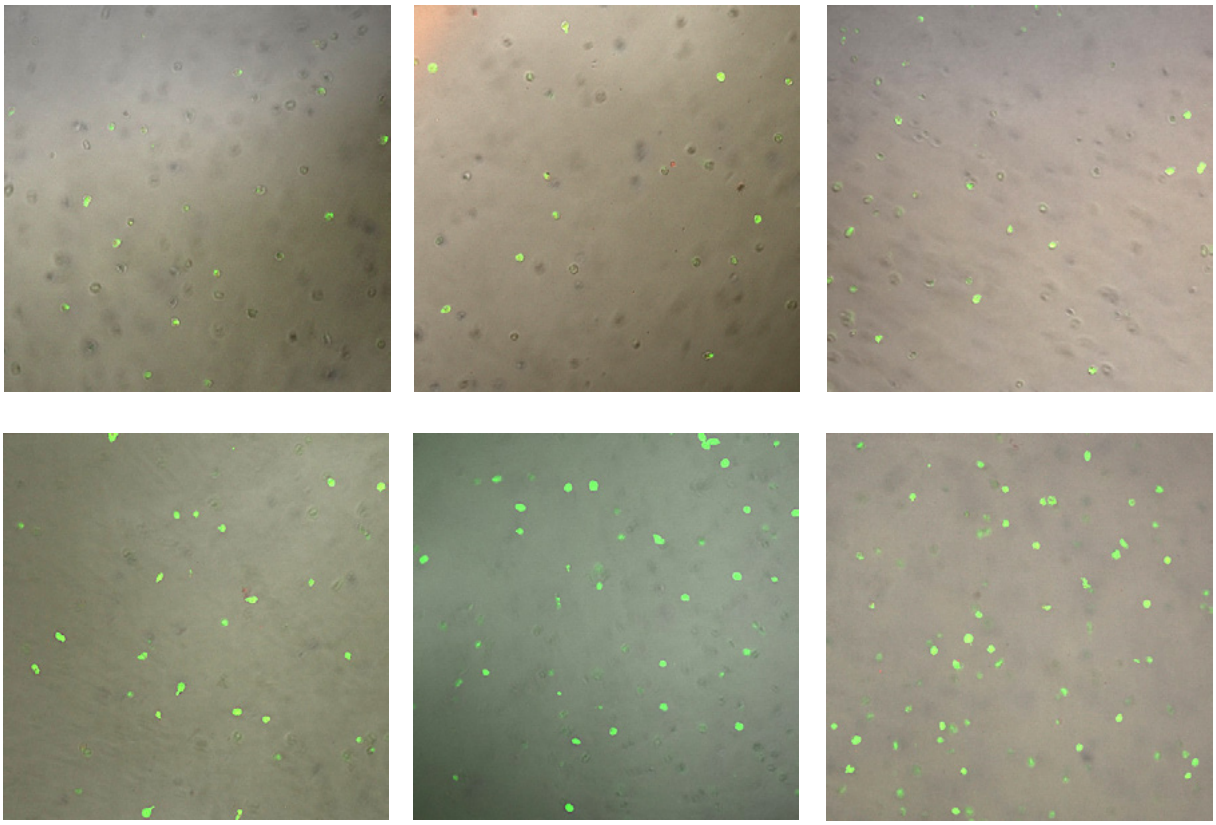

Figure 9: Row 1: 10 % GelMa at 225 g bloom after 72 h of 3T3 seeding, showing living (green) cells and plenty more in deeper layers; the same result can be seen with the use of 12 %; cells seeded for 48 h at 10 % are showing no recognizable difference to 72 h (left to right); row 2: also for fibroblasts at 12 %, the living cell amount is comparable, to the equivalent at 72 h; 24 h after seeding, at 10 and 12 % a higher number of living cells is visible (left to right); in general, the fibroblasts are staying spherical under three dimensional strain, it needs to be examined, if the lack of spreading leads to cells death on a long term or is still a signal of stable proliferation

3.6 Biocompatibility resin

When examining the biocompatibility of the resin for the printing of the mold, the condition after only one curing period has revealed the same toxicity, as the negative control latex. All the cells were dead when in contact with the resin or supernatant, produced from it. Washing and double-curing the resin, led to a decrease of the toxicity. However, pre-treatment of the mold isn't an optimal solution for our application, as it prevents the fabrication.

The embedding of the resin in hydrogel led to high cell survival. The free binding sites of the GelMa seem to catch the excess free radicals of the photo-initiator and keep the possibility open to print the tissue and its mold within one single process without significantly reducing cell viability.

3.7 Dropwatching

The dropwatching of the hydrogels revealed satellite formation of GelMa at 225 g bloom and 8 % dry mass. The surface tension was already lowered from ~ 72 mN/m to 60 mN/m by 0.4 % of Pluronic F 68. Further decrease of the surface tension could refine the printing result. However, most surfactants are not biocompatible. A promising candidate needs to be found therefore. The Pluronic F 127 ink could be printed in a steady outcome, but with rather slow droplets. Still, it could be used to print small patterns of vasculature in less than 2 s per pass. The printed pattern was moulded in a flexible, transparent resin and embedded in GelMa, which was crosslinked subsequently. The printed vasculature was still visible. After cooling the system down to 6 °C to liquify the Pluronic the channels could be removed by applying a slight vacuum. The process is shown in Figures 10 to 15.

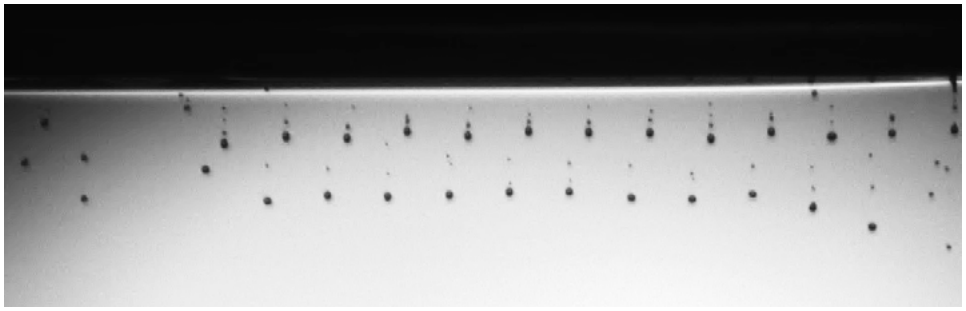

Figure 10: Dropwatching of GelMa (200 µs) at 225 g bloom and 8 % at 25 °C showed some satellite formation, even by adding Pluronic F 68 as surfactant

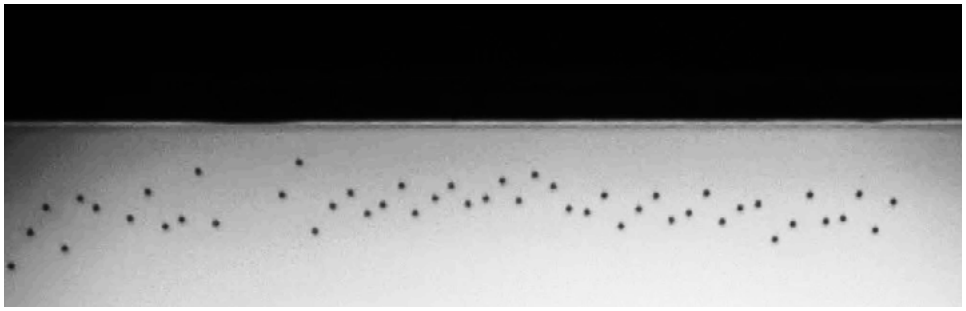

Figure 11: Removal of the cold Pluronic at slight vacuum; the ink leaving the channel can be seen inside the needle

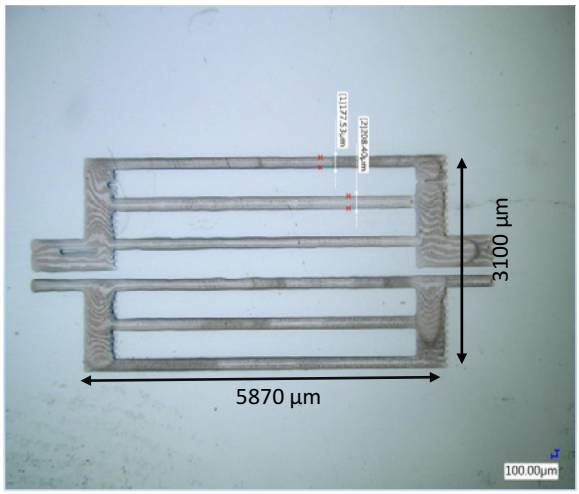

Figure 12: Printed vasculature of Pluronic F127 with 200 µm channel diameter

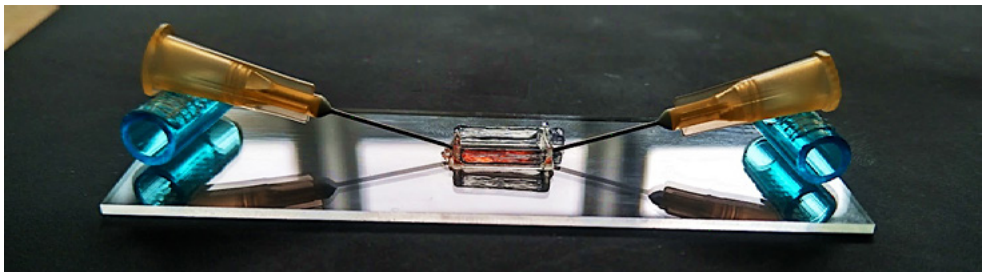

Figure 13: Channel of Pluronic F 127 casted in elastic resin

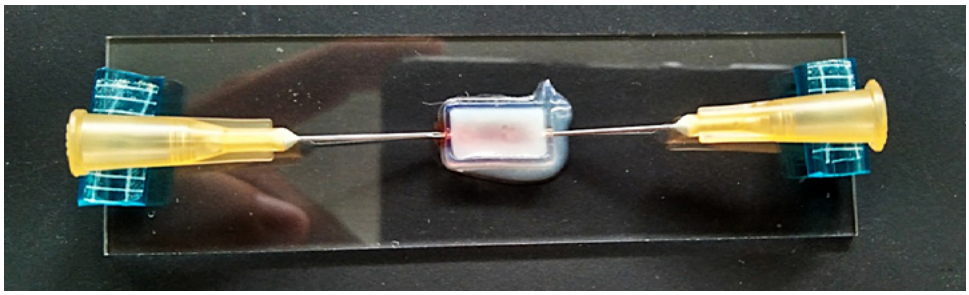

Figure 14: Vasculature embedded in GelMa

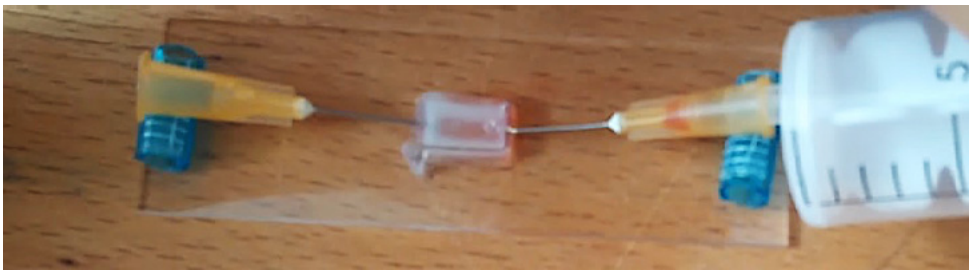

Figure 15: Removal of the cold Pluronic at slight vacuum; the ink leaving the channel can be seen inside the needle

4. Conclusions

The present study aimed to proof the producibility of a thick, vascularized, cell-laden tissue through piezo multi-nozzle inkjet-technology. The preliminary testing has shown satisfactory results in the handling of GelMa as a hydrogel for inkjet application. A gel, stiff enough for the 3D printing of complex structures while supporting cell proliferation was identified. In general, every single concept, which is necessary to combine the processes, could be declared as successful, leaving only some features of improvement. The whole printing of a thick, vascularized, cell-laden tissue by inkjet printing should, therefore, be feasible in future trials. However, it was not possible in the given time and set up to achieve a complete cell-laden microfluidic system. Still, it could be proved, that inkjet technology is able to print very fine vasculature in fast manner. The structures were even smaller than the current state of the art of other technologies. The combination of the concepts to achieve the complete system will be regard of further studies.

References

Bertassoni, L.E., Cecconi, M., Manoharan, V., Nikkhah, M., Hjortnaes, J., Cristino, A.L., Barabaschi, G., Demarchi, D., Dokmeci, M.R., Yang, Y. and Khademhosseini, A., 2014. Hydrogel bioprinted microchannel networks for vascularization of tissue engineering constructs. *Lab on a Chip*, 14(13), pp. 2202–2211. https://doi.org/10.1039/C4LC00030G.

Billiet, T., Gevaert, E., De Schryver, T., Cornelissen, M. and Dubruel, P., 2014. The 3D printing of gelatin methacrylamide cell-laden tissue-engineered constructs with high cell viability. *Biomaterials*, 35(1), pp. 49–62. https://doi.org/10.1016/j.biomaterials.2013.09.078.

Bryant, S.J., Nuttelman, C.R. and Anseth, K.S., 2000. Cytocompatibility of UV and visible light photoinitiating systems on cultured NIH/3T3 fibroblasts in vitro. *Journal of Biomaterials Science: Polymer Edition*, 11(5), pp. 439–457. https://doi.org/10.1163/156856200743805.

Hoch, E., 2014. *Hydrogelsysteme auf Basis UV-polymerisierbarer Biopolymere für den Aufbau von Gewebemimetika mittels Inkjet-Bioprinting am Beispiel von hyalinem Knorpel*. Doctoral dissertation. Universität Stuttgart. http://dx.doi.org/10.18419/opus-2331.

Hoch, E., Hirth, T., Tovar, G.E.M. and Borchers, K., 2013. Chemical tailoring of gelatin to adjust its chemical and physical properties for functional bioprinting. *Journal of Materials Chemistry B*, 41(1), pp. 5675–5685. https://doi.org/10.1039/C3TB20745E.

Jia, W., Gungor-Ozkerim, P.S., Zhang, Y.S., Yue, K., Zhu, K., Liu, W., Pi, Q., Byambaa, B., Dokmeci, M.R., Shin, S.R. and Khademhosseini, A., 2016. Direct 3D bioprinting of perfusable vascular constructs using a blend bioink. *Biomaterials*, 106(November), pp. 58–68. https://doi.org/10.1016/j.biomaterials.2016.07.038.

Kolesky, D.B., Homan, K.A., Skylar-Scott, M.A. and Lewis, J.A., 2016. Three-dimensional bioprinting of thick vascularized tissues. *Proceedings of the National Academy of Sciences of the United States of America*, 113(12), pp. 3179–3184. https://doi.org/10.1073/pnas.1521342113.

Lee, V.K., Kim, D.Y., Ngo, H., Lee, Y., Seo, L., Yoo, S.-S., Vincent, P.A. and Dai, G., 2014. Creating perfused functional vascular channels using 3D bio-printing technology. *Biomaterials*, 35(28), pp. 8092–8102. https://doi.org/10.1016/j.biomaterials.2014.05.083.

Murphy, S.V., Skardal, A. and Atala, A., 2013. Evaluation of hydrogels for bio-printing applications. *Journal of Biomedical Materials Research: Part A*, 101A, pp. 272–284. https://doi.org/10.1002/jbm.a.34326.

Nichol, J.W., Koshy, S.T., Bae, H., Hwang, C.M., Yamanlar, S. and Khademhosseini, A., 2010. Cell-laden microengineered gelatin methacrylate hydrogels. *Biomaterials*, 31(21), pp. 5536–5544. https://doi.org/10.1016/j.biomaterials.2010.03.064.

Pepelanova, I., Kruppa, K., Scheper, T. and Lavrentieva, A., 2018. Gelatin-methacryloyl (GelMA) hydrogels with defined degree of functionalization as a versatile toolkit for 3D cell culture and extrusion bioprinting. *Bioengineering*, 5(3): 55. https://doi.org/10.3390/bioengineering5030055.

Therriault, D., Shepherd, R.F., White, S.R. and Lewis, J.A., 2005. Fugitive inks for direct-write assembly of three-dimensional microvascular networks. *Advanced Materials*, 17(4), pp. 395–399. https://doi.org/10.1002/adma.200400481.

Yue, K., Trujillo-de Santiago, G., Alvarez, M.M., Tamayol, A., Annabi, N. and Khademhosseini, A., 2015. Synthesis, properties, and biomedical applications of gelatin methacryloyl (GelMA) hydrogels. *Biomaterials*, 73(December), pp. 254–271. https://doi.org/10.1016/j.biomaterials.2015.08.045.

Optimisation of Aerosol Jet Deposition for High-Resolution Selective Patterning of Silver Tracks

Ben Clifford, Chris Phillips and Davide Deganello

Welsh Centre for Printing and Coating, College of Engineering, Swansea University, Fabian Way, Swansea, SA1 8EN, UK
E-mails: b.r.clifford@swansea.ac.uk; c.o.phillips@swansea.ac.uk; d.deganello@swansea.ac.uk

Short abstract

Aerosol jet deposition is a digital direct-write additive manufacturing technique capable of producing high resolution and highly customisable electronic and biological functional devices on both two- and three-dimensional substrates. This technology offers important market opportunities in the production of consumer electronics, semiconductor packaging, display technology, aerospace and defence, automotive and life sciences. However, for these opportunities to be realised there is a necessity for greater understanding of how deposition process parameters influence deposition quality. This study has explored the effects of a number of these parameters and their influence on the geometry of printed features. The results of this work outline the operating windows for several deposition parameters including carrier gas flow rate, stage speed working distance and stage temperature. Additionally, a number of relationships have been identified linking deposition parameters to the geometry of printed features.

Keywords: aerosol jet deposition, parameter optimisation, printed electronics, high resolution

1. Introduction and background

Aerosol jet deposition is a direct-write non-contact deposition process suited to the deposition of a wide range of functional materials including metals, polymers and biologicals (Zöllmer, et al., 2006). The compatibility of the technique with such a wide range of materials has seen the development of an assortment of novel applications in key research areas including printed sensors (Clifford, et al., 2018), renewable energy (Mette, et al., 2007) and biological/medical (Marquez, Renn and Miller, 2001).

Whilst the number of publications relating to aerosol jet deposition is increasing year on year, the majority of these are focussed on new applications of the technology and there is a lack of published research and understanding relating to the science and theory behind the process. This limited understanding in the field has resulted in several publications highlighting the need for full and accurate process modelling and optimisation (Hon, Li and Hutchings, 2008; Zhang, Liu and Whalley, 2009).

The aerosol jet deposition process works by atomising, either ultrasonically or pneumatically, a solution or suspension containing a functional material suited to the desired application. Micron sized droplets become separated from the bulk material and become entrained in a carrier gas stream which transports them to a deposition head. This droplet loaded gas stream is then aerodynamically focussed by a secondary gas stream, referred to as the sheath gas, through a converging nozzle forming a collimated beam. The substrate is positioned several millimetres below the nozzle on a motion controlled heated stage, and patterning is achieved by the relative movement of the substrate and deposition head (Clifford, et al., 2018; Hoey, et al., 2012). A photograph of the aerosol jet deposition system at Swansea University with an illustrative diagram of the aerosol jet process is shown in Figure 1 (Clifford, 2017).

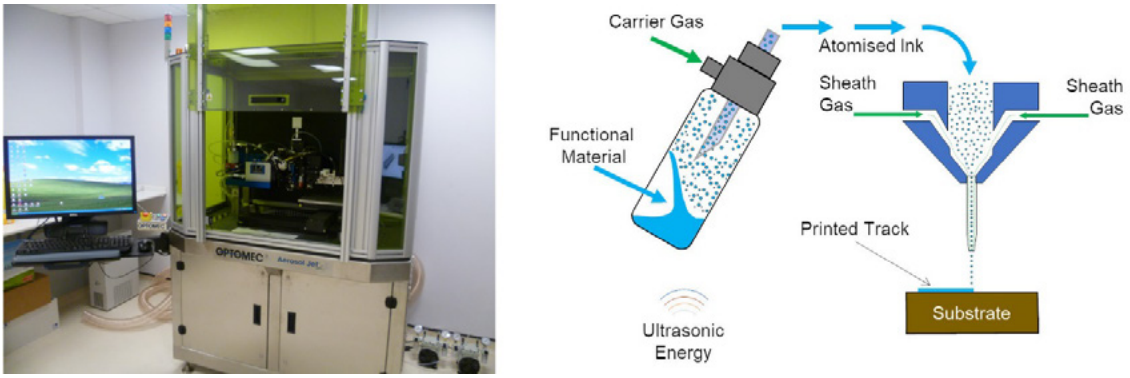

Figure 1: Left: a photograph of the AJ300 aerosol jet deposition system at Swansea University; right: an illustrative diagram showing the aerosol jet deposition process

Process optimisation is complex with a large number of both primary and secondary parameters which can be varied to change the resolution and profile of depositions. On top of this, getting qualitative data from optical measurements of unoptimised prints is often complicated by poorly defined edges and unwanted deposition phenomena including overspray and satellite droplets.

In this paper we present a study of the effects of several of these process parameters, namely; atomiser gas flow rate, working distance, stage speed and stage temperature on the geometry of printed silver lines. The findings of this work can be used to identify the operating window of individual parameters as well to outline those that are critical to achieving high-resolution features as well as secondary and complementary parameters.

2. Materials and methods

2.1 Ink

All printing during the process study was carried out using a commercial nanoparticle silver ink TPS 35 HE (Clariant Produkte (Deutschland) GmbH). This ink is designed to be used for inkjet printing and is quoted as having a dynamic viscosity of 6.5 mPa·s at 20 °C and a surface tension of 28.2 mN/m. The solids loading of this ink is approximately a mass fraction of 35 % with an average particle size of approximately 60 nm. The solvent in which the particles are dispersed is a blend of water and ethylene glycol. In order to make this ink compatible with the ultrasonic atomiser of the aerosol jet system, it was diluted with deionised water at a ratio of 1:2 parts by volume.

2.2 Substrate

Standard glass microscope slides (12383118, Fisher Scientific) of length and width of 76 mm and 26 mm with a thickness between 1 mm and 1.2 mm were used as the test substrate. Glass microscope slides were chosen for their low roughness, transparency and consistency between batches. The low roughness provided a clean base for surface topology and profile measurements whilst the transparency allowed backlit illumination to be used in the detection of overspray. The average surface roughness, S_a, and the root mean square (RMS) surface roughness, S_q, of these microscope slides was measured using white light interferometry to be 9.18 nm and 12.73 nm respectively.

Prior to deposition, the glass slides were prepared by ultrasonic cleaning in acetone, propan-2-ol and deionised water for 10 minutes in each. Following the cleaning process the glass slides were dried at 200 °C

on a hot plate for 30 minutes before they were transferred to the system for printing. The deposited ink showed good levels of wetting with the cleaned glass slides and hence no additional surface pre-treatment/modification was required.

2.3 Printing methodology

Deposition was performed with an AJ300 aerosol jet deposition system (Optomec Inc., Albuquerque, USA) using an ultrasonic atomiser operating at 2.4 MHz. For all experiments a number of parameters including the nozzle, atomiser power and ink temperature were kept constant. The nozzle used had a 200 μm diameter opening with a taper half angle of a few degrees. The atomiser power was set to ≈ 31 W by applying a voltage of 48 V and a current of ≈ 650 mA. For each print run, the atomiser vial was loaded with 1.80 ml of the diluted ink described above and maintained at 20 °C by means of a temperature-controlled water bath. Two designs were selected as test patterns to allow geometric characterisation in terms of line width and height whilst providing the ability to identify the effects of varying these parameters on overspray and satellite deposition. The first toolpath consisted of six parallel horizontal lines each positioned 1 mm apart; three lines of 10 mm in length and three lines of 20 mm in length to allow testing at high (≥ 10mm/s) process velocities whilst ignoring any initial acceleration. The second design was a smaller serpentine pattern of length 8 mm and pitch of 0.5 mm used to create prints which could be optically imaged in a single scan.

Following deposition, samples were dried in a natural convection oven (UNB400, Memmert GmbH) at 200 °C for 60 minutes and stored in sealed Petri dishes prior to measurement and analysis.

Prior to performing the experiments described, a literature survey and initial screening trial was performed to identify suitable parameters and the operating ranges for each. This revealed a number of parameters that have a significant impact on deposition quality. The work presented here shows the results of adjusting these key parameters and full results including secondary parameters can be seen in the thesis titled “Optimisation of Aerosol Jet Deposition for the Development of Printed Electronics” (Clifford, 2017).

The parameters studied in this work are shown in Table 1 along with the ranges used for testing. For each parameter investigated three prints were produced, with 30 measurements made across each sample (5 equidistant points on each line) giving a total of 150 data points per variation.

Table 1: A table showing the parameters tested during this work with a brief description of what they affect with the range of values that were tested

Parameter	**Description**	**Range tested**
Carrier gas flow rate	Controls the quantity of material delivered to the deposition head.	12–24 cm^3/min
Stage speed	The speed the stage (and substrate) moves relative to the fixed deposition head and nozzle.	1–10 mm/s
Nozzle stand-off	The distance material travels between exiting the nozzle and impacting with the substrate.	2–11 mm
Stage temperature	The temperature of the stage that the substrate is positioned on during printing.	25–100 °C

The carrier gas flow rate determines the quantity of atomised material that is transferred to the deposition head and one of two parameters affecting the volume of material deposited in one location on the substrate. The stage speed is the second of these parameters and shares a positive relationship and controls the process velocity of the stage, and substrate, relative to the deposition head. The carrier gas flow rate and stage speed have a positive relationship meaning as the atomiser flow rate is increased the stage speed

must also be increased to produce the same geometry features. As material exits the nozzle has a highly collimated stream the sheath gas immediately begins to diverge giving the stream a limited focussing length. The nozzle stand-off is the distance between the nozzle exit and the substrate whereby the material stream needs to remain focussed. The stage temperature affects the drying rate of the deposited material and as such the final geometry of printed features.

2.4 Surface topography measurement

Optical images of deposited features were gathered using an Alicona G5 infinite focus microscope (Alicona Imaging GmbH,) in order to visually explore deposition quality. As well as visualisation of the deposits, this provided a method to qualitatively assess the deposited features in terms of unwanted features such as overspray and satellite deposition.
White light interferometry (NT9300, Veeco Instruments, Inc., Plainview, NY, USA) was used to obtain surface topography data for each printed line. Measurements were collected at eleven times magnification (achieved using a twenty times magnification lens with a 0.55 times field of view modifier), giving a measurement area of 0.58 mm by 0.43 mm at a resolution of 640 × 480 pixels. For each print, the geometry was measured at ten discreet points along the length of the line. Measurements were taken of the line width and average height (taken as the average height of the substrate subtracted from the average height of the ink) as well as reviewing the profile shape.

3. Results and discussion

3.1 Carrier gas

The carrier gas flow rate is one of two primary parameters affecting the volume of material deposited in one location - the other being the stage speed. In order to investigate the effect of the carrier gas flow rate on the geometry of printed features, deposition was performed at a range of carrier gas flow rates between 12 cm^3/min and 24 cm^3/min whilst maintaining a constant sheath gas flow rate of 90 cm^3/min. Additionally, the stage speed was maintained at a constant value of 1 mm/s with a stage temperature of 100 °C.

The measured line width and average line height data is plotted graphically in Figures 2a and 2b separately. The data shows that as the carrier gas flow rate increases both the width and height of deposited line also increases. Initially, for carrier gas flow rates between 12 cm^3/min and 18 cm^3/min the line width shows a linear trend with low standard deviations but as the flow rate increases further the line width and standard deviation increase rapidly diverging from the trend. This sudden increase is linked to the stage speed being too low allowing large quantities of material to build up in one location. This can be seen visually in the optical microscope images shown in Figures 3a-3d taken of lines deposited at carrier gas flow rates of 12, 16, 20 and 24 cm^3/min respectively.

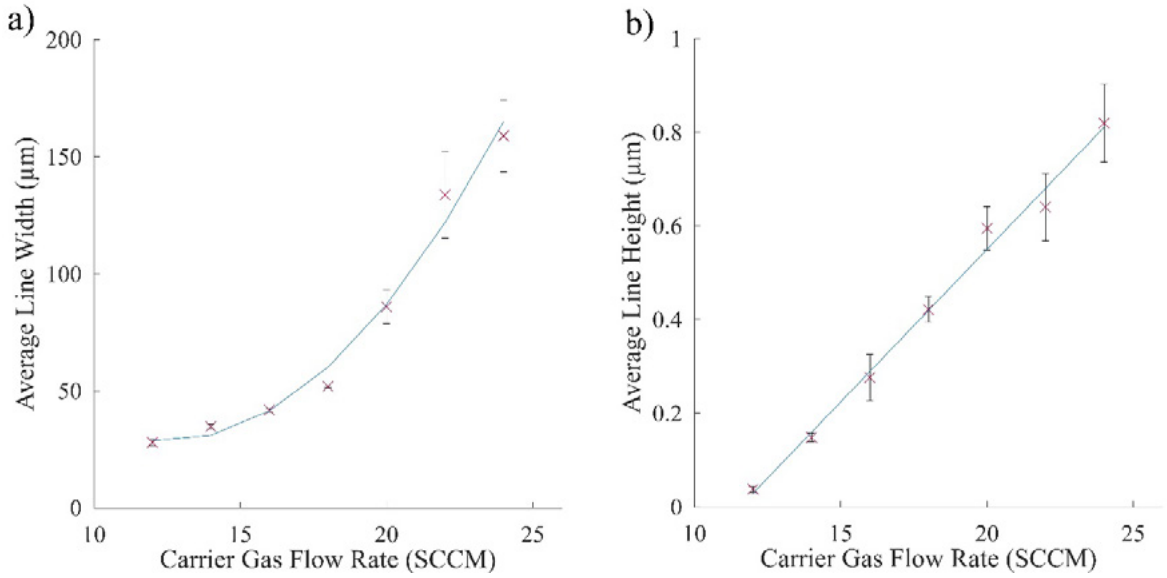

Figure 2: Graphs showing the effect of carrier gas flow rate on (a) Average line width, and, (b) Average line height

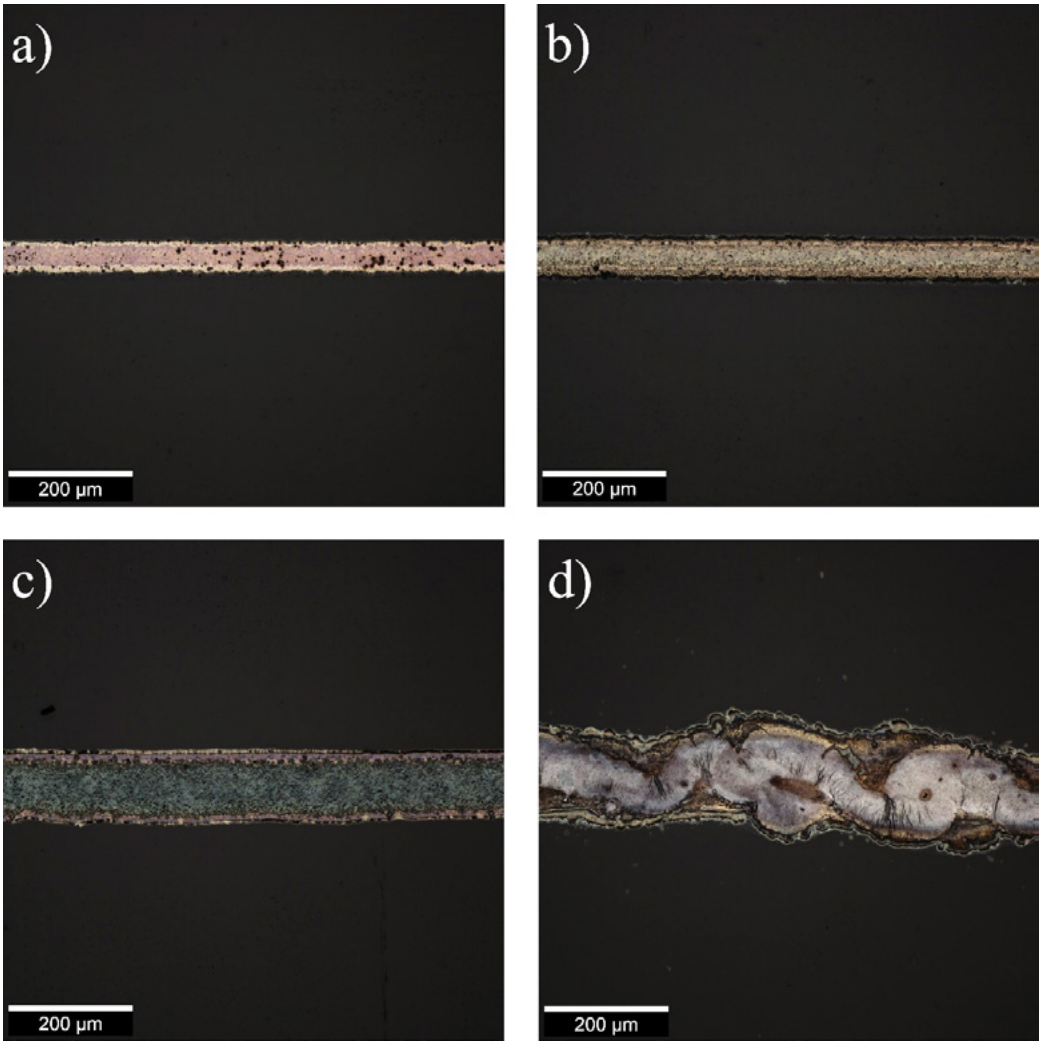

Figure 3: Optical microscope images showing the effect of carrier gas flow rate on deposited line geometry using a constant sheath gas flow rate of 90 cm^3/min; (a) Carrier gas flow rate of 12 cm^3/min, (b) Carrier gas flow rate of 16 cm^3/min, (c) Carrier gas flow rate of 20 cm^3/min, and, (d) Carrier gas flow rate 24 cm^3/min; Scale bar for reference is 200 µm

3.2 Stage speed

The stage speed is the second parameter affecting the volume of material deposited in one location. In order to investigate the effect of stage speed on the geometry of printed features, deposition was performed at stage speeds between 1 mm/s and 10 mm/s. During the experiment, the sheath and carrier gas flow rates were kept constant at 112 cm^3/min and 16 cm^3/min respectively. The stage temperature was maintained at a constant value of 100 °C.

The average line width and line height data is plotted graphically in Figures 4a and 4b separately. From these graphs it can be seen that as the stage speed increases there is a decrease in both line width and line height as less material is deposited in each area. The line width and height decrease steadily as stage speed increases from 1 mm/s to 3 mm/s. After this point, the sensitivity of the deposit to stage speed is reduced. The rate of decrease in line width and height is higher at low speed transitions due to the larger printed length for the given carrier gas flow rate. As an example, with the sheath and carrier gas flow rates measured, an increase in stage speed from 1 mm/s to 2 mm/s causes a decrease in line width of 11.22 µm. In contrast at the same flow rates, an increase in stage speed from 6 mm/s to 7 mm/s causes a much smaller drop in line width – 1.29 µm. This highlights the relationship between the carrier gas flow rate and the stage speed previously discussed.

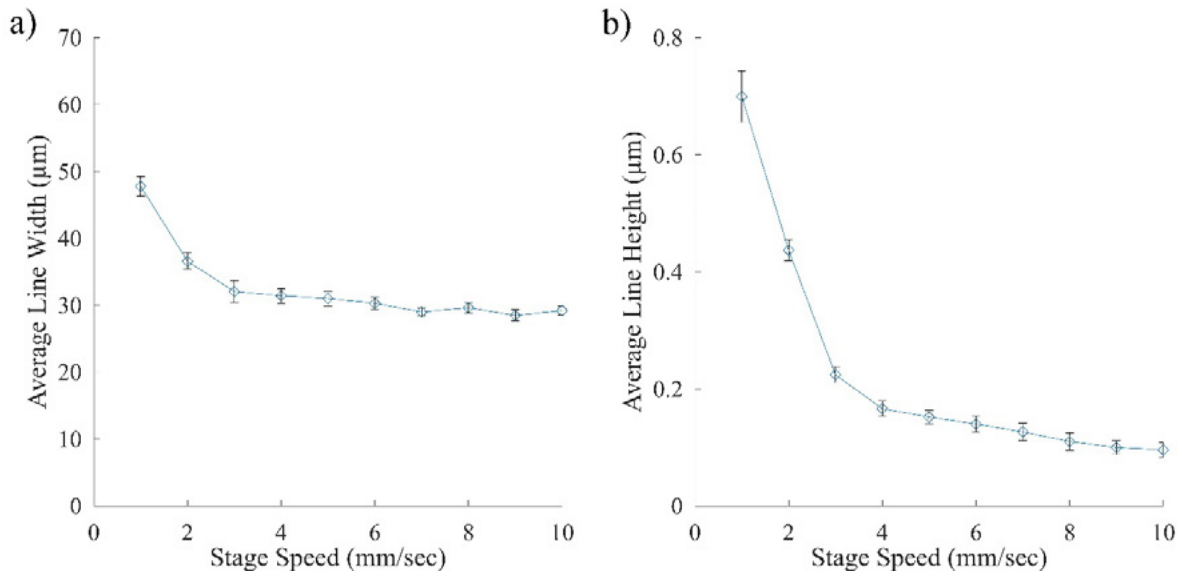

Figure 4: Graphs showing the effect of stage speed on (a) Average line width, and, (b) Average line height

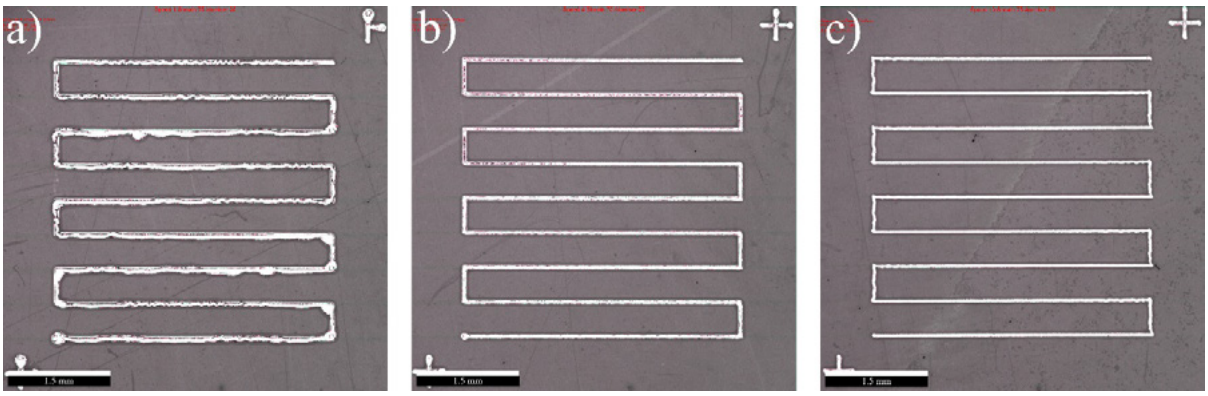

Figure 5: Optical microscope images showing the effect of stage speed on deposited line geometry; (a) Stage Speed of 1 mm/s, (b) 4 mm/s, and (c) 10 mm/s; scale bar for reference is 1.5 mm

3.3 Nozzle stand off

As a result of the nozzle profile and annular sheath gas flow, the material exits the nozzle as a highly collimated converging beam which becomes finest at a focal point before rapidly diverging. In order to investigate the effect of working distance on the geometry of printed features, deposition was performed with the nozzle positioned between 2 mm and 11 mm above the substrate. During the experiment, both the carrier and sheath gas flow rates were kept constant at 20 cm^3/min and 100 cm^3/min respectively. The stage speed was set to 2 mm/s with the temperature at 100 °C.

At each working distance, measurements of line width and height were taken using white light interferometry as well as imaged using optical microscopy. For each printed line multiple measurements were performed using white light interferometry, and the results are presented graphically in Figure 6. Due to the poor quality and large amounts of overspray and satellite deposition seen in the lines deposited at working distances greater than 9 mm it was not possible to obtain line width and line height measurements.

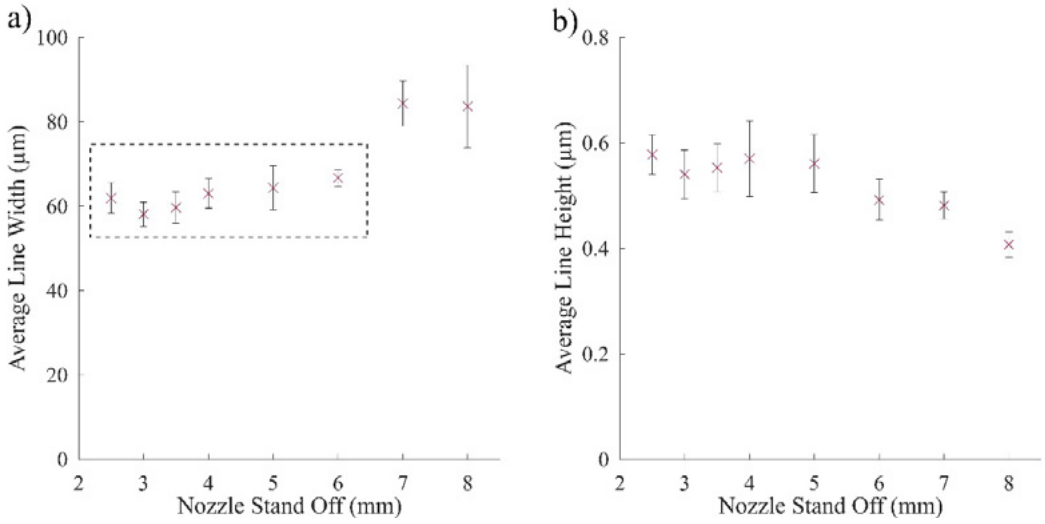

Figure 6: Graphs showing the effect of stage speed on (a) Average line width, and (b) Average line height

Figure 7 shows microscope images of a low-density serpentine pattern deposited at stand-off distances of 3 mm, 7 mm and 11 mm. The line deposited at a working distance of 3 mm has well defined edges with no visible overspray, the line deposited at a working distance of 7 mm has some observable waviness at the edges with small amounts of overspray. In contrast the line deposited at a working distance of 11 mm has poorly-defined edges with large amounts of overspray obscuring the printed pattern.

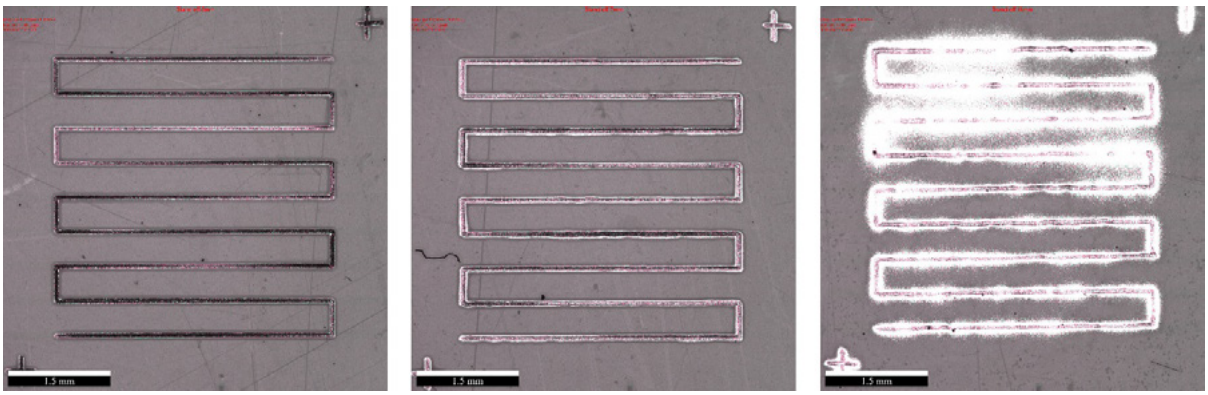

Figure 7: Optical microscope images showing the effect of nozzle stand off on deposited line geometry; left: Deposited line with a nozzle stand-off of 3 mm, centre: Deposited line with a nozzle stand-off of 7 mm, right: Deposited line with a nozzle stand-off of 11 mm; Scale bar for reference is 1.5 mm

3.4 Stage temperature

During deposition the substrate is positioned on a heated stage to aid in the drying of the ink. In order to investigate this parameter, the carrier and sheath gas flow rates were kept constant at 18 cm^3/min and 72 cm^3/min respectively with the stage speed set to 3 mm/s. The stage temperature was varied between 25 °C and 100 °C in increments of 25 °C with the purpose of investigating its effect on the deposited line geometry.

For each printed line multiple measurements were performed using white light interferometry, and the results are presented graphically in Figure 8.

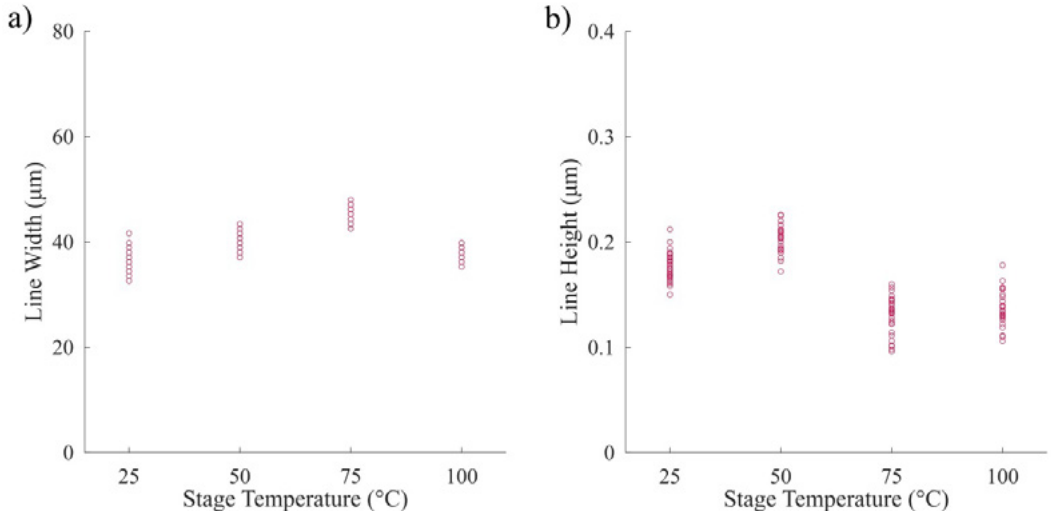

Figure 8: Graphs showing the effect of stage temperature on (a) Average line width, and (b) Average line height

Figure 8 shows the effect of increasing stage temperature on line geometry. For stage temperatures below 100 °C, as the temperature increases the width of line also increases. In contrast, at a stage temperature of 100 °C a decrease in the line width is observed. Additionally, as the stage temperature increases the standard deviation in the average line width decreases from 1.99 at 25 °C to 1.32 at 100 °C. Since the ink contains approximately a volume fraction of 84 % water which has a boiling point of around 100 °C, a large percentage of the water content is readily evaporated upon impact with the substrate. This could explain the decreased average line width at a stage temperature of 100 °C but further investigation is required involving inks containing different boiling point solvents. This explanation is also supported by examining the profiles of deposited lines at each stage temperature as shown in Figure 9.

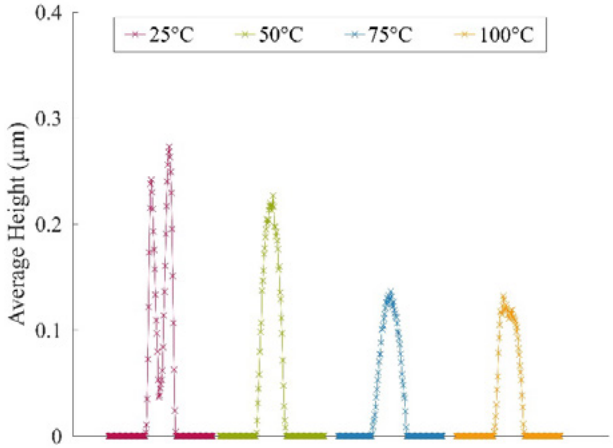

Figure 9: A graph showing the effect of stage temperature on the profile shape of deposited lines

By studying the visualisation in Figure 9, significant differences can be seen between the line profiles as a result of different stage temperatures. At 25 °C the profile shows two distinct peaks with a central void often described in printing terminology as coffee-stain effect. As the stage temperature increases the height of the line profile reduces and the profile becomes more rectangular at 100 °C.

4. Conclusions

From this study, the stage temperature and nozzle stand-off have been identified as critical parameters to obtaining high resolution defect free deposition. The stage temperature has been shown to have a significant effect on the geometry and resolution of printed features which has been theorised to be as a result of the formulation of the ink being tested. A relationship has been identified between the nozzle stand-off and unwanted deposition phenomena such as overspray and satellite droplets affecting overall resolution.

The effects of varying the carrier gas flow rate and stage speed have been shown to be linked to one another and whilst they do affect the geometry of deposited features, they do not directly affect resolution within their normal operating ranges. It is also possible to adjust these parameters in parallel to allow for thicker deposits with larger volumes of material or to maintain thinner deposits but reduce overall print time.

The optimisation of the parameters discussed has allowed for deposition of high resolution printed features as shown in Figures 10 and 11. The deposited features have an average line width of around 10 μm with low amounts of overspray and satellite deposition with other lines shown with line widths of 30, 40 and 50 μm.

Figure 10: A microscope image showing a number of example features using aerosol jet deposition; Scale bar for reference is 2 mm

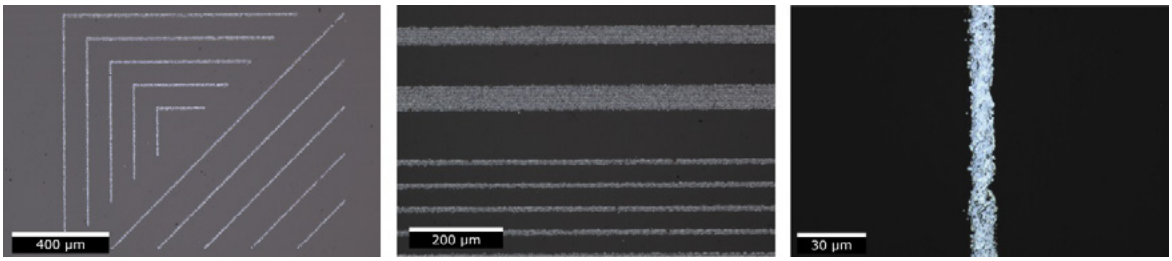

Figure 11: Microscope images showing close up images of the features in Figure 10; Scale bars for reference from left to right are 400 μm, 200 μm and 30 μm respectively

Whilst a significant number of parameters have been evaluated in this work, there are still parameters which have not been reviewed as well as other relationships that may be exist with relation to print design and material formulation.

Acknowledgements

This work was financially supported by the College of Engineering at Swansea University. The authors would also like to acknowledge the Centre for NanoHealth (CNH) at Swansea University for access to facilities and equipment.

References

Clifford, B., 2017. *Optimisation of aerosol jet deposition for the development of printed electronics.* Ph.D. thesis. Swansea University.

Clifford, B., Beynon, D., Phillips, C. and Deganello, D., 2018. Printed-sensor-on-chip devices – aerosol jet deposition of thin film relative humidity sensors onto packaged integrated circuits. *Sensors and Actuators B: Chemical,* 255(February, Part 1), pp. 1031–1038. https://doi.org/10.1016/j.snb.2017.08.086.

Hoey, J.M., Lutfurakhmanov, A., Schulz, D.L. and Akhatov, I.S., 2012. A Review on aerosol-based direct-write and its applications for microelectronics. *Journal of Nanotechnology,* 2012: 324380. http://dx.doi.org/10.1155/2012/324380.

Hon, K.K.B., Li, L. and Hutchings, I.M., 2008. Direct writing technology - advances and developments. *CIRP Annals - Manufacturing Technology,* 57(2), pp. 601–620. https://doi.org/10.1016/j.cirp.2008.09.006.

Marquez, G.J., Renn, M.J. and Miller, W.D., 2001. Aerosol-based direct-write of biological materials for biomedical applications. In: *Materials Research Society Research Proceedings,* 698. Boston, MA, USA, 26–29 November 2001. New York: Materials Research Society, pp. 343–350.

Mette, A., Richter, P.L., Hörteis, M. and Glunz, S.W., 2007. Metal aerosol jet printing for solar cell metallization. *Progress in Photovoltaics,* 15(7), pp. 621–627. https://doi.org/10.1002/pip.759.

Zhang, Y., Liu, C. and Whalley, D.C., 2009. Direct-write techniques for maskless production of microelectronics: a review of current state-of-the-art technologies. In: *International Conference on Electronic Packaging Technology & High Density Packaging ICEPT-HDP*. Beijing, China, 10–13 August 2009. Piscataway, NJ, USA: IEEE.

Zöllmer, V., Müller, M., Renn, M., Busse, M., Wirth, I., Godlinski, D. and Kardos, M., 2006. Printing with aerosols: a maskless deposition technique allows high definition printing of a variety of functional materials. *European Coatings Journal,* 2006(7–8). pp. 46–50.

Soy Protein Fluid Inks for Packaging

Alexandra Pekarovicova, Dipesh Sonar, Rahul Pingale, Bilge N. Altay, Veronika Husovska and Paul D. Fleming

Center for Coating and Printing Research, Western Michigan University, Kalamazoo, MI
E-mails: a.pekarovicova@wmich.edu; dipeshravindra.sonar@wmich.edu

Short abstract

Solvent based fluid printing inks use volatile solvents in the formulation, which are hazardous to the environment from emission of volatile organic components (VOC's) point of view. Water-based fluid inks are well established, but synthetic resins in them are not biodegradable. Thus, more environmentally friendly water based inks need to be manufactured. Currently, water based inks contain acrylic polymers made of petroleum. Industry experiences a shortage of acrylics, because they are used in many industrial sectors, not only the ink industry. This problem and particularly the fluctuating and rising price of petroleum are main reasons behind looking for new resources for making more environmentally friendly printing inks, especially for food packaging. Soybean protein is a potential renewable raw material and was used for replacement of acrylic resins in water-based inks. The focus was on formulating inks for linerboards, because linerboard is a substrate printed with 100 % water-based ink formulations, and the linerboard packaging sector is growing rapidly. In this research, inks with partially replaced acrylic resins in the let-down portion of the ink with soy protein were successfully formulated. Various amounts (0–100 %) of soy protein varnish was added to fully acrylic pigment dispersion to formulate water based inks. Formulated inks had very similar solids content. Rheology measured as a function of the shear rate showed shear thinning for both acrylic and soy/acrylic inks. Static surface tension measurements showed similar values for fully acrylic and soy/acrylic inks falling below 30 mN/m. Soy and acrylic vehicle inks performed comparably in selected end use properties, such as rub resistance, tape adhesion test or water resistivity. The ΔE_{CMC} ($CMC_{2:1}$) for all soy formulations were less than 1.5, when the fully acrylic formulation was used as a standard. It was found that mixed acrylic/soy protein inks had similar end use properties as fully acrylic based water based inks.

Keywords: liquid ink, water-based, soy protein, formulation, food packaging

1. Introduction and background

Generally, inks are comprised of main components, such as pigments to add color, resins or polymers to disperse the pigment, and carry the ink to the substrate and anchor it there. Usually, resins or polymers have to be dissolved in the solvent. Depending on the type of the solvent, inks may be solvent based or water based. Solvents may or may not be present in the ink formulation, which depends on the nature of the polymers used (Hutchinson, 2002). Examples of inks that do not contain the solvent are the UV or UV-LED-curable inks. Here the function of the solvent is taken on by the monomer, having low viscosity and is able to dissolve the oligomer. Thus, UV- or LED-UV curable ink may contain monomers or oligomers, which are composed of monomer chains, but are able to further polymerize to create the polymer, thus the cured ink. Pigments, resins and/or polymers, and solvents are so-called main components of the ink. To enhance or modify the final ink properties, additives may be added to the ink formulation. There are some additives, such as waxes, that may be found in many different types of inks. They modify slip, thus coefficient of friction of the ink. On the other hand, depending on the nature of the ink, specific additives may be used. An example may be defoamer, which will be used only in water-based ink formulation, while metal driers added into offset litho inks aid drying by the oxidation polymerization mechanism. Many surfactants are employed as dispersion aid additives in the process of pigment dispersion manufacture. The

common formulation rule is that additives are included in ink formulations in amounts not exceeding 5 %. Functional inks may benefit from addition of certain additives, such as dispersants, while dispersing and printing. There are numerous applications of inks, and each need special consideration at the time of formulation, which leads to successful printing and end-use properties of ink.

Water-based inks contain two different types of resins, solution and emulsion resins (Wyatt, 1999). Solution resins may be dissolved in alkaline water-based environment, to create a true solution. Solution polymers are used in ink formulations to grind and disperse pigments. Their degree of polymerization is around 15 000. Because they have short chains, they are suitable for vigorous shaking and mixing, which happens during the pigment dispersion process. Solution resins enhance the ability of water to wet the pigment particles. They are responsible for ink resolubility on the press, and color stability of the printed ink (Pekarovicova and Husovska, 2016).

Emulsion polymers are a second class of polymers, necessary for water-based ink formulations (Wyatt, 1999). Emulsion polymers have a degree of polymerization around 150 000 to 200 000. They are long-chain polymers, necessary for the development of ink film forming properties. They are added at the end of the ink formulation process, as a let-down vehicle. Because of their emulsion state, they are not suitable for vigorous mixing during pigment dispersion. Emulsion resins do not wet pigments, but exhibit excellent ink drying properties. Emulsion resins form an emulsion, meaning that they cannot be completely dissolved in water. They are responsible for viscosity stability on the press and are able to maintain a relatively stable viscosity under high shear conditions. Depending on their chemical make-up, emulsion polymers impart ink hardness or flexibility after drying, water resistance, and gloss. Both types of resins, solution and emulsion resins, are necessary components of water-based ink formulations and must be present in ink formula (Wyatt, 1999; Pekarovicova and Husovska, 2016).

Both solution and emulsion acrylic resins are copolymerized from various monomers, bringing necessary properties to the final polymer (Table 1). Along with acrylic acid, monomers such as styrene, maleic acid, methacrylates, butadiene, and alpha olefins (Figure 1) are employed in the formulation of water-based inks (Wyatt, 1999). Each of the monomers is responsible for the development of specific ink properties (Table 1). Methyl methacrylates add water resistance to the final ink formulations, while acrylates are responsible for ink flexibility. Therefore, it is always beneficial to use several different chemistries in ink formulations, because each component imparts different properties to the final ink. Acrylic polymers are acidic in nature and need to be neutralized in order to keep them in the solution. Acrylic resins are formulated into vehicles with pH up to 9.0. Today's acrylic polymers are more tolerant to pH drop to neutral. The ammonium ion is the most common base, along with the sodium ion and amines, which are not as volatile, and give better pH stability on the press, and resolubility property to the ink (Zhang, et al., 2007).

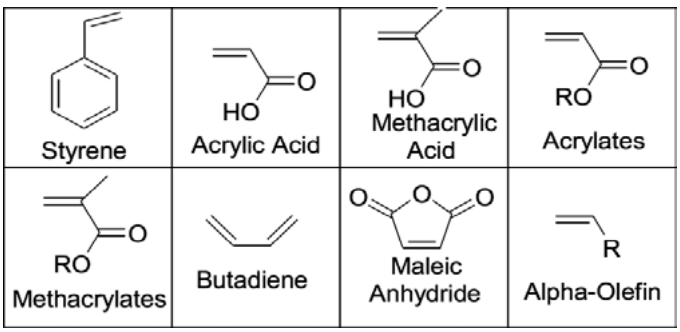

Figure 1: Building blocks of acrylic polymers used in water-based inks

The future calls for biodegradable thermoplastic polymers made from materials such as starch and sugar cane instead of petrochemicals. Mater-Bi polymers (Novamont, 2018) consist of starch, cellulose, and

vegetable oil-based biopolymers made by Novamont of Italy. Biopolymers are more expensive than polymers made from petrochemicals. Some biopolymers were blended with petrochemical polymers and the blends showed no loss of biodegradability (Pekarovicova and Pekarovic, 2008). Another promising option may be the soy protein. Previously, it was used to partially replace acrylic polymers in water-based inks (Khodabakhsh, 2013; Pekarovicova, Khodabakhsh and Fleming III, 2015; Patil, 2015; Pingale, 2018; Pingale, Pekarovicova and Fleming, 2019).

Table 1: Function of acrylic resins in water-based inks

Contributing Monomer	**Final Property**
Methyl methacrylate	Water resistance, block resistance, hardness, gloss retention, fast dry speed
Styrene	Water, block resistance, hardness, initial high gloss, poor gloss retention, fast dry speed
Short-chain acrylates and methacrylates (R < 8)	Flexibility, stain, rub resistance, adhesion
Acrylic and methacrylic acid	Adhesion, resolubility, hardness, solvent, and grease resistance
Long-chain acrylates and methacrylates (R > 10)	Water resistance, flexibility, adhesion

Soybean was introduced to the U.S. in 1765 and used for both food and industrial applications. The soybean is comprised of eight vital amino acids and it is known to be a good source of fiber, iron, calcium, zinc, and vitamins. It includes about 40 % protein and 20 % oil. Soybean oil is known as a vegetable, non-toxic oil that is widely used in cooking and food products, such as mayonnaise. It is available at a reasonable price, so it can be a good candidate for ink manufacture (Erhan and Bagby, 1995). Soybean oil mixed with resins, pigments and waxes was already used to formulate soy oil-based ink for cold-set litho newspaper printing (Erhan and Bagby, 1995). Worldwide, there are about ten thousand newspaper printers that use soy oil ink. However, not much attention was given to soy proteins in ink formulation so far. Soy contains three natural surfactants: soy protein, soy lecithin, and soy saponin. Soy proteins are obtained after the extraction of soybean oil.

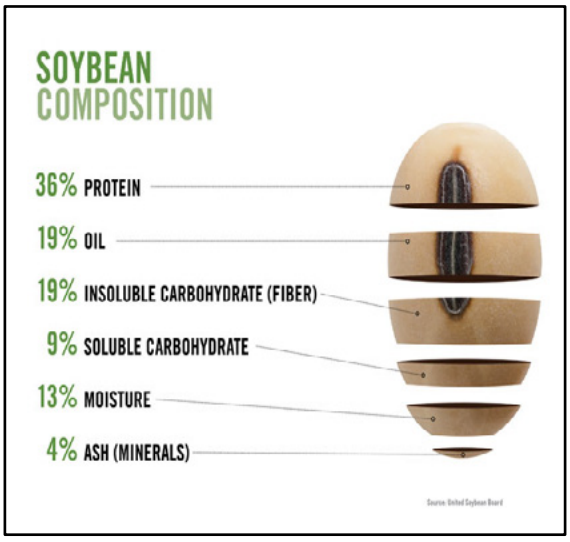

Figure 2: Soybean composition (Farm Progress, 2012)

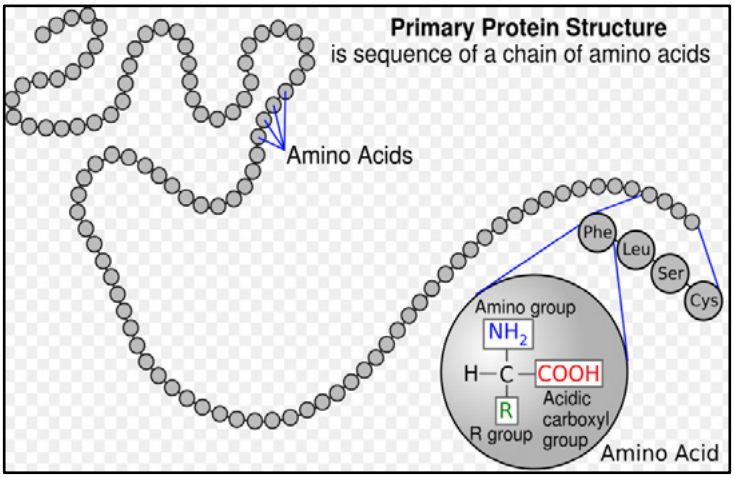

Figure 3: Schematic of soy protein structure (Renkema, 2001)

Soy proteins exist in three major forms: soy flours, soy protein concentrates and soy protein isolates. Proteins are built by condensation reaction of amino acid monomers and create peptide bonds. Water molecules are released as a result of a condensation reaction between amino acids (Figure 2) (Graham and Krinski, 1983). Soy protein has a complex 3-D shape and contains 19 different amino acids, which are held together in a coiled structure by peptide bonds. Proteins contain positive and negative functional groups. Amino, carboxyl, hydroxyl, phenyl and sulfhydryl groups are main building blocks of soy protein (Kinsella, 1979). Schematic of soy protein is illustrated in the Figure 3.

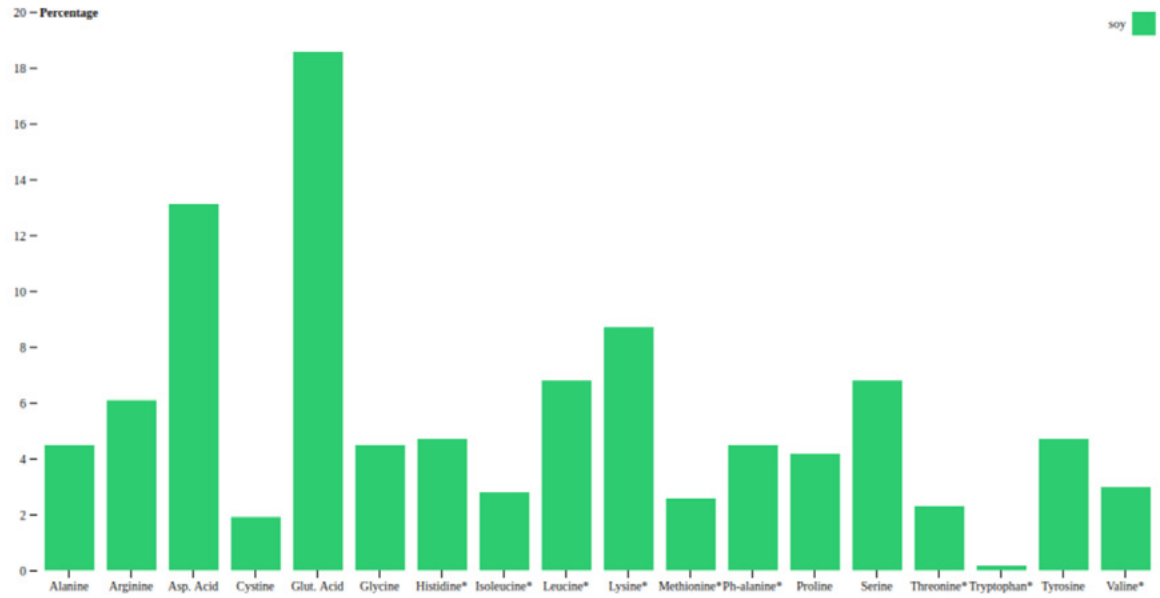

Figure 4: Profile of amino acids in soy protein (Rayaprolu, et al., 2015)

The profile of essential amino acids in soy protein is illustrated in Figure 4, showing that glutamic acid (18. 6%), aspartic acid (13.1 %) and lysine (8.7 %) are its main constituents (Rayaprolu, et al., 2015). The basic application of industrial-grade soy protein is as a binder in paper coatings (Graham and Krinski, 1983). The other industries that use soy protein include adhesives, asphalts, resins, cleaning materials, cosmetics, inks, paints, plastics, polyesters and textile fibers (Smith, 1996). However, their use in the printing industry is at its beginnings. There is not known a commercial production of water-based inks based on soy protein and therefore, it was the topic of this work. Thus, the aim was to determine which soy pro-

tein available on the market can be used to replace acrylic resins to grind pigments and which may serve as film forming and strengthening component of water-based inks. This project will help to achieve the formulation of a truly environmentally friendly and more biodegradable water-based ink, than those made with acrylic inks.

2. Materials and methods

The soy-based polymer used in this research was a chemically and thermo-mechanically processed soy protein designed to be a functional, consistent and cost saving binder for water-based ink. It was provided by Arro Protein Solutions Co., in powdered form. The vehicle was made from soy powder in hot water, adjusted to pH = 9–10.5 by 5 % volume fraction of ammonia water or amines. ProSoy 4575 was added under good agitation for 40 minutes at 60 °C. Out of 5 to 6 different formulations of soy resins, the two best resins were selected for ink formulation. Several different soy protein let-down vehicles were made. Different procedures were applied to make a better vehicle to obtain desired viscosity, and stability. The initial viscosity and pH were noted for every batch produced. It was observed that the soy resin that didn't contain isopropyl alcohol, dispersed better without forming any precipitate and viscosity and flow were also within the required range. When there was higher percentage of pigment dispersion used, viscosity was high and had to be cut down to by adding 5 % ammonia water. A Blue pigment dispersion (PB-15-44) was added (Clean blue, American Inks and Technology, Ltd.). At this point of ink formulation, several additives may be also added in small amounts (less than 5 %). Examples of additives to be used are defoamers or biocides. The mixing protocol for making inks 1–8 is given in Table 2. Besides soy-based inks, a conventional acrylic ink was made using the same pigment dispersion as used for soy polymers, but applying solely acrylic polymers. Fully acrylic ink water based ink was used as control for measurement of needed properties.

Rheology of ink samples was characterized using an AR 2000 dynamic stress rheometer equipped with conical concentric cylinder geometry (*TA Instrument: New Castle, DE*). The steady state flow test was conducted applying shear rates from 0.1 to 3 000 s^{-1} at room temperature. A 30 s pre-conditioning was performed for equilibration before the steady state flow tests. Static surface tension of inks was measured using an FTA 200 instrument according to Woodward (2019).

Inks were printed on a K-printing proofer, a laboratory gravure proofing press (Testing Machines Inc.: New Castle, DE). A printing plate with tone steps 5-100 % was used. The plate was electromechanically engraved with 45° compression angle and 150 LPI resolution. Some ink applications were also done with Meyer rod #11. A Byk chart was employed as a substrate (Byk Gardner, USA). After printing, print analysis was done such as CIELAB or rub resistance measurements were done. Printed strip 2 in × 7 in (~ 50 mm × 178 mm) was used for the test of rubbing printed sample on 4 lb (~ 1 814 g) weight block over nonprinted substrate. 60 strokes cycle was used. The grading was done from poor to excellent rub resistance on a scale of 0 to 5, respectively.

3. Results and discussion

Soy proteins were tested for their suitability to partially or fully replace acrylic emulsion resins in water-based gravure packaging inks. The focus was on formulating inks for linerboards, because linerboard is a substrate printed with 100 % water-based ink formulations, and the linerboard packaging sector is growing rapidly (Kishbaugh, 2018). The first step was formulating water-based ink based on fully acrylic solution and emulsion polymers as resins. Next, the let-down portion of the ink was formulated with soy polymers, adding them in increments 10-20-30 up to 100 % replacement of acrylic emulsion portion of fluid packaging ink or fully replacing acrylic emulsion polymer as shown in the Table 2.

Table 2: Inks formulated with acrylic pigment dispersion and soy vehicle in let-down portion of the ink (1–6), or acrylic emulsion resin (7–8); PB-15-44 is proprietary blue pigment dispersion

	Water-based inks formulation with ProSoy 7475 varnish							
Component	**1**	**2**	**3**	**4**	**5**	**6**	**7**	**8**
PB-15-44 Pigment dispersion	50	40	40	50	40	40	50	60
H20 (DI Water)	0	10	10	0	12	10	0	0
Varnish ProSoy 7475 (no IPA)	40	40	50	0	0	0	0	0
Varnish ProSoy 7475 (with IPA)	0	0	0	40	40	50	0	0
Acrylic emulsion resin	0	0	0	0	0	0	45	40
NH_4OH 5%	3	3	5	3	3	5	5	5
Defoamer (FC-613)	0	0	0	0	0	0	1	1
Isopropyl alcohol	5	5	5	5	5	5	0	0

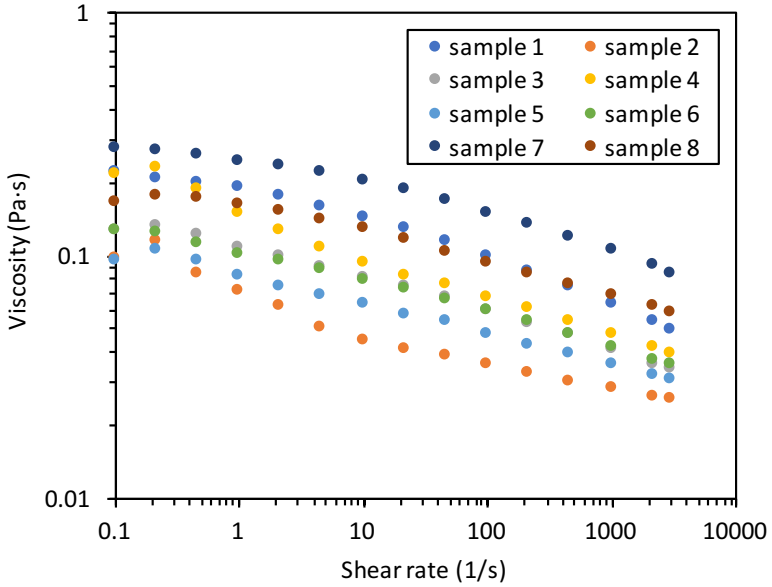

Figure 5: Acrylic and soy/acrylic inks viscosity as a function of shear rate; samples 1-6 are made with soy acrylic let-down vehicle, 7 and 8 are inks made with acrylic emulsion let-down vehicle

For easy application, printing ink should be shear thinning and show a decrease in viscosity upon increased shear rate (Mai, Pekarovicova and Fleming III, 2007). Both soy/acrylic inks 1–6 and acrylic ink 7–8 exhibited higher viscosity at low shear rates and decreasing viscosity at higher shear rates as shown in steady state flow curves in Figure 5. All ink samples displayed shear-thinning flow behavior. Shear-thinning could occur due to the pigment particles aligning in the direction of shear upon increased shear rates, causing less resistance to flow (Altay, et al., 2017). Also, inks with acrylic let-down vehicle had higher viscosity. All the ink samples were within the range of desired viscosity level gravure proofing press printing, which ranged from 0.1 Pa·s to 0.25 Pa·s.

Surface tensions of all inks were below 30 mN/m and there was minimal difference between different ink formulations (data not shown). Generally, most printing inks have surface tension around 25–40 mN/m, solvent based having closer to 25 mN/m, water based inks surface tension tends to be higher (Podhajny, 2003). However, inks subjected to dynamic conditions on the press show much higher values, e.g. ink with static surface tension of 25 mN/m can exhibit 40 mN/m dynamic surface tension on the press (Podhajny, 2003). Thus, dynamic surface tension measurement would be more appropriate method to determine ink surface tension than static (equilibrium) measurement.

End use properties of soy inks such as rub resistance, and adhesion were tested and compared to fully acrylic formulations. It was found that the soy polymer did not affect the final color of packaging ink in terms of CIELAB (Figure 6), and also when measured as ΔE_{CMC}, which was for all inks less than 1 (Figure 7). As shown in Figure 8, acrylic ink showed a rub resistance of 5, which means excellent rub resistance property as compared to 20 %, 40 % and 60 % increments of soy vehicle to acrylic ink. The 80 % and 100 % soy vehicle ink also exhibited excellent rub resistance similar to 100 % acrylic ink (Figure 8). There is no particular explanation for this, except it could be possible that soy and acrylic vehicle did not bond as strongly with one another as acrylic polymers alone or soy polymer alone could. Thus, lower compatibility between the acrylic and soy polymer may occur at certain blending rates.

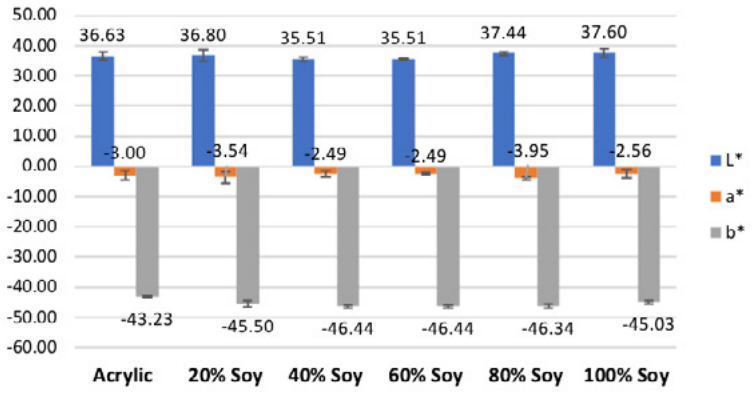

Figure 6: CIELAB (Acrylic ink Vs Increments of ProSoy 7475) measured on 100 % tone

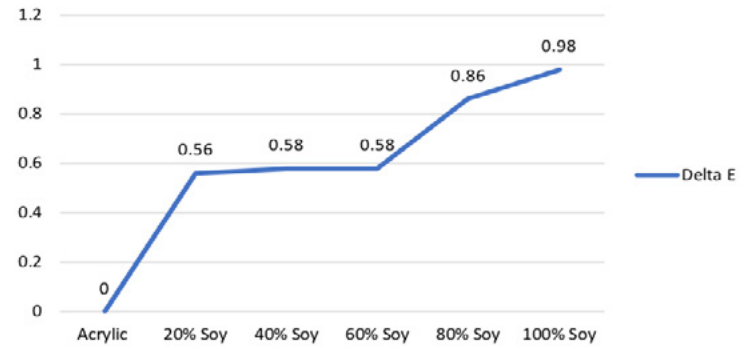

Figure 7: ΔE_{CMC} 2:1 of acrylic vs various increments of soy vehicle inks

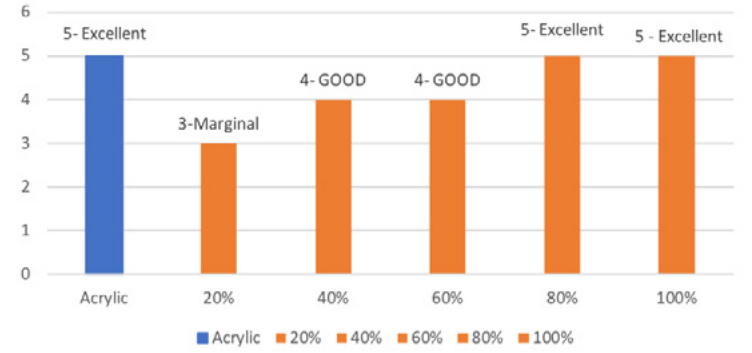

Figure 8: Rub Resistance (Acrylic ink Vs Increments of ProSoy 7475) for 60 strokes at 4 lb weight (scale 0–5)

4. Conclusions

Acrylic solution and emulsion resins are used in many water-based inks, mostly in packaging and product segments of the printing industry. Additionally, acrylics are used in many other sectors and sometimes they are depleted, thus not available. Also, they are products based on non-sustainable petroleum chemistry. Sustainable and biodegradable soy proteins were tested for suitability in water-based packaging formulations for the let-down portion of water-based packaging ink. It was found that viscosity and pH stability of soy containing inks over time of six months were comparable with 100 % acrylic inks. The color comparison between the target acrylic ink and the increments of soy ink in terms of color differences were found below $\Delta E_{CMC} = 1$, which was in accord with the colorimetric tolerances CIE DE2000 used in the graphic and printing industry. Rheology measured as a function of the shear rate showed shear thinning for both acrylic and soy/acrylic inks. The viscosity of the formulated inks was in the desired range for laboratory gravure proofing. Static surface tension measurements showed similar values for fully acrylic and soy/acrylic inks falling below 30 mN/m. Soy and acrylic vehicle inks performed comparably in selected end use properties, such as rub resistance. The 100 % soy and 80 % soy vehicle showed excellent rub resistance equal to fully acrylic ink. Rub resistance was worst at 20 % soy addition, maybe due to lower compatibility between soy and acrylic resin.

Acknowledgement

Authors would like to thank American Inks and Technology, Ltd., and Arro Protein Solutions Co., for materials provided for this research and Gravure Education Foundation for partially funding this project.

References

Altay, B.N., Joyce, M., Fleming, P.D., Pekarovicova, A. and Rong, X., 2017. Towards formulating conductive nickel ink for flexography printing. In: *Proceedings of the 69th Technical Conference, Technical Association of the Graphic Arts*. Houston, TX, USA, 19–22 March 2017. Sewickley: TAGA, pp. 10–19.

Erhan, S.Z. and Bagby, M.O., 1995. Vegetable-oil-based printing ink formulation and degradation, *Industrial Crops and Products,* 3(4), pp. 237–246. https://doi.org/10.1016/0926-6690(94)00040-6.

Farm Progress, 2012. Agriculture Infographics: Soybean composition. *Corn + Soybean Digest*, [online] Available at: <https://www.cornandsoybeandigest.com/issues/agriculture-infographics> [Accessed March 2019].

Graham, P.M. and Krinski, T.L., Ralston Purina Company. 1983. *Heat coagulable paper coating composition with a soy protein adhesive binder*. U.S. Pat. 4,421,564.

Hutchinson, G.H., 2002. Ink technology past, present and future. *Surface Coatings International Part B: Coatings Transactions*, 85(3), pp. 169–176. https://doi.org/10.1007/BF02699505.

Khodabakhsh, Z.M., 2013. *Soy-based inkjet ink*. Master's thesis. Western Michigan University.

Kinsella, J.E., 1979. Functional properties of soy proteins. *Journal of the American Oil Chemists' Society,* 56(3), pp. 242–258. https://doi.org/10.1007/BF02671468.

Kishbaugh, G., 2018. Packaging Outlook 2018: Paperboard Packaging Overview. *Packaging Strategies*, [online] Available at: <https://www.packagingstrategies.com/articles/90260-packaging-outlook-2018-paperboard-packaging-overview> [Retrieved March 2019].

Mai, R., Pekarovicova, A. and Fleming III, P. D., 2007. Correlation between ink rheology and press performance of water-based flexographic inks. In: *Proceedings of the 59th Technical Conference, Technical Association of the Graphic Arts*. Pittsburgh, PA, USA, 18–21 March 2007. Sewickley: TAGA, pp. 416–425.

Novamont, 2018. *Mater-Bi*. [online] Available at: <http://www.novamont.com/eng/> [Accessed March 2019].

Patil, B.H., 2015. *Formulation and evaluation of soy polymer based, gravure printed resistive inks for applications in printed electronics*. Master's thesis. Western Michigan University.

Pekarovicova, A. and Pekarovic, J., 2008. *Ten-year forecast of disruptive technologies in the inks and pigments industries.* Leatherhead: Pira International.

Pekarovicova, A., Khodabakhsh, Z.M. and Fleming III, P.D., 2015. Formulation of drop on demand soy ink jet inks*, Journal of Print and Media Technology Research*, 4(3), pp. 195–204. https://doi.org/10.14622/JPMTR-1415.

Pekarovicova, A. and Husovska, V., 2016. Printing Ink Formulations. In: J. Izdebska and S. Thomas, eds. *Printing on polymers: fundamentals and applications*. Amsterdam: Elsevier. pp. 41–55.

Pingale, R., 2018. *Soy-based flexographic ink for linerboard printing*. Master Thesis. Western Michigan University.

Pingale. R., Pekarovicova, A. and Fleming, P.D., 2019. Water-based soy inks for packaging. In: *Proceedings of the 71st Technical Conference, Technical Association of the Graphic Arts*., Minneapolis , MN, 16–20 March 2019. Sewickley: TAGA.

Podhajny, R.M., 2003. Some things to remember about dynamic surface tension. *Paper, Film and Foil Converter*, [online], Available at: <https://www.pffc-online.com/surface-prep/1568-paper-things-remember-dynamic> [Accessed March 2019].

Rayaprolu, S., Hettiarachchy N., Horax, R., Satchithanandam, E., Chen, P. and Mauromoustakos, A., 2015. Amino acid profiles of 44 soybean lines and ACE-I inhibitory activities of peptide fractions from selected lines. *Journal of the American Oil Chemist's Society*, 92(7), pp 1023–1033. https://doi.org/10.1007/s11746-015-2655-y.

Renkema, J.M.S., 2001. *Formation, structure and rheological properties of soy protein gels*. Ph.D. thesis. Wageningen University.

Smith, K., 1996. Industrial uses of soy protein: New idea. In: *87th AOCS Annual meeting & Expo*. Indianapolis, IN, 28 April–1 May 1996. pp. 1212–1223.

Wyatt, F.C., 1999. Flexographic inks. In: R.H. Leach and R.J. Pierce, Eds. *The printing ink manual*. 5th ed. Dordrecht, the Netherlands: Springer. pp. 547–595.

Woodward, R.P., 2000. *Surface tension measurements using the drop shape method.* [pdf] Portsmouth: First Ten Angstroms. Available at: <http://www.firsttenangstroms.com/pdfdocs/STPaper.pdf> [Accessed 6 May 2019].

Zhang, X.M., He, B.H., Li, J.R., Qian, L.Y. and Zhao, G.L., 2007. Effect of inorganic electrolytes on the colloidal stability of water-based inks*. Zhongguo Zaozhi Xuebao/Transactions of China Pulp and Paper*, 22(1), pp. 59–62.

Investigation of Relationships between Light and Weather Resistance of flexible Packaging Materials applied outside depending on applied Inks and Surface Treatments

Klaudia Maňúrová[1], Csaba Horváth[2], Viktor Vetési[3]

[1] University of Sopron, József Cziráki Doctoral School of Wood Sciences and Technology, Hungary

[2] Óbuda University, Institute of Media Technology and Light Industry Engineering, Budapest, Hungary

[3] CNI Kft., Tiszaújváros, Hungary

E-mails: vach.klaudia@gmail.com; horvath.csaba@rkk.uni-obuda.hu; viktor.vetesi@gmail.com

Short abstract

The production of flexographic printing inks was improved in the last 10 years really rapidly. Nowadays, when the weather conditions are changing, more and more flexible packaging is used in the outside space and the printed designs for outside use are getting more colourful, we need to react on this claim of the market. As a theoretical background of the topic we focused on some questions, like the foil treatment before the printing process, the influence of the corona treatment, naturally the possibilities of the control of these two treatments. We also describe some points of the ink production, the functionality of ink systems and the production of the examined inks. The intention of our survey is to find out which way of the flexographic printing is the best suitable to print for packaging used in the outside area under specific light and weather conditions. We describe the behaviour of the printed foil, when is over, normal and undertreated. The first measurements we made on simple printed samples, but after getting this results we made further measurements on foil printed by ink and also by one and two componential varnishes. All the measurements were made at a certified laboratory. As conclusion we bring a defined solution, how to achieve the best weather and light resistance. We wanted to get reasoned results, because in our praxis some printers are not always aware of the methods, how to have the production process of an exterior foil under control. Forasmuch the storage conditions of some products are often also not the suitable ones, the printed packaging should be as qualitative as it is possible.

Keywords: flexography**,** weather and light resistance, flexographic printing inks, foil resistance

1. Introduction and background

It is the fundamental interest of all packaging manufacturers and users to provide prospective customers with packaging products that protect products from external impacts, and – not negligibly – are suitable for drawing the attention of the customers and fulfilling the marketing goals, as well as for representing the interests of the company selling the product. The purpose of their activities is to use the packaging also for generating the greatest possible marketing value. Creating packaging that is professional and functional from all aspects is far from being an easy task. In general, the product owner focuses on the relevant legal provisions, and targets creating the desired design during the process of producing each new product packaging. For this reason, it is important that the work processes of the manufacturers, as well as the raw materials they use, should comply with all quality requirements – and be verifiable at the same time. In this article, we examine a part of the mentioned issue. Our goal is to examine the operational efficiency of a specific ink series, the effect of varnish on resistance, and – through presenting laboratory results – to draw attention to the fact that thoughtful planning as a print press can save our customers from various problems. In our research we have focused on plastic and multicomponent flexible packaging materials, which can primarily be printed using flexography as the printing technology.

2. Materials and methods

In order to produce packaging materials in the appropriate quality, one needs to be aware of the properties of the raw material uses, as well as the opportunities to achieve maximum results (Szentgyörgyvölgyi, Várza and Veidinger, 2011).

2.1 Surface treatment of packaging materials

Appropriate adhesion of different materials is the result of molecular forces. In the case of liquids it is the cohesive force, while in the case of liquid and solid materials it is the adhesion force that determines the intermolecular interaction. It is determined by the adhesion force on the contact surface of two different or similar materials between the molecule lines. The wettability of most plastics by printing inks, solvents, aqueous polymer dispersions or adhesives is poor. This is particularly true to polyethylene, polypropylene and polyester films, therefore printing, further processing, or lamination is not possible, since printing ink or adhesive do not adhere to them. This is a special property of these materials – also called surface free energy or surface tension – and this property significantly influences the extent a liquid may dampen the substrate, and it can be easily determined by measuring the contact angle. The contact angle is the angle between the contact point and the horizontal line. In case the base, that is the substrate, is highly wettable, the contact angle is zero, while in case it is only partially wettable, the contact angle is determined as 1–180° or greater (Hlawacek, 2005).

2.2 Corona treatment of packaging materials

Corona discharge is used for increasing the surface free energy of plastic films – paper and metal films in part – that is, for improving the adhesion of the applied inks, varnish, or adhesives. The essence of this is that electric discharge – and as a result, plasma – is created between a high voltage electrode and the roller – as a counter electrode – over the film fed through a roller. Owing to the dielectric coating applied to the surface of the electrode and the counter electrode, the micro discharges are evenly distributed over the surface to be treated, and there will be no sparks generated that could cause warming (Pál, et al., 2017). Corona treatment with appropriate dose increases the adhesion properties of film. We could even come to the conclusion that stronger corona treatment could compensate for loss over time. However, if the dose is too large, it would have the opposite effect of decreasing adhesion properties. This is due to the fact that excessive energy intake makes too much damage to the surface. Surface bubbles are formed preventing the adhesion of printing inks or adhesives. In contrast, in the case of undertreatment, wettability is jeopardized, and it may result in the poor adhesion properties of the treated film.

2.3 Checking surface treatment

In view of the importance of surface treatment, it is absolutely necessary – prior to further processing – to check the surface tension strength and adequacy both in positive and negative directions. There are several options for measuring and checking the actual values and parameters which ensure fair assessment. In our investigation we used a Dyne Test Pen to check the corona treatment, specifically the corona and plasma test pen from the company Ferrarini and Benelli.

The most obvious solution is to purchase surface treatment markers or ink – available in sets or in the required strengths – from companies specialized in this area. Their accuracy is ±0.5 mN/m, and the reading time is 2 seconds. It complies with ISO 8296 and DIN 53364 standards (International Organization for Standardization, 2003; Deutsches Institut für Normung, 1975).

2.4 Inks used for flexographic printing and their properties

Ink manufacturers define ink as dispersion or solution that includes several chemical ingredients with different properties in dissolved or dispersed form (File and Németh, 2009). Some of these ingredients ensure the printability of the ink and the properties of the dried ink film, while others set the spectral reflectance and the colorimetric properties of the spectrum. The composition of flexographic ink is similar regardless of the manufacturer: the main components are coloring agents, binders, diluents, and additives (Vetési, 2016).

In the case of flexographic printing, primarily pigments are used – these can be organic or inorganic pigments. Light fastness is determined according to DIN 16519 standard (Deutsches Institut für Normung, 1985), with the values ranging from 1 to 8 – the greater the value, the more resistant the pigment is. In the case of alkaline acid resistance, these values range between 1 and 5 (Heylen, 2017). The higher the value, the more resistant the pigment is to chemical impacts. In practice, many errors occur due to incorrect choice of the pigment. For example, in the case of packaging material for potting soil that is generally stored outdoors, if the choice of the pigment is not appropriate, the packaging material may fade within a week.

2.5 Preparation of the sample films

A K Hand Coater pre-press equipment was used for preparing the sample films. Due to the even winding of the equipment – which actually consists of stainless steel wire wound on a stainless steel rod – the grooves are uniform. This will ensure permanent repeatability and precise application, which was a basic requirement of the test performed. The KB1 rod with closed spiral was used for the test, which was intended for guaranteeing the thickness of the ink layer, since the test would have lost its purpose without it. Almost 40 pre-presses were completed during the first test phase, since many samples were needed to ensure the most thorough test in this phase of the work. The dyes used were diluted with ethanol set to a viscosity of 20 s efflux time, which was checked using DIN 4 measuring cup.

2.6 Scratch resistance test

This method is used for testing the mechanical properties of the print ink against scratching. One out of the two printed tests should be checked after 10 minutes, while the second should be stored at room temperature and then checked after 24 hours. Scratch resistance should be checked using fingernails: place the printed test on a smooth surface and scratch its surface 10 times with fingernails. The fingernail scratches created on the surface should be compared with each other. In this way, the scratch resistance of the ink layer on the substrate can be determined. Naturally, this test result will greatly depend on the person who performs it. However, in our opinion, its usefulness lies in the simplicity, providing guidance at the printing presses and revealing non-compliance right away.

2.7 Wet rub test

Wet rub test was performed to check the mechanical resistance of ink layers. The situation is imitated with packaged products – also equipped with a protective layer of shrink film – stored on a pallet. In this way, rub resistance and water resistance can be checked at the same time. A pallet may repeatedly get wet when stored outdoors, water can get into the gaps between the bags, and then stagnant water can induce steaming processes when the temperature rises. This will impair the adhesion of ink to the substrate. This is why we decided to perform combined tests. Pure tap water in a 20-30 l container – for storing the film soaked – is used for the procedure. Water is heated to a temperature of 60 °C. The film is soaked for 30 minutes, 2 hours and 24 hours; it should be completely covered by the liquid. The proof sheets stored for various periods of time are examined immediately after they are removed from the liquid. All the above should be performed as follows: hold the film strip in your

hands and rub the printed surfaces exactly ten times against each other – imitating the above described steaming process and e.g. the moving of the bags during transport.

2.8 The light and weather fastness test

This test is used for determining the effects of light and weather fastness on our printed film samples. Due to the diversity of pigments, some of them are not affected by UV-rays, while others are extremely sensitive to these impacts. In this respect, the most vulnerable is magenta pigment, and this is why we selected this color for our tests. In this chapter the significance of selecting the appropriate pigment before printing is also pointed out.

Atlas Xenontest Alpha+ device was used for the test, which simulates natural weather conditions and provides reliable information – within a short period of time – on all the tested materials regarding their weather stability. It is a universal device for testing light and weather fastness. It meets the requirements of several standards and test methods. Among others, it complies with the standard DIN ISO 12040 on light fastness and standard DIN EN ISO 11341:2004 on weather fastness (International Organization for Standardization, 1997; 2004).

For the testing, size 20 mm × 50 mm film pieces were cut from the print test samples. Piece no. 0 was selected as etalon, and used for comparing the fading of other prints. Pieces of these are removed and pasted on glass after 100, 200, 300, 400 and 500 hours, and placed next to the 0^{th} piece. Then we start the test according to the above set parameters. Naturally, in case no color – only the substrate – can be detected on the film piece before finishing the test, then the test is aborted.

3. Results and discussion

3.1 Corona treatment of the sample films

Softal corona treatment equipment – for laboratory use – was used for preparing the sample films, specifically the Softal Corona 9000 Series Generator. When setting the current used, we took into account the thickness of the film, and after fine tuning the equipment, the surface free energy of the polyethylene film was set to the following values:

- untreated polyethylene film <32 mJ/m^2 (LDPE, Slovpack a.s.)
- optimally treated polyethylene film 40–42 mJ/m^2 (LDPE, Slovpack a.s.)
- overtreated polyethylene film > 46 mJ/m^2 (LDPE, Slovpack a.s.)

These three parameters were considered sufficient to demonstrate the effects that can be achieved, as well as the consequences that can be caused. Naturally, all the above was checked using devices appropriate for checking surface treatment.

3.2 Results of scratch resistance test

After separately examining the untreated, optimally treated, and the overtreated films, we concluded that there are significant differences depending on the selected pigments. Despite the appropriate binder, there were different scratch-resistance results. According to our findings, this result is caused by the pigment resistance property. However, we did not examine it separately. This is summarized in Table 1 as follows (1 stands for the low resistance and 5 is for high resistance):

Table 1: Summary of scratch resistance

Ink type	Surface treatment, surface free energy (mJ/m²)	Scratch resistance	
		Immediately	After 24 hours
Test ink 1 (WZ65-3N3F 75% & WA17-T8RD 25%)	< 32	2	2
Test ink 1 (WZ65-3N3F 75% & WA17-T8RD 25%)	40–42	3–4	3–4
Test ink 1 (WZ65-3N3F 75% & WA17-T8RD 25%)	> 46	2	2
Test ink 2 (WZ64-3P6F 75% & WA17-T8RD 25%)	< 32	3–4	3–4
Test ink 2 (WZ64-3P6F 75% & WA17-T8RD 25%)	40–42	5	5
Test ink 2 (WZ64-3P6F 75% & WA17-T8RD 25%)	> 46	4–5	4–5

3.3 Results of wet rub test

This was performed on untreated, optimally treated, and overtreated films, at the three different time intervals specified above; the digitized results are shown in Figures 1, 2 and 3.

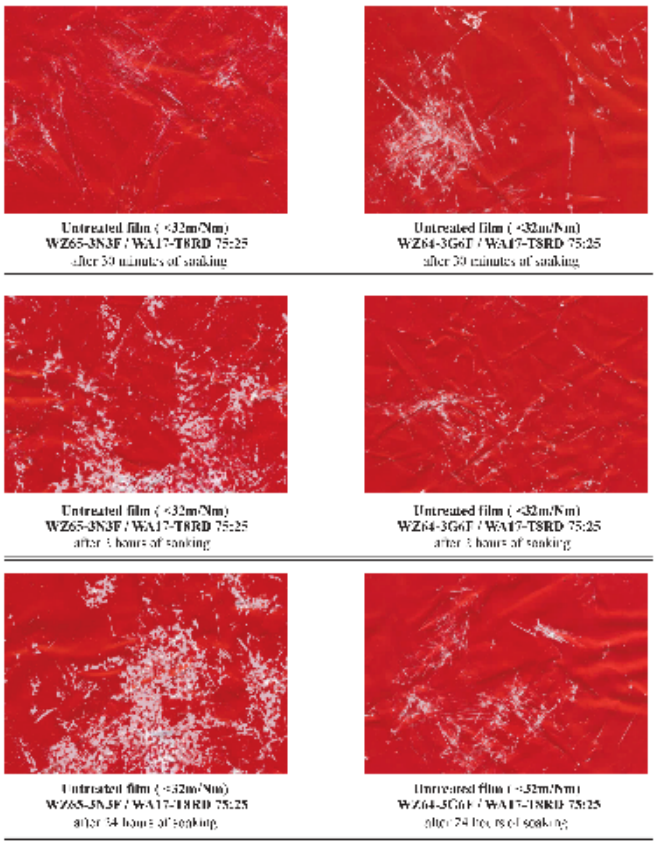

Figure 1: Untreated samples

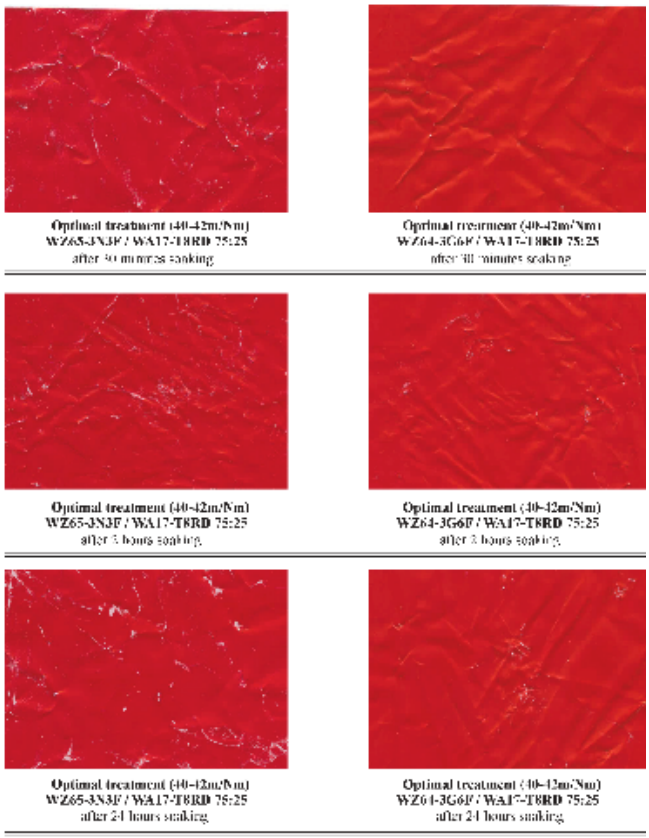

Figure 2: Optimally treated samples

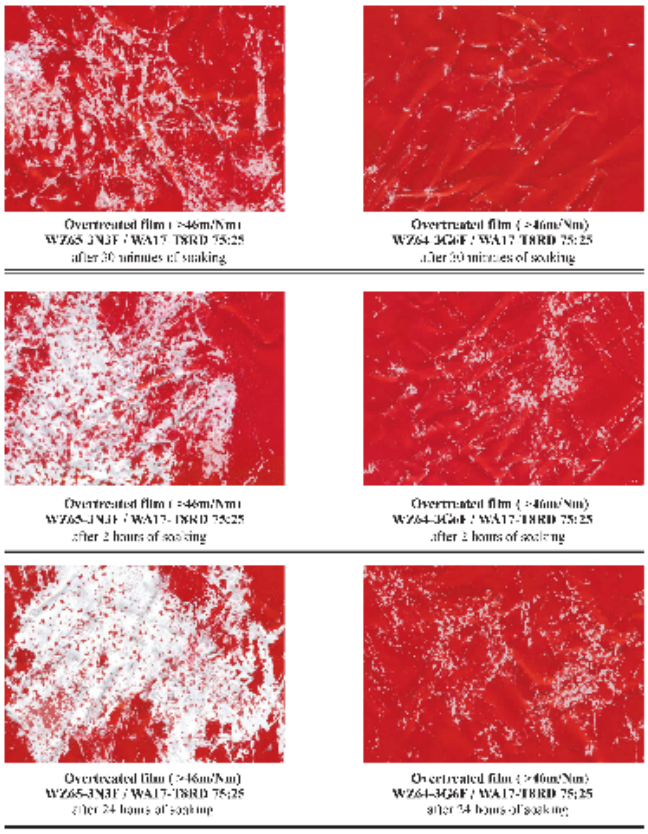

Figure 3: Overtreated samples

During the test series the following has been found:
In case pigment selection is not appropriate, but binder selection is optimal, it can also be observed how important keeping surface treatment at the optimum level (40–42 mJ/m^2) is. In the case of untreated film, the ink layer on the film surface was found to be very worn, especially when checked after 24 hours. However, the figure shows a more critical situation where the disappearance of the ink can be observed as early as in the first test period (after 30 minutes), which is due to overtreatment. It can be concluded in the case of all the three tests, that untreated and overtreated test pieces already show non-compliance in the early phase.

In case the pigment and binder selection is optimal, the extent of wear is not as severe as above, however, the effect on the later quality deterioration of the finished product can be observed. At the same time, in the case of appropriate treatment, it is apparent that the ink layer is also stable at the early checking phases. There was no significant change in rub resistance even after additional soaking for 2 or 24 hours.

After separately examining the untreated, optimally treated, and the overtreated films, we concluded that there were significant differences depending on the selected pigments. Despite the appropriate binder, there were different rub resistance results. According to our findings, this result is caused by the pigment resistance properties.

3.4 Results of the light and weather fastness test

The examined film strips are placed next to each other to visually demonstrate the rate of fading versus time, as shown in Figure 4, for ink samples WZ64-3G6F and WZ65-3N3F.

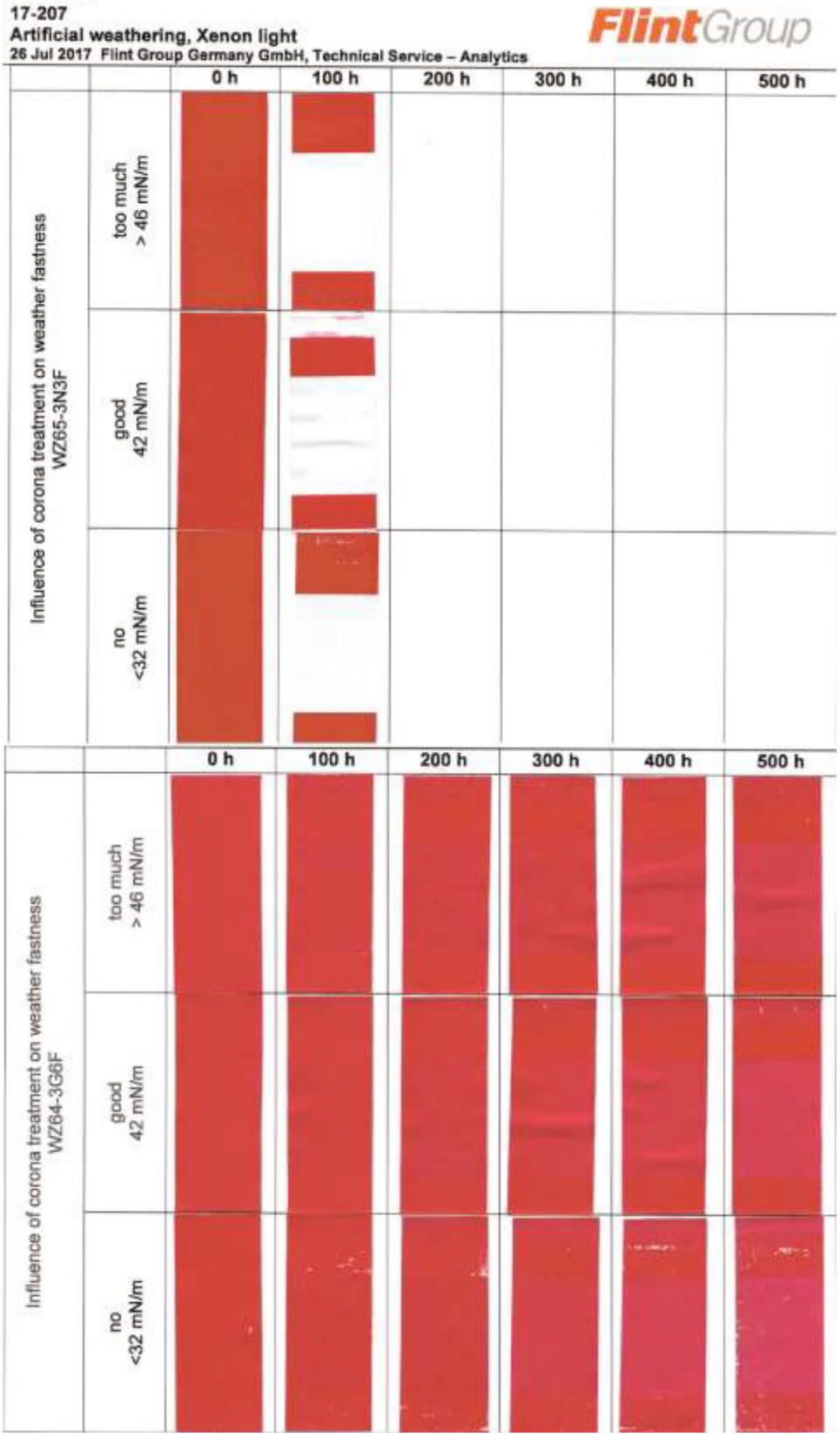

Figure 4: Test samples of the light and weather fastness test

3.5 Final comments and extended research work

In the flexographic printing process there are several pitfalls which – if no proper attention is paid – may cause production or functional defects in the packaging material. This fact inspired the measurements and tests performed in the chapter. The ink developer, as one of the market leading ink manufacturers, is intensively engaged in developments specifically aimed at this area, to ensure that packaging materials used outdoors can withstand the sometimes extreme weather conditions and the impacts of UV radiation. The consequences of selecting inappropriate pigment for our printing ink, or failing to choose the appropriate extent of surface treatment for the given substrate can be clearly concluded from the tests. The essence of our examination was preparing test pieces, then the sample films were subjected to scratch, rub and fade resistance tests.

After these were completed, we came to the conclusion that during front surface printing we should strengthen the protection with a varnish layer, and then check the results. Therefore, we repeated the sample preparation using varnish specifically designed for outdoor use (one and two component varnish). The objective was reached, as we were able to establish that it was important to understand and appropriately apply the above combinations, since the expected outcome could only be guaranteed in this case.

After evaluating the results, we decided to repeat the tests in a more complex way: by applying two different protective varnish layers to ensure that we may supply the manufacturers with more comprehensive knowledge (Vetési, 2010).

4. Conclusions

Our objective was to find and present an optimal combination of pigment, ink and surface treatment which allows producing a printed film that measures up in all aspects to the environmental impacts on packaging when used outdoors. After a short summary of the theoretical background, we examined untreated, optimally treated, and overtreated films using an ink series of Flint Group, where the binder was a constant parameter, but the pigment types varied. From these combinations we received proof sheets for examination, and we intended to test and prove the resistance of the prints to outdoor impacts. Such tests were: rub test, scratch test, light and weather fastness test.

It can be concluded that choosing pigments with the appropriate resistance level is important, since using an inappropriate component will result in fading after only 100 hours (examined using the Xenon light and weather fastness test), which greatly affects the marketability of an aesthetically defective packaged product. Another varnish layer did not help much, on the contrary...

Overall, it was concluded that being aware of the technology, and using it appropriately was very important. By performing simple tests before printing, we could make sure that we acted carefully, and avoided a lot of problems that could have surfaced later.

It is important to address these issues later, since the proportion of using packaging materials outdoors is increasing, the product range is expanded, and the packaging materials are more and more colorful and attractive. The hours of sunshine are increasing, as well as the intensity of sunlight. The tests, examinations and their results all provide knowledge to the manufacturers, which may result in better print inks.

References

Deutsches Institut für Normung, 1975. *DIN-53364 Testing of plastic films; wettability of polyethylene and polypropylene films (superseded)*. Berlin: DIN.

Deutsches Institut für Normung, 1985. *DIN 16519-2:1985-08 Testing of prints and inks; preparation of standard prints for optical tests (withdrawn)*. Berlin: DIN.

File, L. and Németh, N., 2009. Biztos, hogy a legmagasabb pigment-tartalmú festék a legjobb választás? *Magyar grafika*, 53(5), pp. 28–30.

Heylen, M., 2017. Élelmiszer-csomagoló anyagok UV-festékei – Flint Group. In: *Proceedings of Magyar grafika*. Hévíz-Zalaegerszeg, Hungary, 23-24 February 2017. Budapest, Hungary: PNYME, pp. 30–31.

Hlawacek, G. 2005. *Kontaktwinkelmessung*. [online] Available at: <*https://www.researchgate.net/publication/242304992_Kontaktwinkelmessung/download*> [Accessed 11 January 2019].

International Organization for Standardization, 1997. ISO 12040:1997 Graphic technology — Prints and printing inks — Assessment of light fastness using filtered xenon arc light. Geneva: ISO.

International Organization for Standardization, 2003. *ISO 8296:2003 Plastics — Film and sheeting — Determination of wetting tension*. Geneva: ISO.

International Organization for Standardization, 2004. ISO 11341:2004 Paints and varnishes — Artificial weathering and exposure to artificial radiation — Exposure to filtered xenon-arc radiation. Geneva: ISO.

Pál, M., Novaković, D., Dedijer, S., Koltai, L., Jurič, I., Vladić, G. and Kašiković, N., 2017. Image processing based quality control of coated paper folding. *Measurement,* 100(March), pp. 99–109. https://doi.org/10.1016/j.measurement.2016.12.033.

Szentgyörgyvölgyi, R., Várza, F. and Veidinger, P., 2011. BOPP és PE fóliákra flexónyomtatással készített nyomatok vizsgálata. *Magyar grafika,* 55(1), pp. 8–10.

Vetési, V., 2010. Festékkonyha felépítése, alapadatbázis elkészítése flexónyomtatáshoz. In: Óbudai *Egyetem*, Szakdolgozat.

Vetési, V., 2016. Új trendek, innovációk és specialitások a nyomdafestékekben. In: *Proceedings of Magyar grafika.* Debrecen, Hungary, 18 January 2016. Budapest, Hungary: PNYME, pp. 34–35.

Techniques for Static, Dynamic and Surface Compressibility Measurements of Paper Substrate

Lars Granlöf and Li Yang

Research Institutes of Sweden (RISE), Drottning Kristinas väg 61, 11486 Stockholm, Sweden
Email: li.yang@ri.se

Short abstract

This report highlights three measurement techniques of compressibility, which complement each other. The Material Testing System (MTS) measures the static compressibility and the *Z*-D Tester measures the dynamic compressibility. The former reveals elastic and plastic deformations, while the latter reveals even viscoelastic deformation which becomes important when the compression rate is high. Unlike these two methods that measure the total compressibility in paper thickness direction, the third method, PST (Printing Simulation Tester), provides quantitative evidence of deformation of the paper surface while being compressed. Combinations of these techniques will provide us with comprehensive insights and eventually a full picture of the compressive behaviour of paper in a printing nip, which is essential part of printing dynamics of conventional printing techniques, calendaring, and even perforation processes.

Keywords: printing dynamics, board compressibility, surface compressibility, calendaring, packaging

1. Introduction

In conventional printing techniques, e.g. offset and flexography, ink transferring from a print nip to a paper (board) surface relies on mechanical contact between the print form (nip) and the paper surface (Biermann, 1996, Chapter 23). To promote the contact between them, a nip pressure is applied, bringing the paper surface into closer contact in the nip. Under the nip pressure, both the print form and the paper (board) undergo dynamic compressions and deformations which improve the contacts between the print form and board surfaces and even out surface defects. Thanks to the nip pressure, ink is either fully or partially pressed into the pore structure of the paper surface (Hsu, 1961), strongly depending on the relationship between the ink viscosity and the largeness of the pores, a feature predominantly occurring on uncoated substrates. For a pigment-based ink, only the ink vehicle is pressed into a fine coated surface, while the pigment stays on the surface.

In the papermaking industry, compressibility of paper products is measured by the Parker Print-Surf (PPS) method (International Organization for Standardization, 2017). It is calculated from two PPS roughness values measured at two different clamping pressures, namely,

$$K = \frac{100(G_1 - G_2)}{G_1} \qquad [1]$$

where G_1 and G_2 are the PPS roughness values obtained at the nominal clamping pressures 1 MPa and 2 MPa, respectively.

The PPS Compressibility has intrinsic deficits when applied to a printing process as it only measures the static compressibility, being given a sufficiently long time for the paper (board) to deform under the pressure load. This differs significantly from what occurs at a print nip where the nip pressure time is very brief. A typical flexographic printer runs at a speed 300–600 m/min. The corresponding nip time when nip

compression occurs ranges 3–6 milliseconds (ms), provided that the length of contact, for example, is 3 cm. Hence, to understand a print process one needs to measure the dynamic compressibility of the substrate, especially in the case of packaging and printing board. Another weakness of PPS compressibility is it is based on the relative deformation between two already deformed/compressed board structures, because it is calculated from the difference of PPS roughness values obtained with two clamping pressures, 1 MPa and 2 MPa. This is particularly problematic as the deformation of a paper board is partially plastic. It means that in addition to the pressure magnitude and time duration, even the history of mechanical deformation/compression matters. Moreover, detailed characteristics of surface compression of the board are important from an ink-transfer point of view, which has also been lacking in the definition of compressibility provided by the PPS.

Dynamic compressibility measurement is also essential for studying printing dynamics, as paper's viscoelastic nature can cause variability in test data (Dwan, 1987). From a mechanics point of view, the mechanical response of a viscoelastic deformation is linearly proportional to the rate of deformation. The higher the deformation rate the stronger the stress (mechanical response).

In this report, we present three measurement methods, two of which are commercial devices and one homemade. The focus is to obtain appropriate measurement methods that can be used to understand the dynamic nature of nip-paper/board interaction and print quality.

2. The measurement methods and results

Three measurement techniques are presented below. These methods have been used to measure the static and dynamic compressibility in the thickness direction (the overall compressibility) and surface compressibility of board structure. Compression in the thickness direction, may result in lateral extension of the print form, which is important for print raster reproducibility (Olsson, et al., 2006).

2.1 The Material Test System (MTS) for static compression measurement

The MTS is a commercial device used for material properties measurement. It is a hydraulic system where the actuator is a piston controlled by hydraulic valves. During the measurement the distance between the steel blocks (piston and load cell) and the force were recorded. Figure 1 illustrates the working principle (Figure 1a) and the compression-relaxation cycles in form of strain-stress curves. The curves of different colours correspond to measurements at different positions of the same board sample.

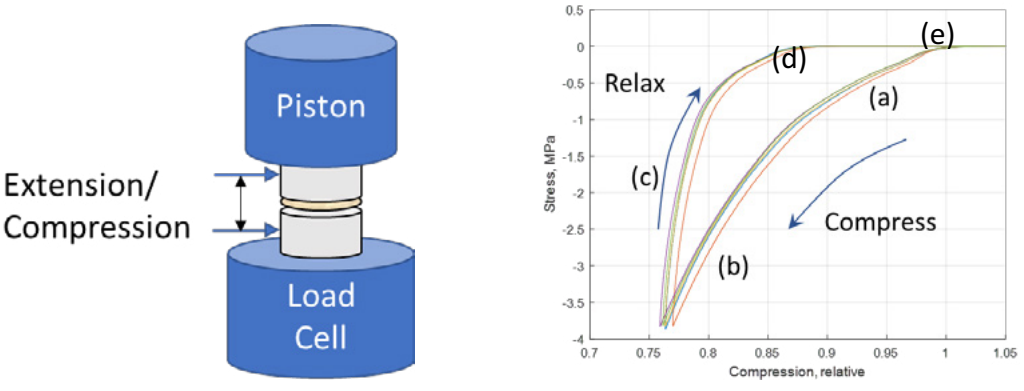

a) *b)*

Figure 1: The MTS z compression test setup (a) and the stress against compression (relative board thickness) curves (b) denoted by different colours corresponding to measurements at different positions of the board

A measurement cycle consists of two major regimes, compression and relaxation. In both regimes, the force increased/decreased linearly with time except for the final part in the relaxation regime, where the thickness did not recover any further (Figure 1b). It is clear that in the compression regime the initial slope (a) is lower than the final slope (b), indicating that the board was easier to be compressed at the beginning due probably to deformation in the middle ply of the board via void compression prior to direct fibre-fibre contact, but it became harder to be compressed when the board structure became denser. During the relaxation regime, the slope is very high at the beginning (c), suggesting that the stress reduced rapidly with recovering board thickness. Then the stress releasing significantly slowed down in (d), and eventually stopped in the final stage (e). A higher slope in the relaxation regime (c) than its adjacent counterpart in the compression regime (b) implies there were plastic deformations in the board structure, which did not recover when the stress was removed.

Typically, a MTS measurement cycle takes a few seconds. The compression rate of the measurement is low and the result reflects mainly elastic and plastic deformations of the paper substrate. Viscoelastic deformation of paper substrate becomes profound at a high compression rate (Meyers and Chawla, 1999, pp. 98–103), as it is the case in flexographic and offset printing processes, thus cannot be revealed with the MTS technique. In other words, the compression behaviour obtained from a MTS measurement gives only a partial image of printing dynamics.

2.2 The *Z*-D tester for dynamic compression measurement

The *Z*-D tester measures the dynamic compressive behaviour of board. This is done by dropping a heavy probe onto the board to create the force that compresses the board, as illustrated in Figure 2.

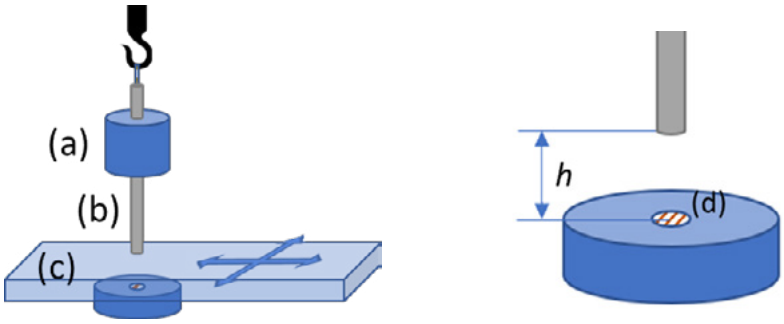

Figure 2: Illustration of the Z-D tester: (a) weight, (b) probe, (c) sample, (d) distance sensor

The probe consists of a heavy brass cylinder attached to a rod, which is 5 mm in diameter. The position of the probe, *h*, is registered by a distance sensor using electromagnetic induction, which can detect the metal probe approaching the sensor without physical contact with the probe. The *Z*-D tester resembles what happens at a printing nip, as illustrated in Figure 3.

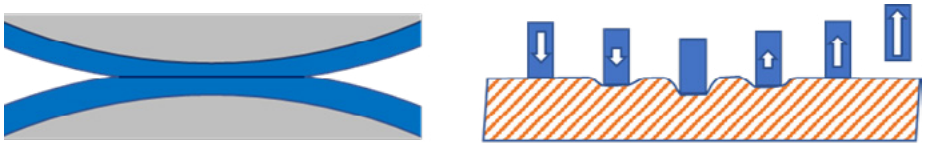

a) *b)*

Figure 3: Schematic of probe-striking process (b) to nip compression (a)

The *Z*-D tester does not directly measure the colliding force (pressure) while the probe strikes the paper board instead it records the position of the probe as a function of time. The force that the probe exerts on the board sample has to be calculated from the movement of the probe. According to Newton's law, the

force equals the mass of the probe multiplied by the acceleration it experiences, i.*e.* $F = m \cdot a$, provided that the position where the probe sits statically on the board surface is set as the reference ($z = 0$).

The velocity v and the acceleration a of the probe can be calculated from the derivatives of the position, h, namely,

$$v = \frac{\mathrm{d}h}{\mathrm{d}t} \qquad [2]$$

$$a = \frac{\mathrm{d}^2h}{\mathrm{d}t^2} \qquad [3]$$

Pressure (stress) = F/A, where A is the cross section of the probe. Figure 3 depicts the time evolution of the probe's position as well as the calculated values of velocity, acceleration and pressure, all of which are time dependent. One can also see that the peak compressive pressure is slightly higher than 1 MPa.

Unlike the MTS technique, a typical measurement cycle of the *Z*-D tester is about one millisecond or so (see Figure 4), which is comparable to the nip duration of a modern flexographic printing press running in 600 m/min. Therefore, with the *Z*-D tester one has the possibility to study the true dynamic compression behaviour of the paper substrate in the printing nip.

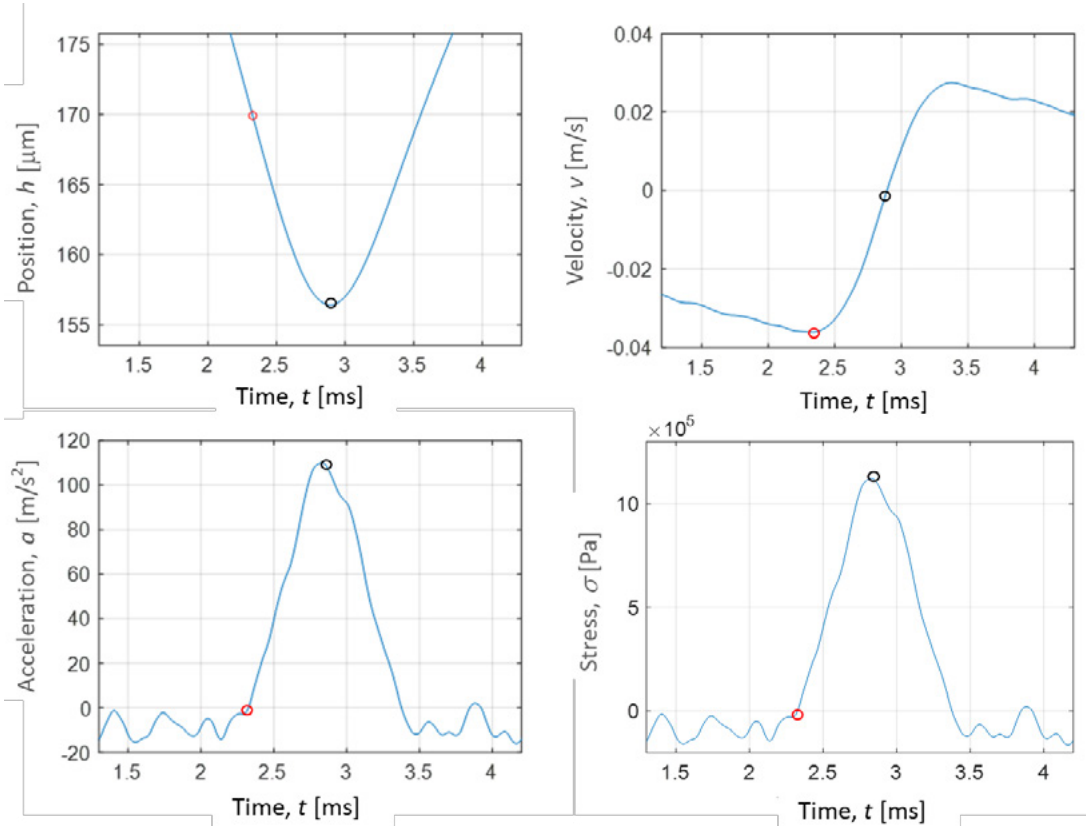

Figure 4: The recorded position of the probe, its derivatives and the striking pressure; the positions where the probe began to contact the board surface and bounced back are denoted by red and black rings, respectively

2.3 Print Simulation Tester (PST) for surface compressibility measurement

In a printing process ink transfer relies on mechanical contact between the print form and the board surface. The probability as to whether the contact occurs or not depends not only on the intrinsic topology of the board surface, often known as surface roughness, but also deformability (surface compressibility) of the board surface under the nip pressure.

The Print Simulation Tester (PST) consists of a glass prism and an imaging system, as illustrated in Figure 5. The prism is made of glass, of which refractive index is 1.5 or higher. The incident ray(s) will be totally reflected at the bottom surface of the prism if the bottom area is not in contact with the paper/board surface. In areas where the board surface and the bottom of the glass body are in contact, light will be diffusely reflected in all directions. The camera sitting directly above the board captures the light that propagates vertically towards the camera. As the result, areas that are not in contact will appear dark, while areas in contact will appear bright.

The sample holder can move vertically toward the prism, controlled by compressed air. The pressure is adjustable in the range 0.5–8 MPa. The measured area is 8 mm × 12 mm. The PST captures three images with different time delays after contact: 10 ms, 100 ms and 1 000 ms. The detail of contact-area change with respect to pressure and duration time is registered by the camera, which provides useful insights to how the board surface is deformed under a given pressure and compression time.

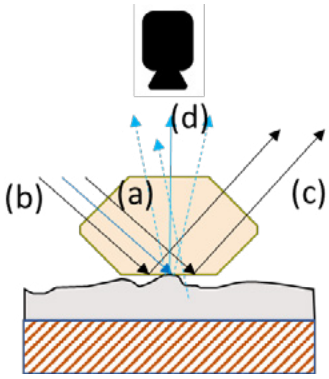

Figure 5: The board is pressed between a glass prism (a) and a soft backing material; incoming light (b) at total reflection (c), and diffuse reflection (d)

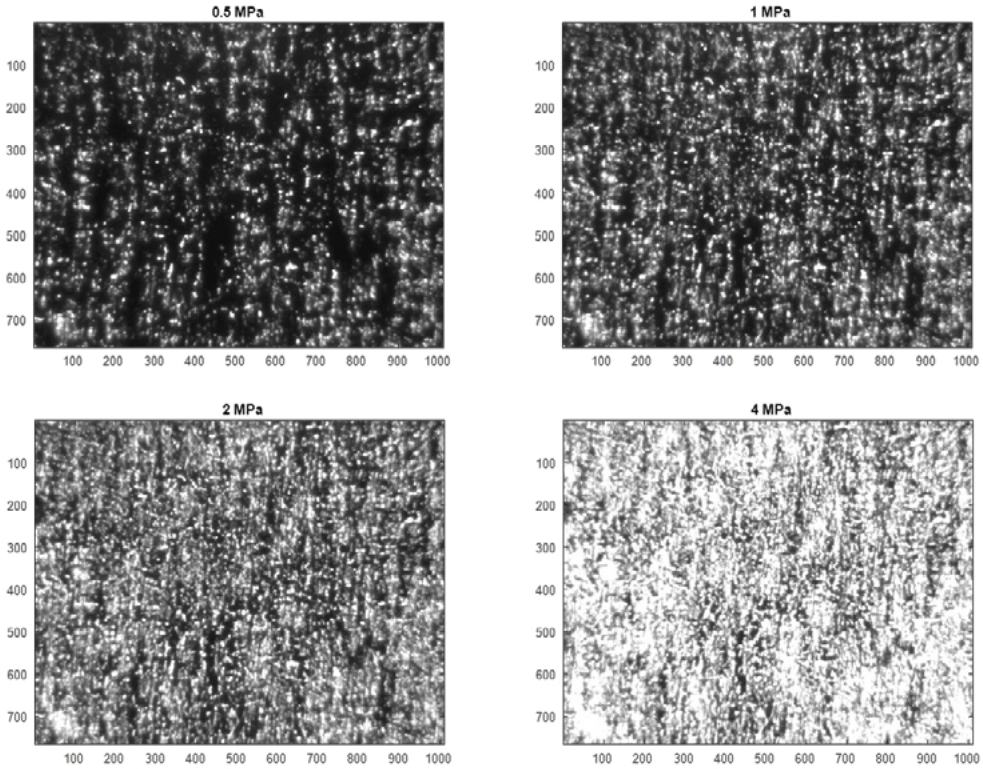

Figure 6: The images from the PST measurements under different pressures, 0.5 MPa, 1 MPa, 2 MPa, and 4 MPa; the white spots represent areas in contact with the prism

Figure 6 depicts the images of the PST measurements corresponding to different pressures. As expected the area of contact grew with the increasing pressure. The relationship between the pressure and the contact area indicates the surface compressibility of the paper substrate.

3. Conclusions

This report highlights three methods for compressibility measurement, which operate in different working principles and reveal different aspects of paper compression behavior. Their measurements are complementary to each other. The semi-static measurement technique (MTS) reveals the elastic and plastic compression behaviors while the highly dynamic testing method, (ZD tester) reveals even viscos-elastic deformation as well. The viscos-elastic deformation becomes an important part of nip pressure when the rate of thickness compression is high as it is the case of printing. The high the printing speed, the strong the impact of viscoelastic deformation to the nip pressure. Unlike MTS and ZD tester which measure the total compression in paper thickness direction, the PST technique reveals how paper surface (topography) deforms under a nip pressure. An easier deformed paper surface is in favor of direct contact between the paper surface with the nip thus in favor of ink transferring. With these methods one has the opportunity to obtain a full picture of board compression in a printing nip, e.g. flexography, offset, and gravure. This is probably applicable even to calendaring.

Acknowledgments

This work was conducted within RISE Bioeconomy Research Programme, program area Packaging. Financial supports from government founding through SK medel and from industrial partners: BillerudKorsnäs, ITC, Miller Graphics, Stora Enso, Tetra Pak, and UPM are acknowledged.

References

Biermann, C.J., 1996. *Handbook of pulping and papermaking*. 2nd ed. San Diego, CA, USA: Academic Press.

Dwan, A., 1987. Paper complexity and the interpretation of conservation research. *Journal of the American Institute for Conservation,* 26(1), pp. 1–17. https://doi.org/10.1179/019713687806027924.

Hsu, B., 1961. The influence of paper compressibility on ink penetration. *Applied Science Research,* 10: 277. https://doi.org/10.1007/BF00411920.

International Organization for Standardization, 2017. *ISO 8791-4: 2007, Determination of roughness/ smoothness (air leak methods) – Part 4: Print-surf method*. Geneva: ISO.

Meyers, M. and Chawla, K., 1999. *Mechanical behavior of materials*. Upper Saddle River, NJ, USA: Prentice-Hall.

Olsson, R., Yang, L., van Stam, J. and Lestelius, M., 2006. Effects on ink setting in flexographic printing: coating polarity and dot gain. *Nordic Pulp and Paper Research Journal,* 21(5), pp. 569–574. https://doi.org/10.3183/npprj-2006-21-05-p569-574.

Inorganic Printed LEDs for Wearable Technology

James Claypole[1], Alex Holder[1], Caitlin McCall[1], Amy Winters[2], William Ray[3] and Tim Claypole[1]

[1] Welsh Centre for Printing and Coating, College of Engineering, Swansea University Bay Campus, Crymlyn Burrows, Swansea, SA1 8EN, UK

[2] Rainbow Winters

[3] Nth Degree Technologies Worldwide Inc

E-mail: T.C.Claypole@swansea.ac.uk

Short abstract

A new form of inorganic printed electronics has been developed that allows for high speed production of solid-state lighting on flexible substrates. Light emitting diodes (LED) become more efficient as their size is decreased. However, the difficulties in making the electrical connection to micro LEDs has previously prevented these benefits being exploited outside the laboratory. Standard Indium gallium nitride (InGaN) film, grown on a defined substrate (heteroepitaxy), was fabricated into micro LEDs (approx. 30 μm) and dispersed in a carrier fluid to form an ink, which can then be printed using established printing technologies. During printing and curing, the geometry of the individual micro LEDs causes them to orientate into a single preferential direction. Connections can then be made via further printed layers of conductive and dielectric ink to create flexible lamps consisting of areas of discrete LED. These lamps have low power consumption and high light output making them ideal for incorporating into garments and for packaging. The "Thunderstorm" dress (a Rainbow Winters project) was developed for the "Wired to wear" exhibition in the Chicago Museum of Science and Industry to demonstrate the potential of this technology. The concept was to turn the wearer into a living representation of a thunderstorm. The concept had previously been realised using electroluminescent elements (EL) to create a lightning flash in the panels of the dress. However, this required the wearer to carry high voltage devices, bulky electronics and heavy batteries. Instead, using inorganic printed LEDs afforded the potential to create a truly wearable piece of haute couture, using low voltages, miniature electronics and small batteries. The work reported here describes the fabrication technique used to create the micro LED lamps and the issues related to their integration into a piece of wearable technology. The lamps could be driven in such a way as to create a more realistic flash compared to the EL version.

Keywords: printed electronics, inorganic LEDs, wearable technology

1. Introduction

Although there have been significant amounts of research into printed organic electronics, the performance and applications are limited by low mobility, short lifetime and difficulty in achieving the required feature size (Subramanian, et al., 2008; Arora, Hauser and Roulston, 1982; Yan, et al., 2009; Li, et al., 2011) Several approaches have also been proposed using inorganic semiconductors by using the direct layer by layer approach (Jackson, et al., 2007, Martins, et al., 2011; Han, et al., 2008), using directed self-assembly of fabricated devices (Knuesel and Jacobs, 2011; Yeh and Smith, 1994) and through pad printing of fabricated devices (Kim, et al., 2011). For the most part, these techniques suffer from both cost and manufacturability problems even though the performance of, particularly, printed fabricated devices is effectively equivalent to current discrete electronics.

An alternative approach is presented where a standard film of Indium gallium nitride (InGaN) is fabricated in heteroepitaxy and removed to form micro LEDs. These are dispersed into an ink so they can be printed

in combination with conductive ink and dielectrics to create robust, flexible and efficient lamps. The potential for wearable technology is demonstrated by combining these with conventional microelectronics and power supplies to create an example of interactive haute couture.

2. Printable inorganic micro LEDs

Silicon or sapphire wafers were used as a base for InGaN epitaxial deposition via Metal-Organic Chemical Vapour Deposition (MOCVD). The 450 nm wavelength emitting micro LED structures were then fabricated using a die mask set developed for this purpose. The 27 µm die segments were released into an ink binder (Figure 1) and printed onto a 125 µm polyester substrate previously patterned with a micro silver metallic conductive. The nature of printing is statistical, in that the LED will have a random dispersion and orientation. The statistical electronics model assumes that printed devices fall into two groups – functional orientation or non-functional orientation and that there can be no other orientation. Statistical builds presuppose that devices are printed in functional areas and that, within a given area, the devices are wired in parallel where an individual device failure does not yield a function failure

The initial LED designs had a random predominantly up/down orientation with a less likely sideways orientation. By refining the design of the micro LED, a shape was developed which would preferentially orientate in one direction.

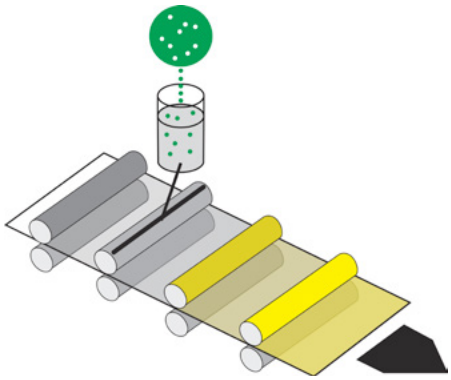

Figure 1: Micro LED lighting manufacturing process

To complete the lamps, two transparent dielectric layers and a transparent conductive layer were added to make a vertically connected, randomly spaced diode array (Figure 2). The phosphor layer is a doped yttrium-aluminium garnet (YAG) phosphor to convert the blue light produced by high bright LEDs into white light via a Stokes shift. No water or oxygen barrier is needed as these LEDs are inorganic. The environmental barrier layer was added to prevent mechanical damage to the YAG phosphor.

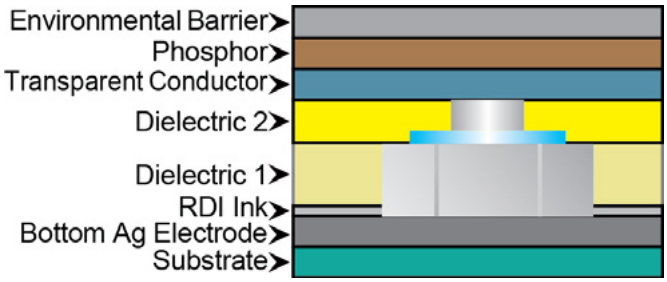

Figure 2: Layer build for printed LEDs

A scanning electron microscope (SEM) image of the resulting printed 27 µm die with the printed nano-fibre transparent conductor just prior to the phosphor lay down is shown in Figure 3. The silver nano-fibre transparent conductor was developed to provide high conductivity and flexibility.

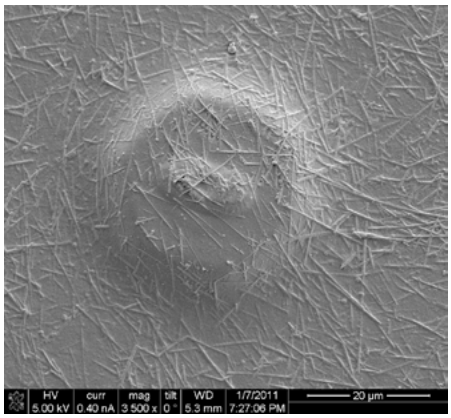

Figure 3: SEM of a printed micro LED with a nano fibre transparent conductor (one-shot transmission T = ~97 %, and resistance 50 Ω/□)

3. Application to wearable technology

The concept of the "Thunderstorm dress" was to turn the wearer into a living representation of a thunderstorm, creating a flash in response to a clap. In 2014, this had been realised using electroluminescent elements to create a lightning flash in the panels of the dress. However, this required the wearer to carry bulky electronics and heavy batteries. While it was used in marketing videos and at exhibitions the high voltage and power consumption made this impractical as wearable technology.

The opportunity to demonstrate the potential of this technology came when the Chicago Museum of Science and Industry commissioned a "Thunderstorm" dress for the 2019 "Wired to wear" exhibition. The inorganic printed micro LEDs afforded the potential to create a truly wearable piece of haute couture, using low voltages, miniature electronics and small batteries. The pattern of printed electrodes, micro LEDs and interconnects creates a seamless version which illuminates to the edge, so that butting panels together produces a continuous light. The pattern allows the individual panels to be cut to shape and then wired via any two terminals.

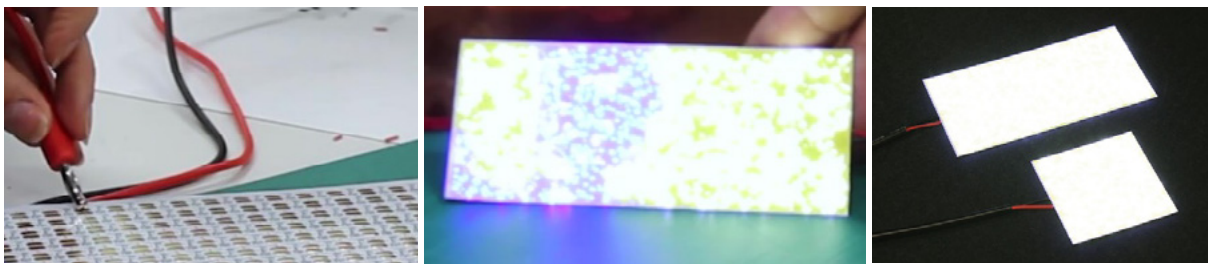

Figure 4: Seamless inorganic LED lamps

While the LEDs are ultra-bright, they produce distinct points of light, which require a diffuser to create a smooth illumination lamp. There was scope within the design of the dress to include a small air gap (2 mm) over the panel to allow the light to spread. The spacer also acted as a mask to limit the lit area. On top of this was attached a paper pattern containing the image of the flash (Figure 5).

The lightning flash was created by assembling discrete lamps along the image, which could be individually addressed (Figure 6). A programmable control board designed for the wearable technology (Adafruit Pro Trinket) was combined with power electronics to allow it to drive all 8 panels used simultaneously in the firing sequence indicated. By pulsing the power to the lamps, it was possible to build up the intensity creating a more realistic flash.

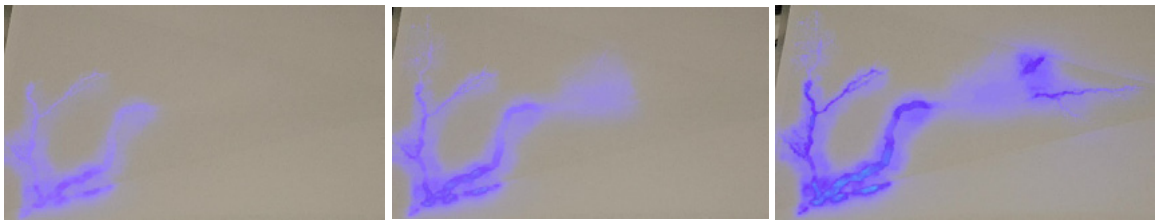

Figure 5: Prototype lightening flash with paper diffuser

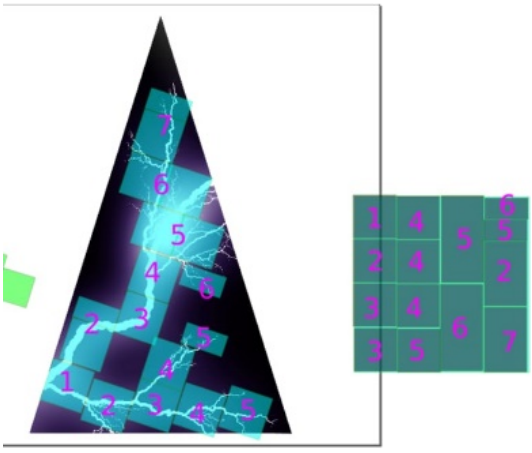

Figure 6: Arrangement and sequencing of lamps

The paper panel highlighted the need to cut the outline of the mask more closely to the image and to improve the graphics. Several different films and diffuser combinations were evaluated. The improved flash can be seen on all 8 panels during testing prior to assembly into the garment (Figure 7).

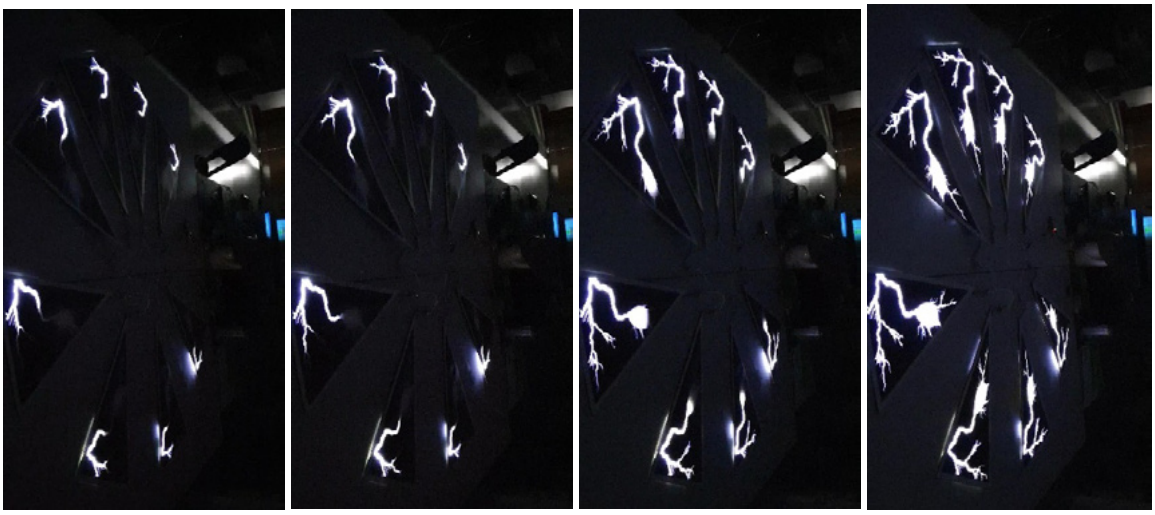

Figure 7: Bench test of finished panels

The panels were assembled into the dress with the wiring harness and electronics incorporated (Figure 8). This is now on display in the Chicago Museum of Science and Technology in the 2019 "Wired to Wear" exhibition.

Figure 8: "Thunderstorm dress" for Eye of the Storm exhibit

4. Conclusions

An alternative route to the fabrication of printed electronics has been presented based on inorganic semiconductors dispersed in a conductive binder to create an ink. These axial lead micro LED devices can be accurately printed using conventional graphics processes (screen, flexo and gravure). This approach will act as a template for further development of inks and techniques for new devices that employ fabricated silicon or III-V semiconductors.

The potential for these lightweight, flexible form factor lamps has been demonstrated by inclusion in a sound activated light emitting haute couture dress. This technology also has potential for application in flexible and display packaging.

Acknowledgements

The support of Nth Degree Technologies and icmPrint is acknowledged for this work.

Caitlin McCall acknowledges the financial support of the EPSRC, M2A and icmPrint Ltd.

References

Arora, N.D., Hauser, J.R. and Roulston, D.J., 1982. Electron and hole mobilities in silicon as a function of concentration and temperature. *IEEE Transactions on Electron Devices*, 29(2), pp. 292–295. https://doi.org/10.1109/T-ED.1982.20698.

Han, S., Dai, X., Loy, P., Lovaasen, J., Huether, J., Hoey, J.M., Wagner, A., Sandstrom, J., Bunzow, D., Swenson, O.F., Akhatov, I.S., and Schulz, D.L., 2008. Printed silicon as diode and FET materials – preliminary results. *Journal of Non-Crystalline Solids* 354, pp. 2623–2626. https://doi.org/10.1016/j.jnoncrysol.2007.10.090.

Jackson, W.B., Perlov, C., Almanza-Workman, M., Braymen, S., Chaiken, A., Jeffrey, F., Hauschildt, J., Jeans, A., Kwon, O., Luo, H., Mei, P. and Taussig, C., 2007. Electronics produced by roll-to-roll self-aligned imprint lithography. In: *2007 Digest of the LEOS Summer Topical* Meetings. Portland, OR, USA, 23-25 July 2007. IEEE, pp. 125–126. https://doi.org/10.1109/LEOSST.2007.4288364.

Kim, H-S., Brueckner, E., Song, J., Li, Y., Kim, S., Lu, C., Sulkin, J., Choquette, K., Huang, Y., Nuzzo, R.G. and Rogers, J.A., 2011. Unusual strategies for using indium gallium nitride grown on silicon (111) for solid-state lighting. *Proceedings of the National Academy of Sciences of the United States of America,* 108(25), pp. 10072–10077. https://doi.org/10.1073/pnas.1102650108.

Knuesel, R.J. and Jacobs, H.O., 2011. Self-tiling monocrystalline silicon; a process to produce electrically connected domains of Si and microconcentrator solar cell modules on plastic supports. *Advanced Materials,* 23(24), pp. 2727–2733. https://doi.org/10.1002/adma.201004533.

Li, S., Chen, W., Chu, D. and Roy, S., 2011. Self-aligned high-resolution printed polymer transistors. *Advanced Materials,* 23(35), pp. 4107–4110. https://doi.org/10.1002/adma.201101291.

Martins, R., Nathan, A., Barros, R., Pereira, L., Barquinha, P., Correia, N., Costa, R., Ahnood, A., Ferreira, I. and Fortunato, E., 2011 Complementary metal oxide semiconductor technology with and on paper. *Advanced Materials,* 23(39), pp. 4491–4496. https://doi.org/10.1002/adma.201102232.

Subramanian, V., Chang, J.B., Vornbrock, A. de la F., Huang, D.C., Jagannathan, L., Liao, F., Mattis, B., Molesa, S., Redinger, D.R., Soltman, D., Volkman, S.K., and Zhang, Q., 2008. Printed electronics for low-cost electronic systems: technology status and application development. In: S. Hall and A. Walton, eds. *ESSDERC 2008 Proceedings of the 38th European Solid-State Device Research Conference.* Edinburgh, UK, 15-19 September 2008. IEEE, pp. 17–24. https://doi.org/10.1109/ESSCIRC.2008.4681785.

Yan, H, Chen, Z, Zheng, Y, Newman, C, Quinn, J.R., Dötz, F, Kastler, M. and Facchetti, A., 2009. A high-mobility electron-transporting polymer for printed transistors. *Nature,* 457, pp. 679–686. https://doi.org/10.1038/nature07727.

Yeh, H.-J.J. and Smith, J.S., 1994, Fluidic self-assembly for the integration of GaAs light-emitting diodes on Si substrates. *IEEE Photonics Technology Letters,* 6(6), pp. 706–708. https://doi.org/10.1109/68.300169.

Flexible and Stretchable Inks for Wearable Applications

Andrew Claypole and Tim Claypole

Welsh Centre for Printing and Coating, College of Engineering, Swansea University Bay Campus,
Crymlyn Burrows, Swansea, SA1 8EN, UK
E-mail: T.C.Claypole@swansea.ac.uk

Short abstract

The inks used to create printed electronics for wearable technology, especially if it is to be attached directly to garments, must be able to bend and stretch to conform to the wearer's body and to accommodate the movement of the wearer. The performance of a conductive ink consisting of a thermoplastic polyurethane and a blend of functionalised Graphite Nano Platelets with Carbon Black developed for application to high stretch garments has been fully characterised from its viscoelastic properties as an ink through to the impact of stretching and flexing the printed ink film. The inks were subjected to full rheological testing including shear flow measurements and viscoelastic measurements using Small Amplitude Oscillatory Shear (SAOS). Extension tests of the printed layers were undertaken using a Hounsfield Tensile testing machine whilst the effect of this extension on the electrical resistance of the sample was simultaneously monitored. The addition of the nano carbons to the resin increases the elastic properties of the inks and has a direct impact on the printability. The electrical conductivity of the ink is unaffected by flexing without stretch. A change of < 5 % was observed following creasing of the samples using a 300 N load. Nominal strains of 10 % and 100 % were selected for cyclic extension testing. Following an initial stretch cycle that increased the resistance of the ink, the ink and substrate exhibited consistent resistance change with extension. This repeatable performance would allow for predictability of ink performance in wearable applications. It also suggests the potential for use as a low resistance strain sensor. Beyond this point there is an increasing loss of conductive paths as the material permanently deforms and there is an exponential increase in resistance. The ink was pulled to maximum extension, becoming non-conductive at > 300 % strain.

Keywords: conductive inks, wearable technology, rheology, tensile testing

1. Introduction and background

The ability of inks used to create printed electronics for wearable technology, especially if it is to be attached directly to garments, to be able to bend and stretch to conform to the wearer's body and to accommodate the movement of the wearer is of paramount importance (Pahalagedara, et al., 2017). An appropriate choice of binder is important in producing a flexible ink, while all other aspects of the ink will depend on functional pigments, such as Nano carbons and silver plate, used to create the ink. The composition of the ink, from the binder which gives the final coating many of its final mechanical properties, to the functional particles, such as the graphite Nano-platelets and silver flake used to impart electrical performance, will impact on the rheology and printability, as well as its physical characteristics when cured. The performance of a conductive Nano carbon ink developed for application to high stretch garments has been fully characterised from its viscoelastic properties as an ink through to the impact of stretching and flexing the printed ink film.

2. Materials and methods

The inks were subjected to full rheological testing including shear flow measurements and viscoelastic measurements using a Malvern Panalytical Kinexus rheometer. The linear viscoelastic forces (elastic shear modulus, G', viscous shear modulus, G'', and the phase angle, δ, were established using Small Amplitude Oscillatory Shear (SAOS) (Willenbacher and Georgieva, 2013). The printability was evaluated using a test pattern with a range of lines and solids appropriate for printed electronics and sensors, as well as patterns appropriate for tensile testing. These were printed on a DEK-248 screen press using a 54-70 mesh onto a thermoplastic polyurethane substrate. Surface characterisation of the prints was achieved using white light interferometry (Vecco), and sheet resistance was measured using a 4-point probe. After a simple flex test, to establish the ability of the ink to bend without changing resistance, crease testing was performed by applying a 300 N load to a bend in the sample and the effect on the electrical resistance measured. Extension tests were undertaken on 3 separate printed samples using a Hounsfield Tensile test machine, at a speed of 50 mm/min over a gripping distance of 100 mm, to measure the change in resistance of the sample when subjected to cyclic strains of 10 % and 100 % nominal strain and a maximum extension (Figure 1).

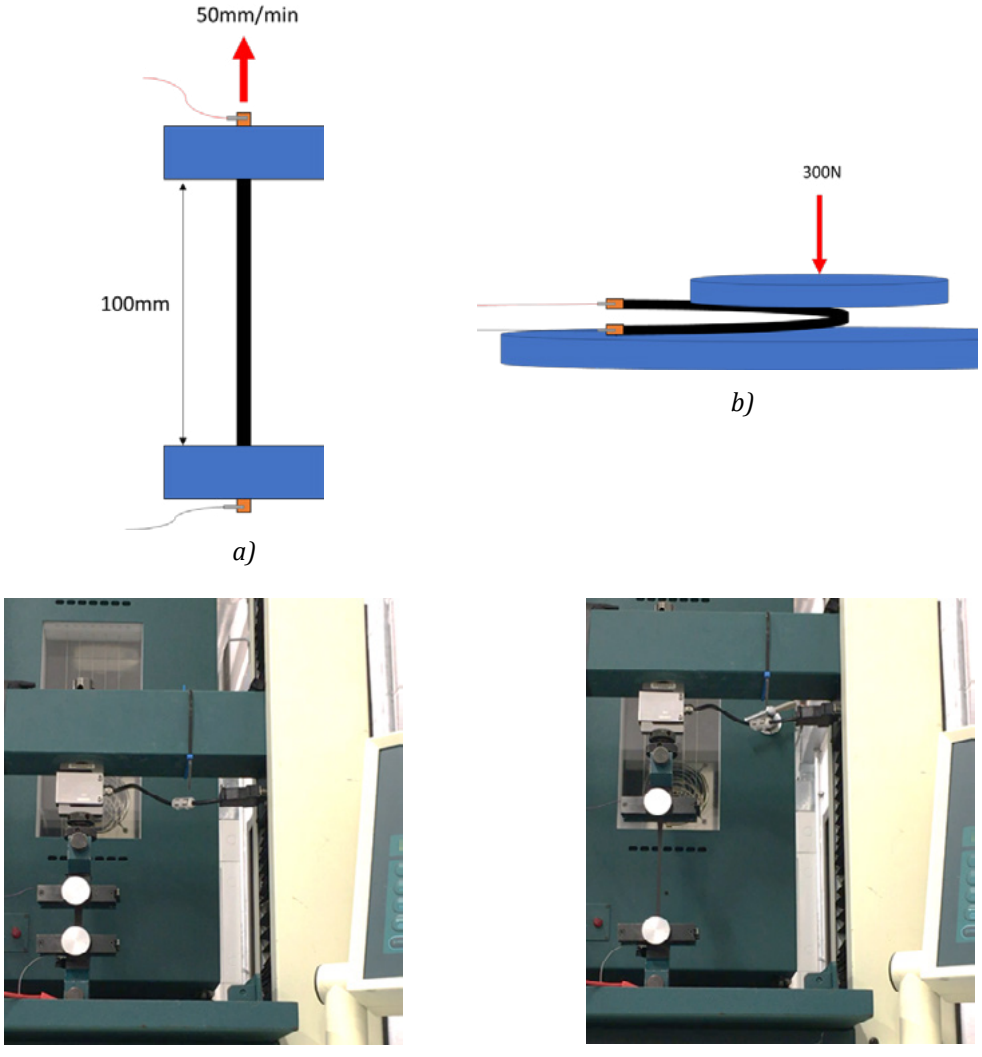

a) *b)*

c) *d)*

Figure 1: a) Extensional testing, b) Crease testing,
c) and d) Sample undergoing repeat strain tests in the Hounsfield tensile tester

3. Results and discussion

The thermoplastic polyurethane resin (TPU) used as a binder in this ink exhibited near-Newtonian behaviour over the range of shear rates tested (Figure 2). The addition of the nano carbon blend comprising functionalised graphite nano platelets (GNP) and carbon black increased the viscosity of the formulation relative to that of the pure resin and led to the development of shear thinning behaviour over the whole range of shear rates measured. This overall increase in the viscosity is due to the diversion of flow lines around particles and the enhanced distortion of these flow lines. The more pronounced increase in the low shear rate viscosity is likely due to the fractal nature of carbon black, as it freely flocculates to form a weak 3D network (Aoki, Hatano and Watanabe, 2003). Upon applying even modest shear this weak network is broken down and the carbon black particles can flow between the GNPs which in turn align with the flow. The shear stress at the limit of zero shear rate is related to the amount of force required to make a fluid flow, known as the yield stress, an artificial concept to provide an approximation of the structure strength. There is approximately zero intercept on the shear stress axis for the TPU, indicating the absence of a high yield stress in the resin itself. The addition of particles increases the amount of force required to get the materials to flow, developing significant yield stress values.

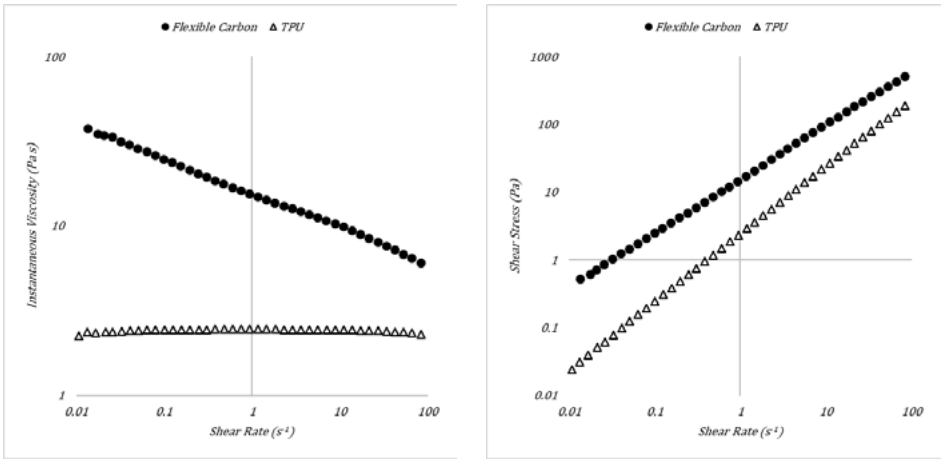

a) *b)*

Figure 2: Equilibrium viscosity and shear stress for a) the TPU, and b) the nano-carbon inks

The elastic shear modulus, G' = 6.1 Pa (Figure 3), of the unfilled TPU resin originates from the uncoiling of unstretched polymer chains and the stretching of inter-entanglement of polymer chains (Barnes, 2000). The addition of the nano carbon blend produces an increase in elastic forces caused by increased particle-polymer interactions with the GNP, increased in particle-particle interactions, whilst the carbon black increases the elastic storage, due to the fractal nature of carbon black (Figure 3). Under low flow, the carbon black particles begin to form a 3D network capable of elastically storing energy (Aoki, Hatano and Watanabe, 2003), as when a force is applied it compresses like a spring but does not break.

The phase angle is representative of the ratio of viscous to elastic forces, with a Newtonian fluid having a phase angle δ of 90° and a Hookean elastic solid having a phase angle δ of 0° (Willenbacher and Georgieva, 2013). If the viscous forces dominate, the viscous modulus is greater than the elastic modulus, $G'' > G'$, and so the phase angle δ is above 45°, and the behaviour tends to be fluid-like (Figure 3). The TPU resin has a phase angle δ of 85.6° and, thus, as supported by the almost zero yield stress, has largely Newtonian behaviour. The addition of the nano carbon blend increases both viscoelastic parameters with a decreased phase angle δ as the elastic modulus, indicating elastic forces, is increasingly dominating. This is also a result of the carbon black flocculating to form a network capable of storing energy.

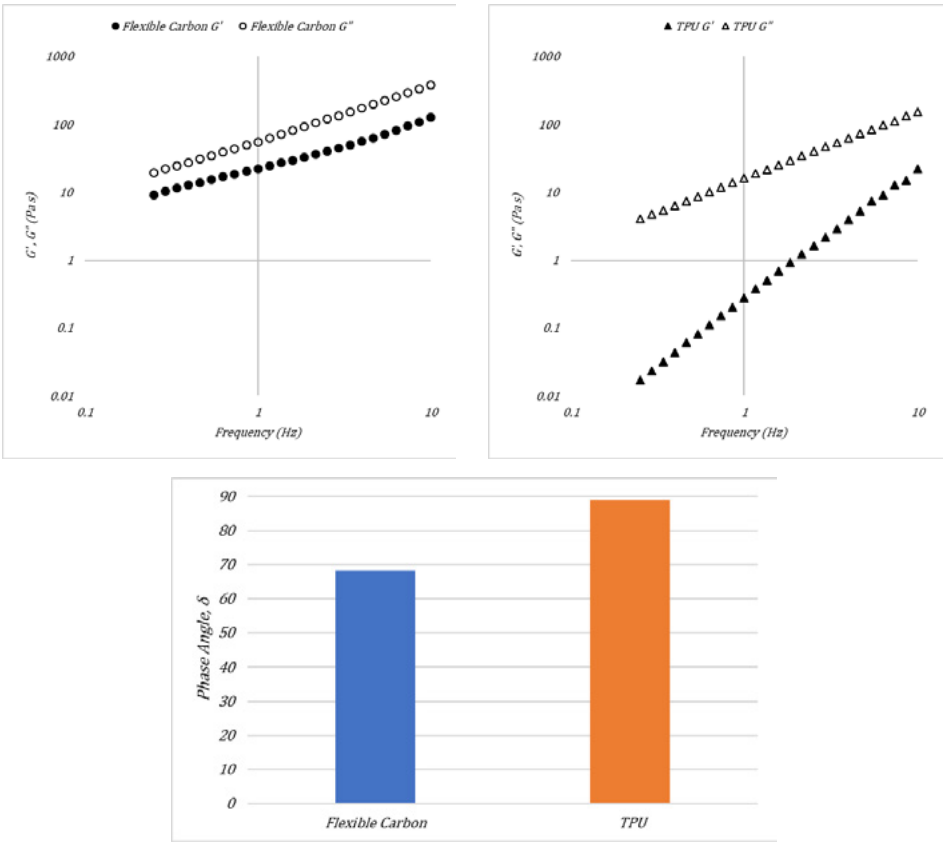

Figure 3: Viscoelastic components

The ink produces a flexible conductive print with normalised sheet resistance < 75.57 Ω/□/mil at a printed film thickness of 7.96 ± 0.78 µm. Although the ink film has a low surface roughness, there is evidence of print screen mesh marking (Figure 4). The elastic nature of the ink caused by the nano carbon loading affects the release from the screen, leading to the ink being extended elastically by adhesion to the mesh as it pulls away from the substrate linked with the increased viscosity reducing the ability to level before curing. Although addition of more carbon black would improve the bulk conductivity, it has a significant impact on the printability, as evidenced from the increased mesh marking and breakdown of the profile of the edge of the solid. This leads to a reduced function.

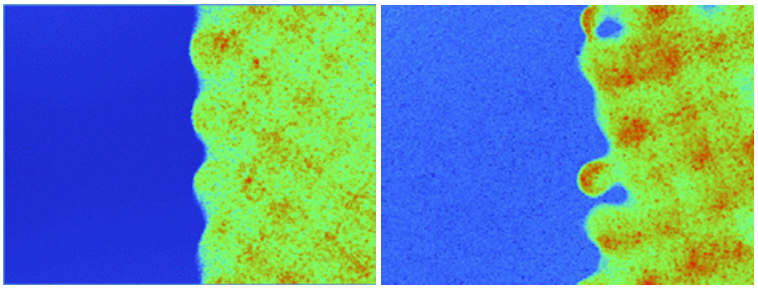

Figure 4: Mesh marking on the edge of the printed sample: increased carbon black on the right

The samples were connected to a multi-meter to measure their resistance under strain and flexing. The electrical conductivity of the ink is unaffected by flexing without stretch. Repeated bending and flexing had no impact on resistance of the printed film (Figure 5). The Hounsfield tester was used to apply a 247 N load to the sampled to create a crease. The ink showed good resistance to creasing (Figure 6) with the resistance increasing to 3.87 % during the compressive loading with this change in resistance reducing to 1.83 % once the load was removed (Table 1).

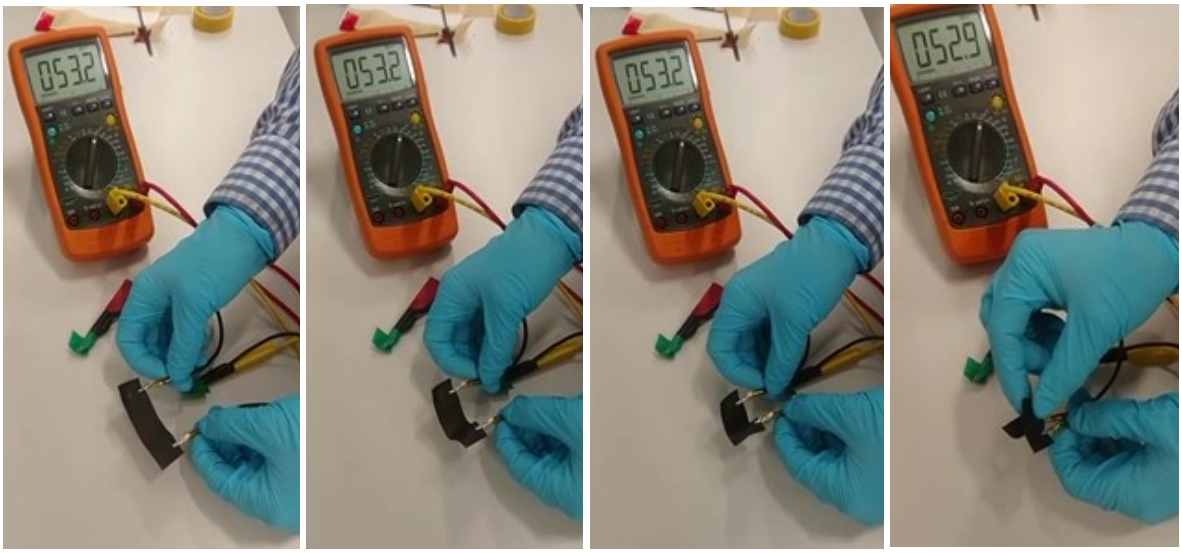

Figure 5: Conductivity flex test of the printed film

Table 1: Response of ink to applied compressive load

	Compressive loading force (N)	Resistance (Ω)	Change in resistance (%)
Before load	0	8 476 ±150	0
Compression	−247 ±35	8 809 ±150	3.87 ±0.06
Relaxation	0	8 631 ±87	1.83 ±1.00

The ink relies on percolation to achieve conductivity. The resistance remains sensibly constant over the initial extension region, below 80 % strain. Although there will be relative motion and adjustment to the alignment of the nano carbons, there is sufficient material to retain contact with a multitude of parallel paths (Figure 6). Beyond this point there is an increasing loss of conductive paths as the material permanently deforms and there is an exponential increase in resistance. The ink was pulled to maximum extension, becoming non conductive at > 300 % nominal strain.

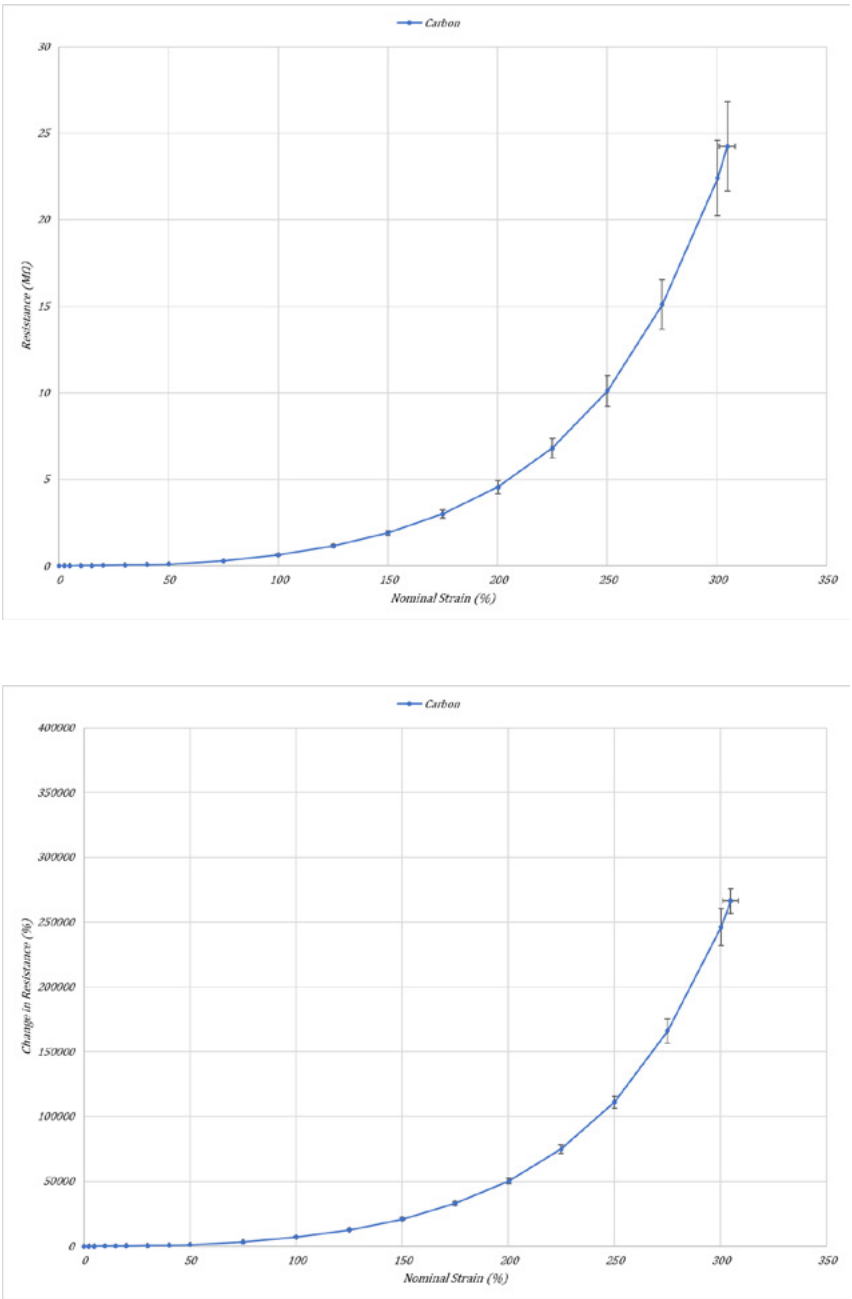

Figure 6: Resistance with strain to maximum extension

A cyclic 10 % nominal strain test was applied to the ink (Figure 7). There is an 102 % increase in resistance at 10 % during the first strain cycle, with the resistance not returning to its unstrained value and a permanent 65 % increases in the resistance of the sample when the nominal strain returned to 0 %. The sample was observed to go slack suggesting that there had been a plastic deformation of the substrate, increasing the distance between the two contacts and the resistance. This causes a realignment of the ink in the substrate interface region. Some of this change could also be due to sample settling in the grips of the tensile tester. When the cycle was repeated, there was considerable consistency. The hysteresis graph of resistance change against extension enables the repeat cycles to be overlaid. The first two cycles exhibit some permanent deformation. However, for cycles 3 to 10, the resistance is repeatable.

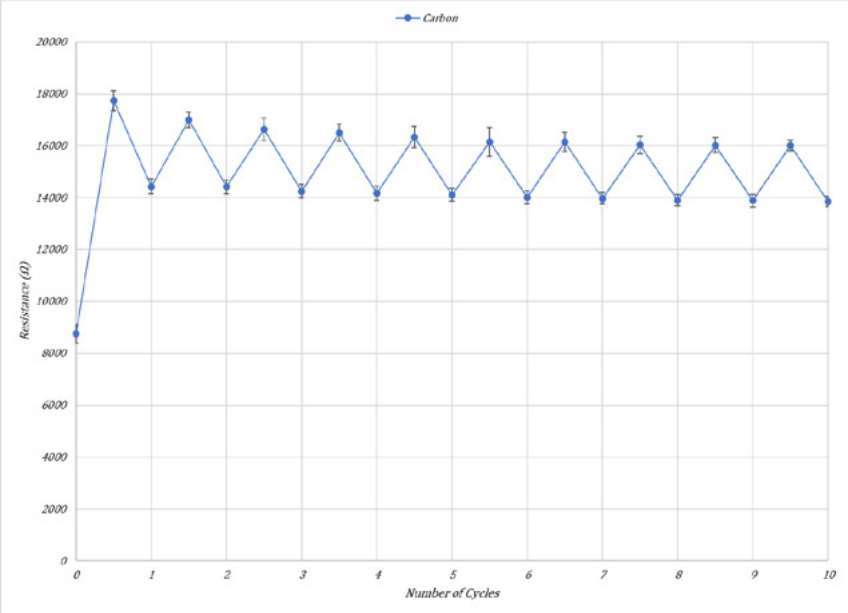

Figure 7: 10 % nominal strain – 10 × cycle, 50 mm/min extension rate

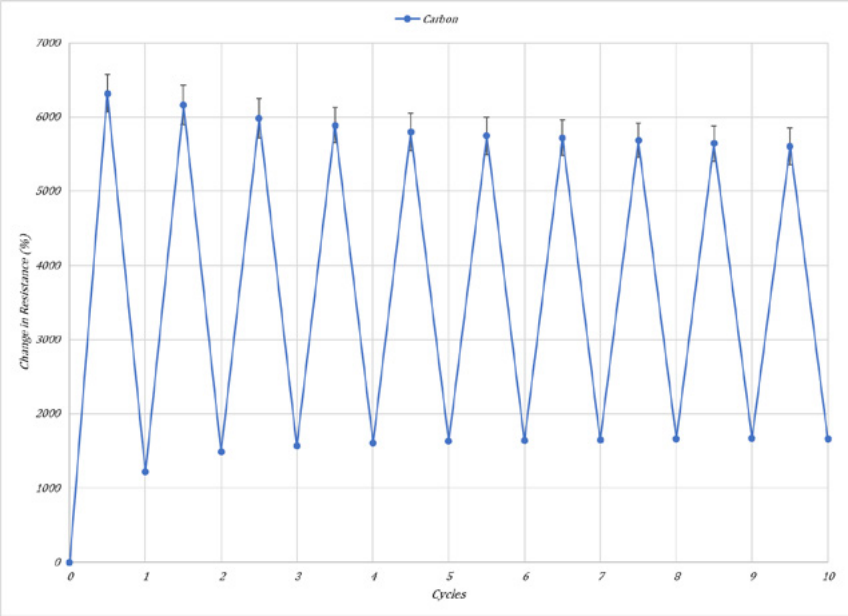

Figure 8: 100 % nominal strain – 10 × cycles, 50 mm/min extension rate

Extending the inks to 100 % nominal strain saw changes in resistance > 6 000 % at 100 % nominal strain during the first cycle (Figure 8), however after this initial deformation the change in resistance at 100 % decreases at 100 % before the change in resistance with strain becomes more consistent after 5 cycles.

4. Conclusions

A conductive ink consisting of a thermoplastic polyurethane and a blend of functionalised graphite nano platelets with carbon black developed for wearable technology has been extensively tested. The addition of the nano carbons to the resin increases the elastic properties of the inks and has a direct impact on the printability. When tested for the ability to flex and stretch, at 10 % and 100 % nominal strain, which is comparable with normal distortions of clothing, after one initial stretch cycle, the ink and substrate exhibited consistent performance. This would allow for predictability in wearable applications. It also suggests the potential for use as a low resistance strain sensor.

A simple bench-top flex test was used to demonstrate qualitatively the bendability of the ink, a more quantitative crease test was used to examine the effect of high bending forces on the ink. This will need to be refined to create a quantitative combined bend and fatigue test appropriate for wearable applications. This work is being extended to include flake and nano particle silver conductive inks.

Acknowledgements

Andrew Claypole acknowledges the financial support of Swansea University Coatings Doctoral Training Centre, which is funded by EPSRC and ESF, with additional funds from Haydale Graphene Industries.

References

Aoki, Y., Hatano, A. and Watanabe, H., 2003. Rheology of carbon black suspensions. I. Three types of viscoelastic behavior. *Rheologica acta*, 42(3), pp.209–216. https://doi.org/10.1007/s00397-002-0278-3.

Barnes, H.A., 2000. *A handbook of elementary rheology*. Aberystwyth, UK: University of Wales, Institute of Non-Newtonian Fluid Mechanics.

Pahalagedara, L.R., Siriwardane, I.W., Tissera, N.D., Wijesena, R.N. and de Silva, K.M. N., 2017. Carbon black functionalized stretchable conductive fabrics for wearable heating applications. *RSC Advances*, *7*(31), pp.19174–19180. https://doi.org/10.1039/C7RA02184D.

Willenbacher, N. and Georgieva, K., 2013. Rheology of disperse systems. In: U. Bröckel, W. Meier and G. Wagner, eds. *Product design and engineering: formulation of gels and pastes*. Weinheim, Germany: Wiley VCH, pp.7–49.

Invasive Plant-based Paper as a Substrate for Electroconductive Printing Inks

Urška Kavčič and Igor Karlovits

Pulp and Paper Institute, Ljubljana, Slovenia
E-mails: urska.kavcic@icp-lj.si; igor.karlovits@icp-lj.si

Short abstract

Invasive plant species or noxious weeds are non-native invasive plants which are harmful to the local ecosystem. Some of these plants contain enough amount of cellulose to be used for paper-based products. In this paper, three different printing materials were tested regarding suitability as a substrate for printed electronics. The samples (1) invasive plant-based paper produced by Pulp and Paper Institute made partly from Japanese knotweed (lat. Fallopia japonica), (2) commercially available Kraft cardboard and (3) Synthetic paper were printed using electroconductive printing ink with inkjet printing technology. The comparison regarding substrates roughness and contact angle (with water and inkjet printing ink) was performed. Besides that, the sheet resistance of several printed layers as well the abrasion resistance of the printed conductive ink was tested. The results indicate higher surfaces roughness and porosity for the invasive plant-based paper which resulted in higher sheet resistance on a lower number of printed layer, while already on 3 layers of ink deposition the results are similar to smoother commercially available printing materials. The invasive plant paper also resulted in weaker abrasion resistance due to higher surface roughness and smaller surface strength of the base paper.

Keywords: invasive plant paper, printed electronics, sheet resistance, abrasion resistance

1. Introduction and background

Although many European cities and urban areas are facing the issue of invasive alien plant species, only a few are using them as a useful resource for local cellulose production or manufacture of useful products. The Pulp and Paper Institute from Ljubljana has among first produced papers from different types of these plant species in cooperation with the local community towards a circular economy. Although paper substrates have been previously studied from the prospect of printing them with conductive inks, there are no researches in the field of invasive plant-based paper as a substrate for printed electronics. Paper properties which determine the printability and thus good conductivity are roughness, porosity, wettability, dimensional stability and reaction to humidity. A thorough review of cellulosic material properties as a green material for electronics can be found in Toivakka, Peltonen and Österbacka (2017). Several authors developed novel specially designed papers using several coating layers (Bollström, 2013; Trnovec, et al., 2009) where the paper substrate was modified with additional layers to mimic the behaviour of very smooth foils needed for printed electronics. The recent development of nanocellulose materials also enable testing it with classic paperboard products, as Hoeng, et al. (2017) presented the addition of cellulose nanocrystals coating significantly limits the ink diffusion into the porous substrate by modification of the ink drop absorption kinetics, leading to the printing of well-defined conductive patterns. Some of the solutions question the sustainability of these materials as plastic mimicking can impose a hidden cost of production and recycling of these materials as presented in an overview of deinking of these type of products by Blayo, et al. (2018). There was some research done regarding the possibility of printing RFID and other printed electronics elements on recycled boards (Kavčič, et al., 2013). It was concluded, that the printing material has an impact on the printing properties of the printed RFID antennas but it has a small effect on the final sheet resistance and final antenna operation. But not all printed electronics application needs such high demands on paper regarding surface and structural properties. For example, thermochromic displays

(Kavčič, et al., 2019) can be printed on cardboard, as well as UHF RFID (Kavčič, Maček and Muck, 2015), while there is no need to print very precise lines with small spacing. One of the alternatives is to use invasive plant fibres which can be locally harvested and processed to paper substrates. There have been done some researches regarding printability of invasive plant-based papers (Lavrič, et al., 2018), but no data regarding the suitability of these type of papers for printed electronics. The research presents a part of the ongoing study of printing conductive ink on paper made of unconventional, invasive plant fibre resource.

2. Materials and methods

In the present research, three different printing materials as a substrate for printing electronics were used. As a paper substrate, 240 g/m^2 cardboard made from Japanese knotweed fibres (Japanese knotweed) which has a 40 % of alien plant fibres combined with softwood and hardwood fibres, fillers and other additives, was used. For comparison, commercially available 250 g/m^2 Excellent Top brown cardboard (producer MM Karton) made of kraft fibres (Kraft cardboard) and 250 g/m^2 Agfa Synapse synthetic paper (Synthetic paper) were used.

The printing substrates were characterized through PPS print surf roughness, contact angle and penetration dynamics of liquids on five testing samples. The print surface roughness was determined using PPS print surf roughness tester according to DIN ISO 8791-4 standard (International Organization for Standardization, 2017) and using 1960 kPa contact pressure and with SEM microscopy. The dynamic contact angle was evaluated with Fibrodat 1100 measuring device using water drops of 6 µl as the inks are aqueous dispersions and with the used silver conductive ink (with drop size 1 µl). Penetration dynamics of liquid with porosity evaluation was carried out by using an ultrasound method using Emtec PDA 02 instrument with IPA (a mass fraction of 15 % isopropyl alcohol) testing liquid.

After substrate analysis, the samples were printed with FujiFilm Dimatix DMP-2831 printer using Metalon JS-A102A nanosilver conductive printing ink (Novacentrix). Conductive lines were printed in 1, 2 and 3 layers deposition using 21.8 µm drop spacing (800 dpi) and head angle of 7.2°. The platen temperature was set to 50 °C. During the printing, the following thickness settings were used: 400 µm for Japanese knotweed, 500 µm for Kraft cardboard and 300 µm for Synthetic paper. The printed samples were dried in a heated oven at 90 °C for 60 minutes. After drying the electrical resistance of all printed lines was measured using a multimeter, while abrasion resistance was conducted using Pruefbau Quartant Abrasion tester using 100 cycle abrasions. After the abrasion resistance test, samples were scanned with a Canon CanoScan 5600F scanner and evaluated using ImageJ software. The total area percentage of the printed ink that remains after the abrasion test was presented.

3. Results and discussion

The PPS surface roughness of the papers was measured on multiple sheets and location. As wettability of the surface is an important factor in inkjet printing, the dynamic contact angle of the surfaces was also measured. The average results for PPS surface roughness and contact angles of the surfaces (with water drop) after 1 second are presented in Figure 1. Besides measurements of roughness, SEM images of testing material surfaces and cross sections as well are also presented in Figure 2, to better understand the difference between the printing materials surfaces.

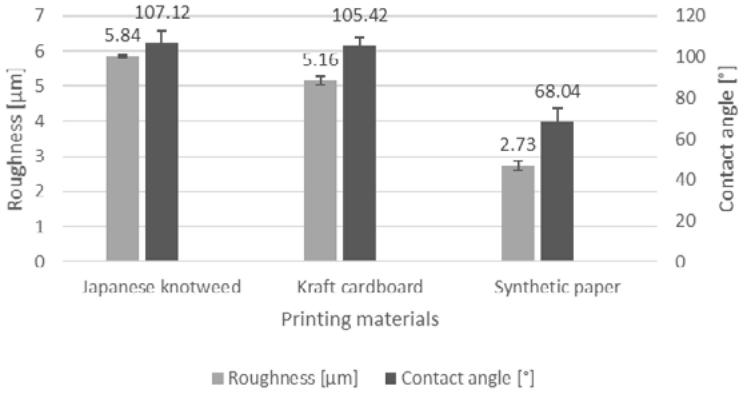

Figure 1: Average values of surface roughness and contact angles

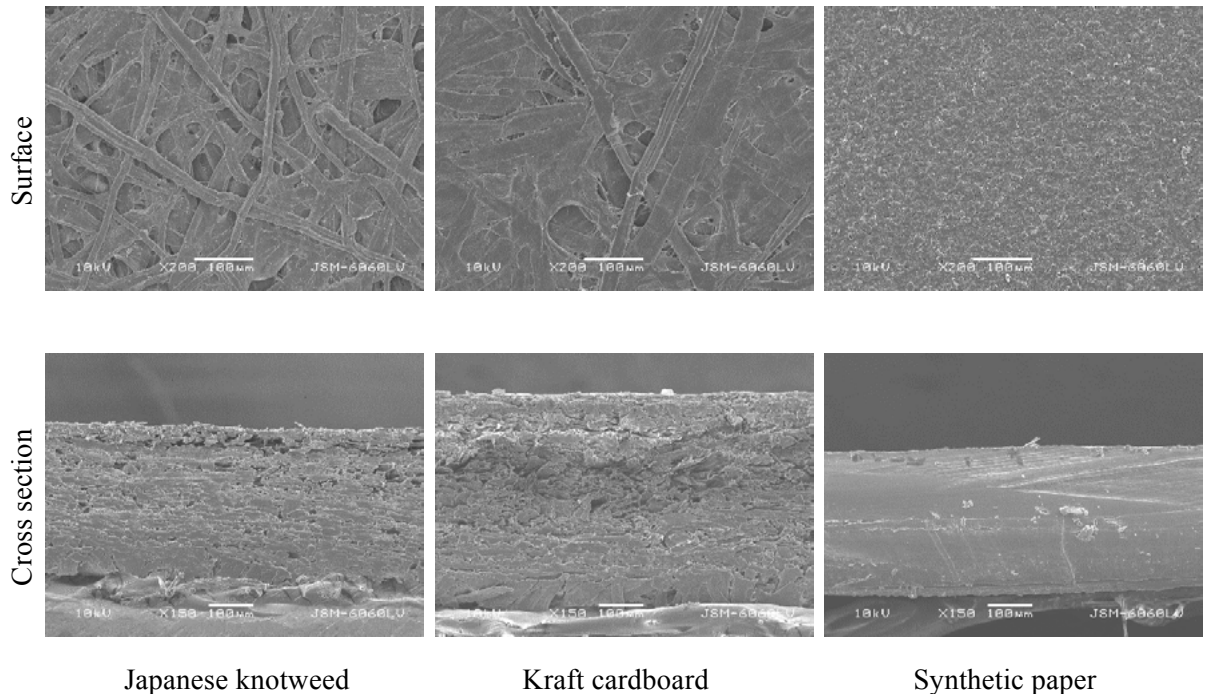

Figure 2: SEM images of surfaces (200 × magnification) and cross sections (150 × magnification) of printing materials

From Figure 1 one can observe that the Synthetic paper had the lowest roughness value (2.73 µm) while the invasive plant-based Japanese knotweed paper has similar roughness properties than virgin Kraft commercially available cardboard (5.84 µm and 5.16 µm respectively), which is seen also from the SEM images presented in Figure 2. The highest contact angle of the three samples after 1 second had the Japanese knotweed sample with a value of 107° (similar as Kraft cardboard) while the Synthetic paper had the lowest value of 68°. To further evaluate the surface porosity regarding ink spreading and absorption, the absorption properties of the samples were evaluated using dynamic liquid penetration measurements with IPA testing liquid.

The appropriate absorption curves which present the intensity of the signal in first 10 seconds after immersion of the sample into the liquid are presented in Figure 3.

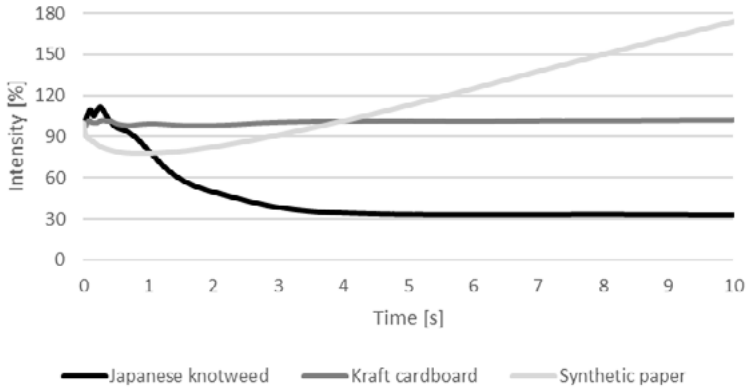

Figure 3: Dynamic absorption curves of different paper substrates

The absorption measurement indicates that the Japanese knotweed-based paper has the highest absorption rate and thus porosity while the intensity of the ultrasound signal drops intensively in the first few seconds. On the other hand, the Kraft cardboard and Synthetic paper have very low absorption and porosity.

To better simulate and compare contact angle with the inkjet printing process, besides the contact angle with water and penetration dynamics, the dynamic contact angle with the real silver inkjet printing ink was performed (Figure 4). It is seen, that contrary to contact angle with water, the highest angle after 1 s is measured on Kraft cardboard (44°), while for Japanese knotweed (30°) and the lowest for Synthetic paper (20°). The Synthetic paper had very fast ink spreading mechanism on the surface as no absorption was present, while the Japanese knotweed had lower contact angle than Kraft cardboard, due to absorption.

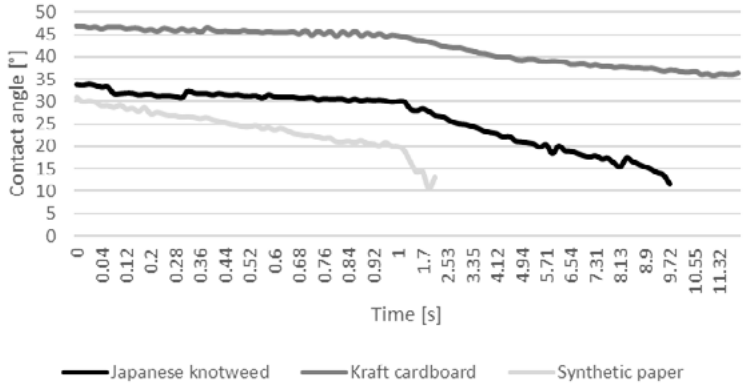

Figure 4: Dynamic contact angle of silver ink jet printing ink on printing materials

To evaluate the adequacy of printing materials for using as a substrate for printing electronics, the sheet resistance of the printed lines was measured using multimeter Voltcraft LCR-300. As presented in Figure 5, lines printed just in one ink layer do not conduct regardless of the printing substrate (which is most probably due to high line spacing). All lines printed in two ink layers conduct; the lowest sheet resistance of lines is observed on Kraft cardboard (229 kΩ/sq), and the largest (658 kΩ/sq) on Japanese knotweed. The differences among samples are large and can be related to roughness, porosity and contact angle of all printing materials. When three layers of printing ink are printed on substrates, differences between samples diminishes. The lowest sheet resistances have lines printed on Synthetic paper (30 Ω/sq), but lines printed on Japanese knotweed and Kraft cardboard have same sheet resistance (70 Ω/sq), which can indicate that the ink thickness is large enough to balance a small difference in roughness. The printed line sheet resistance results are presented in Figure 5.

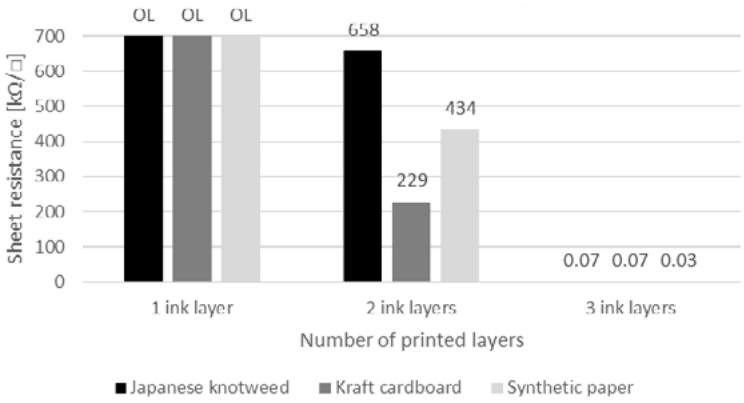

Figure 5: Sheet resistance on a different type of printing materials

Besides wetting, which represents substrate-ink interface behaviour mechanism for the wet phase adhesion, a property and factor regarding bonded and cured ink-paper structure is also important. The abrasion was performed using Pruefbau Quadrant Abrasion Tester with 100 cycle testing. The patches were scanned and image processing in ImageJ was used to evaluate the remaining surface of the printed conductive ink of the abrasion patches. In Figure 6 the results of the patches after 100 cycle abrasion are presented.

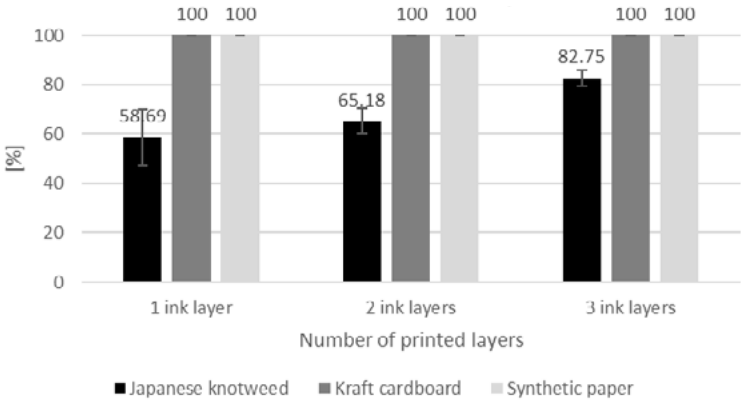

Figure 6: The abrasion results of the conductive ink printed on Synthetic paper, Japanese knotweed and Kraft cardboard

Conductive ink printed on Japanese knotweed has very poor abrasion resistance, which can be seen in Figure 6. When printed in one layer, only about 58.69 % of conductive ink area remains, while when printed in two layers, about 65.18 % and 82.75 % with three layer ink deposition. The reason for lower abrasion resistance is low printed ink thickness, high surface roughness and lower surface strength of the fibre bonding in the paper structure. Kraft cardboard and the Synthetic paper has good abrasion resistance at all layers after 100 cycles. It should be noted, that even though no surface has appeared on the printed sample, due to abrasion on the Synthetic and Kraft paper, some ink was noticeable on the paper which was used for abrasion.

4. Conclusions

On the base of the results, it can be concluded that the invasive plant-based paper has a higher roughness, contact angle and porosity as the Synthetic paper and virgin Kraft fibre cardboard. Also, it has shown a lower abrasion resistance which is due to higher roughness and especially due to lower surface strength of

the fibre bonding in the structure. The abrasion resistance of Japanese knotweed could be enhanced with the addition of bio-based materials (instead of latex) to enhance surface strength and will be further investigated. On the other hand, the sheet resistivity of lines printed on Japanese knotweed in three layer ink deposition is the same as when printed on Kraft cardboard and comparable to lines printed on Synthetic paper. Printing with more conductive ink layers will be investigated in the future. No larger line structure deviations were observed which implicates the possibility of using invasive plant-based paper in printed electronics applications where the conductive lines do not need to be printed very precisely and with small line spacing. Besides all the obvious problems with paper-based substrates regarding moisture, these results indicate that invasive plant-based papers can be a viable alternative for lower end printed electronics products.

Acknowledgements

The work was carried out within the RDI project Cel.Cycle: »Potential of biomass for development of advanced materials and bio-based products« (contract number: OP20.00365), co-financed by the Republic of Slovenia, Ministry of Education, Science and Sport and European Union under the European Regional Development Fund, 2016–2020. The authors would like to thank Faculty of Mechanical Engineering, University of Maribor, Slovenia, especially Dr Matej Bračič and Natalija Virant for the opportunity and help with using Dimatix printer.

References

Blayo, A., Marlin, N. and Chrétien, C., 2018. About deinking of paper-based printed electronics. In: *Advances of Printing and Media Technology: Proceedings of the 45th International Research Conference of iarigai*. Warsaw, Poland, 3–7 October 2018, pp. 157–164.

Bollström, R., 2013. *Paper for printed electronics and functionality*. Doctoral thesis. Åbo Akademi University.

Hoeng, F., Bras, J., Gicquel, E., Krosnicki, G. and Denneulin, A., 2017. Inkjet printing of nanocellulose–silver ink onto nanocellulose coated cardboard. *RSC Advances*, 7(25), pp. 15372–15381. https://doi.org/10.1039/C6RA23667G.

International Organization for Standardization, 2017. *ISO 8791-4: 2007, Determination of roughness/ smoothness (air leak methods) – Part 4: Print-surf method*. Geneva: ISO.

Kavčič, U., Pavlovič, L., Pivar, M., Đokić, M., Batagelj, B. and Muck, T., 2013. Printed electronics on recycled paper and cardboards. *Journal of Microelectronics, Electronic Components and Materials*, 43(1), pp. 50–57.

Kavčič, U., Maček, M. and Muck, T., 2015. Ultra-high frequency radio frequency identification tag antennas printed directly onto cardboard used for the manufacture of pharmaceutical packaging. *Journal of Imaging Science and Technology*, 59(5), pp. 50504–1–50504–8. https://doi.org/10.2352/J.ImagingSci. Technol.2015.59.5.050504.

Kavčič, U., Mraović, M., Bračko, S. and Muck, D., 2019. Printed thermochromic displays. *Coloration Technology*, 135(1), pp. 60–66. https://doi.org/10.1111/cote.12372.

Lavrič, G., Pleša, T., Mendizza, A., Ropret, M., Karlovits, I. and Gregor-Svetec, D., 2018. Printability characteristics of paper made from a Japanese knotweed. In: N. Kašiković, ed. *Proceedings, 9th International Symposium on Graphic Engineering and Design GRID 2018.* Novi Sad, Serbia, 8–10 November 2018. Novi Sad: University of Novi Sad, Faculty of Technical Sciences, pp. 99–102. https://doi.org/10.24867/GRID-2018-p11.

Toivakka, M., Peltonen, J. and Österbacka, R., 2017. Paper Electronics. In: M. Irimia-Vladu, E.D. Glowacki, N.S. Sariciftci and S. Bauer, eds. *Green Materials for Electronics*. Weinheim: Wiley-VCH & Co. KGaA, pp.163–189.

Trnovec, B., Stanel, M., Hahn, U., Hübler, A.C., Kempa, H., Sangl, R. and Forster, M., 2009. Coated Paper for Printed Electronics. *Professional Papermaking*, 1, pp. 48–51.

Study of Colour Change in the Course of Drying on Prints created using Offset Printing Technology

Pál Görgényi-Tóth, Csaba Horváth and László Koltai

Óbuda University, Institute of Mediatechnology and Light Industry Engineering, Budapest, Hungary
E-mails: gorgenyi.pal@rkk.uni-obuda.hu; horvath.csaba@rkk.uni-obuda.hu; koltai.laszlo@rkk.uni-obuda.hu

Short abstract

For recurring orders, printing customers tend to present earlier prints as colour samples. When these samples are used for printing, and the prints are rechecked after 24–36 hours, differences will be seen between the colours of the printed image and the sample. The goal of this study is to eliminate such differences, or – in other words – describe the colour changes resulting from the drying of printing ink, suggest solutions for the measurability of the differences. Different print technologies use varied inks (solvent-based, inks dried by oxidation, inks dried by UV radiation), but all of them are affected by colour change called dryback. This means that the ink that is still wet after printing has colour properties that differ from those of the ink after drying. During the printing process, it is usually possible to measure the colour of the still wet print accurately. A polarizing filter is installed in spectrophotometers in order to perform this study, which tries to measure the colour characteristics of the print, eliminating surface reflection. This research work determines the point when the ink can be considered to be dried on the carrier (paper), until when the colour of the printed ink changes, what physical properties influence the drying of the ink and how (for instance, the carrier surface, temperature, air humidity, composition of the ink, etc.). By altering these physical variables, such a mathematical correlation is defined that specifies how colour properties change in the course of drying, and an instrument will also be devised to determine – with the use of a mathematical model – what colour characteristics the still wet print will have after complete drying in order to eliminate colour differences between the two printing runs. This paper intends to present the first tests and the resulting conclusions.

Keywords: printing inks, carrier drying, autotype prints, colour stimulus difference, colour change

1. Objectives of the research

Industrial printing inks solidify on the paper through various drying mechanisms. There are differences between the dying processes of the “conventional” ink drying by oxidation, a solvent-based ink and any ink drying by UV radiation (Kipphan, 2001). In the case of the offset technology, ink drying is a complex process. Polymerization caused by oxidation (that is why prints are powdered in case of sheetfed offset ink; due to their size, the particles create an air gap between two sheets, allowing free airflow in between the sheets (Huber Group, 2013), evaporation (for example gravure or flexo ink), and penetration (ink of coldset printing dries this way) also play their part in the process of drying. As experience shows during the drying process, different values in terms of colour characteristics (density, colour stimulus difference) can be observed once ink has fully dried on the paper, as compared to colour characteristics measured right after printing (Schulz, 2008). This phenomenon is called dryback (Sahinbaskan and Köse, 2010; Schulz and Endrédy, 2005).

Factors influencing the ink drying process:

- Additives in the ink containing dryers
- Ink viscosity
- Quantity and quality of the lubricant used during printing

- Ambient air temperature
- Ambient air humidity
- Paper surface
- Paper volume and
- Air flow (oxygen concentration changes in case of air flow).

Our research looks into these factors, as well as their role in the drying mechanism. 2^P experiment planning is one of the methods for the Design of Experiments (DOE). It is also known as factorial (with reference to the input characteristics) experimental design. In the course of printing, ink drying is affected by several factors (paper surface, air temperature and humidity, pH of the liquid lubricant, etc.), and varying them raises the number of experiments to be conducted to thousands. It is where 2^P experiment planning is applied in order to determine which of the factors have strong influence on the drying of the ink, as then they should be examined, varied (Breyfogle III, 1999). This method is used to determine which factors influence drying, as well as the most dominant parameters by measuring colour changes in the course of drying after as many ways of modifications as possible.

Our goal is to define the change based on the exact measurements, design of a mathematical model, develop a software application for the existing measuring devices (densitometer, spectrophotometer) with the help of an algorithm based on the mathematical model, or make a new measuring instrument. This software would be suitable for determining (by entering variable data, i.e. temperature, humidity prevailing in the course of printing, the type of paper and ink used for printing, etc.) the post-drying colour characteristics of a specific colour in order to achieve the same colours on the still wet print after dryback as those of the reference standard.

For the research, two phases of the experiments have been defined. The first stage of experiments is carried out under laboratory circumstances, while the second phase of experiments are intended to include pilot measurements under production conditions to confirm, amend or sometimes disprove the results obtained in laboratory tests.

For the pilot measurements under production circumstances, primarily offset printing has been selected. This is the technology where the applied ink dries in the most complex way, and colour changes also tend to be the most striking. Offset printing is the most complex printing technology: liquid lubricant is necessary for the selectivity of the image and non-image areas, while rheological properties (viscosity, tack value) need to be changed; it is achieved with the use of a roller chain, the process of printing is indirect, meaning that the ink is applied to the carrier from a blanket and not the printing plate for improved pressing, and all these factors influence the spread and drying of the ink.

To conduct the experiments, from among the papers most frequently used in the printing industry 2 different print media types of the same square meter weight (100 g/m^2) have been used, but with different structures and characteristics:

- offset (uncoated)
- glossy paper (coated)

The measurements were started with the 4 colours [cyan, magenta, yellow and black (key)] of autotype printing, since these are the colours that are basically used for colour printing. These 4 colours are suitable for determining the mathematical correlations among the colour properties, and later the basic colours of the direct colours are used for checking, adjusting the mathematical formula.

Today's technologies produce inks that dry "immediately". In fact, it means that the ink layer on the surface hardens to become touch-safe (it cannot be smeared), but within the layer the process of drying takes a

long time, up to 24–36 hours (Bisset, et al., 1979). As the ink used in any printing technology has some thickness, surface drying is followed by a similar process in the inside of the layer, while its colour changes. Therefore, the study was launched with a laboratory experiment to determine the time period during which the offset ink becomes fully dry. Virtually, the setting of the printed ink was examined as a function of time.

This study was followed by a second, similar laboratory experiment conducted at the Hungarian company of Sun Chemical Corporation, where the colour changes of the printed inks were examined for a preset period of 1 hour at fixed temperature and humidity. For each sample, the density and hues (CIE L^*, a^*, b^*) were measured, and then comparable values were calculated in the form of an Excel spreadsheet prepared in line with the calculations for chromatic stimulus differences published by Sharma, Wu and Dalal (2005).

The next measurements are planned to be performed on an offset printing machine to see what colour changes can be measured with the alteration of variable values in the course of ink drying.

2. Materials and methods

An IGT C1 Offset and Letterpress Proofer Series test printing machine was used for the basic experiments conducted at the ink laboratory (Figure 1).

Figure 1: IGT C1

The test strip (on coated and uncoated papers) made with the test printing machine represented the measurement fields with 100 % fill ratio.

The inks of Sun Chemical SunLit Intense Process were used for the tests with all the three selected carriers (INT41: yellow ink, INT 39: a magenta ink, INT 38: cyan ink and INT 24: black. Rheological data of the inks are shown in Table 1.

Table 1: Data of the examined inks

Inks	INT41	INT39	INT38	INT24
Viscosity Rheometer 50 s^{-1}, 23 °C, [Pa·s]	45–60	70–90	75–95	42–55
Yield value Rheometer 2 s^{-1}, 23 °C, [Pa·s]	65–120	90–170	90–170	60–100
Tack Thwing Albert 800 rpm [g·m]	7.5–10.5	8.5–11.5	9–12	8.5–11.5

Ink density was set to similar values in the case of all carriers (for coated paper: D_C=1.5, D_M=1.6, D_Y=1.4, D_K=1.5; for uncoated paper: D_C=1.45, D_M=1.45, D_Y=1.25, D_K=1.45). For the first measurement, in a specific period of time after printing a setting test was performed, meaning that a clean sheet of paper featuring the same properties as the printed paper was placed over the printed section, and run through the IGT C1 test

printing machine. Thereafter, density values were measured in the set print, and Murray-Davis equation was used to calculate the filling ratio (**7**), which was in correlation with the ink coverage on the paper. For the second laboratory test, the colour properties of the samples were measured at preset time intervals after printing.

The colours were measured with an X-Rite eXact type spectrophotometer (instrument settings: D50 and 45°/0° diffuse illumination, 2° viewing angle, without M1 filter). The test focused on the measurement of the CIE L^*, a^*, b^*; L^*, C, H; X, Y, Z and density values for colours. Instrument repeatability could be described by 0.01; 0.02 accuracy (Szilágyi, 2011).

In the test room, air temperature and humidity were monitored continuously. During the measurements, both temperature and humidity were constant (the temperature was 26 °C, while relative humidity fell in the range of 48–52 %).

3. Results and discussion

As for all the 4 colours, the same conclusions could be drawn, here only the setting of the magenta printing ink is analyzed. During the first laboratory measurement, setting was examined by measuring ink density on the paper used to test setting (Figure 2), and then from the resulting density values filling ratios were calculated (Figure 3). The filling ratio is to be understood as the optical filling ratio. In setting tests, it means the ink-covered part of the given paper surface (in this case, the area corresponds to the area of the aperture of the eXact measuring instrument). Measurements can be made with the use of the program incorporated in the measuring instrument, while the density values can be determined by applying the Murray-Davies equation for calculation.

The dots on the curve indicate the times of the setting on the given paper type with the same time intervals used for each of the carriers. In the first period (1–5 minutes), high filling ratios can be seen for both carriers.

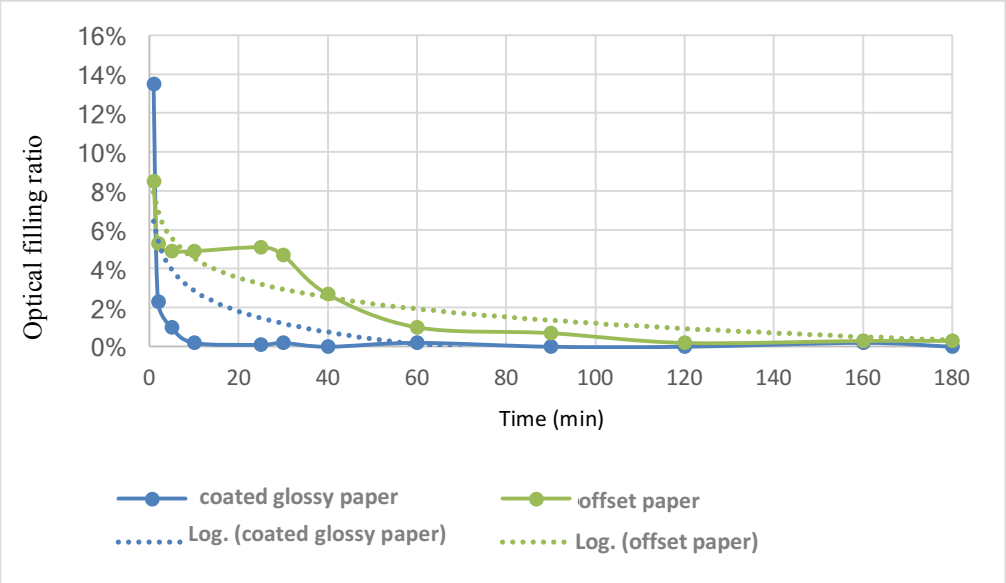

Figure 2: Degree of the setting of the magenta ink

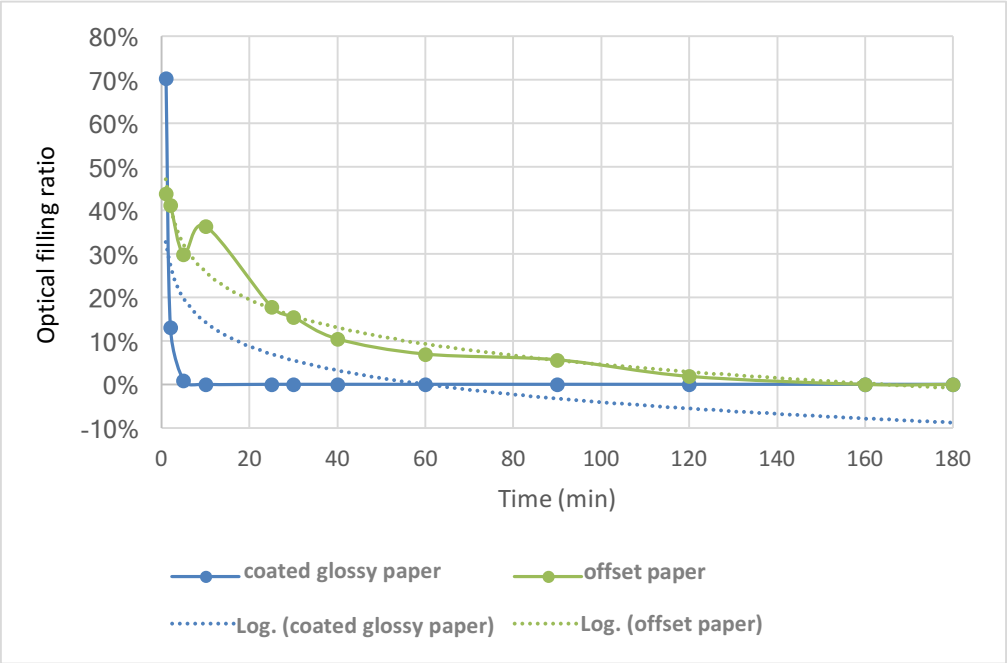

Figure 3: Calculated filling ratio for the magenta ink

To each curve, a regression curve was applied. Showing monotonically decreasing tendencies, these logarithmic trend curves properly model the process of ink drying. 120 minutes after printing, the filling ratio for the coated glossy paper and offset paper was 0.0 % and 0.02 %, respectively, indicating the point where the smallest setting values were measured for all the three carriers. It was also visible for the naked eye that over time less ink was transferred to the paper, meaning that the colour of the ink was gradually fading, which could be visually detected. The last setting test was conducted in 180 minutes, when no setting could be observed at all.

During the setting test, the percentage ratio of the paper covered in ink was considered to assume full drying. By measuring the density values of the set prints at several locations, the Murray-Davies equation was used to determine the degree of the set. The Murray-Davies equation:

$$A = \frac{1 - 10^{-D_h}}{1 - 10^{-D_f}} \cdot 100 \qquad [1]$$

A – covered area, %
D_f – density of the fulltone area
D_h – density of the halftone area

For each of the inks, curves that were similar to the one in Figure 3 resulted.

During the second series of laboratory measurements, changes in the colour components were measured as a function of time, for 1 hour, and then the measurements were repeated exactly after 3 days (when the ink was expected to be completely dry) in order to compare the previous values to the values of the completely dry ink colours (see Figures 9–11). We also intend to perform the examination of the ink drying process in order to determine when an ink layer can be considered to be completely dry, and no further colour changes can be expected (in this respect a remark in relation to the X-Rite company is that it would be nice to design an application allowing measurement intervals for automatic measurements so that measurements could be made for 24 or even 48 hours in every 15 minutes).

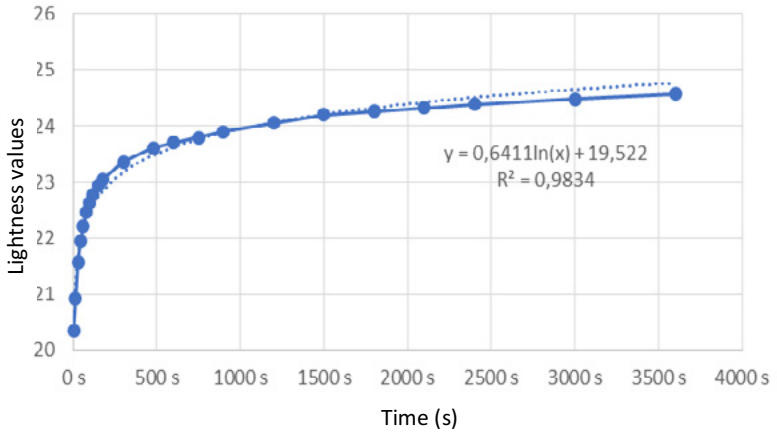

Figure 4: Lightness values L for black ink on uncoated paper*

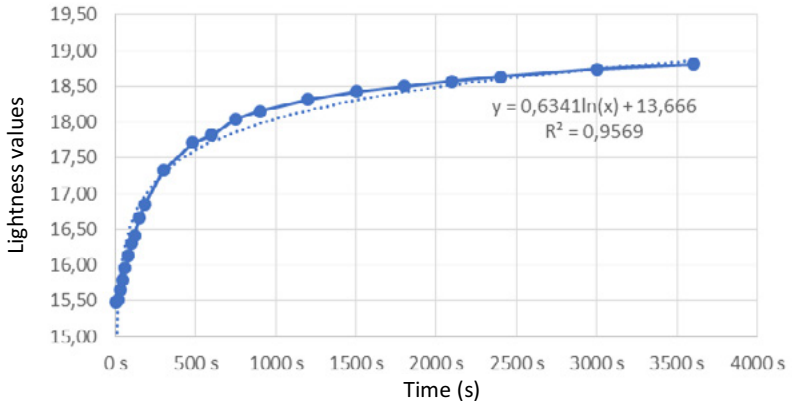

Figure 5: Lightness values L for black ink on coated paper*

The changes are illustrated in diagrams as well, and the diagrams include the formula of the function best fitting the curve, as well as its regression. The regression values are 98–99 nearly at all times, which means that the calculated curve fits the measured data. For all the four colours, the same conclusions could be drawn (that are also detailed in this paper), and therefore here only black printing ink is analyzed. Illustrating the lightness values versus time, the following changes were detected (Figures 4 and 5).

In the large part of the measurements, the brightness values changed versus time according to a natural logarithm function. The exceptions included yellow colour in the case of coated and uncoated papers, as well as magenta for coated papers.

The colour changes measured on CIELAB a^*b^* plane are shown in Figures 6 and 7 (the time of the measurement is indicated at the measurement points to identify the curve changes):

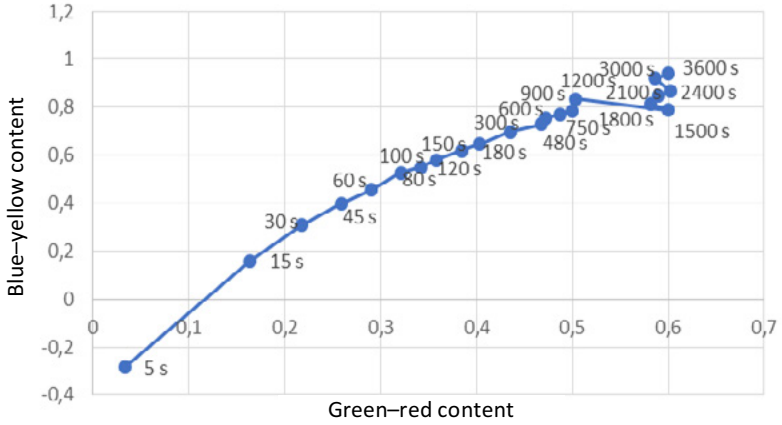

*Figure 6: Changes shown in the CIELAB a*b* plane for black ink on uncoated paper*

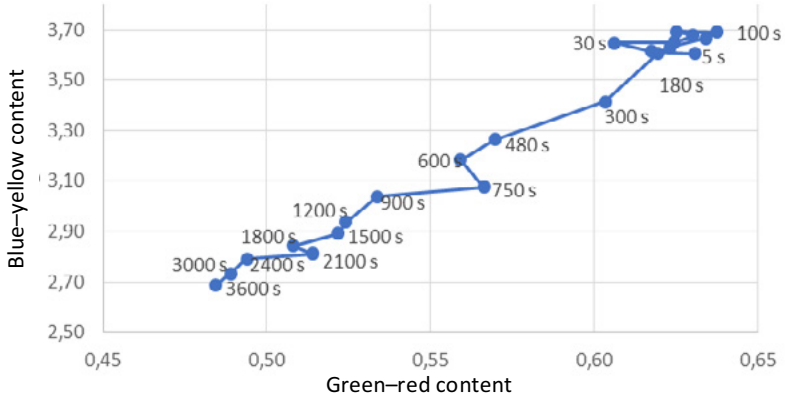

*Figure 7: Changes shown in the CIELAB a*b* plane for black ink on coated paper*

The graphs show how colours changed in the course of drying. For both paper types, black colour was monotonically increasing with a shift towards yellow–red, meaning that the colour became darker. The graphs of the cyan colour indicate that the blue–yellow content shifted towards blue for both paper types, whereas the green–red content moved towards red. In all paper types, the colour of the cyan ink shifted towards a reddish blue tone. The magenta colour changed towards yellow and red colours, or blue in the case of coated paper. On the other hand, yellow colour changed differently on the two types of papers in the course of drying: shifts towards yellow–green, red–blue and blue–green were equally observed.

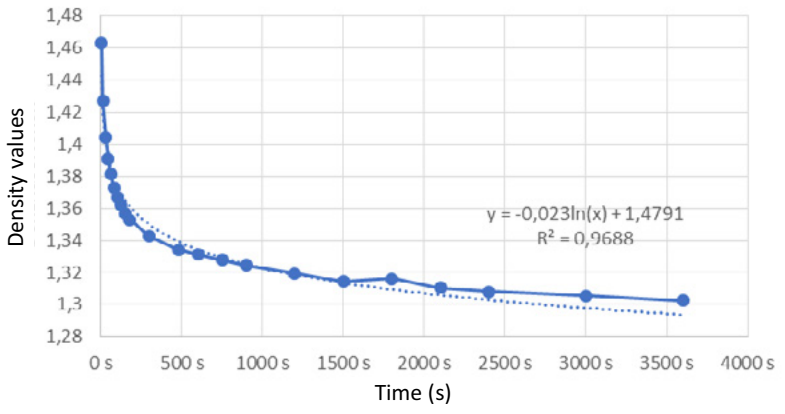

Figure 8: Changes in density values for black ink on uncoated paper

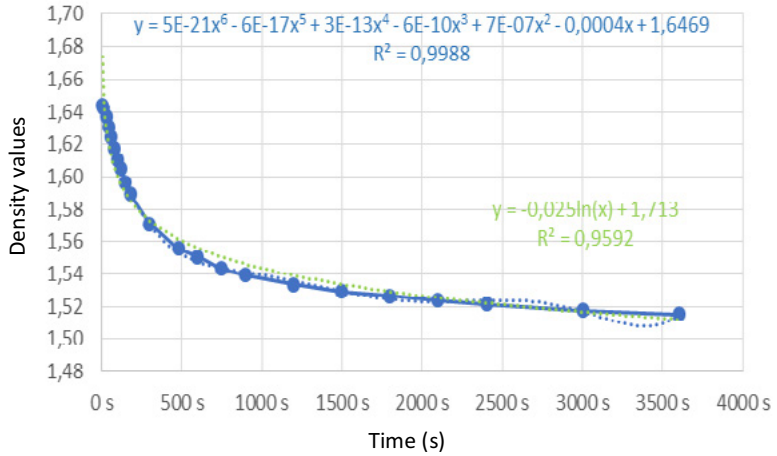

Figure 9: Changes in density values for black ink on coated paper

The curves of the density values are monotonically decreasing, following a natural logarithm (at some points, n-degree polynomial) function, growing fast up to 500 s, and then slowing down (Figures 8 and 9). It is due to the reflection of the red ink, which can be eliminated by a polarization filter.

After a certain period of time (3–4 days later) the ink was fully dry. At this point, the measurements were repeated on the colour components, and with the use of the method mentioned above we calculated the colour stimulus difference between the colour of the dry ink and the ink in the drying process. The results are shown in Figures 10 and 11.

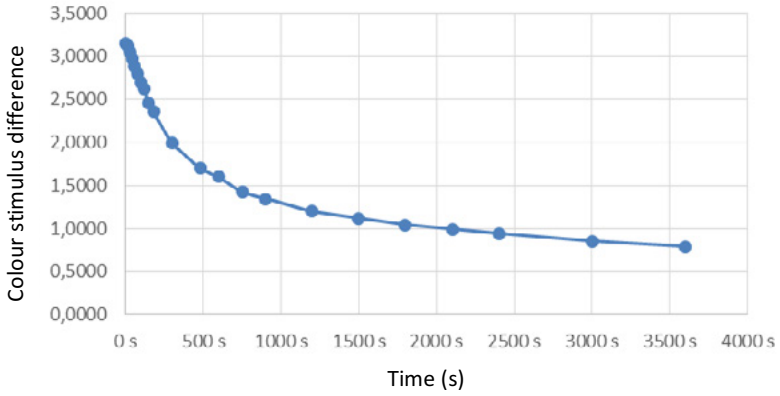

Figure 10: Changes in colour stimulus difference ΔE_{00} for black ink on uncoated paper

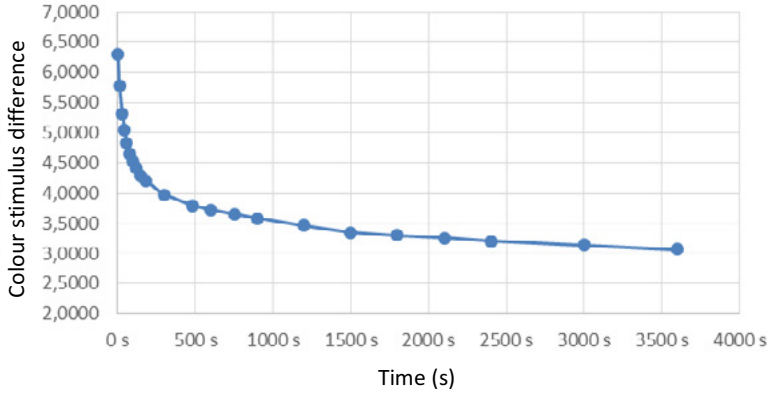

Figure 11: Changes in colour stimulus difference ΔE_{00} for black ink on coated paper

The colour stimulus difference calculations clearly show the trend of drying, that is – although none of the inks reached the final colour on paper – the colour stimulus difference between the colours becomes gradually smaller. It is also true to these diagrams that changes take place faster during the first 500 seconds, and as the ink starts to dry the ΔE_{00} change becomes less pronounced, too.

4. Conclusions

In the light of the measurements on drying, it has been concluded that on coated paper carriers all the four basic colours of offset printing ink tends to dry faster than on uncoated paper carriers. With respect to the filling ratio, the monotonically decreasing tendency is apparent, that is the degree of drying is consistent for inks, and the shortest time period of drying falls in the 1–10 minutes interval. The ink virtually dries to a touch-safe state, but to make the further processing of prints to be safe a time interval of 25–30 minutes or 180 minutes need to be left for coated paper carriers and uncoated offset paper, respectively. Consequently, for both print carriers three hours are sufficient to have the ink dried without setting.

In the second series of measurements, it has been found that the colour changes of ink on the different paper types follow the same curves (except for a few cases), and the colour alters similarly over time on the same type of paper. The colour stimulus difference of the fully dry ink changes by following the same trend (monotonic decrease), only the magnitude of the difference varies.

The functions describing these deviations and changes will be further studied under pilot production conditions. In addition to examining colour and density values, we intend to study changes in the colour angles and the brightness of colours so that from among the variable parameters mentioned at the beginning of this paper the variables defined under our 2^P experiment plan will be altered.

References

Bisset, D.E., Goodacre, C., Idle, H.A., Leach, R.H. and Williams, C.H. eds., 1979. *The printing ink manual*. 3rd ed. London: Van Nostrand Reinhold.

Breyfogle III, F.W., 1999. *Implementing Six Sigma: smarter solutions using statistical methods*. New York, USA: John Wiley & Sons.

Huber Group, 2013. *Test methods for offset inks and substrates*. [pdf] Available at: <http://hubergroup.net/pdf-files/inkformarion/INKFORMATION_4_en_02.pdf> [Accessed April 2019].

Kipphan, H. ed., 2001. *Handbook of print media*, Heidelberg: Springer.

Sahinbaskan, T. and Köse, E., 2010. Modelling of time related drying changes on matte coated paper with artificial neural networks. *Expert Systems with Applications*, 37(4), pp. 3140–3144. https://doi.org/10.1016/j.eswa.2009.09.068.

Schulz, P., 2008. Mi az igazság? *Nyomdavilág,* 1, p. 28.

Schulz. P. and Endrédy, I, 2005. *Angol-magyar nyomdaipari* értelmező *szótár*. Budapest: Mérnök és Nyomdász Kft.

Sharma, G., Wu, W. and Dalal, E.U., 2005. The CIEDE2000 color-difference formula: implementation notes, supplementary test data, and mathematical observations. *Color Research and Application,* 30(1), pp. 21–30. https://doi.org/10.1002/col.20070.

Szilágyi, T., 2011. Nyomatok kitöltési arány mérése. *Nyomdavilág*, 5, pp. 26–27.

Index of authors